Chiral Perylene Bisimide Cyclophanes

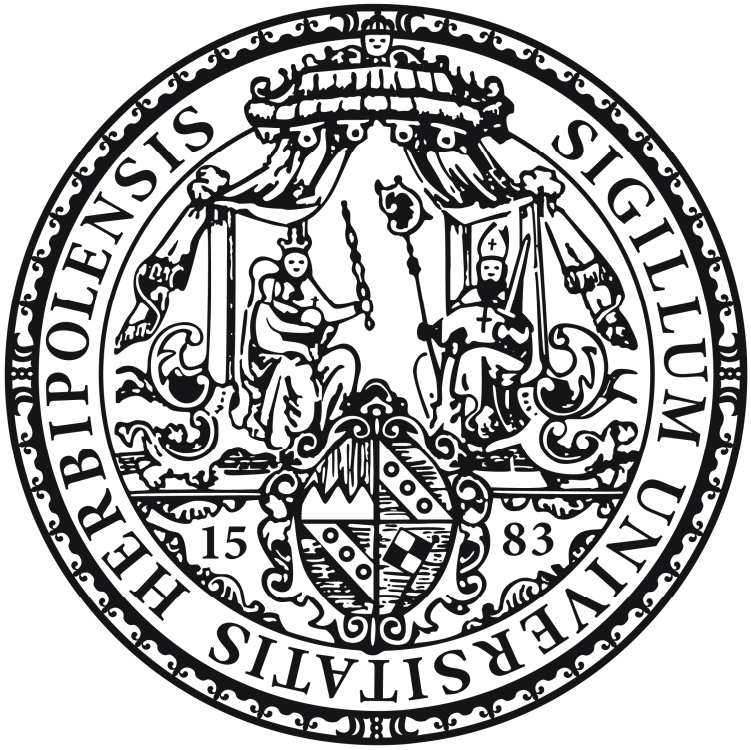

Dissertation zur Erlangung des

naturwissenschaftlichen Doktorgrades

der Julius-Maximilians-Universität Würzburg

vorgelegt von

Manuel Weh

aus Kempten (Allgäu)

Würzburg 2023

Eingereicht bei der Fakultät für Chemie und Pharmazie am

21.02.2023

Gutachter der schriftlichen Arbeit:

1. Gutachter: Prof. Dr. Frank Würthner

2. Gutachter: Prof. Dr. Florian Beuerle

Prüfer des öffentlichen Promotionskolloquiums:

1. Prüfer: Prof. Dr. Frank Würthner

2. Prüfer: Prof. Dr. Florian Beuerle

3. Prüfer: Prof. Dr. Tobias Hertel

Datum des öffentlichen Promotionskolloquiums: 28.04.2023

Doktorurkunde ausgehändigt am:

_____

List of Abbreviations:

Boc	*tert*-butoxy carbonyl
2D	two dimensional
a.u.	arbitrary unit
ALMO	absolutely localized molecular orbitals
CD	ciruclar dichroism
COSY	correlation spectroscopy
CPL	ciruclar polarized luminescence
DCM	dichloromethane
DCTB	*trans*-2-[3-(4-*tert*-butylphenyl)-2-methyl-2-propenylidene]malononitrile
DESY	Deutsches Elektronen-Synchrotron
DFT	density functional theory
DMF	dimethylformamide
EDA	energy decomposition analysis
ee	enantiomeric excess
eq.	equivalents
ESI	electrospray ionization
EXSY	exchange spectroscopy
GPC	gel permeation chromatography
HPLC	high-performance liquide chromatography
HRMS	high resolution mass spectrometry
i.e.	that is (latin: id est)
MALDI	matrix-assisted laser desorption/ionization
MCH	methylcyclohexane
mp.	melting point
NMR	nuclear magnetic resonance
NOESY	nuclear Overhauser effect spectroscopy
PAH	polycyclic aromatic hydrocarbon
PBI	perylene bisimide
PC	product complex
PES	potential energy surface
ppm	parts per million
RC	reactant complex

ROESY	rotating-frame Overhauser effect spectroscopy
r.t.	room temperature
TCE	1,1,2,2-tetrachloroethane

Physical Constants, Variables and Units:

$\Delta\varepsilon$	molar circular dichroism extinction coefficient
A	absorbance
Å	ångström
c	concentration
ΔG	Gibbs free energy
$\Delta G^{\ddagger}$	Gibbs free energy of activation
ΔH	molar enthalpy
$\Delta H^{\ddagger}$	molar enthalpy of activation
ΔS	molar entropy
$\Delta S^{\ddagger}$	molar entropy of activation
ε	molar extinction coefficient
ϕ_{fl}	fluorescence quantum yield
h	hour(s)
h	Planck constant
Hz	Hertz
J	coupling constant
K_a	binding/association constant
k_b	Boltzmann constant
k_{cat}	rate constant for the catalyzed process
K_d	dissociation constant
k_e	enantiomerization rate constant
k_{obs}	observed rate constant
k_{off}	dissociation rate constant
k_{on}	association rate constant
k_r and k_{-r}	isomerization rate constant
k_{rac}	racemization rate constant
k_{uncat} (or k_{non})	rate constant for the uncatalyzed process

I	intensity
mdeg	millidegree
R	ideal gas constant
v:v	volumetric ratio

Table of Contents

Chapter 1

Introduction and Aim of the Thesis

"The fact that contemporary supramolecular systems are highly programmable means that there is every reason to believe that the pathway to a next generation of technology, capable of addressing the challenges of wellness, environmental remediation, energy production and storage, is at hand."

This quote from a recent review article on the "emergent behavior in nanoconfined molecular containers"[1] by J. Fraser Stoddart emphasizes the importance of supramolecular chemistry as a field of research and predicts its flourishing future, but also attaches great importance to the targeted "programmability" of these systems as a prerequisite to achieve the desired various functions. Indeed, supramolecular chemistry has attracted considerable attention worldwide in recent decades and therefore a substantial progress can be observed since its beginnings. However, the role of molecular design remains paramount to the aforementioned "programmability" and, accordingly, represents one of the biggest challenges in supramolecular systems.

The impetus for the award of the first Nobel Prize in the field of supramolecular chemistry in 1987 was the development and use of molecules with structure-specific interactions of high selectivity by Donald J. Cram, Jean-Marie Lehn and Charles J. Pedersen. The forefathers of this research domain introduced the first artificial macrocyclic receptors, including (among others) crown-ethers,[2-3] cryptands,[4-5] spherands[6-7] and carcerands.[8-9] Hereby, they not only enabled ion or small neutral molecule complexation,[10-12] but also recognized that supramolecular host-guest chemistry[13] is in many ways reminiscent of substrate binding by natural receptors. Hence, in his Nobel lecture Cram described the motivation for his work as the design and synthesis of simple organic compounds that imitate processes in natural organisms. Interestingly, his considerations on the structural conception of these molecules were mainly achieved by Corey-Pauling-Koltun (CPK) molecular models, "serving as a compass on an otherwise uncharted sea full of synthesizable target complexes".[10] Thus, "in the hundreds of hours"[10] of building CPK models of desirable complex candidates, the choice of the most

promising ones was made based on geometric shape matches between potential substrates and the active binding site of a receptor.

The pioneering work of Cram, Lehn and Pedersen was followed by decades of intense research on a variety of sophisticated synthetic host structures,[14] such as pillarenes,[15-19] calixarenes,[20-22] curcurbiturils[23-26] or cyclodextrins[27-28] to name only a few of the most prominent examples. By now, such assemblies have been explored in a plethora of academic publications and in industry where significant effort has been devoted to make practical use of host-guest chemistry in numerous applications, including sensing,[29-31] drug delivery,[32-34] catalysis,[35-36] bio-imaging[37] or stabilization of reactive species.[38-39]

Already in the 1980s, cyclophanes, another class of macrocyclic hosts, had emerged as efficient receptors for guest encapsulation.[40-41] A milestone in this context is the famous "*Blue Box*" (cyclobis(paraquat-*p*-phenylene), **BlueBox^{4+}**, Figure 1) cyclophane[42-43] of J. Fraser Stoddart, which was employed in quite a few supramolecular architectures and certainly contributed significantly to his Nobel award in 2016, which he shared with Bernard Feringa and Jean-Pierre Sauvage for their work on molecular machines.[44-46]

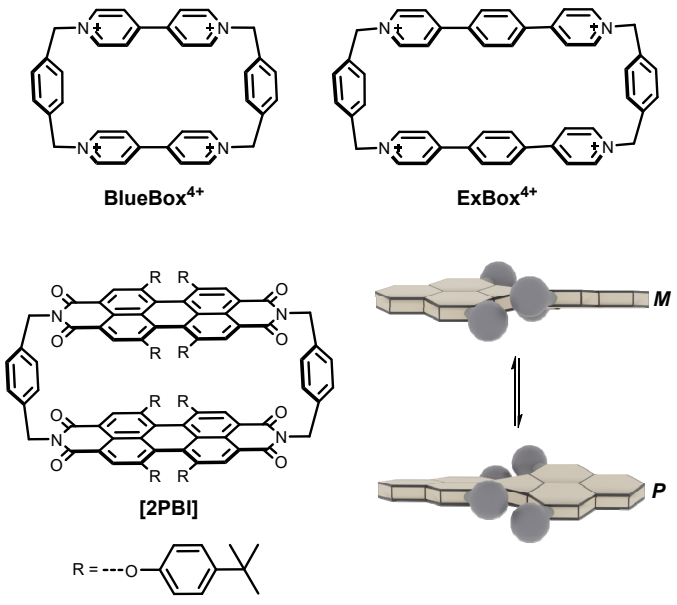

Figure 1. Chemical structures of **BlueBox^{4+}**, **ExBox^{4+}** (counterions are omitted), PBI cyclophane **[2PBI]** and schematic equilibrium between the *M*- and *P*-enantiomers of fourfold bay 4-*tert*-butyl phenoxy substituted PBIs.

Analogous to the early work of Pedersen, Cram and Lehn, the cavity of the rigid macrocyclic structure of **BlueBox^{4+}** serves as a custom fit template, which matches the size and shape of flat aromatic guest molecules. The synthetic concept of two aromatic units, connected *via* a spacer

moiety, was later exploited to tune the cyclophane's cavity size in all dimensions in order to adjust the template to the size or number of the desired guest molecule(s).[47-49]

In 2014 Siegel, Stoddart and Baldridge presented how **ExBox^{4+}** (Figure 1), one of the larger congeners of **BlueBox^{4+}**, can serve as a host for corannulene, a non-planar polycyclic aromatic hydrocarbon (PAH). A geometric distortion could be observed in the ground state of the complex, originating from a low stereoelectronic shape complementarity with **ExBox^{4+}** due to the curved nature of corannulene.[50] In comparison, corannulene's flattened transition state structure leads to optimized noncovalent interactions with the cyclophane binding site, tuning this system into a simple enzyme mimic according to the Pauling-Jencks model.[51-52] Accordingly, as a result of a distorted ground state structure and a stabilized transition state structure, the guest's bowl-to-bowl motion is significantly accelerated upon complexation. The mechanism of the rate enhancement was denoted as "induced fit catalysis" in the style of Koshland's famous "induced fit" mechanism, developed to rationalize conformational changes of enzymes or other natural receptors upon substrate recognition.[53-54]

The incorporation of perylene bisimide (PBI) chromophores, a unique class of dyes with outstanding photophysical properties and numerous functional applications,[55] in a rigidified macrocyclic structure was only recently achieved by Spenst and Würthner in 2015 (Figure 1).[56] Besides the pronounced optical response of this fluorescence probe upon PAH complexation, this cyclophane is characterized by a high conformational flexibility of the fourfould phenoxy bay substituted perylene core.[57] Accordingly, a fast interconversion even at low temperatures between the different isomers, i.e. the "*PP*", "*MM*" and "*MP*" isomers, prevents to utilize the inherent chirality of this receptor. Moreover, computational models are quite complicated due to the additional flexibility of the phenoxy substituents and thereby the resulting existence of several conformers. Therefore, it is desirable to accomplish the synthesis of a PBI cyclophane, composed of chromophores with locked core twists to get insights into the binding properties of an artificial binding site whose presumable asymmetric complexation tendency is governed only by the π-surface of a twisted aromatic.

Inspired by the role of shape complementarity and induced fit complexation and catalysis in host-guest architectures, the goal of this thesis is the design and synthesis of cyclophanes, bearing tailored chiral binding pockets, which serve as receptors of high selectivity. To this end, two different approaches, i.e. 1,7-bay bridging and fourfold bay arylation, should be applied to obtain stable helically twisted PBIs, which should be integrated into a cyclophane structure by

linking them *via para*-xylylene bridges (Figure 2). Apart from detailed studies on the binding properties of the envisioned host molecules, the enantiospecifc binding and the transfer of chiral information to flexible guest molecules should be investigated and rationalized with the help of both, experimental and computational models. The mimicry of natural enzymes is furthermore tested with the help of kinetic studies on the performance of one of the chiral cyclophanes as a π–π catalyst.[58]

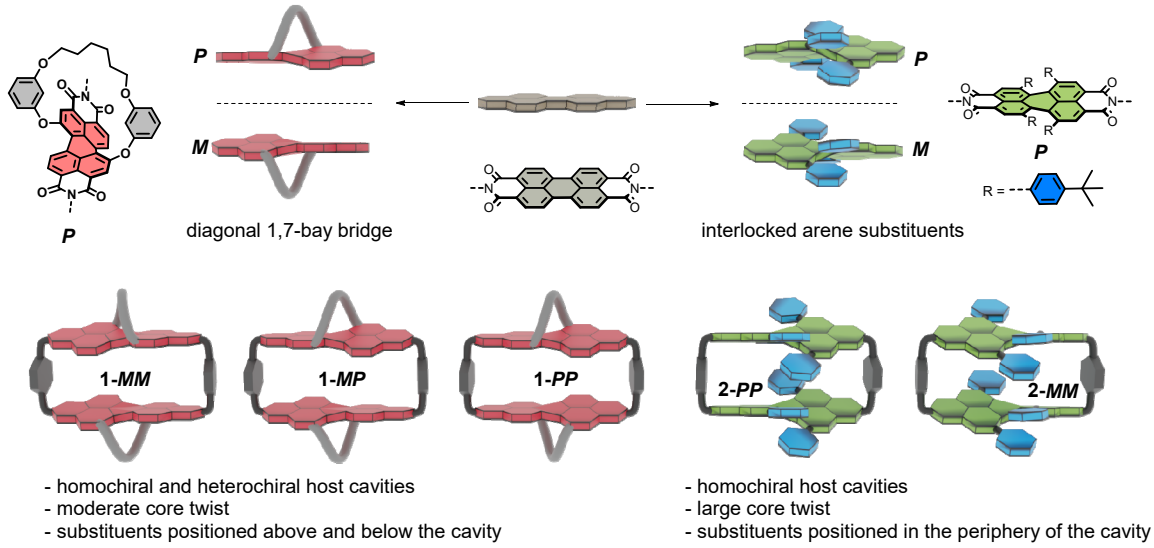

Figure 2. Schematic overview on the concepts (top) applied in the present thesis for the realization of different *para*-xylylene linked chiral PBI chromophores **1-*MM***, **1-*MP***, **1-*PP***, **2-*PP*** and **2-*MM*** (bottom), which should serve as supramolecular host molecules.

Chapter 2 summarizes recent literature on chirality transfer in host guest assemblies and gives an overview as well as a historical background on the literature of "induced fit" phenomena in supramolecular chemistry. Here, the origin of this concept and its changing definition over time will be reviewed to put the term "induced fit catalysis", coined by Siegel, Stoddart and Baldridge, into the right context. Furthermore, a brief summary on previous work on PBI cyclophanes and on inherently chiral PBIs is presented.

In *Chapter 3* the first inherently chiral PBI cyclophanes (**1-*PP*** and **1-*MM***) are introduced and investigated as hosts for small carbohelicene complexation in detail. Here, the ability of these cyclophane templates to imprint their configuration onto [4]- and [5]helicene and the resulting complex structures are elucidated by different experimental techniques.

The following *Chapter 4* builds on the previous chapter and deals with the impact of the PBI cyclophane **1-*PP***, introduced in *Chapter 3*, on the enantiomerization kinetics of [5]helicene,

which is investigated by time dependent spectroscopic studies and compared to the corresponding meso cyclophane congener (**1-*MP***). Finally, the unprecedented observations on the helicene enantiomerization within the cyclophanes are rationalized by theoretical methods.

The structural influence of the twisted chromophores of **1-*PP*** on the flat transition state structure of corannulene is investigated by DFT calculations and proven experimentally with the help of a transition state analogue in *Chapter 5* to explore the mutual conformational adaption of both parts of the complex, i.e. host and guest, in the transition state.

In order to tune the complexation specificity of the host receptor, the synthesis of newly designed chiral PBI based cyclophanes (**2-*PP*** and **2-*MM***) is presented in *Chapter 6*. Hereby, the introduction of sterically demanding interlocked bay substituents is employed to rigidify the host and subsequently to study the importance of the guests' structural adaption upon encapsulation. Furthermore, fourfold bay arylation should allow, as opposed to *Chapter 3,* the preferential formation of heterochiral complex structures, which is demonstrated by an elaborate experimental and theoretical analysis of the resulting host-guest assemblies.

Chapter 7 and *Chapter 8* conclude this work and give a summary of this thesis in English and German.

Chapter 2

Literature Survey

Stereoelectronic shape complementarity is crucial for strong and specific binding in both, natural systems and artificial supramolecular assemblies. While receptors or substrates in the unbound state often exist in multiple conformations that are in equilibrium by overcoming small kinetic barriers, complexed species usually exist in the form of structurally more defined entities. Accordingly, the focus in this chapter is on the role of structural optimization during or before the binding process. Indeed, the following literature survey will elaborate why the question of "during" or "before" may play a significant role in this context. First, however, chirality transfer in host-guest complexes will be discussed, leading seamlessly to the concept of "induced fit", its origin and role in supramolecular complexes, before the term "induced fit catalysis" is introduced. The last parts of this chapter deal with the helical chirality of core-twisted perylenes and relevant previous work on PBI-based cyclophanes.

2.1 Chirality Transfer in Host-Guest Assemblies

The fundamental work of Louis Pasteur on the first successful resolution of the enantiomers of ammonium tartrate in the middle of the 19th century laid the foundation for the scientific field of molecular chirality.[59-60] Today, the use and role of chirality in bioactive substances,[61-63] agriculture[64-65] and organic electronics and photonics[66-69] is omnipresent. Many of these applications require enantiomerically pure or enriched compounds, which is often challenging to achieve. Therefore, different methods have been developed to obtain non-racemic compounds by breaking the symmetry of racemic mixtures. One approach for the realization of enantiomerically pure or enriched compounds represents the method of deracemization,[70-74] a concept that constitutes any process during which a racemate is converted into a non-racemic product in quantitative theoretical yield without intermediate separation of materials.[75] In contrast to the frequently used classical kinetic racemate splitting, this method can therefore achieve yields of more than 50% of the desired enantiomer and is accordingly much more economical.

Chirality transfer in supramolecular host-guest assemblies, sometimes also denoted as chirogenesis, is a powerful tool to induce a specific configuration *via* suitable synthetic cavities. Upon complexation, the transfer of asymmetric information through noncovalent interactions from a chiral host to a substrate or vice versa can be achieved.[76] More than 20 years ago, the group of Rebek Jr. has for instance demonstrated how dimeric capsules, consisting of two achiral monomers, held together by hydrogen bonding, produce dissymmetric cavities, which bind chiral guests in a diastereoselective fashion with apparent associations constants of around 10^2–10^3 M^{-1} in *para*-xylene-d_{10} at r.t.[77-78] In the presence of symmetrical guests, the dimeric assembly exists as a racemic mixture of enantiomers. However, upon chiral substrate binding, the dynamic nature of the capsules, which can undergo interconversion by association and dissociation, allows the enrichment of the energetically preferred complex as demonstrated by ^{1}H NMR spectroscopy. In the case of (+)-pinanediol as a guest a diastereomeric excess of 50% was achieved. Notably, the memory effect of this system allows the chiral imprint on these capsules for hours as a result of slow re-equilibration upon chiral guest removal.

Metalorganic coordination cages emerged as another popular and well-established class of supramolecular hosts over the last decades. The mechanistic interplay between light switching and guest binding in photochromic [Pd_2dithienylethene$_4$] coordination cages was investigated by the group of Clever in 2019 and represents another example of supramolecular deracemization.[79] The cage exists as a mixture of *P* and *M* helical conformations in its "open" photoisomeric form. After the binding of *R*-(−)- or *S*-(+)-camphor sulfonate (CSA), chirality transfer from guest to host could be detected by CD spectroscopy. Upon irradiation of the host-guest complex, the induced chirality was locked due to the formation of a configurationally stable "closed" isomer and could be quantified with an *ee* value of 25% for the closed state of the formerly racemic host.

In the same year, Yashima and co-workers reported a systematic study on the deracemization of a racemic double-stranded spiroborate helicate with bisporphyrin units upon encapsulation of chiral aromatic guests (Figure 3a).[80] The authors referred to the so called "Pfeiffer-effect"[81] as a general concept, which describes the deracemization of a racemic mixture into a non-racemic one in the presence of chiral species. After guest inclusion by the helicate host **3**, a complex is formed which exists as a mixture of right- and left-handed double helices. The double-stranded helicate-guest complex is kinetically inert toward racemization. However, upon the addition of catalytic amounts of water (Figure 3b), a reversible diastereoselective B-O bond cleavage and reformation is initiated, which allows the interconversion of the helicity

and thus produces an optically active helicate in the presence of a chiral guest due to the preferred formation of one diastereomeric complex (Figure 3c). Eventually, the chiral recognition ability of the host was additionally proven by ^{1}H NMR spectroscopy, supporting the diastereoselective complex formation (Figure 3d).

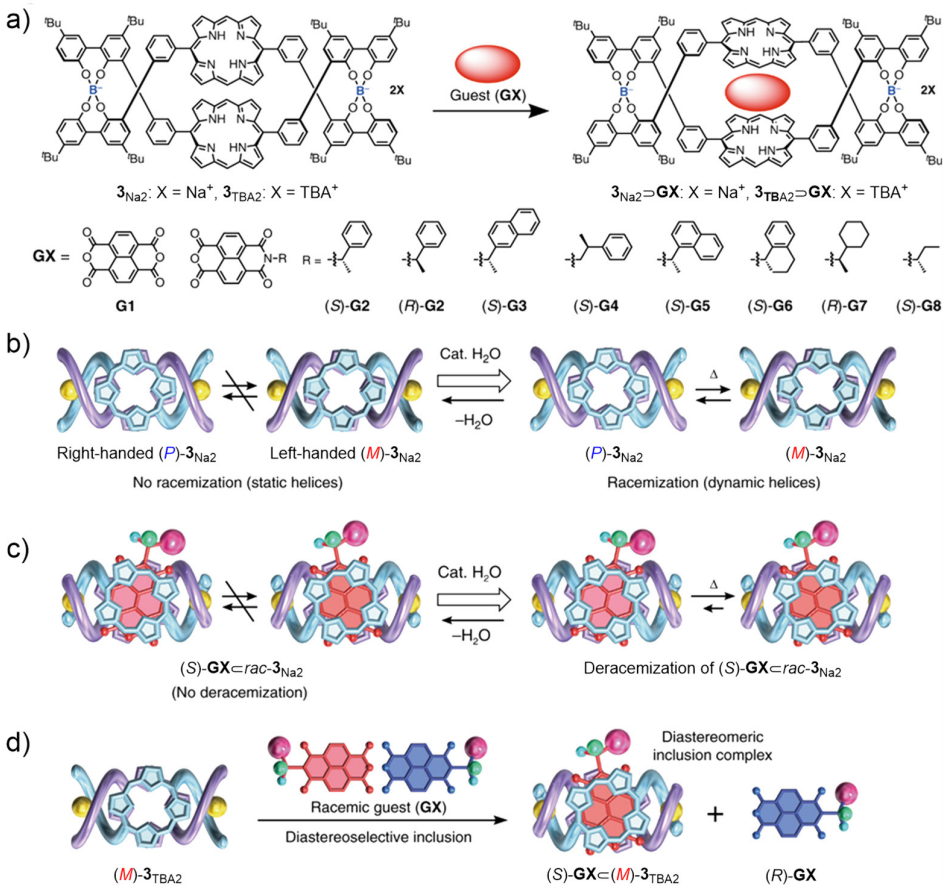

Figure 3. a) Chemical structures of double-stranded bisporphyrin helicates $\mathbf{3}_{X2}$ (X = Na$^+$ or TBA$^+$ (= tetra *n*-butyl ammonium)) and a schematic representation of their inclusion complexes with electron-deficient aromatic guests **G1**–**G8**. Schematic representations of b) the water-catalyzed racemization of *rac*-$\mathbf{3}_{Na2}$, c) the deracemization of *rac*-$\mathbf{3}_{Na2}$ upon complexation of an enantiopure guest and d) the diastereoselective encapsulation of racemic guest with left-handed (*M*)-$\mathbf{3}_{TBA2}$. Adapted with permission from Ref [80]. Copyright 2019, Springer Nature.

Despite the potential application of chiral host-guest complexes in the field of deracemization, most examples of chirality transfer in host-guest chemistry are concerned with the idea of sensing,[82] to determine the enantiopurity of substrates[83-84] or to assign the absolute configuration of guest molecules.[85-86] Especially noteworthy in this context are *bis*-porphyrin based receptors, which show distinct CD signals upon chiral guest encapsulation due to excitonic coupling between the chromophores, thus allowing the discrimination of enantiomers, which was explored in detail by several groups.[87-90]

A particularly inspiring application for the transfer of chiral information was presented by Huang, Wang, Hong and co-workers in 2020.[91] The authors addressed the problem of cryptochiral compounds, which exhibit chirality but lack a measureable optical rotation and are therefore difficult to characterize. Water-soluble pillarene hosts (**4** and **5**) were shown to act as detectors for some of these compounds like arginine or lysine by inducing a CD signal upon guest complexation in water (Figure 4a). NMR and ITC studies revealed binding constants of around 10^3 M^{-1}. The observed amplified CD signal upon the encapsulation turned out to be dependent on the binding strength. It originates from a chiral match/mismatch effect of pillarene and the guest within the diastereomeric complexes. Most importantly, however, the two enantiomers of the guest molecules always induce an opposite CD signal, which enables the characterization of cryptochiral compounds by optical spectroscopy.

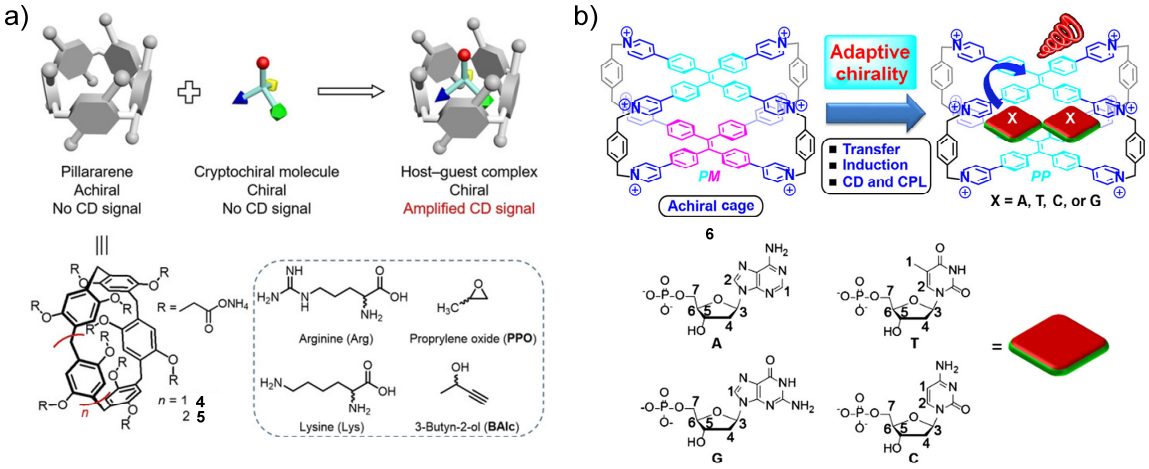

Figure 4. a) Schematic representation of achiral pillarene host and the complexation of several cryptochiral guests, as well as their corresponding chemical structures. b) Structure of tetraphenylethene based host **6** and schematic depiction of the induced chirality upon the encapsulation of deoxynucleotide dimers. Adapted with permission from Ref [91] (Figure 4a) and Ref [92] (Figure 4b). Copyright 2020, WILEY-VCH Verlag GmbH & Co. KGaA, Weinheim and 2021, Chinese Chemical Society.

Similar guest-mediated chirality transfer was investigated by Würthner and co-workers. The encapsulation of enantiopure aromatic guests, equipped with a substituent, bearing a chirality centre, i.e. an asymmetric carbon atom, resulted in chirality induction in a flexible 1,2,6,7-tetraphenoxy PBI based cyclophane **[2PBI]** (see *Chapter 1*). The "central-to-axial chirality transfer" induces a positive or negative CD signal in the absorption range of the twisted chromophores (see *Chapter 2.4.2*), depending on the absolute configuration of the guest.[57] Furthermore, the authors tried to elucidate the mechanism of the chirality transfer by rate constant analysis (see *Chapter 2.2.2*), which could eventually not be achieved.

Analogous to an induced CD effect upon chiral guest encapsulation, in 2020, induced circularly polarized luminescence (CPL) was demonstrated with a tetraphenylethene host (Figure 4b).[92] Hereby, the adaptive chirality of receptor cage **6** serves as a prerequisite for the induced CPL emission. Its octacationic character made studies in water possible, thus enabling the encapsulation of deoxynucleotide dimers, which induced a "*PP*" configuration in the host. As a result of the preferential formation of one epimeric inclusion complex, distinct CPL emission of the host-guest assembly could be detected.

2.2 Induced Fit Complexation

The selected literature examples, presented in *Chapter 2.1*, gave an overview on the role of conformational adaptivity in host-guest complexes for the supramolecular transfer of chirality, which might also be denoted as *induced* chirality. In fact, the famous term "induced fit" describes a kinetic signature of conformational adaption of a receptor to a substrate, whose shape is not complementary with the active binding site. Such kinetic regulations often play an important role in complex physiological processes, which has for instance been demonstrated for DNA replication with a mutant of the T7 DNA polymerase, where an induced fit kinetic mechanism could be observed.[93]

The term "induced fit" is particularly popular in the field of supramolecular chemistry and should be considered carefully in any work here. In the following chapters, first general considerations on guest recognition mechanisms are made to point out the origin of the concept (*Chapter 2.2.1*). Afterwards, a literature overview on "induced fit" in supramolecular chemistry is given. It will be demonstrated that this concept can indeed be applied to artificial host-guest systems (*Chapter 2.2.2*). Nevertheless, the original meaning got lost in this community (*Chapter 2.2.3*) and the term is applied rather loosely today, describing conformational distortion upon complex formation.

2.2.1 Origin and Mechanistic Background

The recognition of substrates by suitable receptors is of paramount importance not only for the design of effective drugs and therapeutics but also for a basic understanding of many natural processes with confined environments for specific functions.[94-95] This is probably also the reason why the mechanisms for these binding events were first perceived from a biochemical and biophysical point of view. Hermann Emil Fischer recognized already more than 100 years

ago the different behavior of stereoisomeric hexoses in the presence of yeast and consequently hypothesized that yeast's active chemical agents can interfere only with those sugars that have a related configuration.[96] Eventually, he explained his observation with the famous "lock-and-key model", which is still often applied to describe and rationalize specific binding: "To use a picture I would like to say that enzyme and glucoside have to fit together like lock and key in order to exert a chemical effect on each other".[97] In this model, perfect shape complementarity between a rigid substrate and an equally rigid receptor is assumed to be responsible for efficient binding due to optimized noncovalent interactions between them (Figure 5).

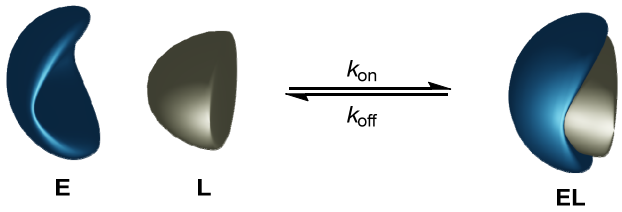

Figure 5. Schematic representation of Fischer's "lock-and-key principle" with an equilibrium between a natural enzymatic receptor E and ligand L, which have a perfect shape complementarity and form the complex EL without undergoing conformational changes.

Besides the thermodynamic parameters that describe the complexation and decomplexation event, i.e. the association and dissociation constants, the kinetic profile is in this context especially meaningful as it is characteristic to assign the respective binding mechanism. The complexation step and the reverse process are characterized by the second-order rate constant k_{on} [M^{-1} s^{-1}] for ligand binding and the first-order rate k_{off} [s^{-1}] for ligand dissociation and can be therefore expressed as the two differential equations[98]

$$\mathrm{d[E]}/\mathrm{d}t = -k_{on}[\mathrm{L}]\,[\mathrm{E}] + k_{off}\,[\mathrm{EL}] \tag{1}$$

and

$$\mathrm{d[EL]}/\mathrm{d}t = k_{on}[\mathrm{L}]\,[\mathrm{E}] - k_{off}\,[\mathrm{EL}] \tag{2}$$

which are in matrix form as follows:

$$\begin{pmatrix} \mathrm{d[E]}/\mathrm{d}t \\ \mathrm{d[EL]}/\mathrm{d}t \end{pmatrix} = \begin{pmatrix} -k_{on}\,[\mathrm{L}] & k_{off} \\ k_{on}[\mathrm{L}] & -k_{off} \end{pmatrix} \begin{pmatrix} [\mathrm{E}] \\ [\mathrm{EL}] \end{pmatrix} \tag{3}$$

The non-zero eigenvalue $-\lambda$ of this 2 × 2 matrix corresponds to the observed rate constant k_{obs} and can be expressed as:

$$-\lambda = k_{obs} = k_{off} + k_{on}[L]. \quad (4)$$

The observed rate constant k_{obs} increases according to the lock-and-key principle linearly with the ligand concentration. As a result of the linear dependence of k_{obs} on [L], the association and dissociation rate constants k_{on} and k_{off} can be derived from the slope and the intercept of the function.

Emil Fischer is still a coriphae of organic chemistry today and was undeniably awarded rightly with the Nobel Prize in 1902 for his scientific achievements. However, the quite simple and descriptive model proposed by him has an essential disadvantage: Proteins and other natural receptors, e.g. enzymes, are inherently dynamic and sample a vast ensemble of conformations with three-dimensional structures. To achieve strong binding in an enzyme-ligand complex, the corresponding receptor must optimize noncovalent interactions by adjusting its conformation. A single step mechanism with two rigid reactants, fitting together like a lock and a key is in most cases therefore not applicable to describe the kinetics of complex formations. Furthermore, the inclusion of conformational changes is crucial for many biochemical processes, especially for allosteric control.[99-104] The probably most prominent example in this context represents the positive allosteric control of oxygen binding in hemoglobin[105] whose binding affinity increases after each complexation step owing to favorable conformational changes in the neighbouring binding sites.[106] Accordingly, Fischer's concerted model was finally extended by Koshland in 1959 to the “induced fit model” (or “Koshland-Némethy-Filmer (KNF) model”).[107]

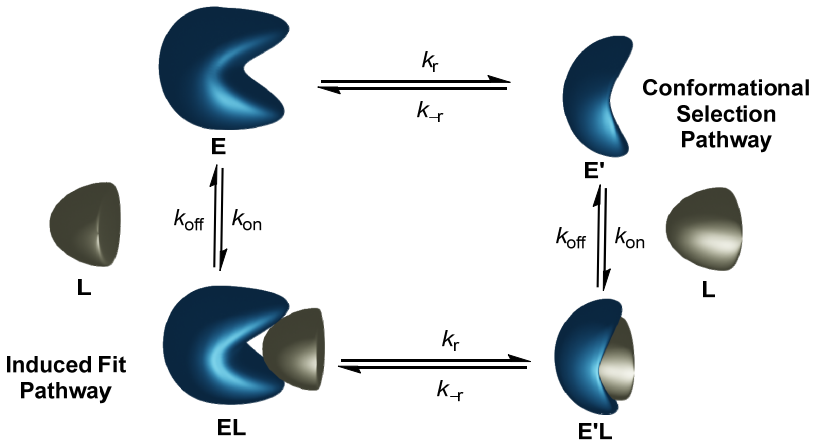

Figure 6. Schematic depiction of the induced fit model and the conformational selection model for an enzyme (blue) with two conformations E and E’ and a rigid guest L (light brown).

Alternatively, Monod, Wyman and Changeux have proposed a model named after them, also known as "conformational selection mechanism".[108] In both mechanisms, complex formation is divided into two steps, i.e. the complexation step itself and the conformational change of the receptor, which is schematically depicted in Figure 6. In contrast to conformational selection, the induced fit mechanism describes a shape adjustment of the receptor *after* the substrate has already been bound by the receptor. An expression for the rate constant k_{obs} can also be derived for these two cases, in analogy to the lock-and-key principle (*vide supra*).[98] Accordingly, one can deduce an expression for k_{obs} for an induced fit (equation 5) and for conformational selection (equation 6) as follows:

$$k_{obs} = k_{-r} + k_r \frac{K_a[L]}{1+K_a[L]} = k_{-r} + k_r \frac{[L]}{K_d+[L]} \quad (5)$$

$$k_{obs} = k_r + k_{-r} \frac{1}{1+K_a[L]} = k_r + k_{-r} \frac{K_d}{K_d+[L]} \quad (6)$$

In equations 5 and 6, the association constant K_a and the dissociation costant K_d can also be expressed as $K_a = k_{on}/k_{off}$ and $K_d = k_{off}/k_{on}$. Besides the association and dissociation rate constants k_{on} and k_{off}, the additional rate constants k_r and k_{-r}, which describe the equilibrium between two conformations of the receptor, need to be considered. Notably, both equations are only valid under the assumption of the "rapid-equilibrium approximation", which states that the ligand binding event is fast compared to the conformational changes. According to these equations, some important parameters can be extracted from the corresponding plot of k_{obs} over [L] by limit value considerations (Figure 7).

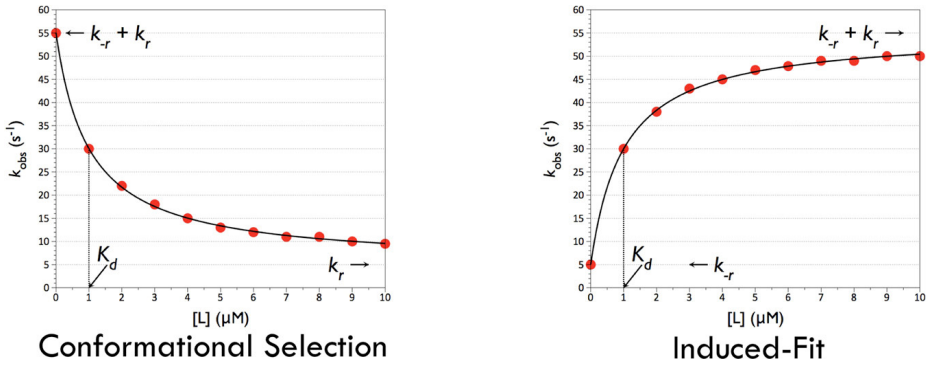

Figure 7. Under the rapid equilibrium approximation, the rate of approach to equilibrium, k_{obs}, is an inverse hyperbolic function of the ligand concentration for a conformational selection mechanism (equation 6), from which the values of k_r and k_{-r} can be derived. In the case of an induced fit, the rate of approach to equilibrium, k_{obs}, is a hyperbolic function of the ligand concentration (equation 5) from which the values of k_r and k_{-r} for the complex interconversion can be derived. For both cases, the dissociation constant K_d is also accessible from the corresponding plot. Adapted with permission from Ref [98]. Copyright 2012, American Chemical Society.

Derived from equations 5–6, it has long been assumed that a hyperbolic increase of k_{obs} with increasing ligand concentration is a proof for an induced fit mechanism while a hyperbolic decrease indicates a dominant conformational selection. Hence, under the rapid equilibrium approximation, the dependence of k_{obs} on ligand concentration [L] should be diagnostic of the mechanism of binding. However, more recent considerations without the simplification of the rapid-equilibrium approximation have shown that only a hyperbolic decrease allows an unambiguous finding and that a hyperbolic increase can be explained by both mechanisms under certain circumstances.[98, 109] Accordingly, this finding also explains the dominance of the induced fit mechanism in the biochemistry literature as the kinetic profile that conformational selection produces, overlaps with that of induced fit.

Besides the use of computational modelling of protein structures,[110] general theoretical results for the chemical relaxation rates of binding mechanism processes beyond the pseudo-first-order kinetics (which are commonly applied for rate constant analysis) revealed that sufficiently large protein concentrations (host concentrations) allow more characteristic features of k_{obs} as a function of the ligand concentration.[111] Moreover, another practical solution for indistinguishable kinetic patterns might also be a comparison of kinetics with excess of the host *versus* excess ligand. While for induced fit no changes can be expected, the hyperbolic increase with excess ligand should turn into a straight line or a constant value with excess host for conformational selection, which has been tested for several systems in literature.[112-113]

An unambiguous mechanistic assignment to one of the two presented models is for the above-mentioned reasons often difficult. Furthermore, competing induced fit and conformational selection mechanisms do not always correspond to reality, as they may not be mutually exclusive and may co-exist in some systems (*vide infra*). In addition, especially large biomolecule substrates, acting as guests, might also undergo conformational changes, resulting in a mutual conformational adaption of both, the host and the guest (*vide infra*). On the other hand, the seemingly obsolete lock-and-key principle is able to describe a system characterized by multiple receptor conformations properly if the isomerization step is rapid, making them indistinguishable on the time scale of practically applicable measurement methods.[114] Therefore, each individual system requires extensive studies and a deep understanding of complex formation (and the corresponding kinetics) to apply the correct model and to draw the right conclusions. One instructive way to better understand these complex natural processes is to use structurally less complicated artificial supramolecular model systems that can provide fundamental insights.

2.2.2 *Excursus*: Study of the Guest Recognition Mechanism

There is less than a handful studies on the guest recognition mechanism in supramolecular systems, where the models described in *Chapter 2.2.1* were applied in their originally intended sense. The first example of elaborate mechanistic studies on the guest binding of a supramolecular host was published in 2017 by the Bergmann, Raymond, Toste collaboration.[115] Extensive NMR studies on the host isomerization, i.e. conventional proton NMR studies and proton SIR (selective inversion recovery) NMR experiments, were carried out to investigate the conformations of a gallium cage **7**, which turned out to exist either in a tetrahedral symmetry *T* or in a conformation of S_4 symmetry (Figure 8a). Subsequent kinetic studies on the complex formation revealed guest inhibition of the relaxation rates and therefore a decrease in the observed rate constant k_{obs} with increasing tetraalkylammonium guest concentration (Figure 8b). Such an inverse hyperbolic increase of the rate with increasing guest concentration is characteristic for the conformational selection mechanism (*Chapter 2.2.1*), which allowed an unequivocal mechanistic assignment. Hence, for the first time, the duality between the two mechanisms, i.e. conformational selection and induced fit, could be clarified experimentally with an artificial host-guest system.

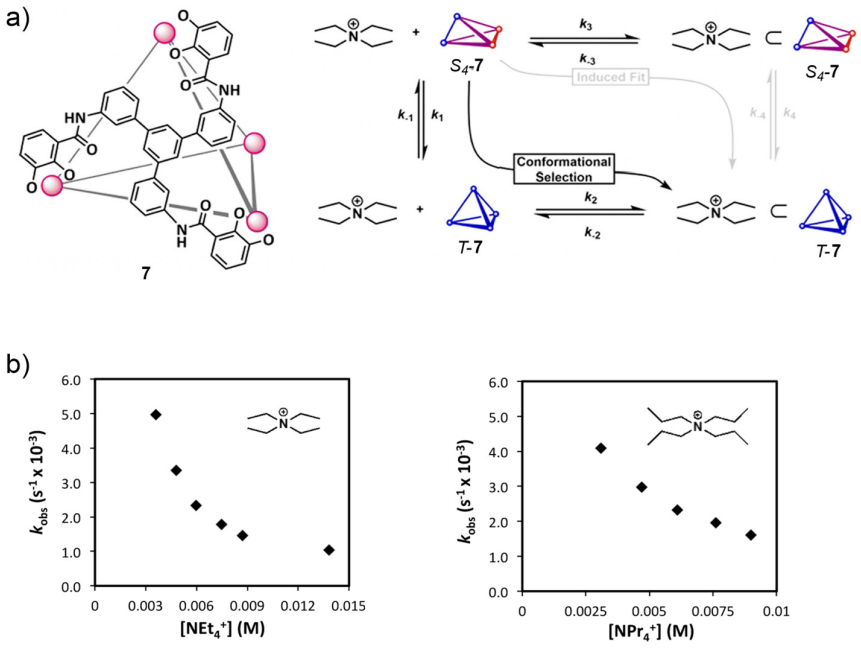

Figure 8. a) Structure of the tetrahedral gallium cage **7** with the chemical structure of the ligand and a schematic depiction of the gallium atoms in pink and the two competing guest recognition mechanisms for the complexation of tetraethylammonium guest by the metal cage. b) Plot of k_{obs} as a function of [NEt_4^+] and [NPr_4^+], showing the characteristic decrease of the relaxation rate with increasing guest concentration for conformational selection. Adapted with permission from Ref [115]. Copyright 2017, American Chemical Society.

The second example of conformational selection as the predominant binding mechanism was presented in 2020 within the framework of a study on a macrocyclic host (**8**, Figure 9a) that exists in solution in two of five possible conformations, as shown by NMR studies and further supported by DFT calculations.[116] In their work, Jiang and co-workers define for the first time three criteria for an ideal host model for conformational selection as follows:

1. Two conformations coexist, and both can be detected.
2. Only one conformation binds to the ligand, and the other one has no obvious affinity.
3. Conformation exchange is kinetically slower than ligand binding.

Upon the addition of small aromatic guests (e.g. **9**) to their macrocycle, the authors observed a preferred complex formation with one of the host isomers. This is reflected in unchanged chemical shifts for one set of proton signals, while the other set of signals is significantly shifted. Further support for the selective binding by only one conformation of the host was found in the solid state structure of the complex, which was accessible by single crystal X-ray analysis.

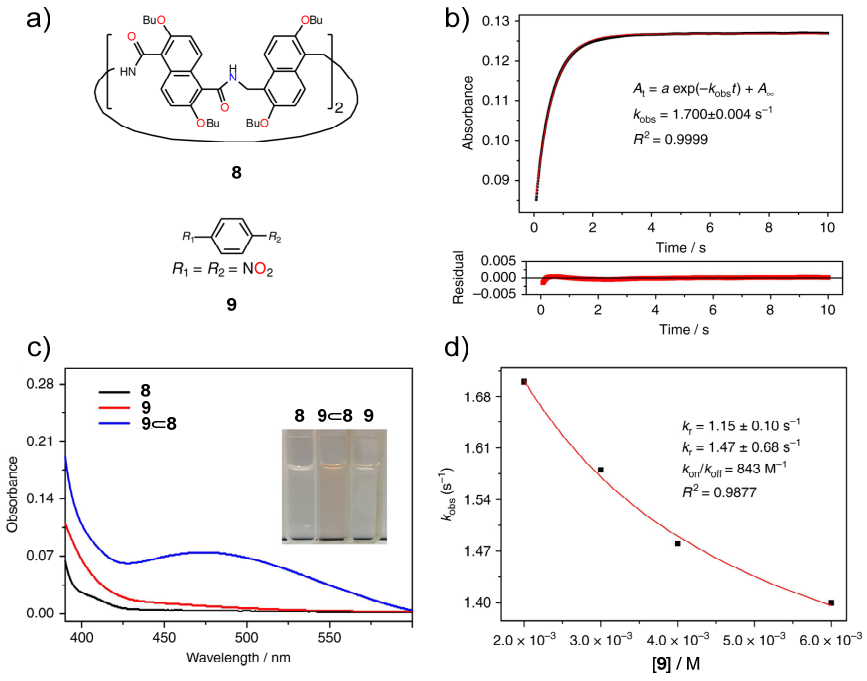

Figure 9. a) Chemical structure of host **8** and of the guest 1,6-dinitrobenzene (**9**). b) Time-dependent UV/vis absorbance at 480 nm after mixing host and two equivalents of 1,6-dinitrobenzene in DCM, fitted with single-exponential function (A_t: absorbance intensity (480 nm) at time = t, A_∞: the final absorbance intensity (480 nm), k_{obs}: observed first-order rate constant). c) UV/vis absorption spectra of the host (black), 1,6-dinitrobenzene (red) and the corresponding complex (blue) in DCM. d) Nonlinear fitting of guest concentration-dependent k_{obs} according to equation 6. Adapted with permission from Ref [116]. Copyright 2020, Springer Nature.

For an unambiguous mechanistic assignment however, a time-dependent increase in the charge transfer band of the complex upon guest addition was followed and subsequently fitted according to first-order kinetics (Figure 9b,c). A plot of the rate constant k_{obs} at different guest concentrations revealed a decreasing relaxation rate with increasing guest concentration, which was eventually fitted according to the conformational selection model (equation 6, Figure 9d). According to these two literature examples, a mechanistic assignment in the case of conformational selection seems to be well possible with the help of rate constant analysis for suitable host-guest pairs. However, as mentioned earlier, this is not always feasible for induced fit, since the presumably characeristic hyperbolic increase of k_{obs} with increasing ligand concentration may also be explained by the conformational selection mechanism (*vide supra*). Furthermore, it is also conceivable that the two mechanisms are not necessarily mutually exclusive and may co-exist with different contributions. This fact was addressed by Badjic and co-workers in 2021, who used an abiotic host as a receptor model (Figure 10a) to study the competition between the two mechanisms in detail[117] with the help of flux (i.e. mass transport rate) analyses.[118]

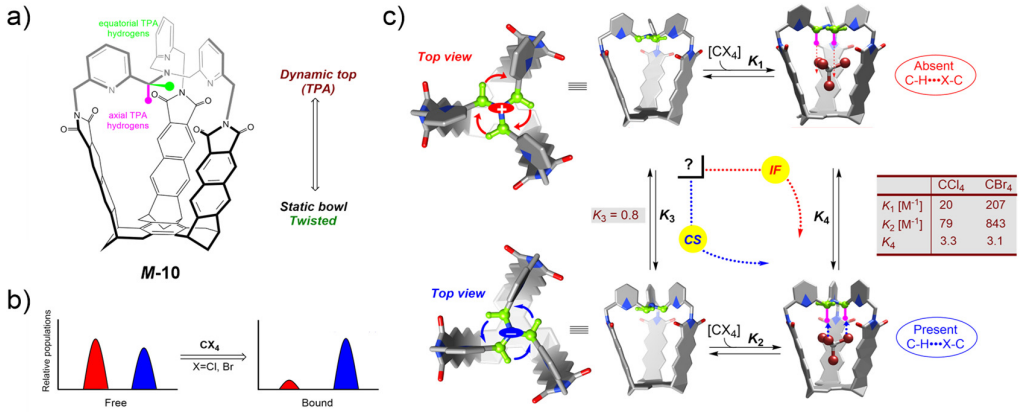

Figure 10. a) Chemical structure of capsule *M*-**10** with a conformationally flexible tris(2-pyridylmethyl)amine (TPA) group with two possible conformations, i.e. a clockwise and a anticlockwise when viewed from the top. b) Schematic depiction of guest-responsive behavior of *M*-**10**. The populations of the two conformations found in equilibrium is altered upon guest binding. c) Equilibrium between *M*-**10**(+), *M*-**10**(−), CBr_4⊂*M*-**10**(+) and CBr_4⊂*M*-**10**(−) with equilibrium constants K_1-K_4 obtained from ^{1}H NMR spectroscopy at −95 °C. Adapted with permission from Ref [117]. Copyright 2021, WILEY-VCH Verlag GmbH & Co. KGaA, Weinheim.

To this end, the various rate constants characterizing all equilibria must be determined, which the authors achieved by using (EXSY) NMR spectroscopy. In their work, a chiral capsule with a flexible tris(2-pyridylmethyl)amine (TPA) group was found to bind tetrachloromethane and tetrabromomethane at –95 °C with a preference for the formation of CX_4⊂*M*-**10**(–) compared

to $CX_4 \subset M$-**10**(+) due to the presence of stabilizing CH···XC (X = Br or Cl) interactions in this complex (studies were carried out in CD_2Cl_2, Figure 10b,c). After having collected all rate constants, describing the guest dissociation and association as well as the conformational changes of the capsule, a guest concentration-dependent plot of the host and complex isomers population could be set up according to a flux analysis (Figure 11a,b). This plot revealed that the dominance of the two mechanisms is strongly correlated with the guest concentration. At higher concentrations, the induced fit mechanism is dominant for the system under investigation while lower guest concentrations favor conformational selection. In addition, a dependence of host concentration on the fraction of flux through the conformational selection pathway was calculated. Hereby, a shift in critical guest concentration to higher concentrations was found for higher host concentrations (shift of the functions's inflection point, Figure 11c).

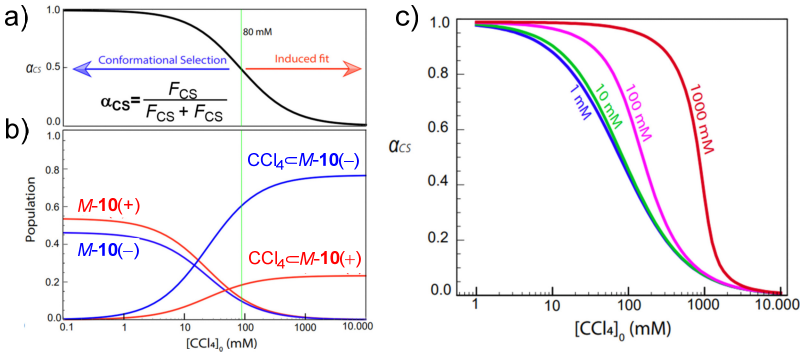

Figure 11. a) Plot of fractional flux through conformational selection, plotted against total guest concentration for [*M*-**10**] = 1.5 mM. b) Distribution of the host and complex species in the thermodynamically equilibrated state as a function of guest concentration calculated for $[M\text{-}\mathbf{10}]_0$ = 1.5 mM. c) Fractional flux through the conformational selection pathway (α_{CS}), calculated for different concentrations of *M*-**10**, plotted as a function of $[CCl_4]_0$. Adapted with permission from Ref [117]. Copyright 2021, WILEY-VCH Verlag GmbH & Co. KGaA, Weinheim.

2.2.3 "Induced Fit" in Supramolecular Chemistry

A mechanistic view on "induced fit", as it is discussed in *Chapter 2.2.1*, is rare in the supramolecular community. Usually, no distinction is made between the two relevant mechanistic models for guest binding and, in case of doubt, "induced fit" is used as a widely known and accepted concept to explain an overall shift in host conformation due to guest complexation. This fact is strikingly illustrated by a 2019 paper in which three different conformations were observed for the "*Blue Box*"-inspired "*White Box*" cyclophane $\mathbf{W}^{4+}$ under acidic conditions (Figure 12).[119] From a ^{1}H NMR titration with 2,7-dihydroxynapthalene in D_2O ($K_a \approx 10^3\ M^{-1}$), the authors concluded that the binding undergoes an induced fit mechanism, due to the shift of only one set of signals. Furthermore, the proton NMR of the

fully complexed host (end spectrum of the titration) suggested the existence of only one species. In the sense of the mechanisms presented in *Chapters 2.2.1* and *2.2.2*, however, this is not necessarily an evidence for an induced fit without further consideration of the different kinetics, but on the contrary rather a slight indication of conformational selection.[116]

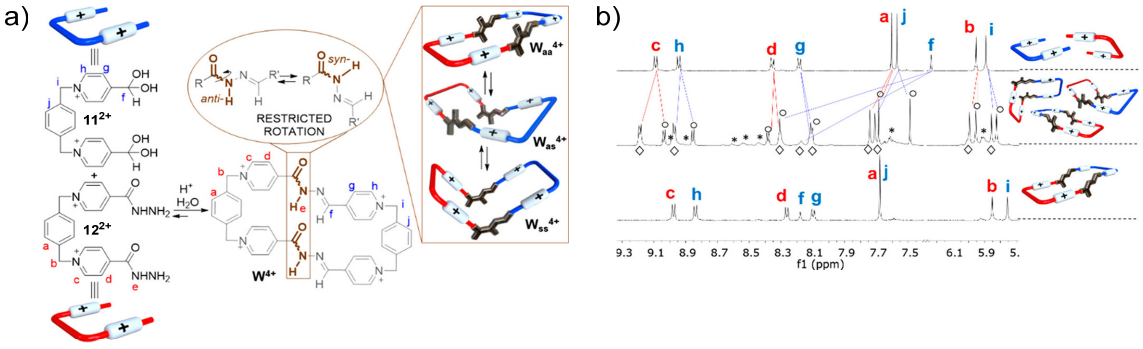

Figure 12. a) Chemical structure of cyclophane $\mathbf{W}^{4+}$ and schematic depiction of its potential isomers. b) ^{1}H NMR (D_2O, r.t., 500 MHz) of a mixture of **11**·2Br and **12**·2Br (upper), the product obtained after ion metathesis of **W**·4PF_6 with TBACl under acidic conditions (pH = 4.0, middle) and in a buffered solution at pH = 7.2 (lower). Legend: $\mathbf{W}_{aa}^{4+}$, diamonds; $\mathbf{W}_{ss}^{4+}$, circles; $\mathbf{W}_{as}^{4+}$, stars. Adapted with permission from Ref [119]. Copyright 2019, American Chemical Society.

The concept of “induced fit” emanated from biophysical questions and was only in the last years transferred to artificial supramolecular systems to gain a better understanding of substrate binding and the corresponding mechanisms. However, there are numerous examples in the literature on supramolecular systems, such as the one shown in Figure 12, in which the term "induced fit" is applied. In most of these examples it is used to describe the occurrence of conformational changes in binding events rather than to assign a mechanism or to discuss mechanistic duality.[120-125]

A perfect example in this regard is provided already in 1992 by Nolte and co-workers. It describes molecular clips that bind small aromatic guests by an induced fit mechanism as stated by the authors (Figure 13).[126] Indeed, however, the receptors were found to exist as different conformers, whose exchange processes were extensively studied by EXSY NMR in order to obtain the corresponding rate constants. One of the three conformers contains a cavity, which binds aromatic guests more efficiently and whose relative fraction increases accordingly during the complexation studies. Although this system seems to be suitable for studies on the guest recognition mechanism by rate constant analysis, likely indicating a conformational selection, the authors refer imprecisely to the term “induced fit” to describe the overall shift in host

conformation. Thus, they do not assign a binding mechanism but rather point out the structural adaption of the host that distinguishes this system from Fischer's simple lock-and-key model.

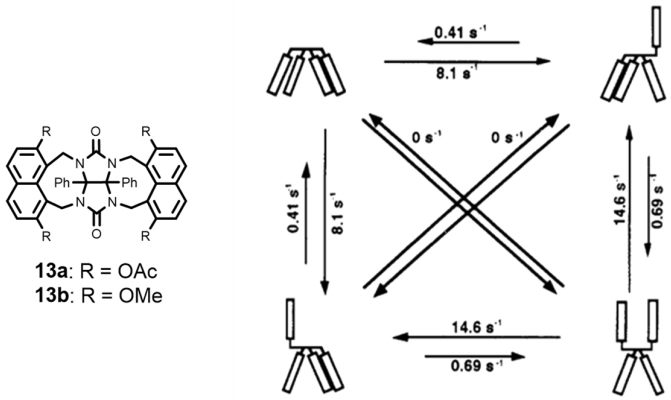

Figure 13. Chemical structure of molecular clips **13a,b** as well as the schematic depiction of the different possible conformers of **13b** and their characteristic rate constants for interconversion. Adapted with permission from Ref [126]. Copyright 1992, American Chemical Society.

Fujita and co-workers reported in 2016 a dynamic complex composed of Pd^{II} ethylenediamine (M) and 1,3,5-tris(3,5-pyrimidyl)pyrimidine (L) units. This host showed a "guest-induced $M_{18}L_6$–$M_{24}L_8$ capsule–capsule conversion" upon the inclusion of large aromatic guests, leading to an increase in the cavity volume by a factor of three.[127] Similar to the work of Fujita, in 2018, a self-assembled nanocube composed of six gear-shaped amphiphiles was shown to recognize the size, shape and the charged state of selected guests (Figure 14a).[128] As a response of complexation, the host gets distorted, i.e. compressed or expanded upon guest complexation. The "induced fit expansion and contraction" was followed by standard proton NMR and DOSY NMR spectroscopy revealing that the neutral guest molecules induce an expansion, while anionic guests lead to a contraction. This behavior was attributed to the polycationic nature of the receptor and the resulting strong electrostatic host-guest interactions.

Another example of a flexible host was presented by Stoddart and Liu in 2021, where they conclude to have an induced fit binding of **TPACage^{6+}** upon the complexation of hexa-*cata*-hexabenzocoronene derivative **OMe-*c*-HBC**, the largest nanographene guest which has been explored in the context of host-guest chemistry (Figure 14b).[129] The design of the host is inspired by the **ExCage^{6+}** (*vide infra*) and is available in a simple three steps procedure from commercially available starting materials. The binding studies on planar coronene and contorted **OMe-*c*-HBC** encapsulation revealed significantly higher binding constants for the latter of around 10^5 M^{-1} in an acetonitrile/chloroform mixture (K_a for binding of coronene is

around 10^3 M^{-1}), which the authors attributed to a better three-dimensional matching between the contorted guest and the adaptive receptor.

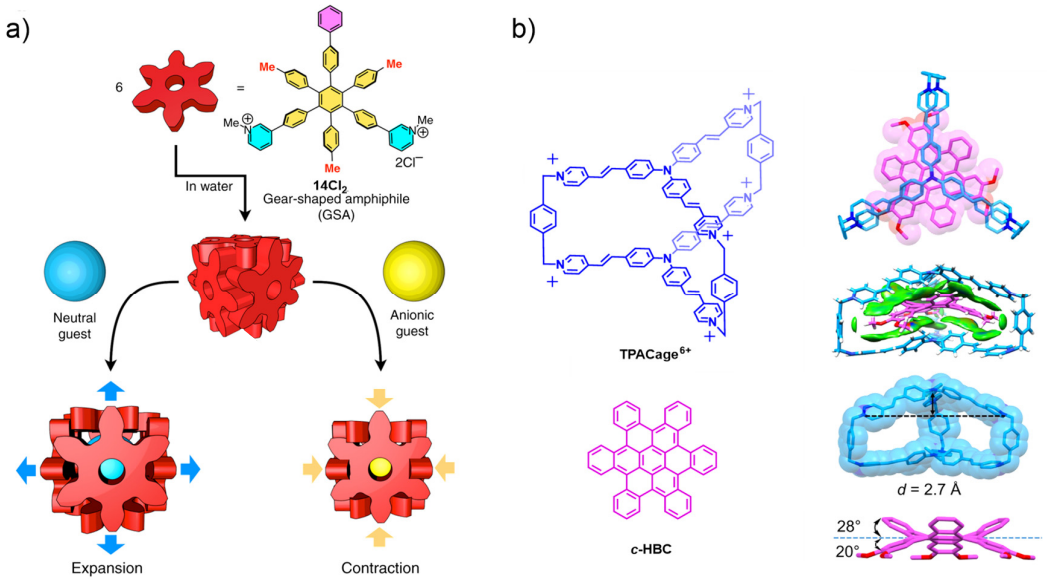

Figure 14. a) Schematic representation of a nanocube as well as the induced expansion and contraction upon guest complexation. b) Chemical structures of **TPACage**$^{6+}$ (counter ions are omitted), ***c*-HBC** and the corresponding solid state superstructure of **OMe-*c*-HBC⊂TPACage**$^{6+}$, its intermolecular binding iso-surface and the corresponding solid-state structures of individual host and guest molecules in their 1:1 complex. Adapted with permission from Ref [128] (Figure 14a) and Ref [129] (Figure 14b). Copyright 2018 and 2021, Springer Nature.

The importance of "induced fit conformational changes" in artificial enzyme-like catalysis has been vividly illustrated using adaptive coordination molecular capsule **15** that mimics a photooxidase for the generation of sulfoxides from sulfides in 2021.[130] A water-soluble capsule, composed of three anthracene-bridged bis-TPT (2,4,6-tris(4-pyridyl)-1,3,5-triazine) ligands and six bpy(Pd)$(NO_3)_2$ (bpy = 2,2'-bipyridine) moieties was hereby found to rearrange its geometry into a bowl-shape upon guest complexation (Figure 15). Phenyl methylsulfides as guests were subsequently photocatalytically oxidized within the bowl shaped capsule, yielding the corresponding sulfoxide in 85–98%. The authors describe their results as the first example of biomimetic substrate-allosteric photocatalysis with a coordination capsule.

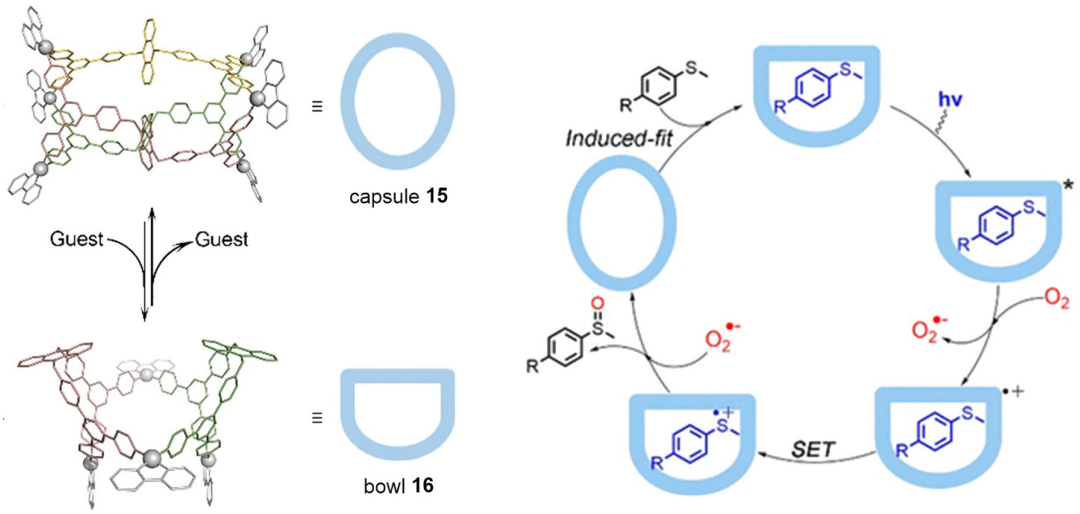

Figure 15. Schematic depiction of the adaptive induced fit transformation of capsule **15** into bowl **16** upon guest encapsulation and the corresponding suggested mechanism for the photocatalytic process of sulfide oxidation within the capsule's cavity. Adapted with permission from Ref [130]. Copyright 2021, American Chemical Society.

Another recent example of conformational adaption upon the complexation of a non-complementary guest was presented in 2020 with tetragold(I) rectangle-like metallocage receptor **19** (Figure 16).[131] Host **19** can be obtained upon deprotonation of **17** by sodium hydroxide, followed by the addition of gold complex **18** in 71% yield, which could be increased in the presence of PAHs (see Figure 16) to 82–91% due to the template effect.[132-133] Titration studies with this host in DCM revealed binding affinities up to 10^6 M^{-1} for coronene. Solid state investigations with the help of single crystal X-ray analysis showed structural differences between the free host and the complexes with flat guest molecules on the one hand and the corresponding corannulene complex on the other hand. The observation of structural adaption in corannulene⊂**19** of both, host and guest, is described as a "mutual induced fit" as a result of decreased binding affinity towards corannulene compared to the other substrates due to the lack of effective π–π stacking.

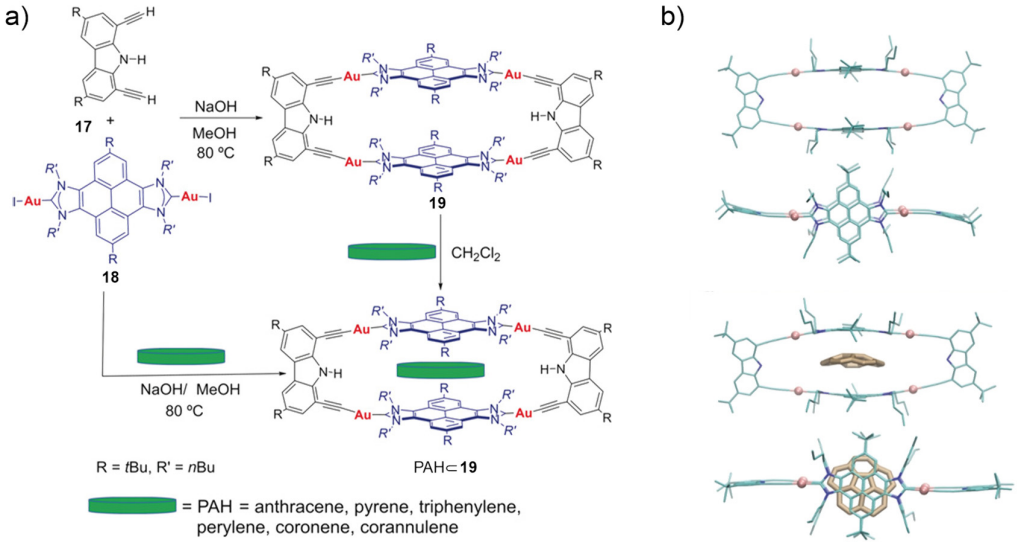

Figure 16. a) Synthesis of metallocage **19** and its complexes with PAHs. b) Molecular structures, obtained by single crystal X-ray analysis of the host and the corresponding complex with corannulene as guest molecule. Adapted with permission from Ref [131]. Copyright 2020, WILEY-VCH Verlag GmbH & Co. KGaA, Weinheim.

It is noteworthy that "mutual induced fit" represents another important but more complex mechanism and can be considered as a supplement to the induced fit binding mechanism (Figure 17a). This extended model is especially important for a complete description of substrate recognition, when large and flexible biomolecules are complexed. A similar observation as for the tetragold(I) metallacage complexation of corannulene was already presented in 2014 by Fujita and co-workers.[134] While these studies are not only based on solid-state observation but also on studies in solution, the term originally used for a binding mechanism is again applied to describe rather the overall shift in conformation than to describe the complexation mechanistically. In this literature example, a triangular ligand is able to form a library of hosts with $(en)Pd(NO_3)_2$ in theory (Figure 17b). ^{1}H NMR spectroscopy revealed a mixture of **20a** and **20b** in a ratio of 94:6. **20a** could be further proven by single crystal X-ray analysis. On the other hand, calix[4]arene (**21**) exists as a mixture of different isomers as depicted in Figure 17b. However, once the two hosts recognize each other ("host-in-a-host-complex") their conformation is fixed and the flexibility existing before is lost (Figure 17c). Thus, only **20b** and **21** in the cone formation could be detected in the complex structure, which was confirmed by single crystal X-ray analysis.

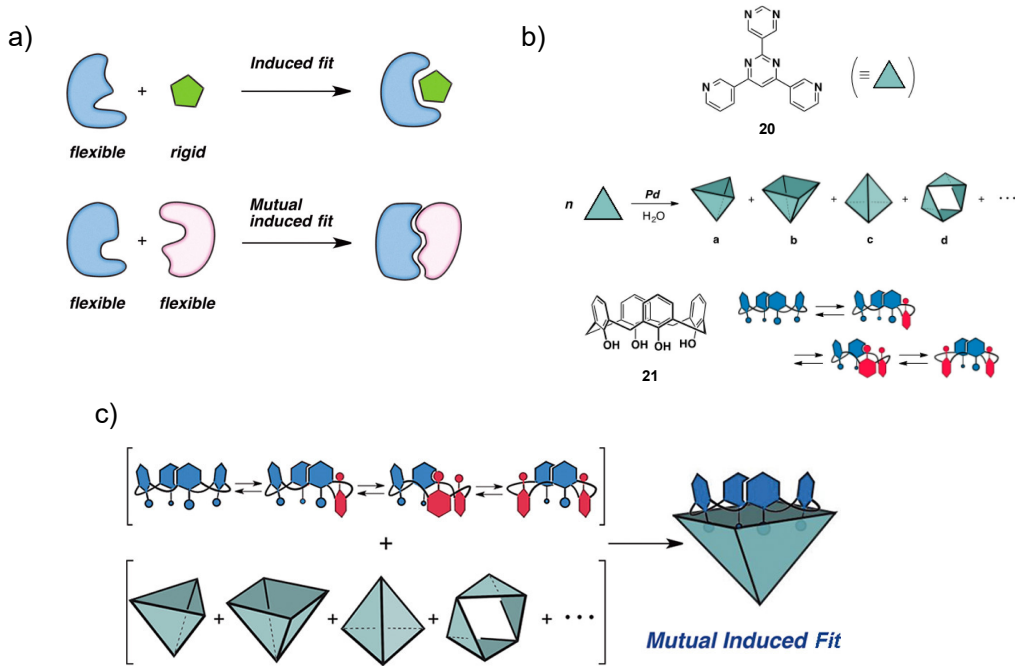

Figure 17. a) Schematic representation of mutual induced fit compared to induced fit guest recognition mechanism. b) Chemical structure of ligand **20** with cartoon representations of potential dynamic host library with (en)Pd(NO_3)$_2$ and the chemical structure of calix[4]arene (**21**) with its schematic representation of conformational isomers. c) Schematic representation of a system of **21**, ligand **20** and (en)Pd(NO_3)$_2$, which undergo a mutual induced fit. Adapted with permission from Ref [134]. Copyright 2014, American Chemical Society.

2.3 "Induced Fit Catalysis"

Supramolecular chemists have managed to get closer and closer to nature with their artificial systems. Whereas a plethora of supramolecular hosts has been synthesized with high binding affinities for a variety of guest molecules, similar to natural receptors, artificial systems that mimic enzyme catalysis according to the Pauling-Jencks model (*Chapter 2.3.1*) are sill rare. The biggest challenge in accomplishing enzyme mimicry is the efficient design of substrate binding sites that must stabilize a transition state to enhance the reaction rate. In addition, enzyme catalysis is not only attributed to the aforementioned transition state stabilization, but also to the less commonly known ground state destabilization. Both mechanisms were addressed and illustratively presented in 2014 by Stoddart, Siegel and Baldridge, who provided an alternative perspective on "induced fit" with the novel term "induced fit catalysis" to account for the observed structural rearrangements in the ground and transition state of a supramolecular cyclophane host-guest system.

2.3.1 Transition State Stabilization and Ground State Destabilization

Transition state stabilization is a fundamental concept in enzymatic reactions and was first proposed by Linus Pauling in 1948. It states that shape complementarity between a reactant and an enzyme is responsible for rate enhancements in biocatalytic processes and Pauling eventually concluded: "I believe that it is molecular size and shape, on the atomic scale, that are of primary importance in these phenomena, rather than the ordinary chemical properties of the substances, involving their power of entering into reactions in which ordinary chemical bonds are broken and formed" and "I think that enzymes are molecules that are complementary in structure to the activated complexes of the reactions that they catalyze, that is, to the molecular configuration that is intermediate between the reacting substances and the product of the reaction […]."[51]

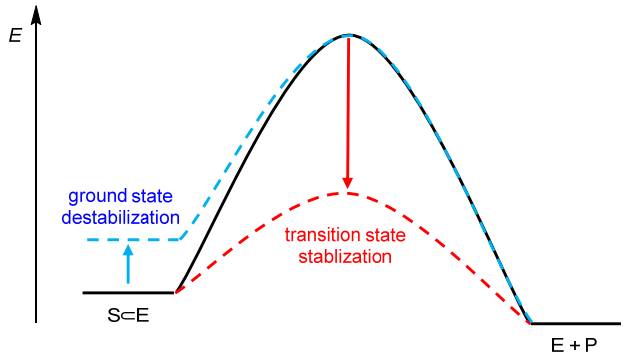

Figure 18. Simplified schematic potential energy surfaces (PES), visualizing the Pauling-Jencks model for enzyme catalysis and thereby the concepts of transition state stabilization and ground state destabilization. The black curve shows the uncatalyzed process, the blue dashed line the lowered barrier due to ground state destabilization and the red dashed line the transition state stabilized process for a reaction of a substrate S within an enzyme E, yielding the product P.

In 1978 Schowen stated that "the entire and sole source of catalytic power is the stabilization of the transition state" and that "reactant-state interactions are by nature inhibitory and only waste of catalytic power".[52] However, it finally turned out that both, the classical transition state stabilization as well as "anti-Pauling" effects, i.e. ground state effects, can contribute to the rate accelerations. Ground state destabilization as a second important concept to rationalize enzymatic catalysis was introduced by William P. Jencks.[135] He justified in his model that "in order for the mechanism of catalysis to be effective it is necessary that the destabilization be relieved at the transition state so that the free energy of activation that is required to reach the transition state is reduced".[136] Accordingly, he stated that the ground state has to be destabilized relative to the transition state to lower a reaction barrier, which is why a complete

picture of enzyme catalysis must comprise both mechanisms, transition state stabilization and ground state destabilization, which is schematically depicted in Figure 18.

2.3.2 Catalysis of Stereoinversion by π–π Interactions

Efficient substrate binding can normally be rationalized by high stereoelectronic shape complementarity between the binding site of a receptor and a guest molecule. However, according to the concept of Pauling (see *Chapter 2.3.1*) a good catalyst should have an elevated affinity towards a substrate in the transiton state compared to the ground state to achieve reaction barrier lowering. Therefore, the design of a supramolecular host catalyst should be guided by the transition state structure of the substrate rather than its ground state. In 2014 Juricek *et al.* presented how **ExBox^{4+}** (see *Chapter 1*) is able to bind corannulene with intermediate binding constants of ~10^3 M^{-1} in acetonitrile and acetone according to ITC and ^{1}H NMR studies, despite the structural mismatch between a curved substrate and a host that offers a box-shaped cavity. More importantly, subsequent investigations with the help of dynamic ^{1}H NMR spectroscopic studies revealed a significant acceleration of corannulene's bowl-to-bowl inversion upon complexation by the **ExBox^{4+}** cyclophane by a factor of 10 at r.t. (Figure 19).[50] For the analysis of the barrier, ethyl substituted corannulene was used for the variable temperature NMR series as the corresponding methylene protons become heterotopic at low temperatures and are thus diagnostic of the dynamic bowl-to-bowl inversion. Accordingly, a comparison of the dynamic motion of the complexed substrate with the free guest revealed a decreased barrier for this process by 8.7 kJ mol^{-1}. This outcome was further supported and rationalized by computational models, which suggested a stabilization of corannulene's flat transition state geometry within the host by π–π interactions as a result of a higher binding affinity of the transition state structure of corannulene compared to its ground state structure. Moreover, it was found that ground state destabilization contributes 20% to the reduction of the total barrier. The observation of a distorted guest molecule was in this context further supported by single crystal X-ray analysis of the complex superstructure. Herein, an adaption of the host's structure towards the guest concomitant with a decrease in the bowl-depth of corannulene within the cavity (ground state destabilization) is revealed, which is, however, outweighed by the complexation energy. Due to the conformational fit and structural optimization that the system undergoes to lower the reaction barrier of the process, the catalytic effect of **ExBox^{4+}** on corannulene was termed "induced fit catalysis", which represents accordingly an alternative perspective on Koshland's "induced fit" binding mechanism (see *Chapter 2.2*).

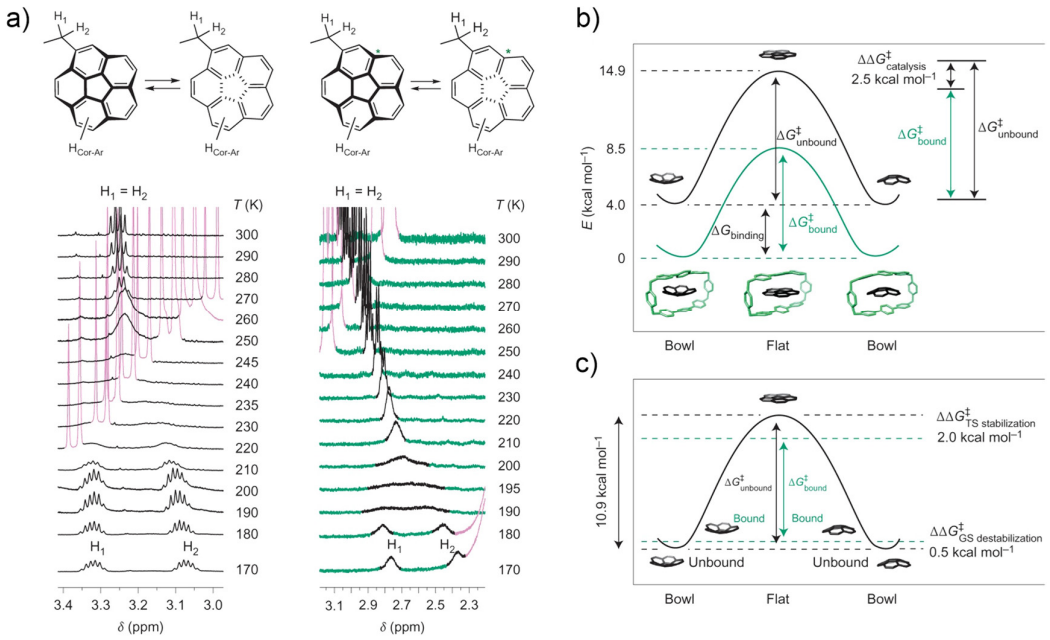

Figure 19. a) Bowl-to-bowl inversion of ethylcorannulene and variable temperature ^{1}H NMR spectra in acetone-d_6 in the absence (left) and in the presence (right) of **ExBox^{4+}**, revealing a significantly lowered coalescence temperature for the methylene protons upon guest encapsulation. b) Potential energy surfaces (PES) for the bowl-to-bowl inversion of corannulene (black) and corannulene⊂**ExBox^{4+}** (green). c) DFT calculated absolute contributions of ground-state destabilization and transition-state stabilization to the overall energy-barrier decrease of the bowl-to-bowl inversion process of corannulene inside **ExBox^{4+}**. Adapted with permission from Ref [50]. Copyright 2014, Springer Nature.

This intellectually inspiring work on the **ExBox^{4+}** cyclophane is an illustrative supramolecular example about the importance of stereoelectronic complementarity between the active site of a receptor and the transition state of a reacting substrate and has very recently, in 2022, been extended by the use of a cage host, i.e. **ExCage^{6+}** (Figure 20).[137] This host turned out to be an even better catalyst for the bowl-to-bowl inversion, and was applied to chiral 2-methoxyindenocorannulene (**iCor**), a corannulene derivative with an elevated barrier for racemization of >113 kJ mol^{-1}.[137] Time-dependent CD spectroscopic measurements of complexed enantioenriched **iCor** revealed a decreased racemization barrier by 32.7 kJ mol^{-1}, which corresponds to an acceleration of $k_{cat}/k_{non} = 3.1 \times 10^4$ compared to the uncatalyzed process at r.t. Notably this number is estimated based on equation 7, considering that the substrate is partially unbound in these experiments. Thus the observed rate constant k_{obs} is composed additively of the catalyzed (described by k_{cat}) and uncatalyzed (described by k_{non}) process and can be weighted by the factor a, describing the proportion of complexed guest.

$$k_{obs} = ak_{cat} + (1-a)k_{non} \quad (7)$$

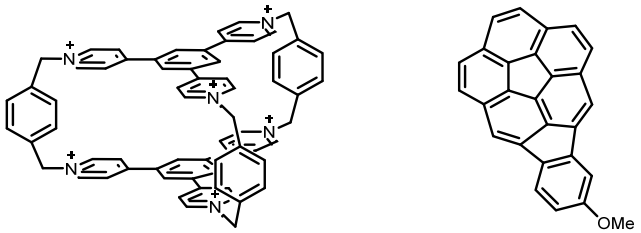

Figure 20. Chemical structures of **ExCage**$^{6+}$ (counter ions are omitted) and 2-methoxyindenocorannulene (**iCor**).

The authors do not discuss the relevant rate of guest-exchange under the chosen conditions, which would be needed to gain additional insights in the catalytic effect for this example. However, they conclusively describe how flat perylene with its suitable stereoelectronic shape and the same number of π-electrons like corannulene, can be used as a transition state analogue for this process. Albeit this approach was subsequently also applied to estimate the bowl-inversion barrier of corannulene within **ExCage**$^{6+}$, no further experimental support was given for this case. In theory, the barrier for the catalyzed process can be estimated according to equation 8, which can be easily understood with the help of Figure 21.

$$\Delta G^{\ddagger}_{\mathrm{cat}} = \Delta G^{\ddagger}_{\mathrm{non}} - \left(\Delta G_{\mathrm{S}} - \Delta G^{\ddagger}_{\mathrm{S}}\right). \tag{8}$$

Accordingly, from the barrier of the uncatalyzed process $\Delta G^{\ddagger}_{\mathrm{non}}$, the binding energy of the substrate under consideration ΔG_{S} and the binding energy of a transition state analogue, which corresponds to $\Delta G^{\ddagger}_{\mathrm{S}}$, an estimate of $\Delta G^{\ddagger}_{\mathrm{cat}}$ is possible.

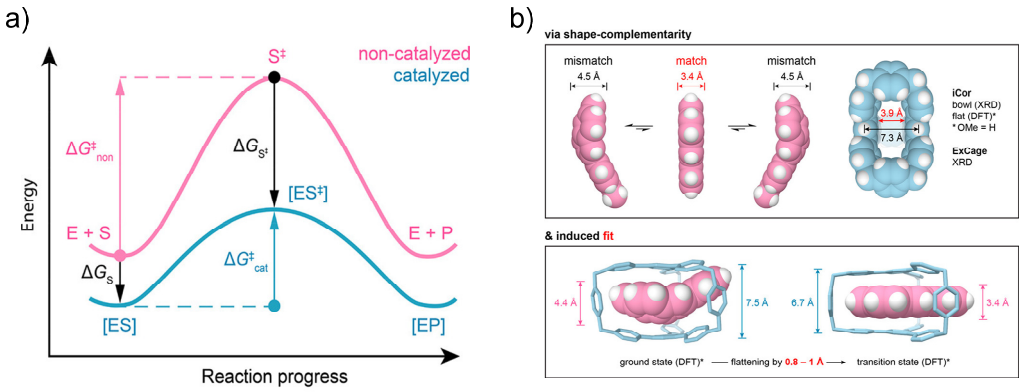

Figure 21. a) Schematic energy landscape for the catalyzed and the uncatalyzed bowl-to-bowl inversion. b) Bowl-to-bowl inversion catalysis in the presence of **ExCage**$^{6+}$ can be explained by shape complementarity between the host and the transition state structure of **iCor** and by an induced fit flattening of the host. Reprinted with permission from Ref [137]. Copyright 2022, American Chemical Society.

Interestingly, the enzyme mimicry of **ExCage**$^{6+}$ could be manifested with an inhibitor experiment where phenanthroline, whose planar structure allows to block the bowl-to-bowl catalysis upon binding as a result of a higher binding affinity compared to **iCor**. The Lewis basicity of phenanthroline enabled furthermore the pH-dependent inhibition control as depicted in Figure 22. Upon protonation of the inhibitor, its binding constant decreases, which favors again the encapsulation of **iCor** and hence switches the catalysis on again.

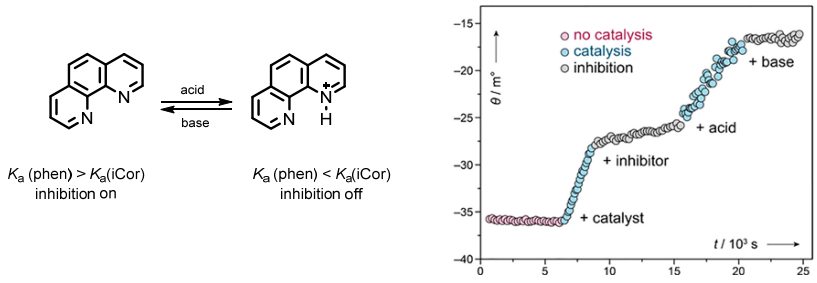

Figure 22. Catalytic inhibition by phenanthroline, which can be turned off in the presence of acid and reversibly turned on upon the addition of base and can be followed by time-dependent CD spectroscopy. Reprinted with permission from Ref [137]. Copyright 2022, American Chemical Society.

Such catalytic processes based on π–π interactions as a main driving force are rarely discussed until today. However, theoretical considerations on achiral PBI cyclophanes predict similar to the work on **ExBox**$^{4+}$ and **ExCage**$^{6+}$ promising properties of such cyclophanes as "π–π catalysts", inspired by cation-π[138–139] and anion-π catalysis,[140] for the stereoinversion of substrates with a planar or near-planar transition state structure, like cyclooctatetraene (Figure 23).[141] Notably, due to the structural complexity of non-planar PBIs, the bay substituents of so far available PBI cyclophanes[56, 142-143] were neglected in these calculations. This fact probably strongly influences the extent of transition state stabilization due to a presumably better shape complementarity between the planar, unsubstituted chromophores and the planar transition state geometry of the selected guests. Thus, even for compounds with high inversion barriers of 389 kJ mol^{-1}, like sumanene, a significant barrier reduction of 16.4% was calculated by DFT as a result of planar transition state structure stabilization and ground state destabilization to a smaller extent. For bisdehydro[12]annulene an impressing reduction of 82.5% for its ring inversion could be calculated. Later, the computational models were extended to the enantiomerization of synthetically relevant biaryls, like 1,1'-binaphthol.[58] Here, the process turned out to be more complex as these substrates have two possible enantiomerization transition states, i.e. the cisoid and the transoid guest conformation. Despite this higher level of complexity, the enantiomerization barrier could be quantified theoretically and was accordingly

found to be lowered by 49.3 kJ mol^{-1} for 1,1'-binaphthol within the PBI host compared to the uncatalyzed process.

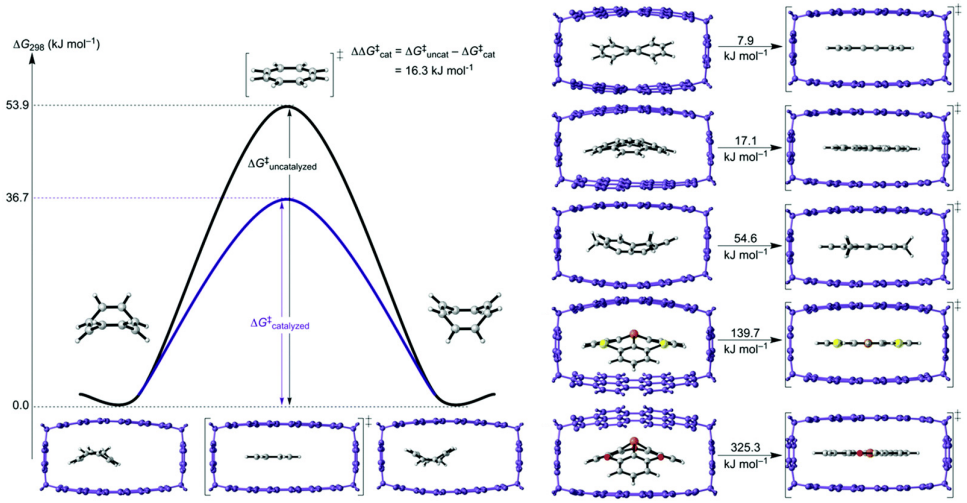

Figure 23. Potential energy surface (PES) for the uncatalyzed and catalyzed ring inversion of cyclooctatetraene (left) and the lowest energy equilibrium and transition structure of a series of host–guest complexes (right). The corresponding activation energies at 298 K are given on the arrows and were calculated relative to the respective reactant complexes. Adapted with permission from Ref [141]. Copyright 2021, Royal Society of Chemistry.

2.4 Helical Chirality of Perylene Bisimide Chromophores

2.4.1 Synthetic Concepts

The long history of PBI chromophores, (derived from perylene-3,4:9,10-bis(dicarboximide)), started with the discovery by Kardos in 1913.[144] Originally, PBIs were applied as pigment dyes in the textile and coatings industries not only because of their high tinctorial strength but also due to their weather resistence owing to a high chemical, thermal and photochemical stability.[145] However, especially in the last decades, PBIs have been further investigated beyond the mere use of their colourfulness as pigments.[55] The structural rigidity of monomeric PBI π-scaffolds in combination with a large aromatic surface makes them ideal candidates as monomeric units for supramolecular architectures, held together by π–π stacking.[146] Supramolecular chemists use them today primarily as building blocks for discrete π-stacks[147-149] or extended aggregates and polymers.[150-151] This provided insights into fundamental photophysical processes[147-149, 152-153] and enabled applications in organic electronics, such as organic photovoltaics (OPV),[154-156] organic light emitting diodes (OLEDs)[157-159] or field-effect transistors (OFET).[160-162] Meanwhile, a variety of PBI derivatives is known, which can

be explained by the easy synthetic modification of all positions of the basic building block (Figure 24).[163]

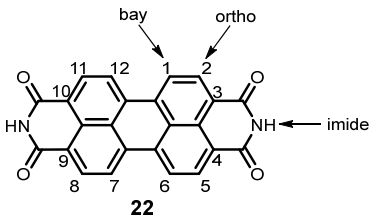

Figure 24. Molecular structure of the parent perylene-3,4:9,10-bis(dicarboximide) (PBI) scaffold.

While substituent variation in imide position in most cases merely serves solubility or affects molecular packing, a substitution of the perylene core leads to altered molecular optoelectronic properties. Additionally, core substitution is a proven way to modify the molecular conformation of PBIs. Apart from the recently shown bending of the chromophore along the long axis by Nuckolls and co-workers,[164-166] especially the twisting of the naphthalene units by a suitable substitution pattern in the bay positions is the method of choice to obtain nonplanar, inherently chiral perylene bisimides.[167] Just like in the case of biaryls, such substitution ensures that the naphthalene subunits twist out of the aromatic plane, yielding a non-planar scaffold.[168] The resulting atropo-isomeric PBIs show a distortion of the π-system of up to 37° for the core twist in the case of the fully bay-brominated species **23** (Figure 25).[169]

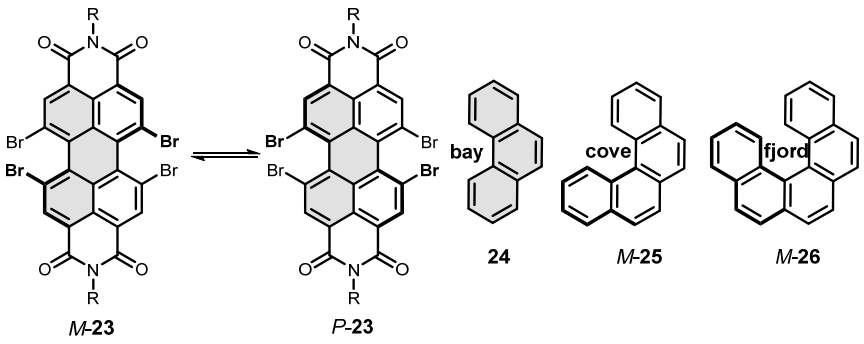

Figure 25. Molecular structure of 1,6,7,12-tetrabromo PBI in comparison to phenanthrene, [4]helicene and [5]helicene.

Similar to biaryls, the conformational stability of these structures depends on the sterical demand of the chosen substituents.[170] While the free enthalpy of activation for the racemization is only 40 kJ mol^{-1} in the case of the fourfold fluorinated derivative, this barrier is increased to 118 kJ mol^{-1} for the corresponding brominated species. Notably, the observed

perylene twist is structurally reminiscent of carbohelicenes and their inherent chirality. Whilst [3]helicene, better known under the name phenanthrene, is flat, the cove and fjord structure motives of [4]- and [5]helicene, respectively, induce a helical groove, comparable to the bay-substitution of PBIs.

Various 1,6,7,12-substituted PBIs are known today and the corresponding tetraphenoxy derivative is one of the best-known representative of these structures. Unfortunately, chiral resolution of the enantiomers by HPLC is not possible under ambient conditions, which can be attributed to the high flexibility of the substituents. On the contrary, direct arylation (Scheme 1a) by a Suzuki-Miyaura cross-coupling can fully suppress the swing-through of the naphthalene subunits, leading to a racemization barrier of 120 kJ mol^{-1} in the case of four phenyl substituents located in the bay positions.[171-173] The first report about this kind of arylation was published already in 2006,[171] where the fully bay brominated PBI **27** was substituted by four phenyl units in 47% yield.

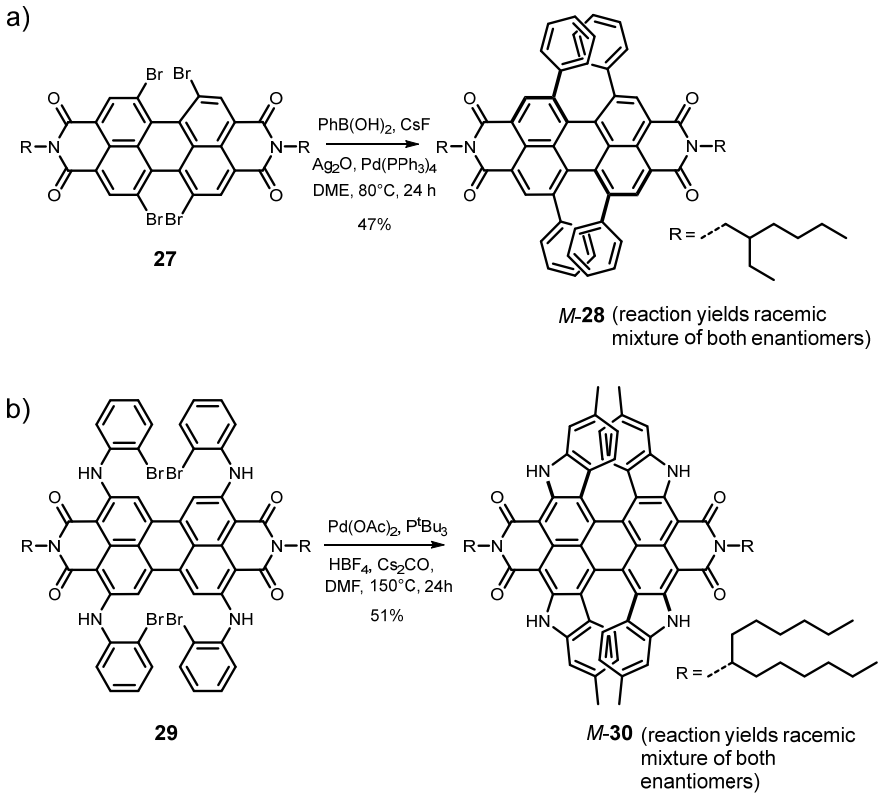

Scheme 1. a) Synthesis of a bay-crowded PBI **28** in a Suzuki cross-coupling reaction. b) Synthesis of a π-extended PBI **30** in a palladium-catalyzed C-H activation.

Accordingly, the bay crowded structures with increased sterical hinderance represent stable atropo-enantiomers (**28**), which can be resolved at r.t. by chiral HPLC. Similarly, a π-extension can also induce the desired effect of a stable core twist as shown by Zhang *et al.* in 2021 (Scheme 1b).[174] For this purpose precursor **29** was synthesized from the corresponding *ortho*-iodinated PBI and 2-bromoaniline in a nucleophilic aromatic substitution reaction. Afterwards, a racemic mixture of **30** was obtained in a palladium-catalyzed intramolecular C-H activation in 51% yield. The corresponding *P*- and *M*-enantiomers were successfully resolved by chiral HPLC and characterized by chirooptical spectroscopy. Notably, this synthetic concept was already exploited in 2014 by Wang and co-workes but without attaching great importance to the inherent chirality of these compounds.[175]

Besides bay arylation and core extension, another strategy to achieve stable PBI enantiomers is to bridge the perylene unit laterally, that is a 1,12-bay connection, with a rigid 2,2'-biphenol[176],[177] or binapthol[178] linker (Figure 26). These compounds can be obtained in a nucleophilc aromatic substitution of the corresponding chlorinated PBI and 2,2'-biphenol or 2,2'-binaphthol, respectively. The advantage of these motives is that they enable high thermal stability with racemization barriers up to $\Delta G^{\ddagger}_{483K}$ = 165 kJ mol^{-1} for **32**.[178]

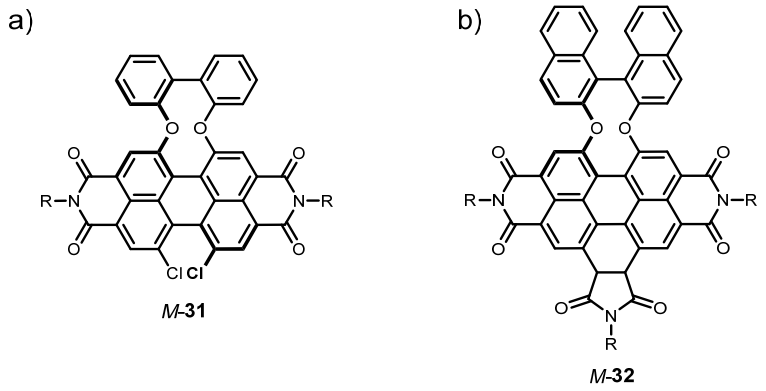

Figure 26. Chemical structures of a) bay-linked PBI **31** and b) benzo[*ghi*]perylene trisimide **32**. The imide substituents are omitted.

However, the strategies shown for the construction of inherently chiral PBIs so far have several disadvantages. On the one hand the high sterical demand in the periphery of the chromophore may be disruptive, e.g. for the incorporation into macrocyclic structures (*vide infra*). On the other hand, it is very difficult to precisely tune the extent of core twisting with these procedures, making tailored chiral building blocks for supramolecular structures difficult to access. Hence, these synthetic approaches may not always be ideal if chiral PBI building blocks for

supramolecular architectures are envisioned. In this regard, a much more elegant and versatile strategy to achieve stable atropo-enantiomers of PBIs is to bridge the core diagonally from the 1 to the 7 position (Scheme 2). A series of such diagonally bridged PBIs with varying lengths of the bay connection was synthesized by Safont-Sempere *et al*.[179-180] The enantiomers were resolved by chiral HPLC and subsequently used for a study on chiral self-recognition. In their work on the phenomenon of chiral self-sorting, the authors could demonstrate that the formation of homochiral dimers prevails over heterochiral aggregation. In addition it could be shown that the more flexible (the longer) the ethylene glycole tether is, the more conformational flexibility of the perylene core is allowed. Hence, this method allows a synthetic fine tuning of the PBI twist but suffers from low yields of 13–15% (which could be elevated to a maximum of 23% for a longer tether)[180] in the macrocyclization step, where the core distortion is introduced to the PBI scaffold.

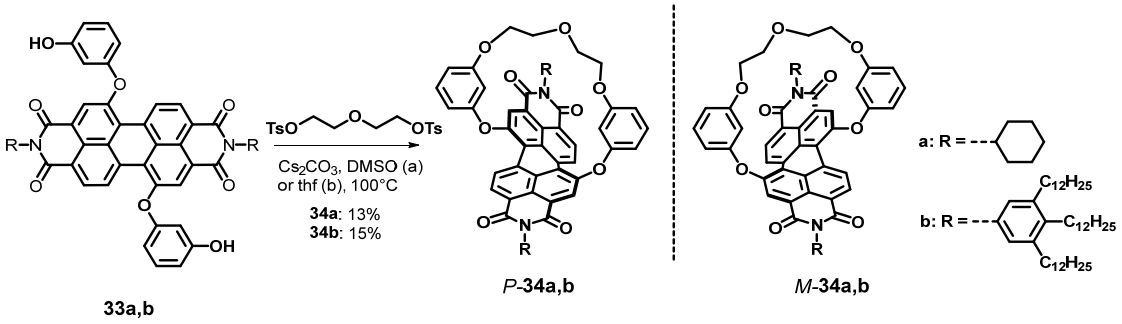

Scheme 2. Synthesis of diagonally connected PBIs **34a**,**b** *via* an diethylene glycole chain.

2.4.2 Chirooptical Properties

Inherently chiral PBIs, as presented in this chapter, are in general characterized by a broad monosignated circular dichroism (CD) signal for the S_0–S_1 transition, resembling the UV/vis spectrum with $g_{abs} = \Delta\varepsilon/\varepsilon$ values of around 10^{-3}.[173, 181] Experimental studies on enantiopure PBIs, supported by TD-DFT calculations have shown that the *P*-enantiomer has a positive CD signal for the lowest energy transition, while the *M*-enantiomer has a negative CD signal. In the naphthalene-related absorption at lower wavelengths, chiral exciton coupling between these subunits yields a characteristic Cotton effect, depending on the absolute configuration of the chromophore.[181]

The circular polarized luminescence (CPL) properties are characterized by the dissymmetry factor $g_{lum} = 2\ (I_L - I_R)/I_L+I_R)$ (I_R and I_L corresponds to the intensity of right- and left-handed circularly polarized light), which is generally low for small organic molecules.[182]

Qualitatively, the CPL spectra of inherently chiral PBIs are mirror images of the lowest energy CD absorption,[173] and yield g_{lum} values of around 10^{-3} for monomeric PBIs.[173]

2.5 Perylene Bisimide Cyclophanes

In 1951, Donald J. Cram succeeded in the synthesis of a rigid system, in which two benzene rings are fixed above each other by short aliphatic chains in the *para*-position, giving birth to the new class of *para*-cyclophanes.[183] Originally, these cyclophane structures were designed to study aromaticity and the concomitant ring current effect, like for example in ^{1}H NMR studies.[184] Today, after several decades of research, numerous different cyclophane architectures with various applications and research interests are known, which makes a uniform definition for this class of substances difficult. However, according to IUPAC, cyclophanes are defined as "compounds having mancude-ring systems or assemblies of mancude-ring systems and atoms and/or saturated or unsaturated chains as alternate components of a large ring".[185] Thus, this definition covers in principle almost all kinds of macrocycles with aromatic units and does notably not include the initial concept of structural rigidity.

Cyclophane hosts take advantage of multiple interaction sites, which allows specific guest embedding within tailored cavities. In the early 1980s, a novel class of cyclophanes with two 4,4'-bipyridinium units was established by Hünig and co-workers, that laid the foundation for a bright future of these compounds as supramolecular receptors.[186] The bipyridinium unit was connected *via* the *ortho*- and *meta*- positions of the corresponding xylylene derivative, yielding a tetracationic, rigid macrocyclic structure. Hünig and Stoddart independently found that electron-rich aromatic compounds can serve as templates during the cyclization step.[42, 187] Thus, Stoddart finally presented the cyclobis(paraquat-*p*-phenylene) cyclophane (see *Chapter 1*).

In 2015, Würthner and co-workers succeeded in incorporating PBI chromophores into rigid, macrocyclic structures to enable for the first time the inclusion of guest molecules within a PBI cyclophane (Figure 27).[56] The use of a *para*-xylylene spacer provides, similar to the work of Stoddart, not only the perfect distance of around 7 Å between the chromophores for the encapsulations of planar PAHs, but also the necessary rigidity to prevent intramolecular aggregation. This circumvents the strong excitonic coupling between the chromophores, observed in the first report about a macrocyclic PBI structure with flexible alkyl linkers,

introduced by Langhals in 1998.[188] Furthermore, the core substituted PBI derivative provides sufficient solubility of the macrocycle **[2PBI]** due to a total number of eight *tert*-butyl phenoxy substituents in the bay positions. The spatial orientation and proximity of the two chromophores results in a weak H-type coupling with a characteristic absorption pattern in the UV/vis spectrum. Spectroscopic studies revealed unique photophysical properties of this cyclophane, depending on the choice of solvent and the electron abundance of the encapsulated guest molecule.[152] Transient absorption spectroscopy enabled deeper insights into the exact photophysical pathways, which can be summarized in the following way: In unpolar solvents, radiative relaxation into the ground state upon excitation is observed (Figure 27b, path B). In contrast, the more polar solvent dichloromethane stabilizes a symmetry breaking charge separation (SB-CS, Figure 27b, path A). Afterwards, the charges recombine and form a triplet excited state, which was used to generate singlet oxygen in a quantum yield of 27%. Similar like in polar solvents, a charge separation (CS) can also be detected when suitable guests are complexed (Figure 27b, path C).

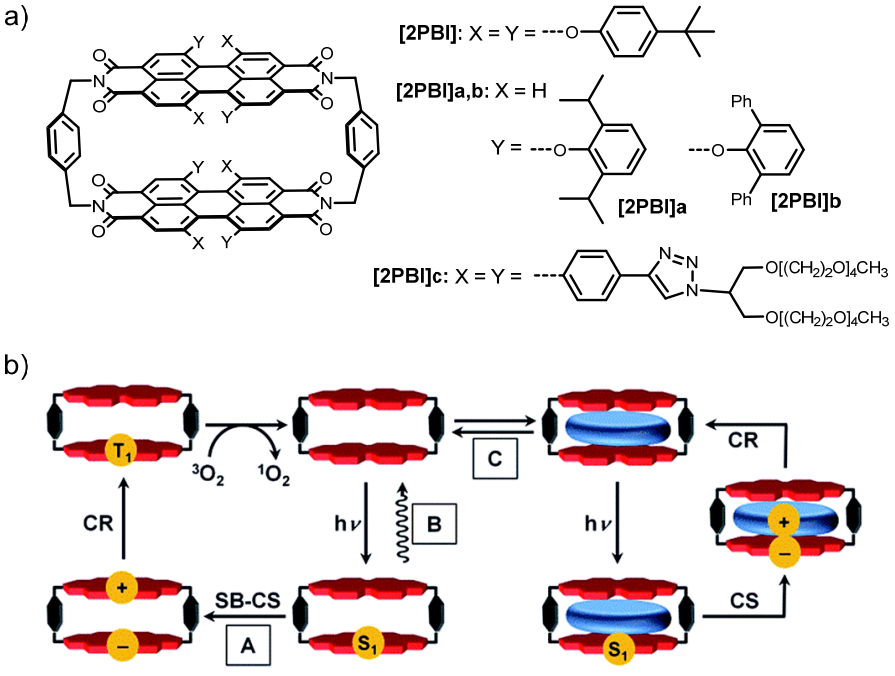

Figure 27. a) Chemical structure of *para*-xylyene bridged PBI cyclophanes **[2PBI]**, **[2PBI]a,b** and **[2PBI]c**. b) Schematic representation of the different excited state photophysics of **[2PBI]** upon excitation. (A) In CH_2Cl_2, a symmetry-breaking charge separation (SB-CS) and recombination (CR) to the PBI triplet within the PBI cyclophane **[2PBI]** is observed and can be used for singlet oxygen generation. (B) Emission in toluene. (C) Complexation of aromatic guests (depicted in blue) and photo-driven charge separation (CS) between guest and host and subsequent charge recombination (CR) to the ground state. Adapted with permission from Ref [152]. Copyright 2016, Royal Society of Chemistry.

Later, in 2017, a modified 1,7-derivative (**[2PBI]a,b**) was reported and showed similar optical properties like the octa-substituted cyclophane, but enabled higher binding affinities towards flat PAHs.[142] Next, Sapotta *et al.* achieved the water solubility of PBI cyclophanes with ethylenegylcole chain substitution, introduced by click-chemistry (compound **[2PBI]c**) to increase the guest substrate scope.[143] Accordingly, the water-solubility of **[2PBI]c** with its hydrophobic cavity enabled this cyclophane to act as a molecular probe for the recognition of some aromatic alkaloids. Substrate complexation was studied in detail by UV/vis and fluorescence as well as 2D NMR spectroscopy to provide the thermodynamic and structural data of the resulting complexes.

In 2020, a new dimeric PBI macrocycle called "*Green Box*" with a larger cavity was introduced by Barendt *et al.*.[189] The two bis-pyrrolidine chromophores were connected *via* the imide positions with a "methylene-biphenyl-methylene-triazole-butyl" linker (Figure 28a). This rather flexible and long connectivity made the complexation of C_{60} and C_{70} fullerenes as guests between the chromophores possible. Studies on the photophysical properties of the complexes showed that partial charge transfer is tunable into a full electron transfer from the donor host to the acceptor guest by adjusting the solvent polarity. In toluene and *ortho*-dichlorobenzene, a new bathochromically shifted absorption band emerged upon the addition of the guests. Further evidence for a charge transfer character of the complex was observed in an attenuated fluorescence emission and a shift of the host's oxidation potential in the cyclic voltammetry. Time-resolved EPR spectroscopy revealed a full electron transfer from the donor host to the acceptor guest upon excitation in toluene while studies in the more polar solvent nitrobenzene revealed a ground state electron transfer without the need for irradiation.

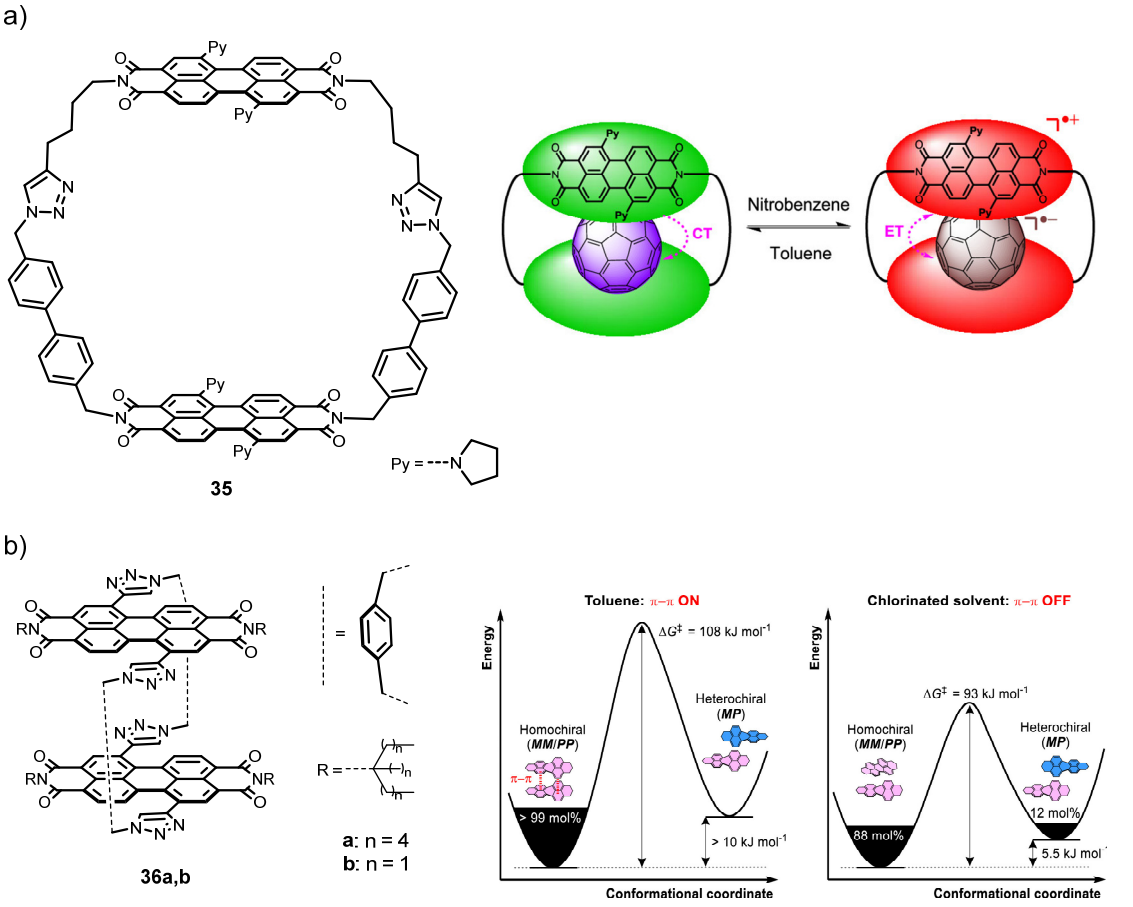

Figure 28. a) Chemical structure of the "*Green Box*" **35** and schematic depiction of the CT to ET switch between encapsulated fullerene and host upon changing the solvent polarity. b) Chemical structure of the "*Pink Box*" **36a,b** and proposed schematical potential energy surface for macrocycle **36a** in toluene and chlorinated solvents. Adapted with permission from Ref [190] and Ref [189]. Copyright 2022 and 2020, American Chemical Society.

Two years later, in 2022, the same group reported another dimeric PBI macrocycle (**36a,b**, "*Pink Box*") with a connecting bridge between the bay positions of the chromophores, synthesized by a copper catalyzed triazole formation (Figure 28b).[190] Single crystal X-ray analysis of the macrocycle revealed an interchromophoric distance of 3.7 Å. Hence, the chosen bay linkage sets the perfect distance for strong π–π stacking between the PBI units. Investigations on the through-space π–π electronic communication of the two chromophores showed that homochiral aromatic stacking interactions anchor their configuration, leading to half-life times of days for the homochiral bis-PBI macrocycle in toluene. On the other hand, the diastereomeric excess was found to decrease in chlorinated solvents faster compared to toluene, which was rationalized by DFT calculations. Accordingly, the decreased energy difference between ***MM/PP*** and ***MP*** in dichloromethane compared to toluene yielded an increased diastereomer population. Eventually, studies on the chirooptical properties revealed one of the

highest dissymmetry factors of small organic molecules in solution for this cyclophane (g_{lum} = 10^{-2} at 675 nm).

Another example of chiral self-recognition within a PBI macrocycle was reported by Hirsch and co-workers in 2021.[191] A cyclophane showed, similar to the work of Barendt, a diastereoselective formation of homochiral dye pairs in a macrocycle, composed of two flexible PBIs, linked by malonates. The covalently connected dimers were found to form an excess of co-facial homochiral π-stacks (*MM* and *PP*) compared to the heterochiral dimers (*MP* and *PM*) in a ratio of 10:1 in $C_2D_2Cl_4$ at low temperatures. Again, the choice of the solvent turned out to be pivotal for the extent of homochiral dimer formation. Thus, in CD_2Cl_2 the diastereomeric excess could be increased to unity. Accordingly, a mutual through-space chiral self-recognition could be mediated by different solvents to different extents in this report.

The works of Barendt and Hirsch suggest that the choice of solvent has a significant impact on chiral intramolecular self-recognition and the transfer of stereoinformation in macrocyclic structures. In 2022 Ouyang *et al*. presented a hetero cyclophane, consisting of a conformationally flexible PBI dye as well as a chiral, conformationally stable BBI (binaphthol bisimide) unit, which were linked in the imide position *via* a *para*-xylylene spacer.[192] While BBI showed the expected CD signature in all solvents, no chirooptical response of the PBI unit was observable in chloroform or bromoform. In contrast, in a series of other solvents, the PBI chromophore exhibited an induced CD absorption with a positive or negative signal, depending on the absolute configuration of the adjacent BBI unit.

Chapter 3

Deracemization of Carbohelicenes by a Chiral Perylene Bisimide Cyclophane Template

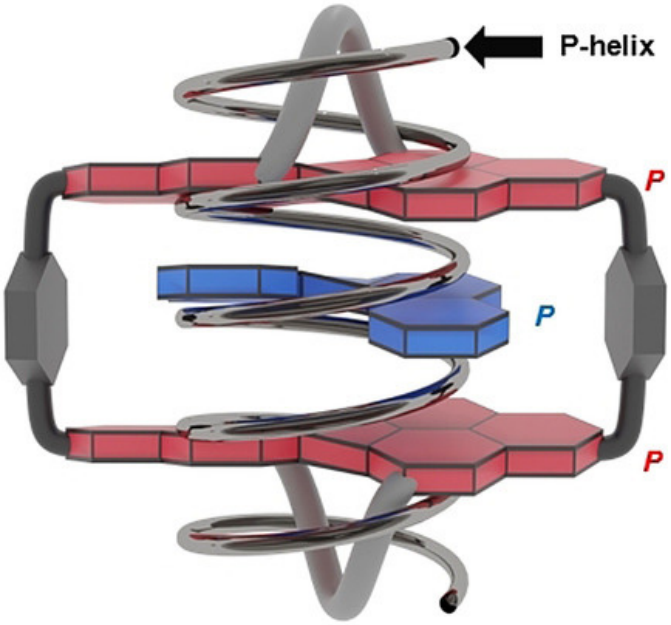

This chapter and the corresponding supporting information (Chapter 9.1) were published in:[i]
M. Weh, J. Rühe, B. Herbert, A.-M. Krause, F. Würthner, *Angew. Chem. Int. Ed.* **2021**, *60*, 15323–15327. (https://onlinelibrary.wiley.com/doi/full/10.1002/anie.202104591).

Abstract. Deracemization describes the conversion of a racemic mixture of a chiral molecule into an enantioenriched mixture or an enantiopure compound without structural modifications. Herein, we report an inherently chiral perylene bisimide (PBI) cyclophane whose chiral pocket is capable of transforming a racemic mixture of [5]helicene into an enantioenriched mixture with an enantiomeric excess of 66%. UV/vis and fluorescence titration studies reveal this cyclophane host composed of two helically twisted PBI dyes has high binding affinities for the

[i] Parts of the results have been described in: M. Weh, Master Thesis, Julius-Maximilians-Universität Würzburg, **2019** and B. Herbert, Bachelor Thesis, Julius-Maximilians-Universität Würzburg, **2020**.

respective homochiral carbohelicene guests, with outstanding binding constants of up to 3.9×10^{10} M^{-1} for [4]helicene. 2D NMR studies and single-crystal X-ray analysis demonstrate that the observed strong and enantioselective binding of homochiral carbohelicenes and the successful deracemization of [5]helicene can be explained by the enzyme-like perfect shape complementarity of the macrocyclic supramolecular host.

3.1 Introduction

The field of supramolecular chemistry started with studies on macrocyclic receptors for the molecular recognition of cations and neutral molecules.[10, 194] For the latter, cyclophanes in particular enjoyed, and continue to enjoy, great popularity because they can provide suitable binding pockets to surround guest molecules and afford both binding strength and selectivity by shape complementarity.[41] Accordingly, cyclophanes and related macrocycles have shown their usefulness for the complexation of various guest molecules,[14] the construction of molecular machines,[44] as molecular sensors,[17] and for supramolecular catalysis.[195] Whereas the earlier examples of synthetic cyclophane-type supramolecular hosts typically were of high symmetry, recent studies have also explored the construction of cavities of lower symmetry for enantioselective recognition and sensing.[91, 196] Furthermore, Yashima and co-workers recently reported double-stranded spiroborate helicates that can be transformed into their optically active forms by the complexation of chiral guest molecules.[80] However, to the best of our knowledge, despite the long history of research on the deracemization of organic molecules[197] by dynamic kinetic resolutions *via* inclusion complexes[198] and chromatography on chiral phases,[199] deracemization by a templating chiral cyclophane host has not yet been demonstrated.

Toward this goal we considered our recently introduced perylene bisimide (PBI) based cyclophane hosts as particularly promising candidates. As a consequence of their large π-surfaces, PBIs bridged with *para*-xylylene spacer units proved to be excellent hosts with high binding affinities for polycyclic aromatic hydrocarbons[56, 142] and even some alkaloids.[143] Furthermore, similar to previously described examples,[91, 196] chirality transfer from chiral guest molecules to achiral PBI cyclophanes could be observed by CD spectroscopy.[57] Inspired by this work, we have now designed the first example of an inherently chiral PBI cyclophane host. As we will show, this host exhibits a very high binding affinity for [4]- and [5]-helicene that can be utilized for the template-catalyzed deracemization of the latter into an enantioenriched mixture with an enantiomeric excess (*ee*) of 66%.

3.2 Results and Discussion

The key step in the synthesis of the inherently chiral PBI cyclophanes **1-*MM*** and **1-*PP*** (Schemes 3 and A1 in the Appendix) is an efficient intramolecular ring-closing metathesis with the second-generation Grubbs catalyst in 82% yield, followed by the almost quantitative hydrogenation of the resulting olefinic double bond.

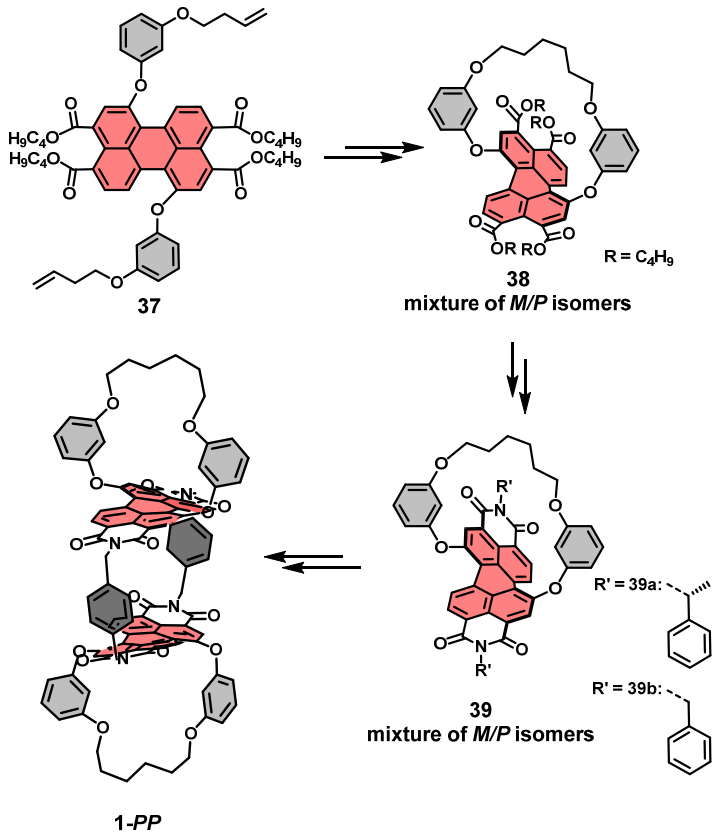

Scheme 3. Synthetic route to PBI cyclophane **1-*PP*** (the route to **1-*MM*** is analogous) *via* diastereomer **39a**. The structure of reference PBI dye **39b** is also shown.

In this way, stable atropisomers were obtained as a racemic mixture of *P*- and *M*-enantiomers.[179-180] The subsequent reaction sequence includes a saponification and imidization with (*R*)-phenylethylamine to afford a highly soluble mixture of diastereomers that could be separated by chiral HPLC (Figures A25 and A26). Subsequent saponification and cyclophane synthesis with *para*-xylylenediamine was accomplished following our previously reported route.[56] For details on the experimental procedures and characterization of all new compounds, see the Appendix.

The properties of chiral cyclophanes **1-*MM*** and **1-*PP*** were studied by UV/vis absorption, fluorescence, and CD spectroscopy in comparison to the reference dyes **39a** and **39b**. UV/vis

absorption spectroscopy (Figure 29a, blue solid line and see also Figure A27b) reveals a H-type coupling between the transition dipole moments of the $S_0 \rightarrow S_1$ transition of the two PBI units, which is manifested in a decrease in the $A_{0\text{-}0}/A_{0\text{-}1}$ ratio from 1.6 for the monomeric PBIs **39a,b** (Figure A27a) to 1.1 for the cyclophanes.[200-201] Furthermore, by comparison of the experimental CD spectra with structurally related enantiopure PBI chromophores,[181] we were able to assign the absolute configuration of the isomerically pure atropisomers of PBI **39a-*M*** and **39a-*P*** that were utilized for the synthesis of **1-*MM*** and **1-*PP***. These results were further confirmed by time-dependent density functional theory (TD-DFT) calculations (Figure A39).

Next, we were interested in the molecular recognition properties of these chiral macrocycles. Host–guest titration experiments were performed in chloroform using UV/vis absorption and fluorescence spectroscopy. In our studies, we investigated the molecular recognition of a homologous series of carbohelicenes,[202-204] starting from the flat phenanthrene, which can be formally regarded as [3]helicene. The next congener, [4]helicene, is the first carbohelicene with a helical structure but cannot be isolated in enantiomerically pure form due to its low barrier for enantiomerization of only 17.2 kJ mol^{-1}.[205] Thus, [5]helicene is the first congener in this series for which the *M*- and *P*-enantiomers can be resolved and whose racemization is sufficiently slow for binding studies. Figure 29a presents the spectral changes of the UV/vis absorption and fluorescence emission bands upon addition of *P*-[5]helicene to a solution of **1-*PP*** in chloroform at 22 °C. The spectral shifts in both experiments provide evidence for a significant charge-transfer character, which affords a red-shifted exciplex-like emission band[56, 206] of lower intensity (Figure 29a and Figure A33c) and an increased lifetime (Figure A28). More importantly, both titration studies with their well-defined isosbestic and isoemissive points could be fitted with the 1:1 binding model[207] to give $K_a = 3.8 \times 10^5\ M^{-1}$ and $K_a = 4.8 \times 10^5\ M^{-1}$, respectively. As expected, similar values, within experimental error, were obtained for the titration of **1-*MM*** with *M*-[5]helicene (Figure A34). From the average of these four titration experiments we derived a Gibbs energy of −32.1 kJ mol^{-1} for the 1:1 complex formed between the homochiral host and guest. For the heterochiral complexes, that is, **1-*MM*** and *P*-[5]helicene or **1-*PP*** and *M*-[5]helicene, binding was much weaker, but could not be evaluated because of an ongoing enantiomerization during the titration experiment (see below).[ii]

[ii]The significantly weaker binding of the heterochiral [5]helicene guest is clear from the significantly smaller optical changes in the binding study compared to the homochiral situation for the same amount of added guest.

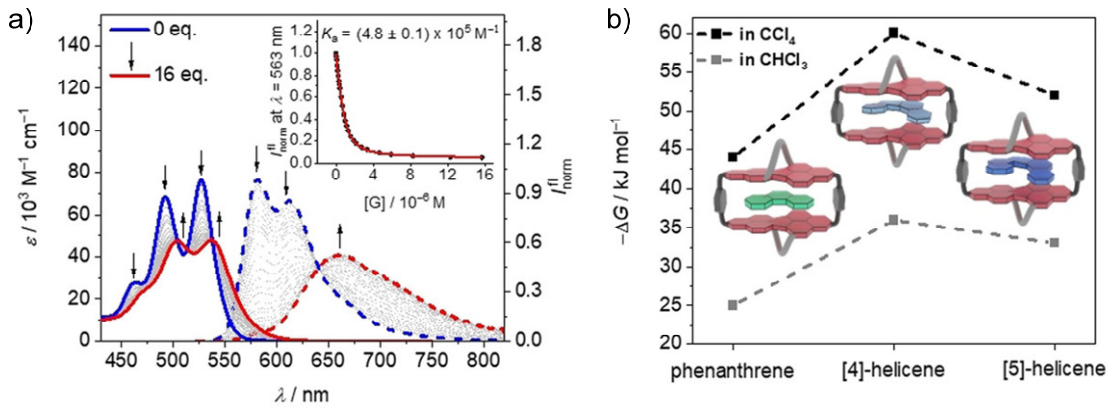

Figure 29. a) UV/vis (solid lines) and fluorescence (dashed lines) titration curves of **1-*PP*** in $CHCl_3$ at 22 °C (c_{host} = 10 μM) upon the addition of *P*-[5]helicene as a guest. Inset: Plot of the fluorescence intensity at λ = 563 nm with a nonlinear curve fit (1:1 binding model, red curve). c) Plot of the Gibbs energy calculated by $\Delta G = -RT\ln K_a$, with T = 295 K and the respective binding constant.

Similar titration experiments for **1-*MM*** (and **1-*PP***) with phenanthrene and [4]helicene afforded averaged binding constants of $K_a = 2.3 \times 10^4$ M^{-1} and $K_a = 2.7 \times 10^6$ M^{-1} in chloroform at 22 °C, respectively (Figures A29–A32). Accordingly, the strongest binding is observed for [4]helicene, and we may assume that in this case host–guest complexes are formed in which the chiral information of the respective host has been imprinted on the guest to afford *P*-[4]helicene⊂**1-*PP*** and *M*-[4]helicene⊂**1-*MM***. Notably, no spectral changes were observed in the visible range for reference compound *rac*-**39b** upon the addition of [4]helicene, thus revealing no significant interaction between these molecules (Figure A35). Accordingly, the strong binding affinity observed for **1-*MM*** and **1-*PP*** arises from the encapsulation of the helicene guest between the two π-faces.

As shown in Figure 29b, significant increases in the binding affinities could be achieved for all carbohelicene guests in the less competitive solvent tetrachloromethane. Indeed, with a value of $K_a = 3.9 \times 10^{10}$ M^{-1}, the binding affinity for the complex with [4]helicene is in the nanomolar range and thus comparable to the binding affinity of modern drugs to their natural receptors. We note that such high binding constants can no longer be recorded by direct titration experiments and, therefore, had to be determined by competitive titration studies (Figures A36–A38).[208]

The structural features of the most strongly bound [4]helicene⊂**1-*MM*** complex were elucidated by NMR spectroscopy and single-crystal X-ray crystallography. For the NMR experiment, we prepared a chloroform solution of **1-*MM*** with an excess of [4]helicene and separated the excess

guest by gel-permeation chromatography (GPC) using chloroform as an eluent. Afterwards, ^{1}H NMR spectroscopic analysis of the remaining mixture revealed a 1:1 host–guest stoichiometry, thereby corroborating not only the high binding affinity but also the kinetic stability of this complex against dissociation during the GPC separation. The protons of the free host and the complex were assigned by 2D NMR spectroscopy (Figures A41 and A42). A comparison of the ^{1}H NMR spectrum of the host–guest complex with the free host in 1,1,2,2-tetrachloroethane-d_2 (TCE) reveals an upfield shift of the perylene receptor protons (marked in red and orange), which is in accordance with a complexation of the carbohelicene inside the cavity (Figure 30a). Furthermore, both the methylene protons (marked in turquoise) and the aromatic protons of the xylylene spacer (marked in green) experience a downfield shift caused by the aromatic ring current of the helicene guest.

To gain further insight into the arrangement of the guest within the cavity, a ^{1}H-^{1}H ROESY NMR experiment was performed (Figures 30b and A42b). This enables through-space correlations between the protons of [4]helicene and the aromatic spacer protons to be observed, which can only be explained by the spatial proximity of these units. Our DFT-optimized structure of [4]helicene⊂**1**-***MM*** is in accordance with this observation (Figures 30c and A40). Alternative binding modes, such as the complexation of the guest with the outer part of the PBI can clearly not explain these signals.

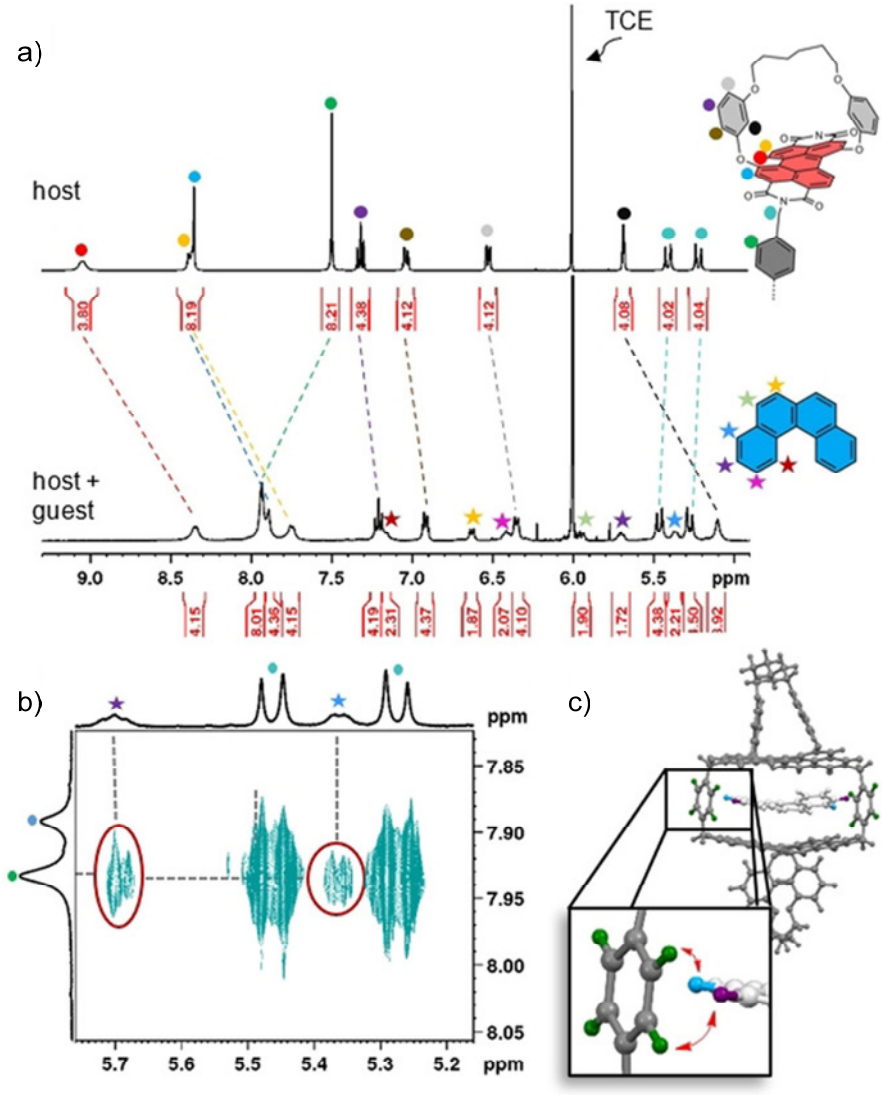

Figure 30. a) Partial 400 MHz ^{1}H NMR spectrum of the free host **1-*MM*** (c = 3.5 mM) and of [4]helicene⊂**1-*MM*** (1 equivalent [4]helicene, bottom) in TCE-d_2 at 298 K, including the assignment of the protons. The filled circles mark the protons of the host and the stars indicate the protons of the guest. b) Excerpt from a 400 MHz ^{1}H-^{1}H ROESY NMR spectrum of [4]helicene⊂**1-*MM*** in TCE-d_2 at 298 K with relevant cross-signals. c) DFT-optimized structure of [4]helicene⊂**1-*MM*** with marked protons that show cross-signals in the ROESY NMR spectrum.

The ultimate proof for the encapsulation of a homochiral *M*-[4]helicene within the **1-*MM*** cyclophane host, that is, molecular imprinting of chirality,[209] could be accomplished by co-crystallization of these molecules from a chlorobenzene/*n*-hexane solution and subsequent single-crystal X-ray analysis (Figure 31, Figure A43, and Table A1). The *M*-[4]helicene⊂**1-*MM*** complex crystallizes in the monoclinic crystal system (space group $P2_1$) with two complexes per unit cell. The solid-state structure reveals that the macrocycle forms a box-like cavity, which offers an ideal distance of about 7.2 Å between the perylene units for the

encapsulation of polycyclic aromatic hydrocarbons through aromatic π-π interactions. As shown in Figure 31 (and in more detail in Figure A43b), the two PBI moieties of the macrocycle have a parallel arrangement without rotational or longitudinal displacements. Furthermore, the core twist of the perylene chromophores, with an average dihedral angle between the naphthalene subunits of 15.4°, appears to be perfect for the accommodation of the homochiral *M*-[4]helicene guest molecule. Accordingly, the structure of *M*-[4]helicene embedded within **1-*MM*** in this single crystal is in very good agreement with the DFT-calculated structure of *M*-[4]helicene (Figure A40). A further contribution to the strong binding of this guest molecule might arise from additional CH···π interactions (Figure 31, inset)[210] between the aromatic spacer units of the host and the protons of the guest at a distance of 2.6–2.9 Å (the range indicates the different distances observed for the two sides in the cavity) in the [4]helicene⊂**1-*MM*** complex. Notably, despite the excellent embedding of the guest by four sides, the crystal structure reveals a good accessibility of guest molecules to the cavity, which will be of relevance for the studies reported next.

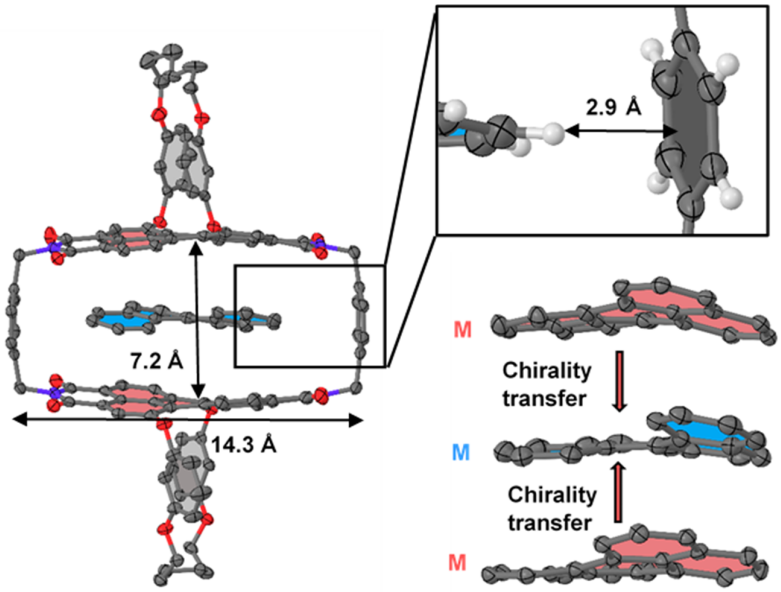

Figure 31. a) Molecular structure of the complex *M*-[4]helicene⊂**1-*MM*** obtained by single-crystal X-ray analysis. Hydrogen atoms are omitted for clarity. The perylene core is colored in red and the guest in blue. An enlarged excerpt of the host–guest complex is shown to illustrate the CH···π interactions between the guest and the xylylene spacer groups. For this purpose, the hydrogen atoms are displayed. In addition, an enlarged view of the perylene units of the host and the guest is shown to illustrate the homochirality of the host and guest.

As discussed above, our binding studies provided strong evidence for the enantioselective binding of helicene guest molecules that have a homochiral backbone to the host. Motivated by the large Gibbs energy observed for these complexes, we conceived an experiment for the

deracemization of [5]helicene, whose racemization barrier of 100.8 kJ mol^{-1} corresponds to a process that takes place within about one day at room temperature (Figure A46b).[205, 211] Accordingly, a 1:1 mixture of chiral host and racemic guest was prepared in chloroform solution and the optical changes were followed over time by CD spectroscopy. The time-dependent data indicate that the complexation takes place successively until an equilibrium between the two enantiomers of the guest, the complex, and the free host is reached (Figures 32 and A45).

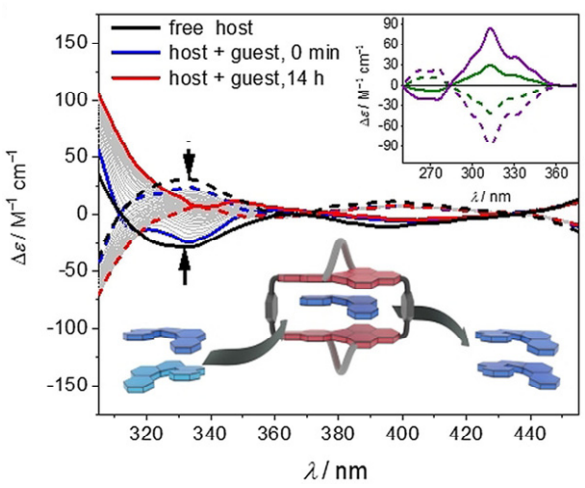

Figure 32. a) CD absorption spectra of **1-*PP*** (solid lines) and **1-*MM*** (dashed lines) and corresponding time-dependent spectra after the addition of *rac*-[5]helicene. Inset: CD spectra of [5]helicene after complexation with **1-*PP*** (solid lines) and **1-*MM*** (dashed lines) and subsequent GPC separation (complexation in chloroform: green; complexation in tetrachloromethane: purple) in chloroform at room temperature. For comparison, the corresponding CD spectrum of *rac*-[5]helicene is also shown (black solid line). Furthermore, an illustration of the template-controlled deracemization of *rac*-[5]helicene is shown.

An increase in the CD signal in the characteristic absorption range of [5]helicene (300–350 nm) is observed, which suggests the preferential molecular recognition of one carbohelicene enantiomer by the chiral host. However, a quantitative evaluation of the chirality transfer leading to deracemization of [5]helicene is hampered in this experiment by the significant overlap of the helicene absorption band with those of the PBI host (**1-*MM*** or **1-*PP***).

Therefore, solutions that had been equilibrated for 14 h were subjected to GPC separation of the host and guest to afford [5]helicene with 27% *ee* (average of results obtained for the *P*- and *M*-enrichment; Figure 32a, inset). A comparison of the CD spectrum with that of enantiomerically pure [5]helicene[212] (Figure A46a) shows that we obtained an excess of *M*-[5]helicene with the **1-*MM*** host, while an enrichment of *P*-[5]helicene was observed after complexation with **1-*PP***. If the same deracemization experiment was carried out in the less-

polar solvent tetrachloromethane, the *ee* value was increased to 66% (Figure 32a, inset). This observation shows that an increased binding affinity leads to a more efficient chirality transfer from the host to the guest and, thus, indicates that the complexation is responsible for the observed deracemization. Time-dependent CD studies suggest that this interconversion between the enantiomeric forms of [5]helicene is catalyzed by the cyclophane template, with a significant acceleration of the enantiomerization process of *M*-[5]helicene in the presence of **1-*PP*** (Figure A47, for details see *Chapter 4*).

3.3 Conclusion

In summary, we have reported the first inherently chiral perylene bisimide cyclophanes and their high binding affinity for carbohelicenes with association constants up to $K_a = 3.9 \times 10^{10}$ M^{-1}. Subsequently, we demonstrated chirality transfer from the cyclophane host to helicene guests by single-crystal X-ray analysis for the complex with [4]helicene as well as the cyclophane-template-catalyzed deracemization of [5]helicene.

Chapter 4

π–π Catalysis Made Asymmetric - Enantiomerization Catalysis Mediated by the Chiral π-System of a Perylene Bisimide Cyclophane

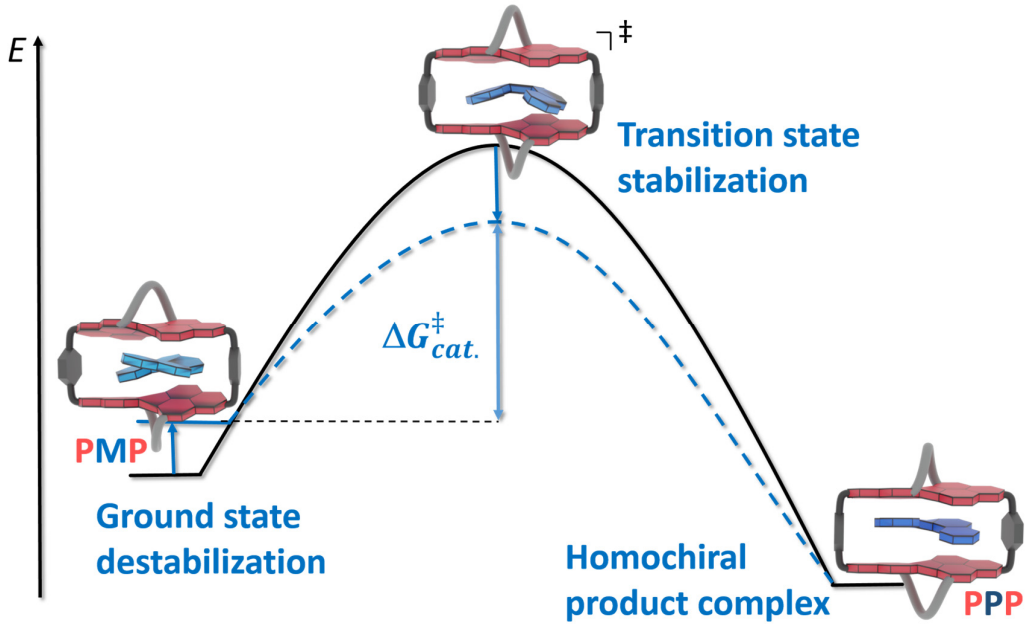

This chapter and the corresponding supporting information (Chapter 9.2) were published in: M. Weh, A. A. Kroeger, K. Shoyama, M. Grüne, A. Karton, F. Würthner, *Angew. Chem. Int. Ed.* **2023**, *62*, e202301301.[iii] (https://onlinelibrary.wiley.com/doi/10.1002/anie.202301301).

Abstract. Enzymes actuate catalysis through a combination of transition state stabilization and ground state destabilization, inducing enantioselectivity through complex chiral pockets in their active sites. Here, we present a combined experimental and computational study of a simple supramolecular model system which employs these basic principles in order to catalyze the enantiomerization of [5]helicene. Catalysis is hereby mediated not through an elaborate

[iii] M. W. and A.A.K. co-wrote this manuscript and contributed equally. See Individual Contribution for details.

network of functional groups but through π–π catalysis exerted from the curved aromatic framework of a chiral *para*-xylylene linked perylene bisimide (PBI) cyclophane, which offers a binding pocket that is intricately complementary with the enantiomerization transition structure of [5]helicene. According to energy decomposition analyses (EDAs) the transition state stabilization originates simply from dispersion and electrostatic interactions. Nevertheless, time-dependent CD (circular dichroism) studies reveal the enantiomerization kinetics of [5]helicene to be accelerated by a factor of ~700 at room temperature. Detailed 2D NMR and crystallographic studies confirm the transfer of chiral information from host to guest. A comparison with the meso-congener of the catalytically active cyclophane shows that upon configurational inversion in only one PBI moiety not only chiral recognition is lost, but also the observed catalytic effect, highlighting the importance of precise transition structure recognition in supramolecular enzyme mimics.

4.1 Introduction

The catalytic efficiency of biological enzymes is controlled by the intricate interplay between the shapes and characteristics of the active site and the substrates throughout the reaction being catalyzed. The general mode of action of enzyme catalysts can be summarized with reference to comparably simple principles introduced by Pauling[51] and Jencks,[214] according to which reaction barriers are lowered through transition state stabilization originating from shape-complementarity between catalyst and transition structure, and ground state destabilization resulting from non-complementarity between reactant and catalyst.

Perfected by evolution, the catalytic cavities of natural enzymes achieve both exceptional efficiencies and selectivities. From the beginnings of the field, one of the main goals of supramolecular chemistry has been the mimicry of these highly optimized natural catalysts,[10] and strategically designed host-guest systems continue to receive attention as simple artificial mimics of their complex biological counterparts.[41, 215-224] In this context, their well-defined structures, and the possibility of precise control over cavity size and geometry, make cyclophanes promising candidates for synthetic mimics of catalytic cavities.[35, 50, 137, 215, 225-229] While many previous explorations of cyclophane catalysis have successfully employed functional groups on the perimeter of the aromatic framework, performing the role of a cofactor,[215, 225, 228, 230] the inherent presence of aromatic planes makes cyclophanes ideal candidates for studying catalysis by noncovalent π-stacking interactions. Whereas the concepts

of cation-π catalysis[226-227] and anion-π catalysis[140, 231] are well known, the application of π-π stacking interactions to drive catalysis (π–π catalysis)[232] remains less explored.

In a seminal paper demonstrating this principle, Juríček *et al.* in 2014 reported the catalysis of the corannulene bowl-inversion by the **ExBox^{4+}** cyclophane.[50] Hereby, experimental and computational analyses revealed that the catalytic effect originates from both, stabilizing π-stacking interactions between the shape-complementary **ExBox^{4+}** host and the planar bowl-inversion transition structure, as well as ground state destabilization due to conformational distortion as a result of non-complementarity between the cavity and the bowl-shaped reagent. Building on this proof-of-concept demonstration of the Pauling–Jencks model, the larger **ExCage^{6+}** host was in 2022 reported to show improved performance as an "artificial racemase" in a study of the inversion catalysis of the less flexible indenocorannulene.[137]

Both in nature, as well as in synthesis, catalysis is often aimed towards an enantiomerically enriched product, achieved through the transfer of chiral information from catalyst to substrate.[233-235] In living cells, a complex interplay of kinetics and thermodynamics continuously ensures, with the help of numerous chiral catalysts, that the most entropically stable state, i.e. the racemic mixture, is not reached.[236] The question hence arises, whether it is possible to expand on the above guest-in-box systems such that an asymmetric transformation could be noncovalently catalyzed in the spirit of the Pauling–Jencks model with a cyclophane template.

To this end, following earlier experimental and theoretical work on the binding of planar aromatic hydrocarbons by perylene bisimide (PBI) cyclophanes,[56, 58, 141-143] some of us reported the first inherently chiral PBI cyclophane and discovered the capability of this host to imprint its chiral information onto small carbohelicene guests.[193] Here, we present a complete experimental and computational description of this process *via* time-dependent CD and 2D NMR spectroscopy, single crystal X-ray crystallography and density functional theory (DFT) calculations. We show that the chiral host not only provides a complementary chiral cavity for binding of the [5]helicene enantiomer of matching helicity, but also provides an ideally shape-matched binding pocket for the enantiomerization transition structure, making this the first example of an artificial "deracemase" capable of effectively catalyzing enantiomerization according to the Pauling–Jencks model of enzyme catalysis purely through the environment of a nonplanar π-system. A comparison with the inactive meso-congener of the active catalyst illustratively demonstrates how, like in natural enzymes,[54] even subtle geometric changes to the binding pocket profoundly affect catalysis. Unlike in previous examples that relied on

planarity vs. three dimensionality,[50, 137] catalysis originates from the matching of the transition structure's non-planarity with the curvature of the catalyst cavity created by the core twisted PBI moieties (Figure 33), as well as the helicity mismatch between reactant and the host.

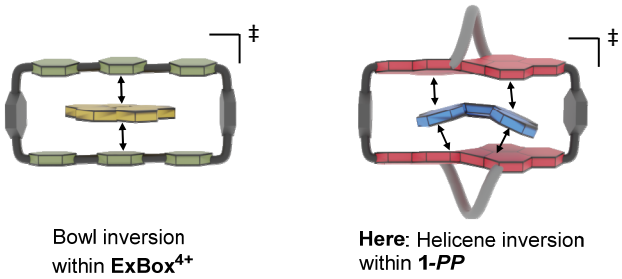

Figure 33. Schematic representation of the transition structure stabilization in the previously reported bowl-to-bowl inversion within the **ExBox**$^{4+}$ cyclophane (corannulene's planar transition structure is depicted in yellow, left) and of the enantiomerization of [5]helicene within the chiral PBI cyclophane presented here ([5]helicene's non-planar transition structure is depicted in blue, right).

4.2 Results and Discussion

4.2.1 Molecular Design and Synthesis

The distortion of originally planar PBI chromophores into propeller-like twisted structures with *P*- and *M*-helicity by appropriate substitution in the bay positions is a well-established approach.[167, 170, 173, 179, 181] While 1,7-di-substitution typically results in conformationally labile derivatives,[170] fast interconversion between the atropo-enantiomers can be prevented *via* 1,7-bridging units, connecting the two bay positions of the PBI moiety and thus introducing a permanent chiral core twist.[179, 181, 193] As illustrated in Figure 34, strategic macrocyclization of the resulting chiral PBI chromophores allows for the construction of cyclophanes with an inherently chiral or achiral binding pocket.

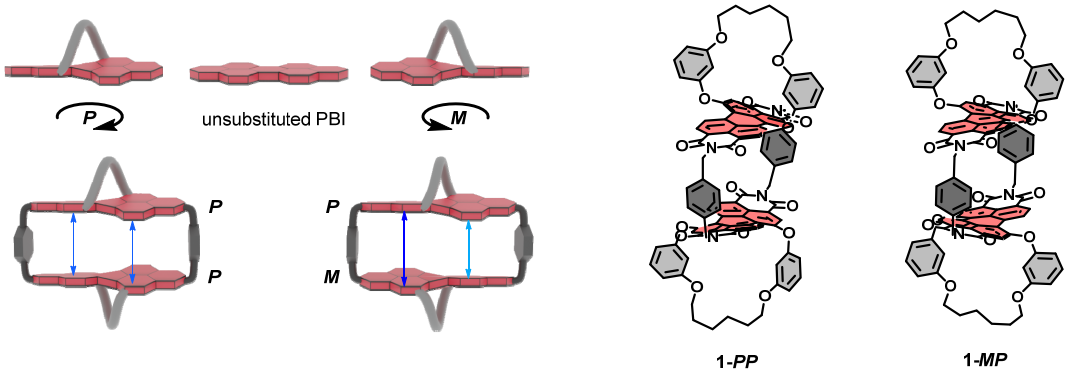

Figure 34. Schematic depictions of the concept of inducing *P*- and *M*-helicity in PBIs as well as the geometrical differences between the two cyclophane isomers **1-*PP*** and **1-*MP*** and their molecular structures. The blue double arrows indicate the non-parallel orientation of the naphthalene units in the case of the meso host, resulting in a varying cavity height, and the parallel face-to-face orientation between them in the homochiral congener.

As compared to the one-step synthesis recently reported for **1-*PP***,[193] we here employed an improved two-step procedure (Scheme A2) for the synthesis of **1-*PP*** and **1-*MP***, involving imidization of enantiopure perylene bisanhydride (PBA) with the *Boc*-protected *para*-xylylene linker moieties and subsequent macrocyclization with the corresponding second PBA of desired configuration (for the full synthetic procedure, see the Appendix). X-ray crystallographic analysis of a single crystal of the newly synthesized **1-*MP*** confirms its structure and reveals a mirror plane perpendicular to the *para*-xylylene spacer units (Figure A70). In contrast to **1-*PP***, where the facing naphthalene units of the PBI chromophores are arranged in a parallel manner, the naphthalene units in the dye moieties of **1-*MP*** have a non-parallel orientation, resulting in an achiral cavity with varying height (~6.5–8.1 Å).

4.2.2 Structural Elucidation of the Complex

Fluorescence titration studies (Figure A54) were employed to provide insights into the effect of the structural difference between the two hosts on the binding strength for the [5]helicene guest. Whereas complexation of *P*-[5]helicene by **1-*PP*** results in a high association constant of $K_a = 1.6 \times 10^9\ M^{-1}$ in tetrachloromethane,[193] a reduced association constant of $K_a = 2.0 \times 10^6\ M^{-1}$ is observed in the same solvent for the complexation of *rac*-[5]helicene by the meso cyclophane. Accordingly, while the inversion of configuration in one chromophoric unit of **1-*MP*** disturbs the shape match between host and guest, a shape complementarity between **1-*PP*** and [5]helicene of the same configuration allows for very efficient complexation.

In order to investigate the influence of the chiral environment on [5]helicene within **1-*PP***, we carried out proton NMR experiments to shine light on the complex structure. Taking into account the enantiomerization barrier of around 100 kJ mol^{-1} for [5]helicene,[211] we prepared an equilibrated 1:1 mixture of racemic guest and **1-*PP*** in 1,1,2,2-tetrachloroethane-d_2, which indeed revealed sharp and well resolved signals at a temperature of 245 K (Figure 35a). The protons of the host split into two sets of signals with equal integrals in the slow exchange regime owing to a desymmetrization of the free host (point group D_2 on the NMR time scale) upon the binding of [5]helicene (point group C_2). The guest protons give one signal set whose integrals fit the expected 1:1 complex. Notably, the additional set of signals for the host protons can not be explained by a splitting due to partial complexation, which was confirmed by a comparison of the spectra in the absence and the presence of the guest molecule, showing that none of the signals in the spectrum correspond to the free host protons. Furthermore, our computational studies (*vide infra*) on the epimeric complexes, i.e. *P*-[5]helicene⊂**1-*PP*** and *M*-

[5]helicene⊂**1-*PP***, give strongly different complexation energies, which is in accordance with our observation that only one complex species is present in solution. All proton signals of the complex could be assigned with the help of 2D NMR spectroscopy at low temperature (Figure A62–A63).

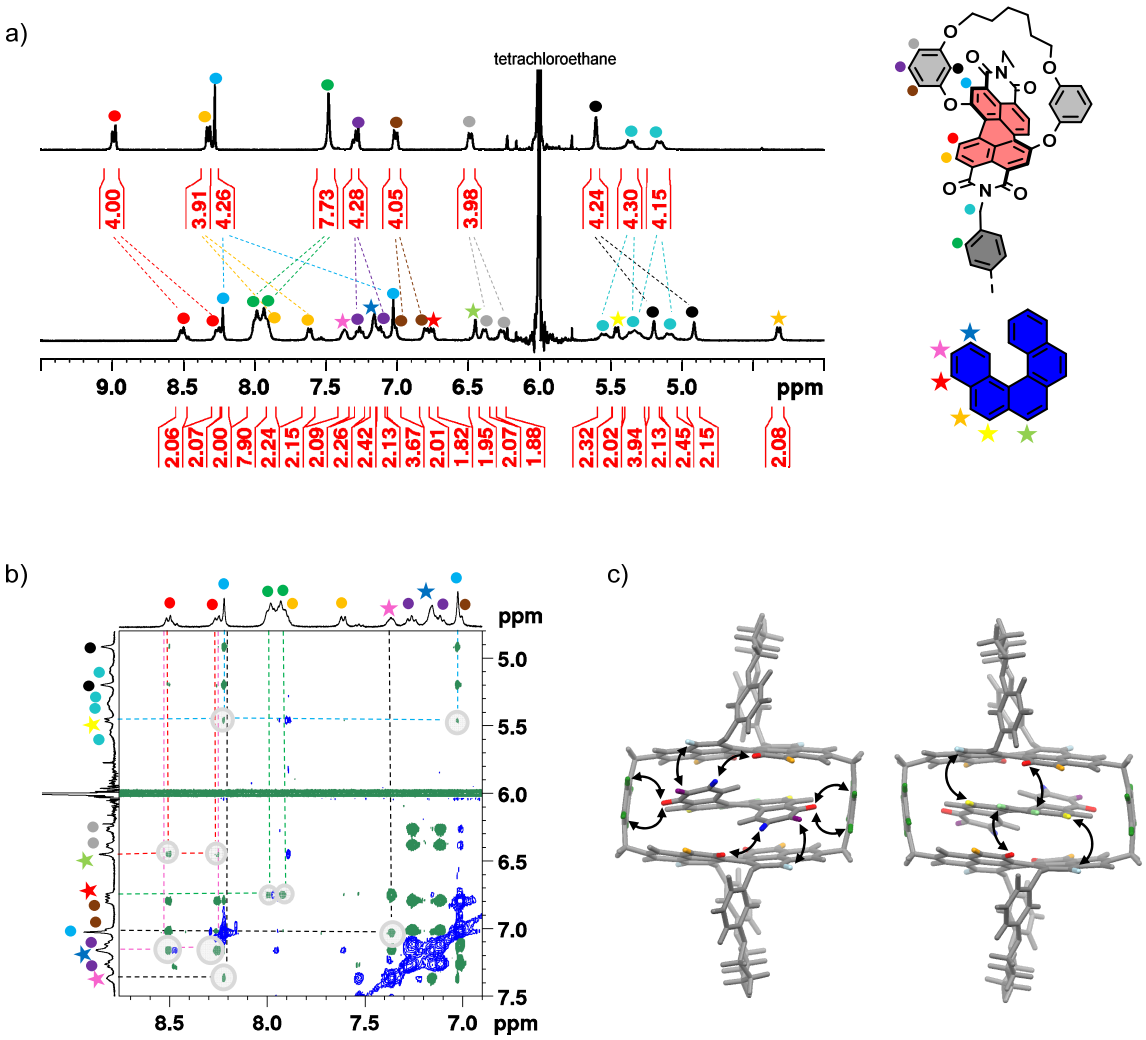

Figure 35. a) Low-temperature NMR (245 K, 400 MHz) spectrum of **1-*PP*** in the absence and in the presence of one equivalent of *rac*-[5]helicene in TCE-d_2 (c (**1-*PP***) ≈ 1.0 mM). The guest proton in the 1-position could not be resolved. b) Excerpt from ^{1}H-^{1}H ROESY NMR (600 MHz) of **1-*PP*** (c ≈ 1.0 mM) and *rac*-[5]helicene (one equivalent) in TCE-d_2 at 245 K. The relevant cross signals are highlighted in grey. c) Geometry optimized structure of *P*-[5]helicene⊂**1-*PP*** viewed from both sides with double arrows highlighting the cross signals between host and guest protons.

In order to elucidate the binding mode, a ^{1}H-^{1}H ROESY NMR (Figure 35b and A63) experiment was carried out. Distinct cross signals were observed not only between the chromophore and the guest unit but also between the aromatic spacer protons of the cyclophane and the guest protons, revealing spatial proximity between the corresponding subunits. These correlations

support a perfectly embedded guest within the receptor's cavity (Figure 35c). Surprisingly, cross signals of identical intensity between the corresponding guest proton and both signal sets of the host can be observed in the ROESY spectrum, indicating a reversible conformational change, proceeding with a similar barrier in both directions. We note that the cross signals indicate a dynamic rotation of the guest within the cavity, which we find from variable temperature NMR and ^{1}H-^{1}H EXSY NMR to proceed with a barrier of around 54 kJ mol^{-1}. For details on this dynamic motion, we refer to the Appendix (*Chapter 9.2, page 169*).

In order to further examine the conclusion drawn from NMR studies, we grew a co-crystal from a mixture of **1-*PP*** and racemic [5]helicene, suitable for single crystal X-ray analysis, by slow diffusion of *n*-hexane into a chlorobenzene solution of the mixture (Figure 36). The molecules in this crystal pack in the monoclinic system with no contact between the π-surfaces of the PBI units of neighboring cyclophanes. The space between the chromophores of the adjacent cyclophane PBI units is filled with solvent molecules (Figure A71), which were partially removed by the SQUEEZE routine in our crystallographic analysis.[237]

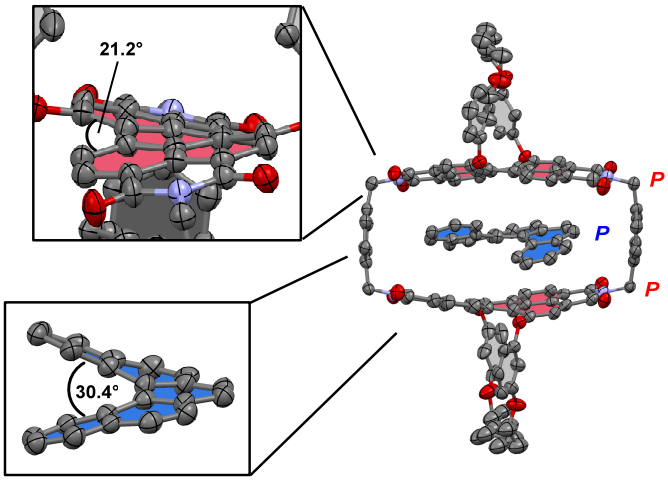

Figure 36. Molecular structure of the *P*-[5]helicene⊂**1-*PP*** complex from single crystal X-ray analysis (thermal ellipsoids set at 50% probability). The guest is highlighted in blue, the perylene units are highlighted in red. Zoom-ins of one chromophore unit as well as of the guest are given in order to visualize the mutual adaption of host and guest in this system. Solvent molecules and hydrogens are omitted for clarity.

The X-ray structure unambiguously confirms the formation of a 1:1 complex as suggested by the NMR studies. More importantly, in line with our expectations based on NMR spectroscopy and theory, the guest exists only in its *P*-configuration within the cavity of the **1-*PP*** host, which supports the conclusion that the homochiral complex is the thermodynamically favored state. The shape match between the helical structure of the guest and the PBI chromophores gives rise to a right-handed supramolecular helix with three turns. For the PBI chromophores, the

angle between the naphthalene units (the core twist) is with 21.2° increased by 6° compared to a crystal structure with [4]helicene[193] in order to accomodate the higher steric demand of the guest. Notably, the solid-state structure further reveals that the dihedral angle spanned by the planes of the outer naphthalene units of [5]helicene, is significantly compressed. While a dihedral angle of 30.4° was found for [5]helicene in the complex with the PBI cyclophane, this angle is, at 41.4°, significantly larger in the crystal structure of the free guest reported in literature.[238] Both values, as well as observed PBI core twists are in good agreement with those obtained from theoretical calculations (*vide infra*).

4.2.3 Enantiomerization Catalysis

Our NMR and single crystal X-ray analyses suggest the formation of one single complex structure from a mixture of racemic [5]helicene and **1-*PP***. Thus, in order to investigate the interaction between [5]helicene and **1-*PP*** further, we carried out detailed studies on the enantiomerization process of the guest. The kinetics of the chirality inversion of [5]helicene were studied in the absence and in the presence of 2 eq. of **1-*PP*** and **1-*MP*** using time dependent CD spectroscopy. Figure 37a shows the CD time course of *M*-[5]helicene in the absence and in the presence of **1-*MP***, while Figure 37b displays the time dependent CD changes of both *P*- and *M*-[5]helicene in the presence of **1-*PP***. We note that repetition of the CD studies using larger excesses of host (5 eq. and 10 eq.) had almost no influence on the enantiomerization kinetics (Figure A60), confirming guest enantiomerization rather than complexation or decomplexation to be rate-determining and therefore allowing quantitative conclusions on the guest isomerization from the optical changes.

As apparent from Figure 37 and Figures A55–A59, in all three cases, the curves of the time courses could be properly fitted according to first-order kinetics (equation A3*, page 161*). The resulting first-order kinetics fits allow calculation of racemization and enantiomerization rate constants. Hereby it is instructive to note that the changing CD signals over the two time courses represented in Figure 37a, namely the time courses for *M*-[5]helicene in the absence of a host (black symbols) and in the presence of **1-*MP*** (grey symbols), indicate racemization of the sample within approximately 35 h. In contrast, the comparison between the time courses of *P*-[5]helicene and *M*-[5]helicene in the presence of **1-*PP*** suggests formation of a stable homochiral complex in both cases.

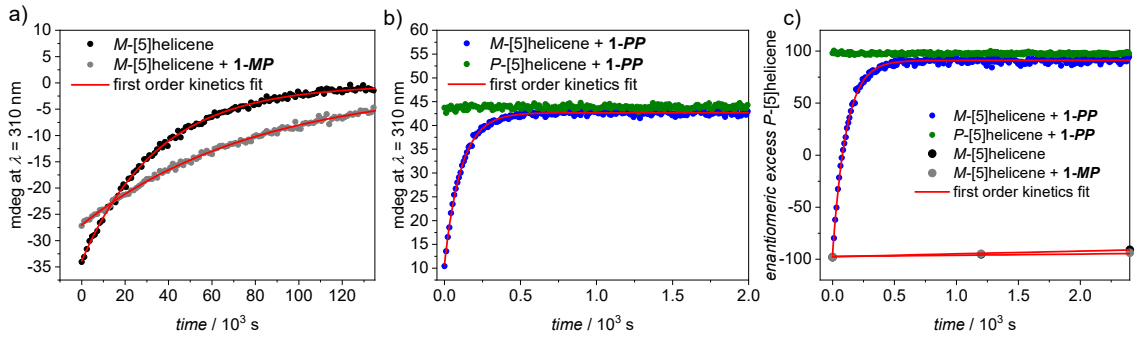

Figure 37. a) Time course of the CD signal of *M*-[5]helicene (c = 10 µM) at 22 °C in the presence and in the absence of **1-*MP*** (c = 20 µM, 2 eq.) and the fitting curves according to first-order kinetics. b) Time course of the CD signal of *M*-[5]helicene and *P*-[5]helicene (c = 10 µM) at 22 °C in the presence of **1-*PP*** (c = 20 µM, 2 eq.). c) The corresponding time courses of the enantiomeric excess of *P*-[5]helicene (–100% corresponds to enantiopure *M*-[5]helicene), calculated according to $ee = \Delta\varepsilon/\Delta\varepsilon_{max}$[80].

Confirming helical self-recognition, the CD signal remains unchanged throughout the time course for *P*-[5]helicene in the presence of **1-*PP*** (Figure 37b, green symbols). The equilibrated state reached for the mixture of **1-*PP*** and *M*-[5]helicene (Figure 37b, blue symbols) gives the same CD signal as the homochiral host-guest mixture, indicating formation of the same homochiral complex and almost full conversion of *M*-[5]helicene into *P*-[5]helicene. Accordingly, the fits given in Figure 37a give rate constants, where $k_{obs} = k_{rac}$, from which enantiomerization rate constants can be obtained as $k_{rac} = 2k_e$.[204, 239] From the fit corresponding to the CD time course of *M*-[5]helicene in the presence of **1-*PP*** in the typical absorption range of the substrate, the enantiomerization rate constant can be obtained as $k_{obs} = k_e$.

For the enantiomerization of [5]helicene at room temperature in the absence of a host, we determined a rate constant of $k_{e,uncat} = 1.4 \times 10^{-5}$ s^{-1}, corresponding to a Gibbs free enantiomerization barrier of 99.6 kJ mol^{-1} (equation A4, *page 165*). This is in good agreement with previous literature.[205, 211] In the presence of an excess of **1-*MP***, it is apparent from the time course that the racemization process is weakly decelerated, indicating a small inhibitive effect of the meso cyclophane on the guest enantiomerization. Confirming this observation, we indeed obtain a reduced enantiomerization rate constant of $k_{e,\mathbf{1}\text{-}MP} = 6.1 \times 10^{-6}$ s^{-1}, corresponding to a slightly increased Gibbs free enantiomerization barrier of 101.7 kJ mol^{-1}. In contrast, in the presence of the homochiral cyclophane **1-*PP***, the observed CD changes suggest a significant acceleration of the enantiomerization of *M*-[5]helicene. While the uncatalyzed racemization of [5]helicene occurred on a timescale of more than a day, we find that in the presence of **1-*PP*** the enantioenriched equilibrium is reached within several minutes. Accordingly, we obtain a notably increased enantiomerization rate constant

of $k_{e,\mathbf{1}\text{-}\boldsymbol{PP}} = 9.1 \times 10^{-3}$ s^{-1}, corresponding to a significantly lowered barrier of 83.7 kJ mol^{-1} at room temperature. This enantiomerization barrier was further validated by an Eyring analysis (Figure A61) using temperature-dependent CD studies (Figure A55–A56 and A58–A59). For the full results, including enthalpic and entropic contributions, see the Appendix (Table A2). In order to illustrate the difference between the kinetics, a combined plot of Figure 37a,b is depicted in Figure 37c, which shows the time-dependent enantiomeric excess of all described processes. From this depiction, the dramatic acceleration of the guest enantiomerization in the presence of **1-*PP*** becomes apparent. The ratio of the enantiomerization rate constants in the presence and the absence of **1-*PP*** reveals a ~700-fold acceleration of the uncatalyzed enantiomerization process, and a catalytic rate enhancement of $k_{e,\,\mathbf{1}\text{-}\boldsymbol{PP}}/k_{e,\,\mathbf{1}\text{-}\boldsymbol{MP}} \approx 1600$ compared to the enantiomerization within the achiral host. Thus, we find not only a notable catalytic effect of **1-*PP*** on the [5]helicene enantiomerization, but also a significant effect of an apparently small change in cavity geometry on catalytic efficiency.

4.2.4 Computational Studies

In order to identify the origin of this catalytic effect, as well as the observed difference in catalytic activity of **1-*PP*** and **1-*MP***, we carried out computational studies to gain insights into the structural features of the complexes and noncovalent interactions along the reaction coordinates of the inversion of [5]helicene in the presence and absence of the hosts. We begin by considering the uncatalyzed enantiomerization process of [5]helicene. Figure 38 shows the resulting equilibrium and transition structure geometries optimized at the B3LYP-D3(BJ)/def2-SVP level of theory[240-246] along with the associated enantiomerization barrier obtained at the SMD-(CCl_4)-PW6B95-D3(BJ)/def2-TZVPP level of theory.[244-248]

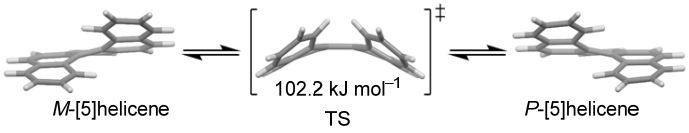

Figure 38. Optimized equilibrium and transition structures pertaining to the enantiomerization of [5]helicene along with the corresponding Gibbs free enantiomerization barrier at 298 K.

Unlike the processes studied in previous research on cyclophane catalyzed isomerizations,[50, 58, 137, 141] the chirality inversion of [5]helicene proceeds *via* a distinctly nonplanar TS with a puckered, C_s symmetric geometry. The associated Gibbs free energy barrier for this process of

102.2 kJ mol^{-1} obtained here is in good agreement with experimental data (*vide supra*), as well as high-level ab initio calculations.[249]

To subsequently determine how this process is affected by complexation with the present hosts, we optimized all reactant, transition structure, and product complexes with **1-*PP*** and **1-*MP*** and performed energy decomposition analyses (EDAs) using the second generation of the absolutely localized molecular orbital (ALMO) EDA scheme by Head-Gordon and co-workers[250] on the resulting complexes. Figure 39 gives schematic potential energy profiles for the chirality inversion of [5]helicene in the presence of **1-*PP*** and **1-*MP***, as well as breakdowns of the relative noncovalent TS stabilizations and destabilizations from EDAs (for full EDA results for all complexes, see Table A6). Table 1 provides a summary of the kinetic and thermodynamic parameters of these processes obtained experimentally and computationally.

In agreement with experimental observations, for the enantiomerization occurring within the cavity of **1-*PP***, we obtain a reduced barrier of 93.7 kJ mol^{-1}, whereas a calculated barrier of 102.8 kJ mol^{-1} in the presence of **1-*MP*** confirms the observed catalytic inactivity of this host. Confirming the observation of deracemization by **1-*PP*** from preceding experimental studies (*vide supra*), we further find a notable relative stabilization of 15.3 kJ mol^{-1} of *P*-[5]helicene over *M*-[5]helicene, which becomes apparent upon visual inspection of the optimized host–guest complexes. In *P*-[5]helicene⊂**1-*PP***, the matching handedness of the guest's and the host's π-systems allows for the complex to arrange into a highly stabilized π-stack resembling a helix with three turns. In contrast, the chirality mismatch between the guest and the hosts' PBI moieties in *M*-[5]helicene⊂**1-*PP*** and both [5]helicene⊂**1-*MP*** complexes leads to non-ideal host–guest complementarity and smaller stabilization energies, which are similar for both types of complexes. As this shows that the observed striking difference in catalytic activities of **1-*PP*** and **1-*MP*** is not due to differential stabilization of reactant complexes, the origin of relative stabilization of the achiral puckered enantiomerization TS by **1-*PP*** is less apparent. Inspection of the optimized TS complex with **1-*PP*** reveals that the parallel orientation of the host's naphthalene moieties creates a consistent cavity height, while the core twist of the PBI moieties creates curvature in the π-systems. This curvature intricately matches the curvature of the puckered TS, allowing for the nonplanar π-system of the TS to be noncovalently stabilized in the binding pocket by π-stacking with the nonplanar π-system of the host. In contrast, the variation in cavity height created by the non-parallel naphthalene units of **1-*MP*** and the opposing orientations of the PBI core twists create noncomplementary nonplanarity in the host's and the TS's π-systems and reduce noncovalent TS stabilization by **1-*MP***.

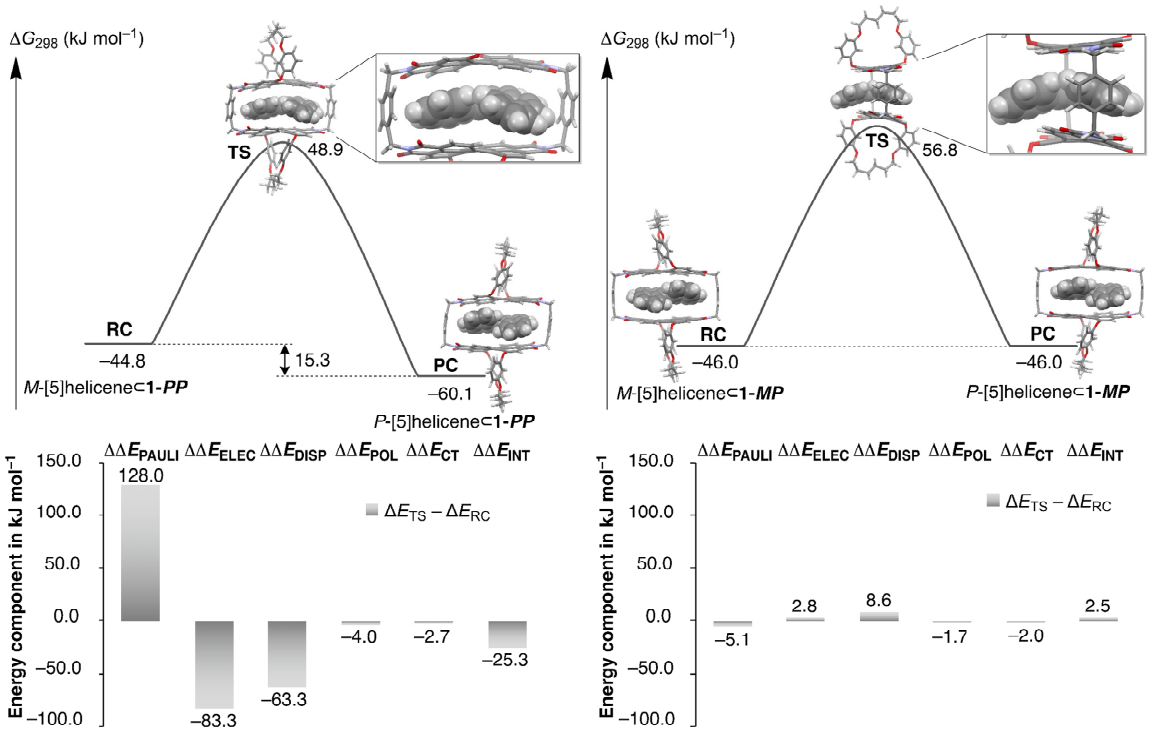

Figure 39. Schematic PESs of the [5]helicene inversions within **1-*PP*** and **1-*MP*** along with breakdowns of relative noncovalent stabilizations and destabilizations of TSs obtained from EDAs, calculated as $\Delta\Delta E = \Delta E_{TS} - \Delta E_{RC}$. (RC = reactant complex, PC = product complex; geometries and energies were obtained at the SMD-(CCl_4)-PW6B95-D3(BJ)/def2-TZVPP//B3LYP-D3(BJ)/def2-SVP level of theory,[244-248] while ALMO-EDA[250] analyses were performed using ωB97M-V/def2-SVP).[244, 251]

Table 1. Summary of the most important thermodynamic and kinetic data of [5]helicene in the presence of **1-*PP*** and **1-*MP***.

	K_a [M^{-1}][a]	$\Delta G_{exp.}$[b] ($\Delta G_{comp.}$) [kJ mol^{-1}]	k_e [s^{-1}]	$k_e/k_{e,uncat}$	$\Delta G^{\ddagger}_{exp.}$ ($\Delta G^{\ddagger}_{comp.}$)[c] [kJ mol^{-1}]	$\Delta\Delta G^{\ddagger}_{exp.}$ ($\Delta\Delta G^{\ddagger}_{comp.}$)[d] [kJ mol^{-1}]
1-*PP*	1.6×10^9	–52.0 (–60.1)	9.1×10^{-3}	6.5×10^2 [e]	83.7 (93.7)	15.9 (8.5)
1-*MP*	2.0×10^6	–35.6 (–46.0)	6.1×10^{-6}	4.4×10^{-1}	101.7 (102.8)	–2.1 (–0.6)

a) Obtained from complexation studies of *P*-[5]helicene with **1-*PP***[193] and *rac*-[5]helicene with **1-*MP***. b) Calculated from $\Delta G_{exp.} = -RT\ln K_a$, with R being the ideal gas constant and the respective binding constant K_a at 295 K. c) Calculated from the Eyring equation with $\Delta G^{\ddagger} = -RT\ln(k_e h/k_b T)$ with the ideal gas constant R, the Planck constant h and the Boltzmann constant k_b at 295 K. d) Calculated from $\Delta\Delta G^{\ddagger}_{exp.} = \Delta G^{\ddagger}_{non.} - \Delta G^{\ddagger}_{exp.}$, where $\Delta G^{\ddagger}_{non.}$ corresponds to the experimentally determined enantiomerization barrier of [5]helicene of 99.6 kJ mol^{-1}. e) With 5 or 10 eq. the ratio is slightly increased to $k_e/k_{e,uncat} = 7.9 \times 10^2$.

Results from energy decomposition analyses provide a breakdown of the overall intermolecular interactions between host and guest structures, allowing us to quantify these qualitative observations. As apparent from Figure 39, in the TS complex with **1-*MP***, relative TS stabilizations and destabilizations are consistently minute, leading to no overall relative

noncovalent stabilization of the TS by **1-*MP***. In contrast, a very different picture emerges for the enantiomerization process within **1-*PP***: Here, the comparably larger Pauli repulsions in the TS complex compared to *M*-[5]helicene⊂**1-*PP*** confirm a more closely interacting TS complex. Outweighing this destabilizing contribution, electrostatic and dispersion interactions, characteristic of π-stacked complexes,[252-253] emerge as the largest source of absolute (Table A6) as well as relative TS stabilization. Notably, these contributions are not just larger in the TS complex than in the *M*-[5]helicene⊂**1-*PP*** reactant complex, but also by 35.2 kJ mol^{-1} (ΔE_{ELEC}) and 20.0 kJ mol^{-1} (ΔE_{DISP}) larger in the TS complex than the homochiral *P*-[5]helicene⊂**1-*PP*** product complex (Table A6). This indicates that π–π stacking interactions are indeed maximised in the complex between the intricately complementary transition structure and **1-*PP***, even when compared to the homochiral *P*-[5]helicene⊂**1-*PP*** complex, thereby corroborating a significant contribution of TS stabilization to the catalytic effect.

Aside from TS stabilization, destabilization of the reactant complex due to geometric distortions in host and guest resulting from the binding of the less complementary reactant is expected to contribute to overall reaction barrier lowering according to the Pauling–Jencks model of enzyme catalysis.[51, 214] In order to quantify this ground state destabilization in our systems of interest, we calculate the differences in electronic energies (ΔE_e) between free equilibrium host and guest structures and the corresponding geometries of the isolated host and guest molecules, respectively, in reactant, transition structure, and product complexes. Figure 40a,b gives the destabilization energies resulting for the host and guest moieties of all complexes.

As clearly apparent from Figure 40a, for the process catalyzed by **1-*PP***, destabilization energies decrease along the reaction coordinate. While host and guest in the "helicity-mismatched" reactant complex receive the largest overall destabilization of 16.8 kJ mol^{-1}, the total destabilizations of the more complementary host and guest of the TS and homochiral product complexes amount to only 11.7 and 7.8 kJ mol^{-1}, respectively. Thus, in accordance with the Pauling–Jencks model, a comparably smaller destabilization of host and guest in the TS complex compared to the reactant complex (by 5.1 kJ mol^{-1}, overall) contributes to the overall catalytic effect observed for this system. By comparison, for the process occurring within the less complementary host **1-*MP***, Figure 40b shows that the reactant and transition structure complexes are destabilized to almost the same extent (by overall 16.2 and 15.7 kJ mol^{-1}, respectively), indicating a negligible effect of ground state destabilization on the enantiomerization barrier. In agreement with the well-documented flexibility of the bay regions of PBIs,[168, 254] we note that the calculated destabilizations of the guest are consistently larger

than those of the host and originate from the guest planarizing in response to the geometric constraints of the hosts' cavities.

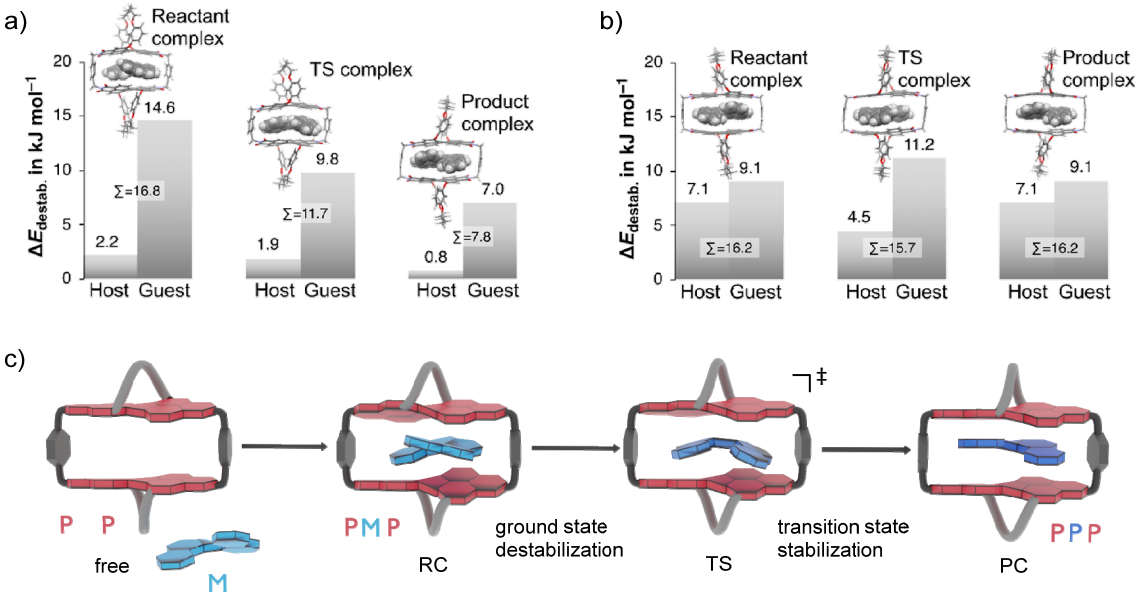

Figure 40. Differences in electronic energies ($\Delta E_{destab.}$) between corresponding host and guest structures from free optimizations and from optimizations of reactant, transition structure (TS), and product complexes for the enantiomerization process within a) **1-*PP*** and b) **1-*MP*** in kJ mol^{-1}. c) Schematic representation of the whole enantiomerization process of [5]helicene within **1-*PP***.

Figure 40c summarizes the results of the computational investigation into the origins of the catalytic effect of the chiral host **1-*PP*** on the [5]helicene enantiomerization. As apparent from the schematic illustrations, the observed reaction barrier lowering originates both from transition state stabilization, as well as ground state destabilization, in line with the Pauling–Jencks model. Hereby, EDAs (Figure 39) showed that TS stabilization is almost exclusively the result of stabilizing electrostatic and dispersion interactions resulting from optimized π–π stacking interactions between the neatly aligned curved π-systems of the enantiomerization TS and the host. While the catalytic cavities of natural enzymes typically rely on complex networks of functional groups, the present system represents an attractively simple example of a catalytic process in which TS stabilization is achieved purely through π–π stacking. Compared to the first examples of such "π–π catalysis", which explored proof-of-principle inversion processes with isoenergetic reactants and products,[50, 58, 137, 141, 232] the inherent chirality of the present PBI cyclophane host for the first time introduces a non-zero reaction energy and thus achieves π–π catalysis with significant enantioselectivity despite its simplicity. Contributing to the catalytic effect resulting from TS stabilization, ground state destabilization results from a shape

mismatch between the *M*-[5]helicene reactant and the *P*-homochiral host, necessitating energetically unfavorable geometric distortions in the reactant complex. This "strain energy" is released in the more geometrically relaxed TS complex. In contrast, the shape-mismatch between the enantiomerization TS and the cavity of **1-*MP*** leads to the loss of relative noncovalent TS stabilization, and destabilizing geometric distortions in the TS complex largely outweigh the contribution from ground state destabilization. Thus, the computational model comprehensively explains both, the origins of the catalytic effect of the "active deracemase" **1-*PP***, as well as the origins of the loss of catalytic activity upon the comparably small geometric modification to the host's cavity that results from chirality inversion in one PBI moiety.

4.3 Conclusion

In summary, we have reported a detailed experimental and computational study for a helicene enantiomerization process that is promoted in an enzyme-like manner by the cavity of an inherently chiral PBI cyclophane. We find that the curvature of the host's π-system not only exhibits favored recognition of the helicene enantiomer of matching handedness, but furthermore an intricate match in cavity shape and π-system curvature between the host's PBI moieties and the nonplanar [5]helicene enantiomerization transition structure also makes the cyclophane a complementary receptor for the transition structure. By comparison, the complex with the helicity mismatched [5]helicene enantiomer receives reduced noncovalent stabilization and experiences more significant destabilizing geometric distortions. In this fashion, the here described host actuates noncovalent catalysis according to the Pauling–Jencks model of enzyme catalysis by stabilizing the transition structure and destabilizing the ground state. EDA analyses show that transition structure stabilization primarily originates from noncovalent dispersion and electrostatic interactions between the nonplanar π-systems of the [5]helicene guest and the host. Time dependent CD studies find the enantiomerization barrier to be significantly reduced, allowing for rapid formation (~700 times rate acceleration) of the homochiral complex, which is confirmed by 2D NMR and crystallographic studies. A comparison with the meso-congener of the catalytically active chiral cyclophane shows that changing the handedness of only one PBI moiety not only affects chiral recognition, but also transforms the host from an effective catalyst into a slight inhibitor of enantiomerization. Thus, this study not only provides a detailed description of deracemization catalysis actuated by a chiral host, but also highlights the importance of precise transition structure recognition in the development of supramolecular enzyme mimics.

Chapter 5

Mutual Induced Fit Transition Structure Stabilization of Corannulene's Bowl-to-Bowl Inversion in a Perylene Bisimide Cyclophane

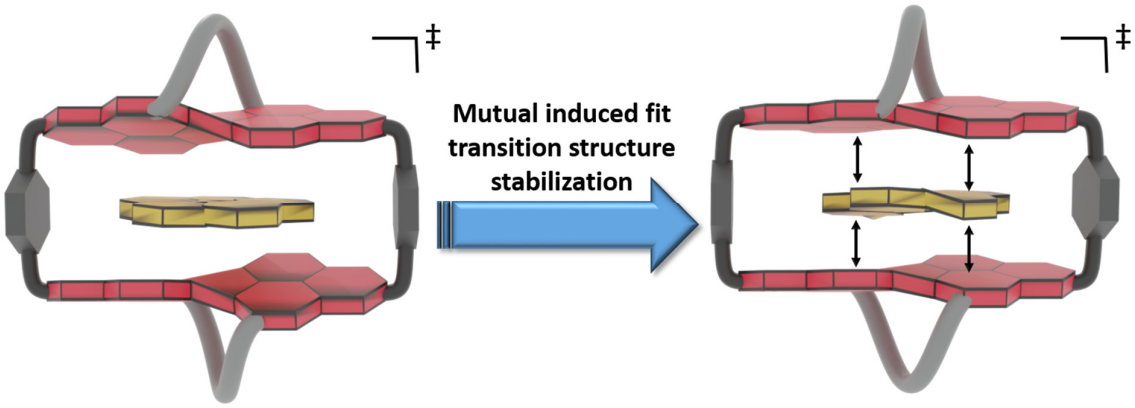

Dr. Asja A. Kroeger (The University of Western Australia) contributed the DFT calculations to this chapter. Olga Anhalt (Universität Würzburg) performed the single crystal X-ray analysis.

Abstract. Corannulene is known to undergo a fast bowl-to-bowl inversion at r.t. *via* a planar transition structure (TS). Herein we present the catalysis of this process within a perylene bisimide (PBI) cyclophane composed of chirally twisted, non-planar chromophores, linked by *para*-xylylene spacers. Variable temperature NMR studies reveal that the bowl-to-bowl inversion is significantly accelerated within the cyclophane template despite the structural non-complementarity between the binding site of the host and the TS of the guest. The observed acceleration corresponds to a decrease in the bowl-to-bowl inversion barrier of 11.6 kJ mol^{-1} compared to the uncatalyzed process. Comparative binding studies for corannulene (20 π-electrons) and other planar PAHs with 14 to 24 π-electrons were applied to rationalize this barrier reduction and revealed indeed high binding constants that reach in tetrachloromethane as a solvent the picomolar range for the largest planar guest. Computational models corroborate these experimental results and suggest that both transition state stabilization and ground state destabilization contribute to the observed catalytic effect. Hereby, we find a "mutual induced fit" between host and guest in the TS complex, such that mutual geometric adaptation of the

planar TS and curved π-systems of the host results in an unprecedented non-planar TS of corannulene. Concomitant partial planarization of the PBI units optimizes noncovalent TS stabilization by π–π stacking interactions. This observation of a "mutual induced fit" in the TS of a host-guest complex was further validated experimentally by single crystal X-ray analysis of a host–guest complex with coronene as a qualitative transition state analogue.

5.1 Introduction

Corannulene,[255-257] also called [5]circulene, has been known for more than 50 years and is probably the most prominent example of a positively curved polycyclic aromatic hydrocarbon (PAH).[258-259] Its bowl shape originates from the incorporation of a five-membered ring in the aromatic system. At room temperature, corannulene undergoes fast degenerate bowl-to-bowl inversion[260-261] with a barrier of approximately 42–46 kJ mol^{-1}.[262] Siegel and co-workers have shown that this inversion barrier of corannulene derivatives is dependent on the bowl depth,[263] which can be tuned by suitable substitution, i.e. benzannulation,[264] with shallower bowl depths leading to lower inversion barriers. Today, the scientific consensus is that this inversion proceeds *via* a fully planar TS, which is why great efforts have been made to obtain flat corannulene as a thermodynamically stable molecule. Flattening of the ground state structure was for example observed by a suitable coordination to a ruthenium complex.[265] Furthermore, it was recently demonstrated that sufficiently strong, metal-free stereoelectronic effects, achieved by a suitable substitution, can convert flat corannulene into a conformer with similar energy as the bowl-shaped isomer.[266]

Aside from the synthetic fine-tuning of the bowl-depth, some groups have investigated the impact of supramolecular host-guest encapsulation on corannulene's inversion process. In this context, Nitschke and co-workers recently showed how a curved host and second guest cooperatively inhibit the dynamic motion of complexed corannulene.[267] In contrast, Siegel and co-workers showed that supramolecular complexation in a suitable box-shaped cyclophane can be used to stabilize the planar geometry of corannulene's inversion TS, which accelerates the rate of swing-through.[50, 137] These results show that the kinetics of the inversion process can be controlled both by synthetic modifications and by supramolecular complexation, and that the geometry of corannulene in the ground state can be adjusted by suitable metal coordination or substitution. However, there is still no example of a non-planar transition structure of corannulene's bowl-to-bowl inversion.

We recently reported the synthesis of a PBI cyclophane composed of chiral chromophores,[193] whose chemical structure is depicted in Figure 41. This macrocycle proved to be an excellent host molecule for the encapsulation of small carbohelicenes due to an optimal shape complementarity between the helically twisted PBI units and the guests. In depth studies showed that this host is able to lower the enantiomerization barrier of [5]helicene by acting as a template catalyst.[193, 268] This example of a delicate process proceeding *via* a non-planar TS has drawn our attention to the possible influence of this cyclophane template, composed of comparably rigid non-planar PBIs, on the planar TS of corannulene's bowl-to-bowl inversion. Based on the seminal work of Juríček *et al*.,[50] as well as on theoretical work on π–π catalysis[232] exerted by PBI cyclophanes with planar chromophores on the stereoinversions of polycyclic aromatic hydrocarbons (PAHs) with planar TSs,[58, 141] we were interested in the impact of this host's rather rigid, non-planar and therefore non-complementary geometry on the dynamic bowl-to-bowl inversion of corannulene.

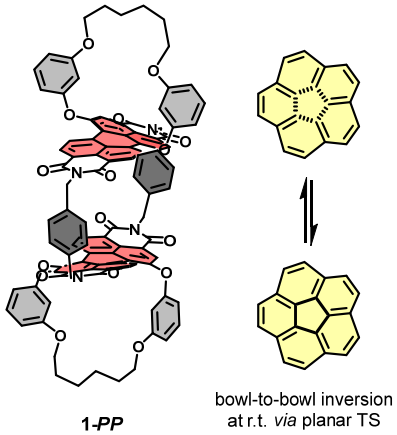

Figure 41. Chemical structure of host **1-*PP*** and equilibrium of bowl-to-bowl inversion of corannulene.

5.2 Results and Discussion

5.2.1 Thermodynamic Properties of Host-Guest Complexes

It is well known that in supramolecular host-guest systems where binding site and guest mainly interact *via* π–π stacking, an increase in the number of π-electrons in the guest is correlated with an increase in binding energy.[56, 269-272] Hence, in order to characterize **1-*PP*** as a host for planar substrate recognition, we selected a series of PAH guests with increasing numbers of π-electrons and carried out UV/vis and fluorescence titration studies in chloroform (Figure A76–A82). For the smaller guests with lower binding constants, UV/vis spectroscopy was

applied to obtain the association constants in chloroform at 295 K. In the corresponding plots of absorption, a decreasing maximum extinction coefficient, well defined isosbestic points as well as an increasing $A_{0\text{-}0}/A_{0\text{-}1}$ ratio of the PBI S_0-S_1 transition can be observed (Figure 42a and Figures A77–A78). Hence, guest encapsulation interrupts the H-type excitonic coupling between the two PBI chromophores by increasing the distance between them.[200-201] Accordingly, the shape of the spectra of the complexes is more reminiscent of a monomeric PBI.[55] Furthermore, a pronounced red-shifted shoulder is apparent for some of the host-guest complex spectra which corresponds to a charge transfer between the electron poor PBIs and the electron rich guests like anthracene and pyrene.[56] From the data evaluation, i.e. non-linear curve fitting of the changes in absorption, an increase in the binding constant from 3.4×10^4 M^{-1} for anthracene (14 π-electrons) to 6.1×10^5 M^{-1} for triphenylene (18 π-electrons) could be determined.

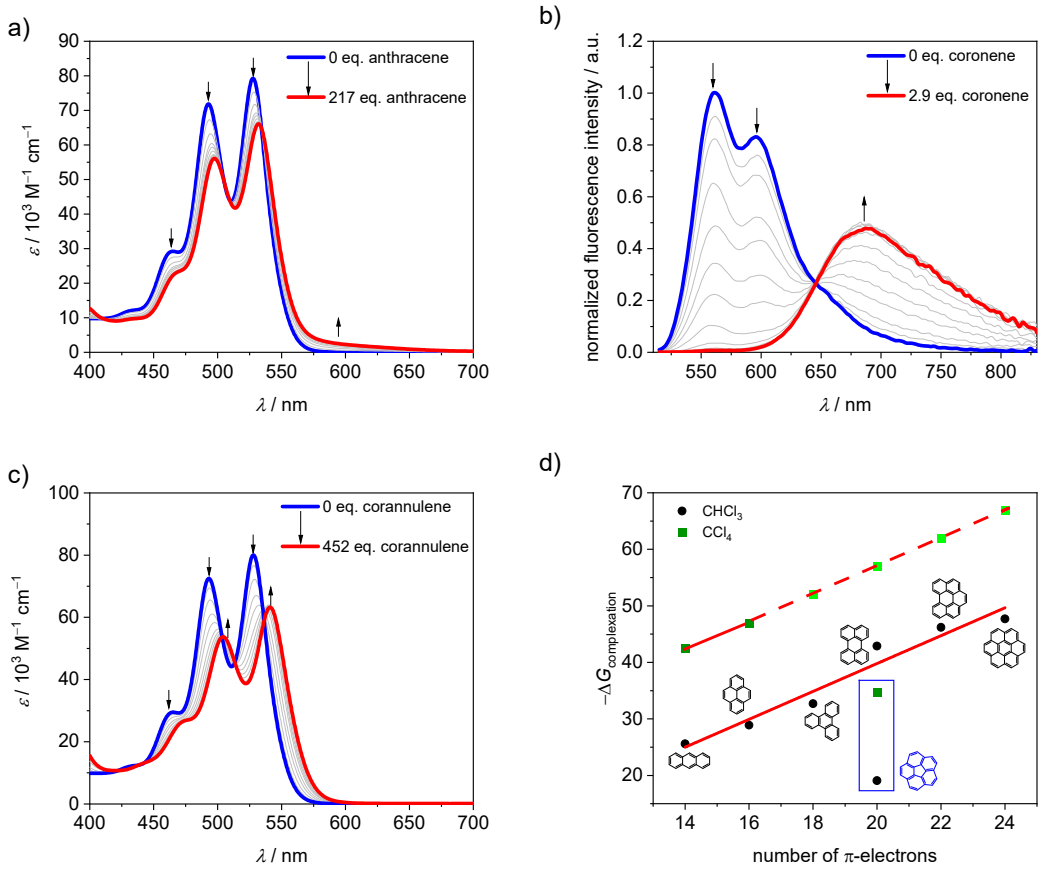

Figure 42. UV/vis or fluorescence titration curves of **1-*PP*** upon the addition of a) anthracene, b) coronene and c) corannulene in chloroform at 295 K. d) Plot of Gibbs free binding energy of complexation for various guests by **1-*PP*** in chloroform and tetrachloromethane at 295 K. The light green symbols indicate that the values are estimated based on linear extrapolation.

For the larger guests, i.e. perylene, benzo[*ghi*]perylene and coronene, fluorescence titration studies were performed. While only a fluorescene turn-off is revealed upon the addition of perylene (20 π-electrons, Figure A79), an exciplex band emerges for benzo[*ghi*]perylene complexation (22 π-electrons, Figure A80). This band is further increased in intensity for coronene (24 π-electrons, Figure 42b and Figure A81) as the largest guest, supporting a significant charge transfer character for these complexes. The corresponding complexation energies fit the expected linear increase with a larger size of the guests' aromatic surfaces (Figure 42d). For coronene, the binding constant in chloroform reaches a remarkably high value of $K_a = 2.8 \times 10^8$ M^{-1}. Upon decreasing the solvent polarity, the binding constants can be further increased for this host if chloroform is replaced by tetrachloromethane as a solvent. For anthracene and pyrene, the association constants could be increased by three orders of magnitude (Figure A83−A84). If a linear free energy relationship is assumed for all PAH guests for the transition from chloroform to tetrachloromethane, the Gibbs free energy can be extrapolated for the larger guests (Figure 42d). This yields a complexation Gibbs free energy of 66.9 kJ mol^{-1} for coronene in tetrachloromethane, corresponding to an impressive binding constant of around 10^{12} M^{-1} in this organic solvent. Table 2 summarizes the binding constants for the guest complexations by **1-*PP*** and the corresponding Gibbs free energies in chloroform and tetrachloromethane.

Table 2. Binding constants for the encapsulation of several guests by **1-*PP*** determined from global nonlinear curve fit routine of UV/vis or fluorescence data at 295 K, as well as the corresponding Gibbs free energies of complexation.

guest	K_a ($CHCl_3$) [M^{-1}]	$-\Delta G^0$ ($CHCl_3$) [kJ mol^{-1}]	K_a (CCl_4) [M^{-1}]	$-\Delta G^0$ (CCl_4) [kJ mol^{-1}]
anthracene	3.4×10^4	25.6	3.3×10^7	42.5
pyrene	1.3×10^5	28.9	2.0×10^8	46.9
triphenylene	6.1×10^5	32.7	1.7×10^{9} a)	52.1 a)
perylene	4.0×10^7	42.9	1.2×10^{10} a)	57.0 a)
benzo[*ghi*]perylene	1.5×10^8	46.2	9.5×10^{10} a)	62.0 a)
coronene	2.8×10^8	47.7	7.0×10^{11} a)	66.9 a)
corannulene	2.4×10^3	19.1	1.4×10^6	34.7

a) Numbers are estimated based on linear extrapolation of the Gibbs free energy in Figure 42d and calculation of the binding constants according to $K_a = e^{-\frac{\Delta G^0}{RT}}$.

Thus, despite the apparent structural mismatch between the helically chiral cavity of the host and the planar guests, we find extraordinarily high binding affinities for the complexes with

planar PAHs. In contrast, curved corannulene (20 π-electrons) shows a much weaker binding by **1-*PP***. The optical changes in the corresponding UV/vis titration study (Figure 42c and Figure A82) are qualitatively comparable to the one of triphenylene (Figure A78), which has 18 π-electrons. However, with a binding constant of $K_a = 2.4 \times 10^3$ M^{-1} in chloroform at 295 K, the complexation energy is by 13.6 kJ mol^{-1} lower, despite the larger aromatic surface of corannulene. Indeed, based on the linear relationships shown in Figure 42 we can calculate Gibbs free energies for a planar 20 π-electron PAH guest of 42.9 kJ mol^{-1} in chloroform and 57.0 kJ mol^{-1} in tetrachloromethane that are significantly larger than those observed for the bowl-shaped corannulene (Table 2).

5.2.2 Structural Properties of Host-Guest Complexes

Computational studies of corannulene⊂**1-*PP*** gave a binding energy for this complex of 41.1 kJ mol^{-1} in tetrachloromethane at the SMD-(CCl_4)-PW6B95-D3(BJ)/def2-TZVPP level of theory,[244-248] which is in reasonably good agreement with the experimental value (*vide supra*). The optimized geometry of the corannulene⊂**1-*PP*** complex reveals that while the chiral PBI host accommodates the guest well, corannulene is significantly compressed by the chromophore planes, resulting in a decrease in bowl depth of 0.17 Å compared to the calculated structure of free corannulene (Figure 43).

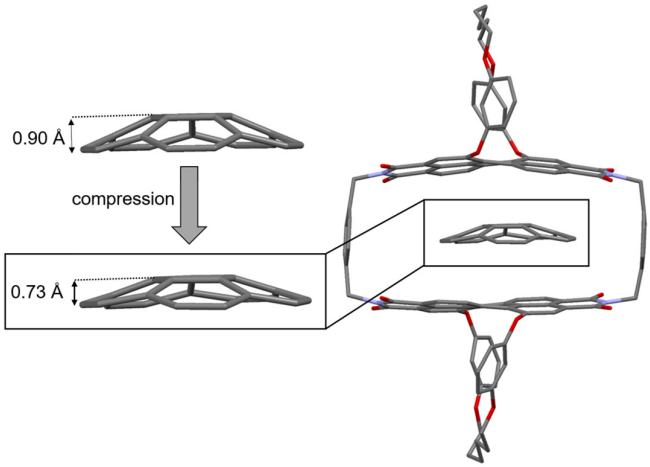

Figure 43. Structures of free corannulene and corannulene⊂**1-*PP*** optimized at the B3LYP-D3(BJ)/def2-SVP level of theory along with a zoom-in on the guest to illustrate its compression upon complexation.

Furthermore, a comparison of the core twists of the PBIs shows that complexation with corannulene either results in an almost unchanged twist (18.5°, PBI facing the convex side of corannulene) or induces a decreased twist (12.3°, PBI facing the concave side of corannulene) compared to the free host (average of 18.1°, see Table A9 for details), illustrating the structural adaptivity of both, the cyclophane host and the bowl-shaped guest. Accordingly, distortion and interaction between the binding site and the substrate are optimized by a mutual structural rearrangement between them upon complexation.

The studies on the guest binding by **1-*PP*** revealed that high binding energies can be achieved for the encapsulation of flat PAHs despite the twisted nature of the PBI units in the cyclophane. To obtain further insights into the structures of these complexes, we grew a co-crystal from a mixture of coronene, the most strongly bound guest, and **1-*PP*** by slow evaporation of *n*-hexane into a chlorobenzene solution. The resulting crystal could be analyzed by single crystal X-ray analysis (Figure 44a). Crystallographic analysis showed that the complex crystallizes in the triclinic system (for details see the Appendix). The crystal structure not only clearly confirms the intercalation of coronene between the twisted PBIs, but also reveals a distorted geometry of flat coronene within the complex. Furthermore, the twist of the naphthalene subunits shows a flattening of the perylene core with a small twist angle of 12.8° (average from both chromophores of the two complexes in the unit cell). Hence, the loss of planarity of coronene is accompanied by a reduction in the PBI core twists. The intermolecular contacts between the twisted perylene units and the distorted coronene guest were further qualitatively investigated with the help of NCI (noncovalent interactions) analysis[273] of the co-crystal (Figure 44b). The green regions in the NCI plot can be attributed to van-der-Waals interactions between the host and the guest and illustrate how the induced structural adaption in this complex optimizes noncovalent interactions between the aromatic planes of the guest and the perylene bisimides. The additional stabilizing interactions between coronene and the *para*-xylylene spacer units further become apparent. When looking from the top on the NCI plot (Figure 44b, right), the intermolecular binding iso-surface also reveals that almost the full aromatic surface of coronene contributes to the host-guest binding, explaining the continuous increase of the complexation Gibbs free energy beyond perylene (as the presumably perfect guest for this host) also for larger substrates.

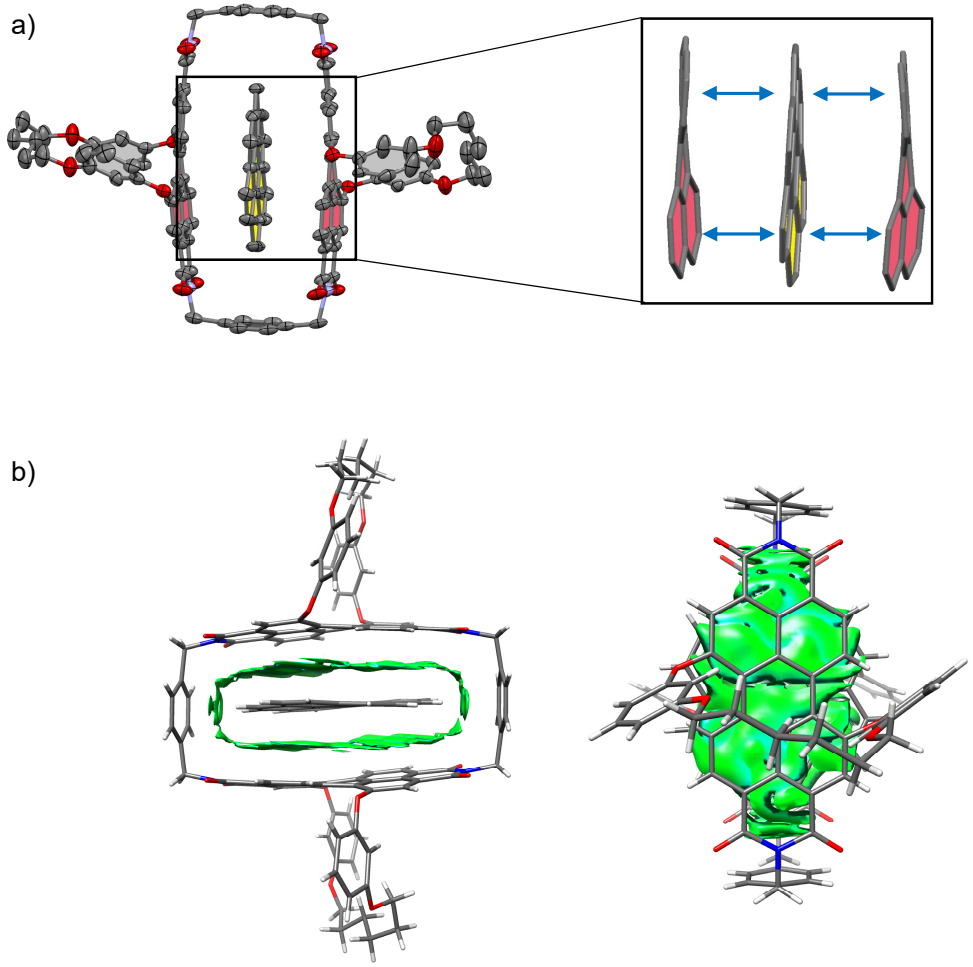

Figure 44. a) Molecular structure of coronene⊂**1**-***PP*** complex, obtained from single crystal X-ray analysis (thermal ellipsoids set at 50% probability) with enlarged excerpt, showing how the perylene units and the guest maximize their interaction by a mutual geometric adaption. The guest is highlighted in yellow, the perylene units are highlighted in red. Solvent molecules and hydrogen atoms are omitted for clarity. b) Noncovalent interactions (NCI) plot of the single crystal structure of coronene⊂**1**-***PP***.

5.2.3 Catalysis of Bowl-to-Bowl Inversion

Despite of structural mismatch between flat guests and core-twisted PBIs, we considered this host to be suited for catalyzing corannulene's bowl-to-bowl inversion. According to our binding studies (Figure 42d, Table 2) we could indeed expect a substantial transition state stabilization from the differences of the calculated Gibbs free energies for a planar 20 π-electron guest and the experimental value for corannulene. Further, the single crystal X-ray analysis revealed that coronene, which is a qualitative transition state analogue for the bowl-to-bowl inversion of corannulene, is complexed with a mutual induced structural adaption of host and guest. Thus, the planar TS of corannulene should experience more stabilization within the cyclophane cavity than the curved equilibrium structure, which should result in catalysis of the stereoinversion.

To study the dynamic bowl-to-bowl inversion process, the alkyl substituent of ethylcorannulene proved to be a good diagnostic group in order to quantify the inversion of corannulene as the methylene protons become heterotopic at low temperatures, when the bowl-to-bowl motion is slow on the NMR time scale.[50] Accordingly, variable temperature NMR studies were performed in deuterated dichloromethane (DCM-d_2), which due to its low melting point is more suitable than chloroform or tetrachloromethane to cover the whole dynamic process. We note that the additional ethyl substituent had no impact on the binding affinity, which was tested by host-guest titration and subsequent data evaluation (Figure A86–A87). We further note in this context that the UV/vis absorption spectrum of the complex in tetrachloromethane is in good accordance with the one in DCM (Figure A89), which indicates that no structural changes in the host-guest assembly are induced by the less polar solvent but only weak solvatochromism is observed.

The binding affinity for corannulene is weaker in DCM than in chloroform. This was also confirmed for the most strongly bound guest coronene (Figure A88), indicating that this is likely to be a general solvent effect. As only one set of signals results for the host protons even at temperatures below 170 K for a host-ethylcorannulene mixture with 2 eq. of **1-*PP*** (Figure A94), guest exchange is fast compared to the bowl-to-bowl inversion over the whole temperature range needed for the studies on this process. Hence, the bowl-to-bowl motion is the rate-determining step which allows direct conclusions on the guest inversion from the dynamic NMR data not only in the absence but also in the presence of the host template and we expect the solvent effect to not affect the studies on the kinetics of interest.

At room temperature, a quartet for the methylene protons of the free substrate is apparent, which becomes more and more broadened upon cooling down until the coalescence at 233 K is reached. At lower temperatures these protons split into two signals. For free ethylcorannulene (Figure 45a and Figure A90), an inversion barrier of 45.8 kJ mol^{-1} could be derived from the coalescence temperature and the signal splitting according to equation A9 (*page 193*), which is in very good agreement with the literature value for corannulene.[262] A similar temperature series was carried out in the presence of 0.5 eq. of **1-*PP*** (Figure 45b and Figure A91), revealing this barrier to be decreased by around 25% to 34.2 kJ mol^{-1} with a coalescence temperature of 176 K for the methylene protons of the guest. This decrease of the barrier towards inversion was further supported by VT experiments with more (Figure A92) or less (Figure A93) than 0.5 equivalents of the host, which had only minor impact on the catalytic effect: While two equivalents of **1-*PP*** lowered the barrier to 33.7 kJ mol^{-1}, supporting the fact that the guest

exchange is fast compared to the bowl-to-bowl inversion (*vide supra*), we determined a slightly higher barrier of 36.8 kJ mol^{-1} with 0.1 equivalents of host. These changes might be attributable to the slow diffusion of the reactants at very low temperatures close to the freezing point of dichloromethane, when the solvent gets more viscous.[274]

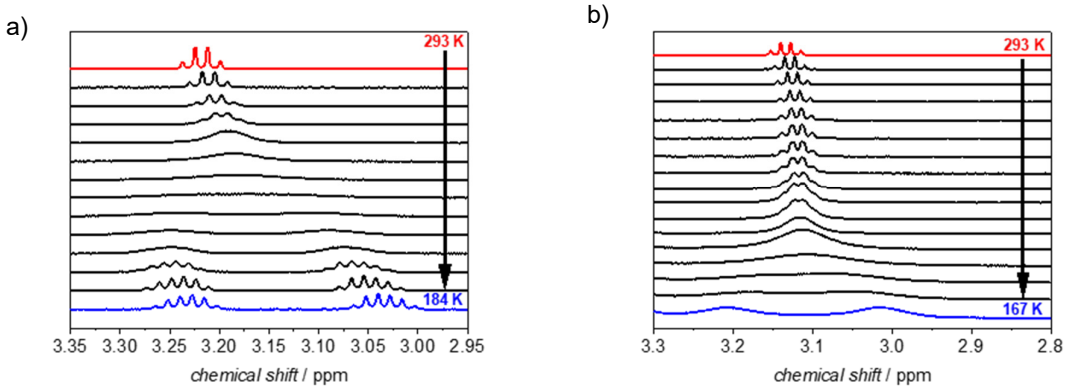

Figure 45. Excerpt from variable temperature ^{1}H NMR of ethylcorannulene in the a) absence and in the b) presence of 0.5 equivalents of **1-*PP*** (*c* (**1-*PP***) ≈ 1 mM).

In order to rationalize the observed acceleration of the bowl-to-bowl inversion within the cyclophane host, we performed computational studies of the uncatalyzed and host–guest catalyzed processes at the SMD-(CCl_4)-PW6B95-D3(BJ)/def2-TZVPP//B3LYP-D3(BJ)/def2-SVP level of theory. For the bowl-inversion of free corannulene, we obtain a Gibbs free energy barrier of 47.7 kJ mol^{-1}, which is in good agreement with the experimentally obtained value (Figure A96). Further, in agreement with the experimental data we find complexation of corannulene with **1-*PP*** to lead to a notable reduction in the bowl-to-bowl inversion barrier. We note, however, that the calculated catalytic effect is somewhat overestimated, with the computational studies giving a Gibbs free inversion barrier for corannulene within **1-*PP*** of 21.4 kJ mol^{-1} (Figure A96).

Most notably, we find the TS in the optimized complex with **1-*PP*** to show the same unusual distortion from planarity that we observed experimentally for the complex between **1-*PP*** and the TS analogue coronene. We equally find that this geometric change in the guest goes along with a flattening of the PBI moieties of the host (Figure 46 and Table A9). Energy decomposition analyses (Figure A96) show that compared to the reactant complex, noncovalent interactions between the guest and the perylene planes are indeed maximized in the TS complex, in which host and guest geometries mutually adapt to optimize π–π stacking interactions. Such "mutual induced fit transition structure stabilization" is a well conceivable

explanation for the observed catalytic effect of this host for the corannulene bowl-inversion, despite the initial non-complementarity between the non-planar PBI chromophores and the planar guest TS.

Apart from transition state stabilization, our calculations further indicate that ground state destabilization contributes to the observed catalytic effect (Table A10). This is mainly the result of a larger compression of the guest in the reactant complex compared to the distortion of the guest in the transition structure complex. While the distortion of the host in the corannulene⊂**1-*PP*** complex results in a negligible destabilization of only 0.6 kJ mol^{-1} due to the rather flexible perylene units, the difference in the electronic energy of the freely optimized corannulene bowl and its geometry in the complex with **1-*PP*** is, at 7.2 kJ mol^{-1}, the main source of destabilization.

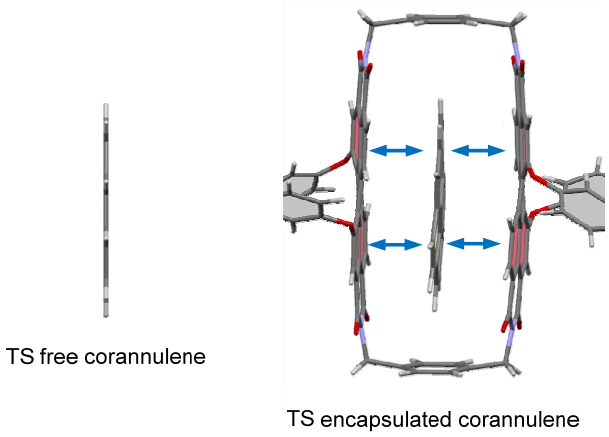

Figure 46. Calculated transition structure for the bowl-to-bowl inversion of corannulene and corannulene⊂**1-*PP***. The 1,7-bridging motif in the cyclophane is cut off for clarity.

5.3 Conclusion

In summary, we have reported strong binding of planar PAHs and π–π catalysis of corannulene's bowl-to-bowl inversion within a cyclophane cavity consisting of twisted PBI chromophores. Computational models of the catalytic process reveal a non-planar geometry of corannulene in the TS when complexed by **1-*PP***, which in turn partially planarizes. Thus, in the case of [corannulene⊂**1-*PP***]‡ not only the core twists of the PBI chromophores in the macrocycle adapt to the favored planar transition structure of the guest but the guest also loses its planar geometry, maximizing the stabilizing π–π stacking interactions between the π-systems of host and guest. This observation was supported experimentally by single crystal X-ray analysis of a coronene⊂**1-*PP*** complex as a transition state analogue and significantly

stronger binding of planar PAHs by **1-*PP***, i.e. approximately five orders of magnitude stronger binding of coronene in chloroform compared to corannulene. In less polar tetrachloromethane, the binding constant for coronene reaches the exceptional high value of around 10^{12} M^{-1}. Accordingly, the solution studies confirm the preferred binding of more planar aromatic guests compared to curved corannulene while the solid-state insights supported a mutual adaption of guest and host and thereby a mutual induced fit transition structure stabilization for the bowl-to-bowl inversion of corannulene.

Chapter 6

Preferential Molecular Recognition of Heterochiral Guests within a Cyclophane Receptor

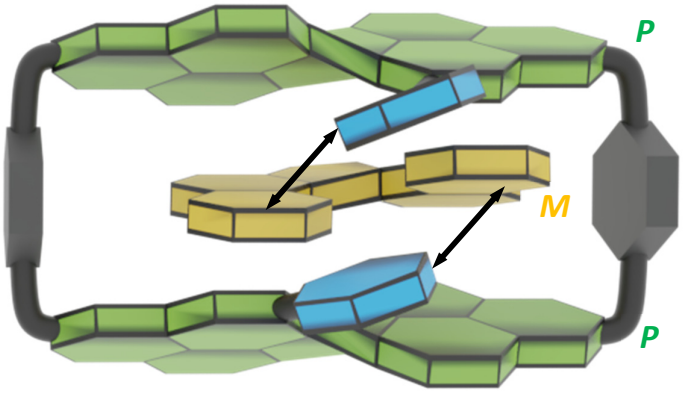

This chapter and the corresponding supporting information (Chapter 9.4) were published in:
M. Weh, K. Shoyama, F. Würthner, *Nat. Commun.* **2023**, *14*, 243.
(https://doi.org/10.1038/s41467-023-35851-3).

Abstract. The discrimination of enantiomers by natural receptors is a well-established phenomenon. In contrast the number of synthetic receptors with the capability for enantioselective molecular recognition of chiral substrates is scarce and for chiral cyclophanes indicative for a preferential binding of homochiral guests. Here we introduce a cyclophane composed of two homochiral core-twisted perylene bisimide (PBI) units connected by *p*-xylylene spacers and demonstrate its preference for the complexation of [5]helicene of opposite helicity compared to the PBI units of the host. The pronounced enantio-differentiation of this molecular receptor for heterochiral guests could be utilized for the enrichment of the *P*-PBI-*M*-helicene-*P*-PBI epimeric bimolecular complex. Our experimental results were supported by DFT calculations, which revealed that the sterically demanding bay substituents attached to the PBI chromophores disturb the helical shape match of the perylene core and homochiral substrates and thereby enforce the formation of syndiotactic host-guest complex structures. Hence, the most efficient substrate binding is observed for those aromatic guests, e. g. perylene,

[4]helicene, phenanthrene and biphenyl, that can easily adapt in non-planar axially chiral conformations due to their inherent conformational flexibility. In all cases the induced chirality for the guest is opposed to those of the embedding PBI units, leading to heterochiral host-guest structures.

6.1 Introduction

Narcissistic self-sorting, is a well-known phenomenon for supramolecular entities[276-277] and can in most cases be explained by a better shape complementarity between the corresponding molecules of the same configuration, leading to less steric hinderance[278] or increased intermolecular interactions, e.g. dispersion interactions[179-180, 190-191, 279-281] or other driving forces.[282-284] In contrast, if enantiomers prefer to bind their mirror image, this is called chiral self-discrimination or heterochiral self-sorting.[285-290] In the case of helicene structures, homochiral self-recognition is accepted to be a general trend in noncovalent bonding events.[203, 291] In this context, the homochiral supramolecular complexes observed upon encapsulation of [4]- and [5]-carbohelicenes within an inherently chiral PBI cyclophane introduced recently by us extends this empirical result to non-identical molecules with structural analogies by revealing the perfect accommodation of substrates with the same configuration as the adjacent PBIs within a tailored cavity.[193]

Such perfect shape matching between a substrate and a cavity supports the common view of receptor-substrate fit in nature that is still often dominated by the picture of tailored cavities for substrate complexation with a perfect shape complementarity between host and guest, leading to efficient binding. This rationale is also present in the three-point attachment (TPA) model, which is applied to explain stereospecific binding in natural systems by a shape match of substrate and the active binding site of a receptor.[62] However, taking conformational flexibility of the system into account is of paramount importance in natural systems as conformational changes in protein-substrate assemblies are responsible for allosteric effects that contribute quite significantly to the regulation of biochemical processes.[292-293] Besides, it is also well known that many artificial complexes, held together by noncovalent interactions, can not be described with rigid geometries of receptor and guest structures. Accordingly, the relevance of structural adaption upon substrate binding is highly topical in the field of supramolecular host-guest chemistry.[57, 119, 128, 131, 134]

For artificial receptors whose guest complexation affinity is mainly driven by π–π interactions,[294] i.e. dispersion and electrostatic interaction, an empirical dependence of the binding strength on the size of the interacting π-surfaces, often related to the number of π-electrons provided by the substrate, has been observed for several examples.[56, 178, 269, 295-297] Nevertheless, the number of π-electrons is not always a meaningful parameter with regard to complexation strength if the π-scaffolds are distorted. Here, we present a chiral PBI host endowed with highly distorted aromatic π-surfaces that hamper the host from efficient noncovalent binding of flat PAH guest molecules. Therefore, for this host, the number of π-electrons that a substrate offers is not a meaningful parameter to predict the binding strength and the guest flexibility and conformational adaptability need to be taken into account. As a more important consequence, the structural influence of the bay substituents prevails over the shape match of the helically twisted perylene and the guest, enabling a pronounced preference for the molecular recognition of heterochiral aromatic guest molecules.

6.2 Results and Discussion

6.2.1 Synthesis and Characterization

The synthesis of the cyclophane *rac*-**2** (Figure 47) begins with the distortion of a PBI chromophore into a chiral π-scaffold. Besides the diagonal or lateral bridging of the 1,7[179-181, 193] or the 1,12[176-177] bay area positions, respectively, another way to achieve helically twisted PBIs[167] is the steric overcrowding by bulky substituents in the bay position.[172-173, 298-299] Accordingly, we started with the fourfold arylation of a PBI in the bay position and a subsequent saponification, which yields the literature known perylene bisanhydride *rac*-**40** as a mixture of atropo-enantiomers.[300] Imidization of bisanhydride *rac*-**40** with mono *Boc*-protected *p*-xylylenediamine resulted in the corresponding perylene bisimide derivative *rac*-**41b**. Thereafter, deprotection of the *Boc*-protecting group of compound *rac*-**41b** and macrocyclization with *rac*-**40** gave access to *rac*-**2** as a mixture of **2-*PP*** and **2-*MM***. Notably, no **2-*PM*** isomer could be detected after the macrocyclization step, which might be explained by a repulsive interaction between the bay substituents in the transition state and therefore a preferred homochiral stacking within the cyclophane host. 2D NMR studies were performed in order to assign the proton signals (Figure A107−109 and text below). The proton signals give, in accordance with the structural properties of the macrocycle, two sets for the perylene protons (Figure 47d) as well as for the substituents: one set for the protons that point towards the cavity

and one for the more distant protons. In contrast, the monomeric reference shows only one set of signals.

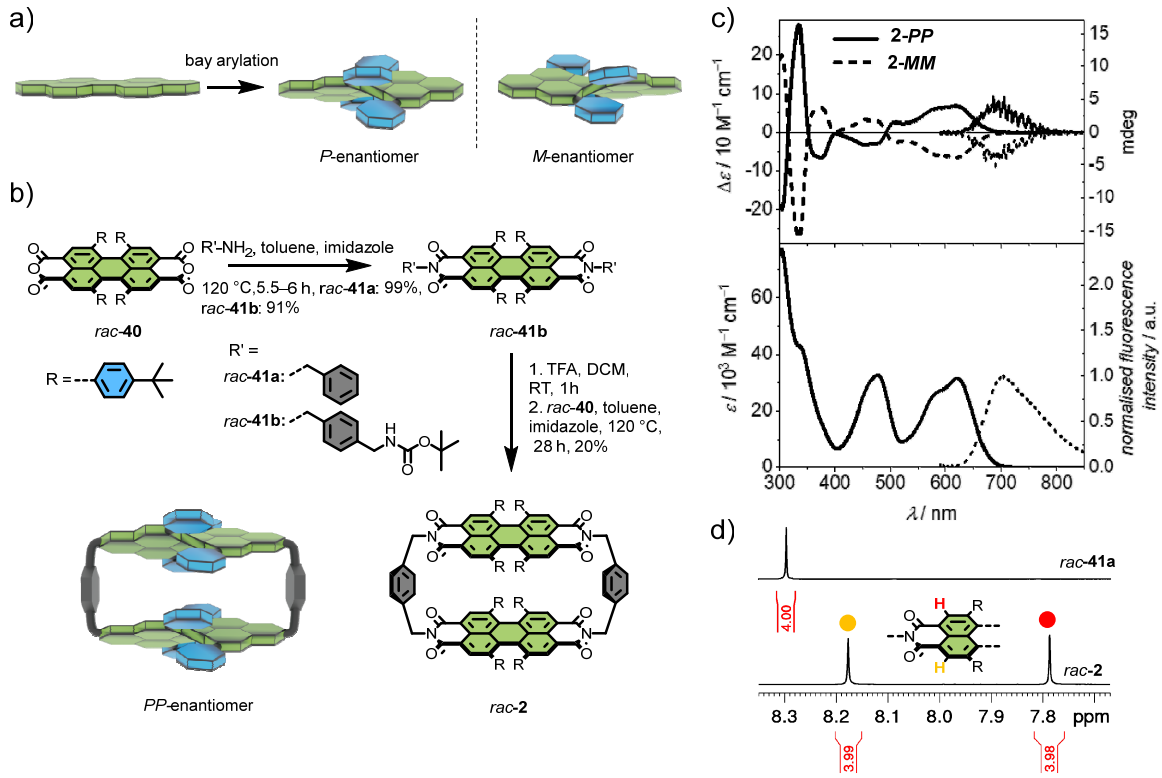

Figure 47. a) General concept of introducing helical chirality to PBIs by bay-arylation. b) Synthesis of racemic perylene bisimide cyclophane *rac*-**2** and monomeric reference *rac*-**41a** and schematic depiction of the *PP*-cyclophane. c) Circular dichroism and CPL spectra of **2-*PP*** and **2-*MM*** enantiomers of the cyclophane (top) and UV/vis absorption and fluorescence spectra of the racemic mixture of cyclophane (bottom) in chloroform. d) Excerpt from 400 MHz ^{1}H NMR spectra of *rac*-**41a** and *rac*-**2** in $CDCl_3$ at 295 K.

Chiral resolution by HPLC (Figure A97) worked efficiently for this system with a baseline separation already in the first cycle, thereby affording the two enantiopure homochiral cyclophanes with an enantiomeric excess of >99% as proven by analytical chiral HPLC. The absolute configuration of the cyclophane could subsequently be assigned by TD-DFT calculations (Figure A113). In addition, we have also synthesized the monomeric reference compound *rac*-**41a**. For details on the experimental procedures and characterization of all new compounds see the Appendix.

6.2.2 Structural and (chiro-)optical Properties

To get further structural insights beyond those from NMR experiments we grew a single crystal suitable for X-ray analysis of the cyclophane *rac*-**2** by slow diffusion of methanol into the

chloroform solution (Figure 48). The molecule crystallizes in the C2/c space group with four cyclophanes per unit cell. The cavity is filled with chloroform molecules and the PBI moieties of adjacent cyclophane molecules pack in a heterochiral fashion with a distance of 3.7 Å between the chromophores of one **2-*PP*** and one **2-*MM*** isomer without π-contact (Figure 48a). The distance between the PBI units within one cyclophane is 7.3–8.3 Å. Accordingly, the choice of the *para*-xylylene spacer provides the expected perfect distance for the encapsulation of polycyclic aromatic hydrocarbons (Figure 48b). From the X-ray structure, the high steric demand of the *tert*-butyl-phenyl substituents becomes apparent as well as the concomitant rigidity of the whole molecule. The close proximity of the phenyl groups leads not only to high twist angles between the naphthalene subunits of 35–37° (Figure 48c) but also supports π–π interactions between the adjacent phenyl moieties, leading to a quadruple π–stack (Figure 48b). As a result of the steric overcrowding and influenced by the size and shape of the respective guests (here solvent molecules, for specific guests see *vide infra*), the whole cyclophane has a distorted symmetry-broken geometry (point group: C_2), leading to a rotational offset of the long axis between the chromophores of approximately 22° in the solid state (Figure 48d).

The optical properties of the cyclophane were studied by UV/vis and circular dichroism (CD) absorption as well as fluorescence and circularly polarized luminescence (CPL) spectroscopies (Figure 47c). For specific details on the optical properties we refer to the Appendix and summarize here only the major results. Thus, we observe several absorption bands in the UV/vis spectral range and only weak solvatochromism (Figure A110c). The vibronic fine structure of the $S_0 \rightarrow S_1$ absorption band at ~ 600 nm is less pronounced than for other bay substituted perylene bisimide cyclophanes[56, 142, 193] and the absorbance of the $S_0 \rightarrow S_2$ band is rather strong which could be rationalized by a significant involvement of the phenyl subsitutents in this transition as supported by TD-DFT calculations (Figure A114). The fluorescence properties are more dependent on the solvent polarity with lower quantum yield ($\phi_f = 0.23$) and lifetime (τ = 11.5 ns) in chloroform that increase in less polar solvents such as tetrachloromethane and methylcyclohexane (Figure A111, Table A11). In the visible range, the CD absorption complies well with the UV/vis absorption with two broad monosignated signals for the $S_0 \rightarrow S_1$ and the $S_0 \rightarrow S_2$ transitions with opposite sign (400–700 nm). Importantly, the naphthalene related absorption in the UV regime is in agreement with our assignment of the enantiomers by exciton chirality method.[301] Accordingly, a positive CD exciton couplet with a zero crossing at $\lambda = 316$ nm is apparent in the CD spectrum of **2-*PP***, indicating a clockwise stack of the naphthalene subunits when looking from the short side of the cyclophane. The corresponding

enantiomer has the expected mirror image CD spectrum. The absorption dissymmetry factor is in the medium range for small organic molecules with $g_{abs} = \Delta\varepsilon/\varepsilon = 2.1 \times 10^{-3}$ (at $\lambda = 620$ nm). The CPL spectra exhibit the expected mirror image of the CD spectrum for the lowest energy transition with g_{lum} values of 2.1×10^{-3} and -1.7×10^{-3} for the two enantiomers, respectively (at $\lambda = 675$ nm, Figure A110b).

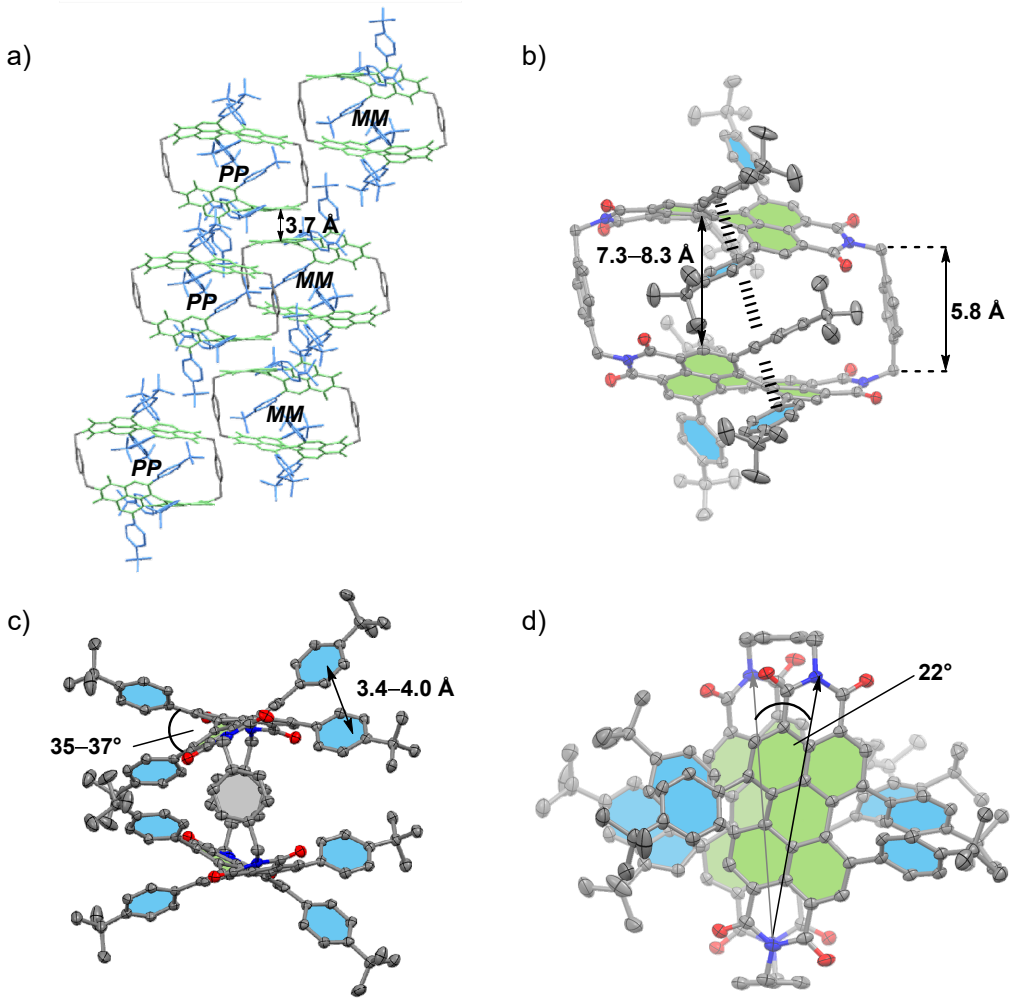

Figure 48. Molecular structure and packing of cyclophane *rac*-**2** in the solid state according to single crystal X-ray analysis. a) Packing arrangement in the crystal is shown in the side view. b) Side, c) front and d) top view of the molecular structure of **2-*PP***. Hydrogen atoms and solvent molecules are omitted for clarity. The perylene units are highlighted in green, the bay substituents in blue and the spacer unit in grey (the thermal ellipsoids are set to 50% probability).

6.2.3 Complexation of Non-chiral Guest Molecules

The suitability of this cyclophane host as a molecular receptor for the complexation of guest molecules was studied by UV/vis and NMR titration experiments. As the guest complexation within PBI cyclophanes is known to be mainly driven by π–π interactions,[35,47] we selected

initially a series of PAHs as guests that should fit into the cavity with a stepwise increase of π–electron count, starting with naphthalene (5 double bonds) until [5]helicene and benzo[*ghi*]perylene (11 double bonds, Figure 49). The association constants were determined by nonlinear curve fitting of data from titration studies (Figure A121–134) and the results are summarized in Table 3. For the titration studies we chose tetrachloromethane as a solvent which yielded binding constants for the guest complexations up to $K_a = 2.9 \times 10^3$ M^{-1} for perylene encapsulation. On first glance, this strong complexation of perylene might be surprising. However, it should be noted that the central ring of perylene is less aromatic with long carbon-carbon bonds and that already the hydrogen substituents in the bay area of perylene suffer from some crowding. Thus, little energy is needed for a rotational twist of the two naphthalene subunits in a propeller-like structure for the perylene scaffold[168] (Figure A117).

Table 3. Binding constants for the complexation of PAHs with *rac*-**2** determined by UV/vis or ^{1}H NMR titration experiments in tetrachloromethane at 295 K and Gibbs free energies for the corresponding complex formation.

guest	$(K_a \pm \Delta K_a)$[a] [M^{-1}]	$-\Delta G^0$ [kJ mol^{-1}][b]
perylene	$(2.9 \pm 0.1) \times 10^3$	19.6
[4]helicene	$(1.47 \pm 0.04) \times 10^3$	17.9
benzo[*ghi*]perylene	$(1.15 \pm 0.03) \times 10^3$	17.3
triphenylene	$(5.5 \pm 0.5) \times 10^2$	15.5
1,1'-biphenyl	$(4.1 \pm 0.1) \times 10^2$	14.8
phenanthrene	$(3.3 \pm 0.4) \times 10^2$	14.2
anthracene	$(2.6 \pm 0.1) \times 10^2$	13.6
rac-[5]helicene[c]	$(2.1 \pm 0.1) \times 10^2$	13.1
fluorene	$(1.6 \pm 0.1) \times 10^2$	12.4
pyrene	$(1.4 \pm 0.1) \times 10^2$	12.1
2-hydroxybiphenyl	64 ± 7	10.2
naphthalene	47 ± 5	9.4
1,1'-binaphthyl[d]	28 ± 4	8.2
phenylnapthalene[d]	11 ± 1	5.9

a) The given error for K_a is the analytical error from the local 1:1 binding fit. b) Calculated with $\Delta G^0 = -RT\ln(K_a)$. The analytical error of ΔG^0 is less than 1.5 kJ mol^{-1} for our titration studies. c) The titration studies of the corresponding enantiopure mixtures can be found in Figure A139: $K_a = 220$ M^{-1} (heterochiral host-guest mixture) and $K_a = 46$ M^{-1} (homochiral host-guest mixture). d) Determined by ^{1}H NMR titration in CCl_4/MCH-d_{14} 3:1 (v:v).

Most of our complexation studies show a decrease in the absorption of the lowest energy PBI-related transition with a concomitant red shifted shoulder which indicates a charge transfer

character of the complex. However, a plot of the corresponding Gibbs free energies (Figure 49) revealed that there is no simple correlation between the π-count of the guest, i.e. the number of carbon-carbon double bonds, and the binding affinity like for other cyclophanes.[56, 295-296] Accordingly, the highly twisted and rigid conformation of this cyclophane leads to a certain guest specificity. Based on the structural properties of the guests, we can classify them into three groups. For guests with a planar rigid structure (marked in grey) we see a trend which shows the expected increasing binding affinity with a larger aromatic π-plane due to increased dispersion interactions between the guest and the PBI units. Only pyrene with its incongruous and stiff geometry compared to the perylene units of the neighbouring chromophores seems to somewhat counteract this trend, which has also been observed previously for cyclophanes composed of core-distorted PBIs.[56, 142] In order to rule out external binding, we carried out a titration with reference compound *rac*-**41a**, revealing negligible changes in the UV/vis spectrum upon the addition of the largest guest (Figure A140).

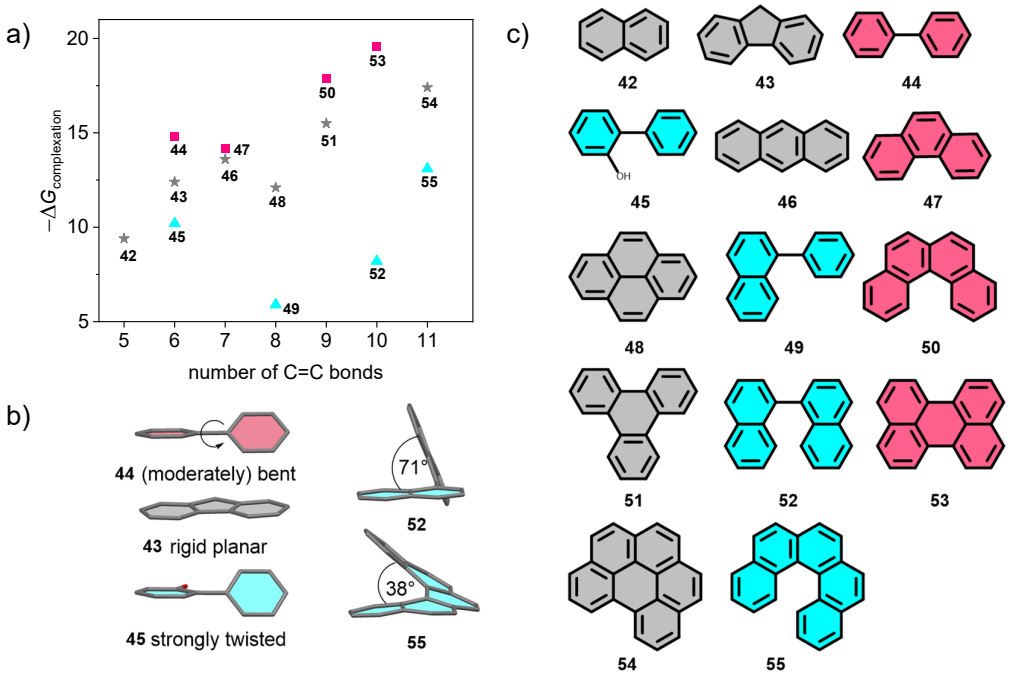

Figure 49. a) Plot of Gibbs free complexation energies at 295 K versus the number of C=C double bonds of the guests' π-scaffold. The guests are classified in three groups: guests with a moderately bent or easily bendable structure that can adapt to the receptor (red), guests with a rigid planar structure (grey) and guests with a strongly twisted three-dimensional structure (blue). b) Energy minimized structures by DFT of selected guest molecules and c) chemical structure of the substrates which were employed as guests in the titration studies.

For strongly twisted more three-dimensional guest molecules which have a restricted flexibility (marked in blue), like for example 2-hydroxybiphenyl, we determined significantly lower

binding energies. Notably are in this context phenylnaphthalene and 1,1'-binaphthyl, whose binding by *rac*-**2** could only be detected at higher concentration in NMR experiments. Thus, the twist between the aromatic subunits in these molecules (71° for 1,1'-binaphthyl, see Figure 49) obviously does not match well within the available space of the cyclophane receptor's cavity. In contrast, [5]helicene, with a significantly lower angle of 38° is again well accommodated within the host. The third group of guest molecules (marked in red) shows the best binding properties and is characterized by planar or only moderately bent structures and some degree of conformational flexibility as before discussed for perylene. Thus, whilst perylene is assumed to be bent upon complexation, twisted molecules like 1,1'-biphenyl or [4]helicene can adapt to the cyclophane cavity by partial planarization, thereby enabling a more efficient binding. Hence, the strongly limited adaptability of PBI dyes with interlocked phenyl substituents and the resulting highly distorted nature of the host's cavity is the reason for a preferential binding of guest molecules that can optimize their shape match with the receptor.

6.2.4 Complexation of Chiral Guest Molecules

The previous complexation studies suggested that cyclophane **2** has the highest binding affinity for non-planar guest molecules. As the helical twist of bay-substituted PBIs with their "phenanthrene unit" in the bay area is structurally related to carbohelicenes, the best shape match might be expected for supramolecular inclusion complexes with homochiral helicene guest molecules. Although [5]helicene has a lower affinity for complexation by the cyclophane compared to [4]helicene, this substrate is particularly suitable for the following studies because it is characterized by a sufficiently high inversion barrier of about 101 kJ mol^{-1}.[205] This allows us to monitor the enantioselectivity of the molecular recognition by the host as well as the conversion of its isomeric forms on a reasonable time scale. Thus, we first carried out ^{1}H NMR studies with either racemic or homo- and heterochiral mixtures of host and guest in a mixture of tetrachloromethane and methylcyclohexane-d_{14} (3:1, v:v). Notably, UV/vis titration study in the same solvent mixture revealed almost no impact of the methylcyclohexane on the complexation thermodynamics compared to pure tetrachloromethane (Figure A135). The corresponding NMR titration (Figure 50a,b and Figure A136) for our initial experiment with host *rac*-**2** with *rac*-[5]helicene in the solvent mixture shows a broadening of most host signals upon guest addition. However, the most strongly downfield shifted *ortho* perylene proton that points away from the cavity can be followed very well during the titration experiment and shows not only a distinct upfield shift upon guest addition but stays also sharp over the whole

experiment. Subsequent nonlinear curve fitting of this proton signal reveals a binding constant of $K_a = 2.1 \times 10^2$ M^{-1}, confirming our data from UV/vis host guest titration studies (Table 3).

As we were particularly interested in the impact of the guest configuration on the binding affinity in epimeric host-guest complexes, we compared next the chemical shift of the selected *ortho* perylene proton upon the addition of a particular amount of [5]helicene (5.8 equivalents) in different configurational combinations of host and guest (Figure 50c).

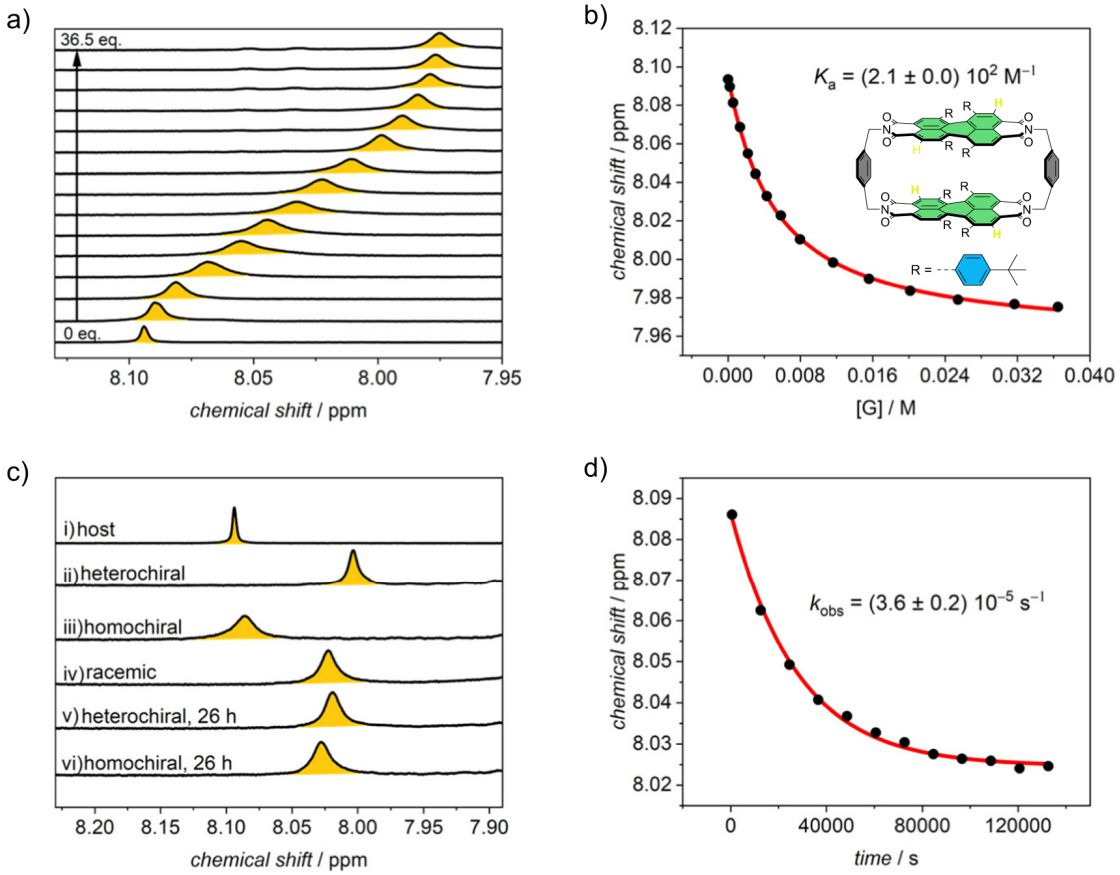

Figure 50. a) Excerpt of ^{1}H NMR (CCl_4/MCH-d_{14} 3:1 (v:v), *c* (*rac*-**2**) = 1.0×10^{-3} M, 295 K) titration experiment of host *rac*-**2** with *rac*-[5]helicene and b) the nonlinear curve fit of the obtained chemical shift of PBI *ortho* proton versus guest concentration according to the 1:1 binding model. c) Excerpt of ^{1}H NMR spectra (CCl_4/MCH-d_{14} 3:1 (v:v), *c* (*host*) = 1.0×10^{-3} M, 295 K) of different configurational combinations of the host and [5]helicene (5.8 eq.): i) host, ii) host+guest heterochiral, iii) host+guest homochiral, iv) host+guest racemic, v) host+guest heterochiral after 26 h, vi) host+guest homochiral after 26 h. b) Plot of time-dependent chemical shift of the most downfield shifted PBI *ortho* proton of **2-*PP*** upon the addition of *P*-[5]helicene (5.8 eq.).

For the samples measured directly after dissolution of **2-*PP*** and the respective guests we see an upfield shift of 0.07 ppm if the racemic guest is added to the racemic host (Figure 50c, iv). Unexpectedly, this upfield shift is with 0.09 ppm more pronounced if we add *M*-[5]helicene (Figure 50c, ii) and less pronounced if we add *P*-[5]helicene (Figure 50c, iii), indicating that for the cyclophane a preferential binding takes place for the guest with the opposite chirality

compared to the configuration of the PBI units of the receptor. In the case of the homochiral mixture, the shift of the proton is indeed almost unchanged (upfield shift of only 0.01 ppm) but only the signal itself is broadened. However, after approximately one day, the signals of both combinations approach the chemical shift for the racemic case (Figure 50c, iv–vi). A plot of the chemical shift over the time for the homochiral mixture and subsequent data fitting with the first-order-kinetics (Figure 50d) reveals a rate constant of $k_{obs} = 3.6 \times 10^{-5}$ s^{-1}, corresponding to a barrier of $\Delta G^{\ddagger} = 99.0$ kJ mol^{-1} according to equation A11 and A12 (see Appendix, *page 234*). This barrier is in accordance with the inversion barrier of [5]helicene[205, 211] and was further confirmed by time-dependent CD measurement in the same solvent mixture in the absence of the host (Figure A138). Accordingly, we see an increasing amount, i.e. enrichment of the heterochiral complex upon enantiomerization of *P*-[5]helicene into *M*-[5]helicene in the presence of **2-*PP***. UV/vis titration experiments confirm this observation, revealing significantly reduced optical changes upon the addition of the same amount of homochiral [5]helicene to the host compared to the heterochiral case (Figure A139). The corresponding binding constants amount to $K_a = 220$ M^{-1} for the heterochiral and $K_a = 46$ M^{-1} for the homochiral complex. From the difference in the binding constants of the two complexes, we deduced a difference in Gibbs free energy of 3.8 kJ mol^{-1} for the complex formations of the two epimeric host-guest structures.

6.2.5 Structural Insights from Computational Studies

In order to rationalize the observed binding affinities for the various guest molecules, we carried out DFT calculations for selected complexes under investigation (Figure A115). Pleasingly, whilst the guest-free structure of **2-*PP*** is of higher symmetry (point group: C_2 or D_2 if the *tert*-butyl moieties are neglected) and characterized by the four *tert*-butylphenyl bay substituents being stacked at the periphery of both sides of the cyclophane, the calculated structures of all host-guest complexes reveal distorted geometries for the cyclophane host that are rather similar to the one observed in the solid state structure (with embedded solvent molecules) in our single crystal X-ray analysis (Figure 48). Thus, the distorted nature of the cyclophane with an opening on one side as well as a rotational offset of the PBI units are apparent both in the crystal structure and in the computational models of the complexes (Figure A115 and 116a). It turned out that the rigid planar guests, e.g. anthracene and pyrene, prevail in a flat geometry within the cyclophane cavity and abstain an adaption of their structure (Figure A115b,c) whilst the other guests are embedded in the host in non-planar geometries (Figure 51a and Figure A115a,d,f).

As the most important outcome of our calculations, we obtained computational support for our experimental data with regard to the complex with [5]helicene for which the opposite configuration compared to the host is indeed energetically preferred (Figure 51 and Figure A115e).

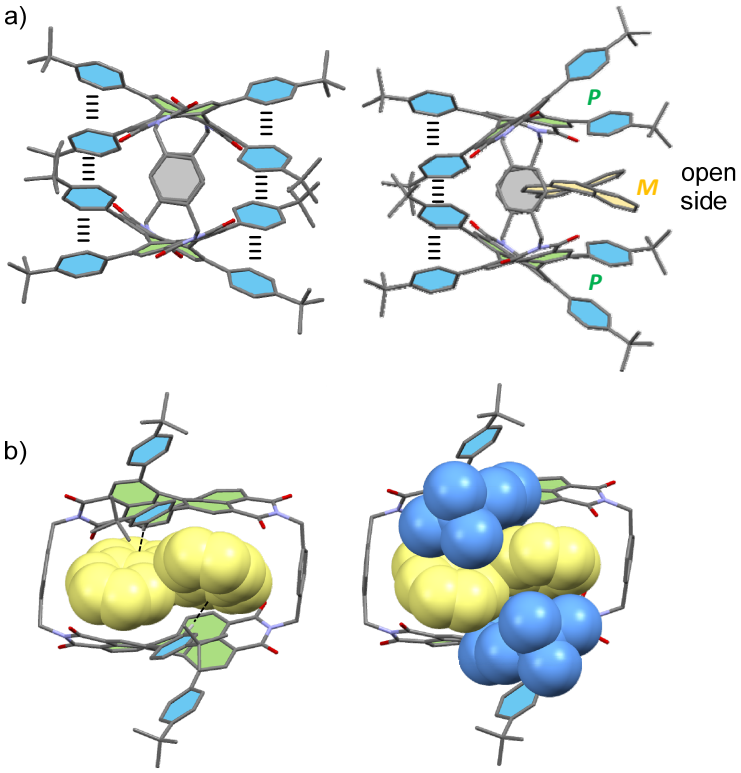

Figure 51. DFT calculated structure of a) **2-*PP*** and *M*-[5]helicene⊂**2-*PP*** from the front view with indicated π–π stacking of phenyl substituents and b) side view of *M*-[5]helicene⊂**2-*PP*** (bay substituents are partially omitted for clarity). The core of the PBI units and the bay substituents are highlighted in green and blue, respectively. The guest is highlighted in yellow. Hydrogen atoms are omitted for clarity.

Eventually, we see from the calculated structures that the distorted geometry of the PBI cyclophane host displaces especially the larger guests like [5]helicene and perylene out of the center of the cavity, which is opened on one side into a cleft-like receptor suitable for substrate recognition (Figure 51a and Figure A115f, 116b). Notably, all calculated host-guest complex structures show embedded guest molecules of opposite chirality that are preferred within the cavity according to DFT calculations and stabilized to some degree by CH-π interactions between the *tert*-butylphenyl bay substituents of the host and the π-cloud of the guest. Thus, the calculated complex structures reveal that the substrates circumvent the shape mismatch between the sterically demanding bay substituents and the helical structure of the substrate by replacing π-π by CH-π interactions, thereby favoring heterochiral ensembles (Figure 51b and

Figure A115a,d,f). ALMO energy decomposition analyses show that the relevant bay-substituents are responsible for 34% of intermolecular interactions in the *M*-[5]helicene⊂**2-*PP*** complex and, remarkably, for 54% of the electrostatic interactions (Figure A116c,d) while in the *P*-[5]helicene⊂**2-*PP*** complex, the close bay-substituents account only for 27% of intermolecular interactions and for 42% of the electrostatic stabilization (Figure A116e,f). Accordingly, the unexpected configurational preference can be explained by the conformationally rigid *tert*-butylphenyl bay substituents that disturb the helical match of host and guest by a steric congestion with the embedded guest in the homochiral epimeric complex that reduces its thermodynamic stability and leads to the preferential formation of the heterochiral epimeric complex. In this cyclophane, the substitution pattern of the chiral PBI chromophore receptor site has therefore a strong impact on the enantioselectivity of guest binding. Thus, by means of such peripheral substituents, the preference of synthetic receptors for molecular recognition of chiral substrates can be switched from homo- to heterochiral epimeric complexes (Figure 52).

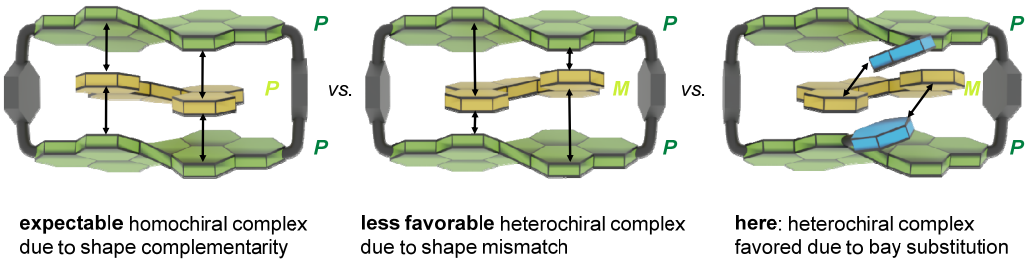

Figure 52. Schematic representation of the expected energetically preferred homochiral complex and the less favourable heterochiral complex in the absence of bay substituents as well as the experimentally observed favored heterochiral complex due to the steric impact of the peripheral bay substituents.

6.2.6 Further Experimental Support

Our conclusions drawn from the DFT structures are corroborated by the chemical shifts observed in the ^{1}H NMR titration study (*vide supra*) for the various protons as analysed in detail in Figure A137 (and text below). As an ultimate proof for the heterochiral molecular recognition, however, we can further provide the crystallographic analysis for a co-crystal grown from a mixture of *rac*-**2** and 1,1'-biphenyl (Figure 53a, for details see the Appendix).

The structural elucidation revealed not only the expected encapsulation of the 1,1'-biphenyl guest within the cyclophane cavity, but also this 1:1 complex being embedded in a 1,1'-biphenyl matrix and thus 4.5 equivalents of 1,1'-biphenyl per cyclophane molecule in the crystal (Figure A119a,b and text below). Accordingly, no solvent molecules are present in this co-crystal. The

cyclophanes pack in a similar fashion as observed for the pure racemic host in chloroform (*vide supra*). More importantly, the complex structure clearly supports the DFT calculation for this complex (Figure A115a), as an opposite twist of the guest compared to the surrounding PBI units of the host is apparent. We would like to note that free 1,1'-biphenyl itself is configurationally unstable and therefore achiral at r.t. However, what we consider here as opposite configuration is the opposite twisting along the phenyl-phenyl single bond compared to the twist of the perylene core of the host as a result of optimized host-guest interactions. Hence, the solid state structure proves the preference for the formation of heterochiral complexes for this chiral cyclophane. Notably, the structure found in the single crystal reveals, similar to our calculated models, that the sterical congestion imparted by the peripheral *tert*-butylphenyl substituents are responsible for this unusual stereochemical preference, which becomes especially apparent in the space filling model (Figure A120) and in our Hirshfeld surface analysis of the guest molecule depicted in Figure 53b, revealing close CH···π contacts between biphenyl and the aromatic protons of the bay substituents.

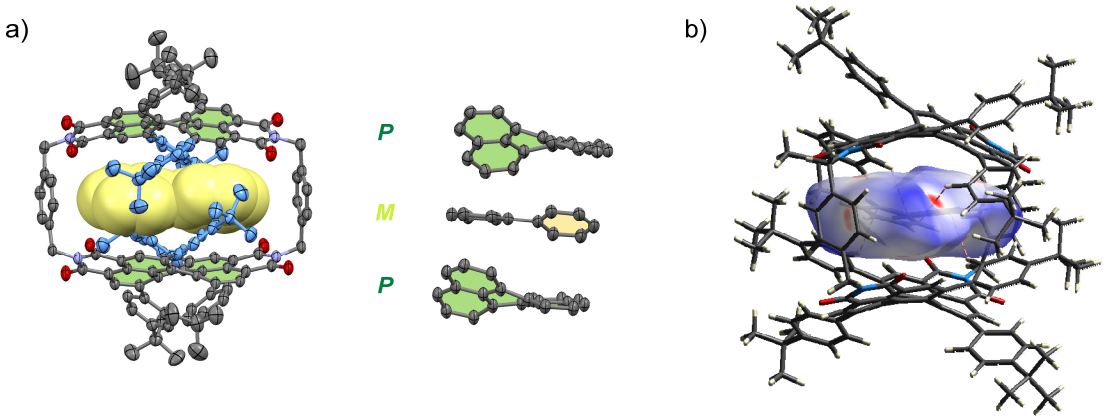

Figure 53. a) Side view of molecular structure of *M*-1,1'-biphenyl⊂**2-*PP***, obtained from single crystal X-ray analysis (surrounding guest molecules are omitted for clarity), corresponding perylene units with the encapsulated guest in order to visualize the heterochiral host-guest stacking. The perylene core of the PBI unit and the relevant bay substituents are highlighted in green and blue, respectively. The biphenyl guest is highlighted in yellow. Hydrogen atoms are omitted for clarity (the thermal ellipsoids are set to 50% probability). b) Hirshfeld surface analysis to visualize CH-π interactions between the substituents and the guest (close C···H contacts shorter than 2.65 Å are highlighted by dashed lines).

6.3 Conclusion

Substrate specific molecular recognition is a hallmark in supramolecular host-guest chemistry. Herein, we presented a chiral cyclophane composed of two core twisted PBI chromophores, which provided unprecedented insights into the molecular recognition of planar and in

particular non-planar aromatic guest molecules. Titration studies revealed that the binding affinity of a series of polycyclic aromatic hydrocarbons towards the cyclophane is not only dependent on the number of π-electrons that the guest offers, but also on its geometrical adaptability. For chiral [5]helicene, unexpectedly, our studies revealed a preference for the formation of the heterochiral epimeric complex, where the helicity of the PBI units and the guest molecule have the opposite helical turn. This is a rare example of a preferential heterochiral guest recognition, which could be tracked by time-dependent NMR studies and rationalized by DFT calculations, indicating a general preference for the complexation of guests with an opposite configuration by the given host cavity. Our conclusions could be corroborated by a co-crystal for one of the complexes and the analysis of the chemical shifts in the NMR spectra of the complexes. From these data we are able to generalize our unprecedented results and to suggest a design principle for molecular receptors for heterochiral recognition based on the smart functionalization of the central recognition site with peripheral substituents that modulate the binding affinities by their sterical bulkiness and thus by repulsive forces and additional noncovalent interactions to the substrate.

Chapter 7

Summary and Conclusion

Since the beginnings of supramolecular chemistry, the development of tailored cavities, mimicking sophisticated natural receptors that enable specific substrate binding was of major interest. This ambitious goal can be achieved by the targeted design of host molecules to obtain complementary noncovalent interactions between the binding site and the guest. The structural flexibility of perylene bisimides offers the possibility to make twisted, inherently chiral PBIs by a suitable core substitution. However, so far any substitution of the chromophore in PBI based cyclophanes served only to enhance solubility in the organic or aqueous medium but has not yet been exploited to obtain novel chiral binding pockets that would enable enantiospecific substrate recognition. Hence, in continuation of earlier work on perylene bisimide cyclophane hosts, this thesis was concerned with the synthesis and investigation of the first chiral PBI cyclophane cavities with the goal to use them as supramolecular receptors.

Chapter 3 provides the synthetic procedures of **1-*MM*** and **1-*PP*** (Figure 54a) and the corresponding characterization of the macrocycles by optical spectroscopy. The key step represents the construction of a covalent connection of the 1,7-bay positions *via* an intramolecular ring-closing metathesis (RCM), yielding stable chiral perylenes. Subsequent hydrogenation of the resulting olefinic double bond, saponification, imidization, chiral resolution *via* HPLC and again saponification gave access to perylene bisanhydrides **57-*M*** and **57-*P***. The envisioned cyclophanes **1-*PP*** and **1-*MM*** were synthesized in a macrocyclization reaction with *para*-xylylenediamine and the enantiopure perylene bisanhydride **57** of desired configuration. **1-*MM*** and **1-*PP*** offer a well accessible chiral cavity, suitable for the complexation of small aromatic guests through π–π stacking interactions. Owing to a perfect shape match between the moderately helically twisted PBI chromophores and [4]- and [5]helicene, UV/vis and fluorescence titration studies revealed decent substrate binding in chloroform with association constants up to 10^6 M^{-1} for the corresponding homochiral host-guest assemblies, which could be further increased to binding affinities in the nanomolar range in less polar tetrachloromethane. Structural elucidation of the thermodynamically most stable [4]helicene inclusion complex by (2D) NMR studies, as well as computational modelling, supported the suggested 1:1 binding mode with the carbohelicene being sandwiched between

the PBI units. Single crystal X-ray analysis revealed that the homochirality of the host enables the transfer of its configuration to [4]helicene, resulting in a perfectly embedded helicene substrate with π–π and CH–π interactions between the guest and the cyclophane (Figure 54b). Moreover, the homochiral cavities afforded the enrichment of *P*-configured [5]helicene in the presence of **1-*PP*** while *M*-[5]helicene could be enriched in the presence of **1-*MM***. Experimental evidence for the host-mediated chirality transfer (Figure 54c) was collected by time-dependent CD spectroscopy of *rac*-[5]helicene in the presence of the host templates.

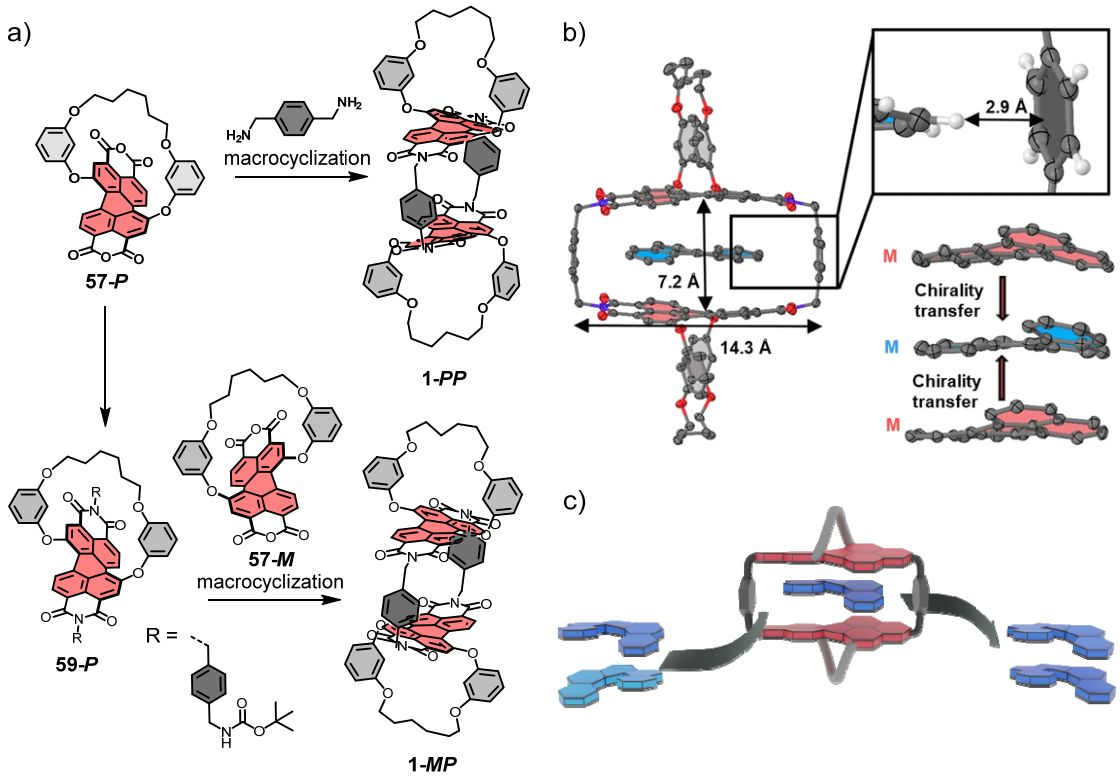

Figure 54. a) Synthetic route to **1-*PP*** (**1-*MM*** analogous) and **1-*MP*** as well as the b) single crystal X-ray structure of [4]helicene⊂**1-*MM*** and c) a schematic depiction of [5]helicene deracemization in the presence of **1-*PP***.

Besides the studies on host-guest binding, this thesis was furthermore concerned with the catalytic effect of PBI cyclophanes on the isomerization of encapsulated guests. Hereby, [5]helicene was identified to be an ideal candidate to gain deeper insights into the observed chirality transfer due to suitable enantiomerization kinetics, which can be monitored on the time-scale of standard spectroscopic methods. Accordingly, in *Chapter 4* of this thesis, the influence of the chiral host **1-*PP*** on the enantiomerization barrier of [5]helicene was investigated in detail. As a reference compound, meso congener **1-*MP*** was additionally synthesized in an improved two step procedure *via* formation of a *Boc*-protected intermediate

before macrocyclization (Figure 54a). Fluorescence host-guest titration experiments in tetrachloromethane revealed a significantly decreased binding affinity of *rac*-[5]helicene towards **1-*MP*** compared to *P*-[5]helicene towards **1-*PP*** by three orders of magnitude to $K_a = 2.0 \times 10^6\ M^{-1}$, which is in accordance with the corresponding calculated binding energy and could be attributed to the stereochemical mismatch between the guest and one of the PBI units.

Low temperature NMR studies were applied to confirm the existence of only one epimeric complex species upon [5]helicene encapsulation by **1-*PP*** (i.e. *P*-[5]helicene⊂**1-*PP***) in solution. This could be further supported by single crystal X-ray analysis of a co-crystal grown from a racemic mixture of the guest and **1-*PP***. The solid state and solution studies revealed not only a mutually induced conformational adaption of host and guest, noticeable through a compressed [5]helicene substrate and an increased core twist of the chromophores. Besides, a dynamic rotation of [5]helicene along the *z*-axis within the host's cavity could be observed, when looking from the side view of the complex (Figure 55c). This dynamic motion was quantified with the help of variable temperature NMR studies as well as low temperature ^{1}H-^{1}H EXSY NMR measurements to proceed with a barrier of ~54 kJ mol^{-1}.

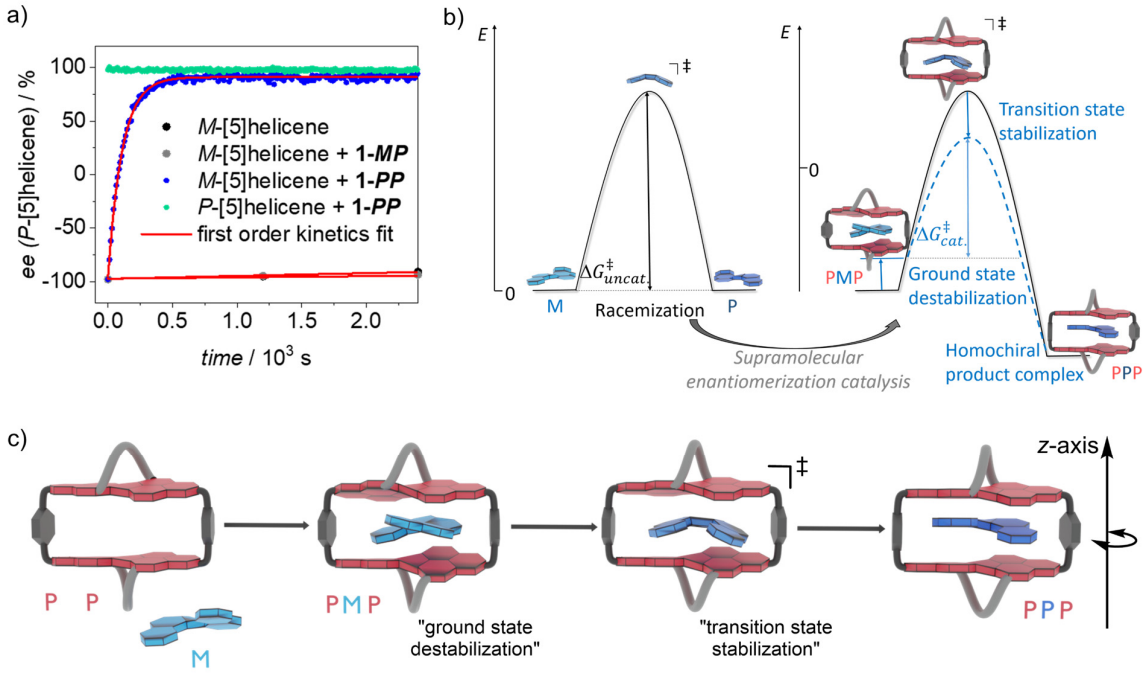

Figure 55. a) Plot of enantiomeric excess of *P*-[5]helicene in tetrachloromethane (*ee* = –100% corresponds to enantiopure *M*-[5]helicene) b) Schematic potential energy surface of [5]helicene in the absence and the presence of **1-*PP***. c) Schematic depiction of the induced fit catalyzed *M*-[5]helicene enantiomerization in the presence of **1-*PP*** as well as the guest rotation in the product complex.

Most importantly, time-dependent CD studies in tetrachloromethane (Figure 55a) revealed that the enantiomerization process of *M*-[5]helicene into *P*-[5]helicene is accelerated by a factor of ~700 at room temperature ($\Delta\Delta G^{\ddagger}$ = 15.9 kJ mol^{-1}) in the presence of **1-*PP***, yielding the same CD signal as the corresponding homochiral host-guest mixture after a time span of minutes. Accordingly, this host's unprecedented ability to deracemize small carbohelicene guests is coupled with the capability of lowering [5]helicene's enantiomerization barrier by a remarkable factor. In contrast, the meso congener had almost no influence on the guest inversion process, but operated as a slight inhibitor for [5]helicene enantiomerization ($\Delta\Delta G^{\ddagger}$ = –2.1 kJ mol^{-1}) and yielded the racemic substrate within a time period of more than one day if the enantiopure guest is added.

Computational models were applied in order to rationalize the observed drastic kinetic differences based on apparently small structural differences in the cavity between **1-*PP*** and **1-*MP***. To this end, EDAs of the relevant complex structures in the ground state and the transition state were performed. The breakdown of supramolecular interactions indicated that a subtle shape match between the perylene curvature in the homochiral host and the non-planar transition state structure of [5]helicene stabilizes the latter mainly by dispersion and electrostatic interactions. The transition state structure of [5]helicene is on the other hand indeed slightly destabilized within **1-*MP*** according to EDA analysis, confirming the experimental data. Besides transition state stablization, ground state destablization was observed to contribute to the lowering of the reaction barrier of guest enantiomerization within **1-*PP***. Destabilization of the groundstate is based on the fact that [5]helicene is structurally more distorted in the reactant complex (*M*-[5]helicene⊂**1-*PP***) than in the transition state complex due to a shape mismatch between the clockwise and anticlockwise helicity of the receptor's perylene moieties and the guest, respectively. The strain in the heterochiral complex serves, figuratively speaking, as an energy storage, which helps to lower the reaction barrier.

Notably, DFT calculations confirmed not only a structural distortion in the reactant complex but also a conformational adaptivity of both, host and guest, throughout the whole enantiomerization process. All these observations suggest that this system represents a unique aritifical "deracemase", following the Pauling-Jencks concept of enzyme catalysis (Figure 55b,c). Moreover, the comparison with reference cyclophane **1-*MP*** showed how sensitive the enantiomerization process of [5]helicene is to small geometrical changes in the cavity and how crucial the precise design of binding sites is to stabilize a transition state structure *via* π–π stacking interactions.

In *Chapter 5*, **1-*PP*** was first investigated as a host for planar PAHs. Here it was shown that the binding energies for the corresponding complexes increase linearly with the number of π–electrons of the guests. Thus binding constants of up to $K_a = 2.8 \times 10^8\ M^{-1}$ could be determined in chloroform at room temperature. Similar to *Chapter 4*, these could be further increased in tetrachloromethane, yielding an estimated binding constant of about $10^{12}\ M^{-1}$ for coronene by linear extrapolation of the binding energies (Figure 56a). In contrast, the binding energy for corannulene is significantly lower than that of other guests with a comparable number of π-electrons. Consequently, the concept of "induced fit catalysis" seems to apply well to the "bowl-to-bowl" inversion of corannulene in the presence of **1-*PP***, since a preferential binding of planar structures, such as the transition structure of corannulene, can be observed. Accordingly, the influence of the twisted PBI units and the resulting structural differences of the non-planar chromophores on the stabilization of the planar transition structure of corannulene was investigated.

VT NMR studies of a mixture of **1-*PP*** and ethylcorannulene, whose methylene protons are indicative for the kinetics of the bowl-to-bowl motion, showed a decreased inversion barrier by around 11.6 kJ mol^{-1} despite the obvious structural mismatch. The observed catalytic effect could nevertheless in analogy to the studies presented in *Chapter 4* be assigned to the concepts of transition state stabilization on the one hand and additionally ground state destabilization as a result of compressed corannulene upon complexation on the other hand. The DFT calculations of the complex structure suggested a mutual structural adaption of both, host and guest, in the transition state, yielding an unprecedented non-planar transition structure of corannulene. The calculated complex structure was further elucidated by single crystal X-ray analysis of complexed coronene, a qualitative transition state analogue of corannulene, which showed similar distortions as the computational transition state complex (Figure 56b). Host and guest thus compromise between structural distortion and optimal noncovalent interactions to achieve transition state stabilization of the bowl-to-bowl inversion mediated by an optimized π-contact through a mutual induced fit mechanism.

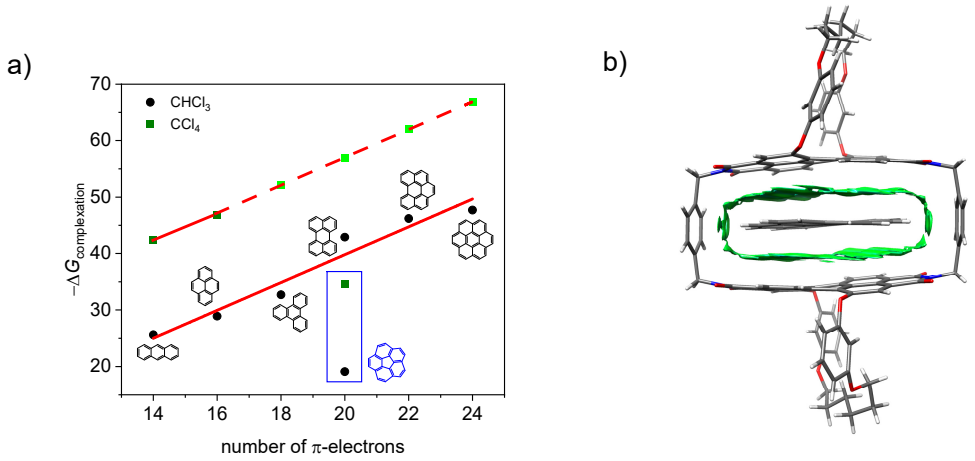

Figure 56. a) Plot of Gibbs free binding energy of complexation for various guests by **1-*PP*** in chloroform and tetrachloromethane at r.t. The light green symbols indicate that the values are estimated based on linear extrapolation. b) Noncovalent interaction analysis of the single crystal X-ray structure of coronene⊂**1-*PP***.

Another synthetic strategy to achieve chiral PBI based cyclophanes is presented in the last part of this thesis (*Chapter 6*). Hereby, direct arylation of the PBI core was applied to obtain a cyclophane composed of highly core twisted chromophores (Figure 57a,b). For this purpose, a Suzuki-Miyaura cross coupling in the 1,6,7,12-positions of the PBI was the key step to synthesize the precursor *rac*-**40**, interlocking sterically demanding 4-*tert*-butylphenyl substituents, which yielded stable atropo-enantiomers. The corresponding *para*-xylylene bridged dimer *rac*-**2** exhibited excellent chiral resolution and could be characterized by several optical spectroscopic methods, including UV/vis, CD, fluorescence and CPL spectroscopy.

UV/vis and NMR titration studies revealed that guest encapsulation is feasible with binding constants up to 10^3 M^{-1} in tetrachloromethane for several PAHs despite the distorted nature of the host. The Gibbs free energies of complexation for a series of guests with varying numbers of π-electrons showed a certain specificity of this cyclophane towards flexible substrates, which are able to adapt their conformation to the distorted nature of the surrounding cavity. Additionally, (time-dependent) NMR studies as well as UV/vis titration studies suggested the preferential binding of guest molecules with the opposite configuration compared to the chromophores of the host. Thus, chirality transfer from the host to [5]helicene yielded an enrichment of the heterochiral epimeric complex, i.e. *M*-[5]helicene⊂**2-*PP***. DFT calculations confirmed this experimental observation (Figure 57c) and revealed that the preferential heterochiral binding of flexible guests is a general feature of this host.

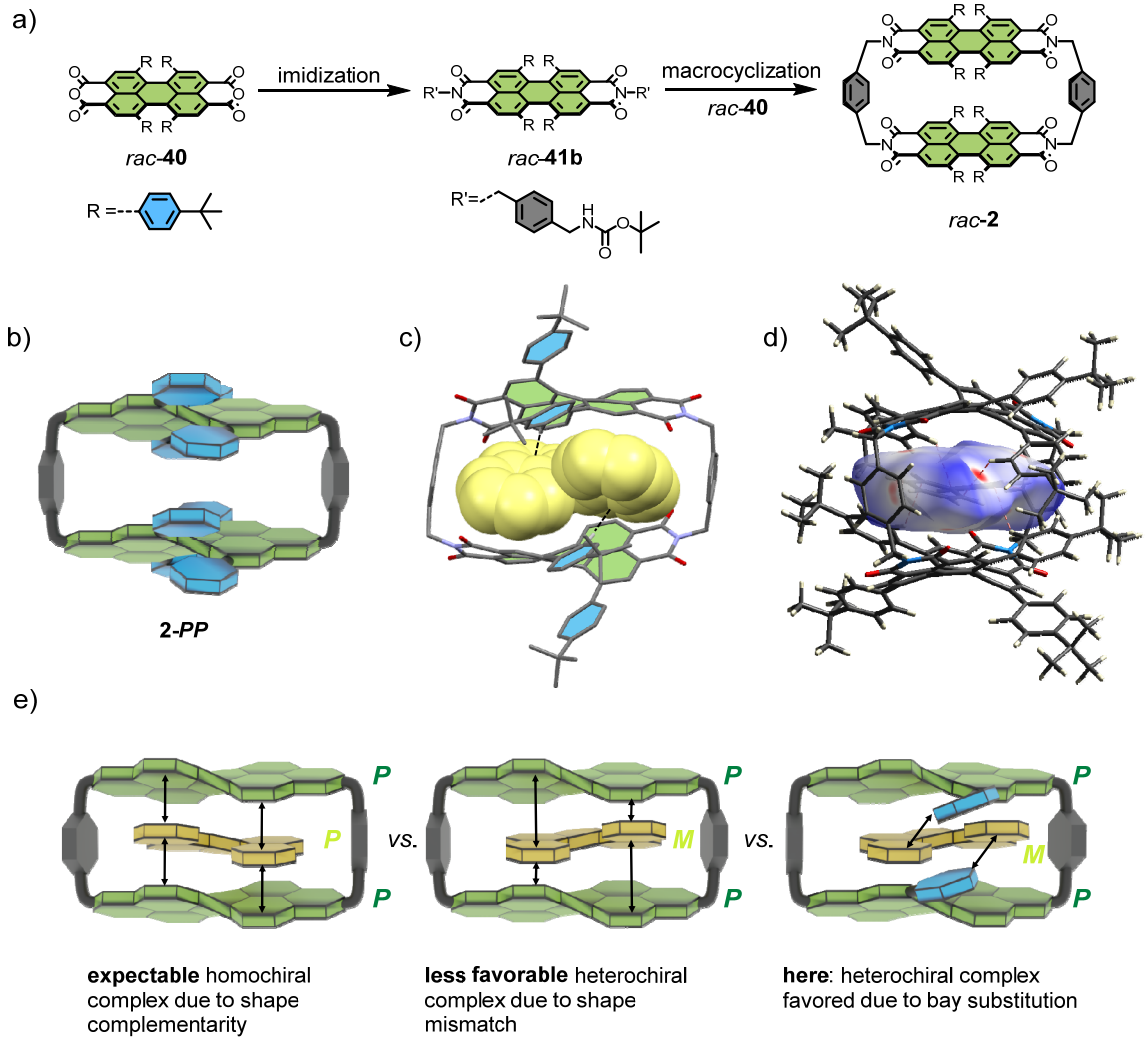

Figure 57. a) Synthesis of *rac*-**2** by macrocyclization of tetraarylated PBA *rac*-**40** and *rac*-**41b**. b) Schematic depiction of **2-*PP*** with interlocked bay substituents. c) DFT calculated structure of *M*-[5]helicene⊂**2-*PP***. d) Hirshfeld surface analysis of a single crystal X-ray structure obtained from 1,1'-biphenyl⊂**2**. e) General concept of switching the preferential homochiral guest binding into heterochiral guest binding within chiral *para*-xylylene bridged PBI cyclophanes.

The calculated structures as well as single crystal X-ray analysis for the 1,1'-biphenyl⊂**2** complex rationalized this unexpected preference, originating from the sterically demanding bay substitution, which forces the substrates into the opposite configuration compared to the adjacent PBIs of the host. In these complexes π–π interactions between the perylene units and the aromatic guests are replaced by stabilizing CH-π interactions between the phenyl substituents of the chromophore moieties and the π-cloud of the guest molecules (Figure 57c,d). Hence, by the refinement of the PBI bay substitution, the preferred formation of homochiral PBI cyclophane inclusion complexes as presented in *Chapter 3* can be switched to heterochiral complexes (Figure 57e).

To sum up, this work illustrates how the targeted tailoring of supramolecular cavities can not only accomplish high binding due to optimized stereoelectronic shape matches between host and guest (*Chapter 3*) but also how molecular engineering of the binding site by a refined substitution periphery of the cavity makes enantiospecific guest recognition and host mediated chirality transfer feasible (*Chapter 3* and *Chapter 6*). Moreover, an enzyme mimic, following the Pauling-Jencks model of enzyme catalysis was realized by the smart design of a PBI host composed of moderately twisted chromophores, which drives the substrate inversion according to the concepts of transition state stabilization and ground state destabilization (*Chapter 4* and *Chapter 5*). The results of this thesis contribute to a better understanding of structure-specific interactions in host-guest complexes as well as the corresponding thermodynamic and kinetic properties and represent an appealing blueprint for the design of new artificial complex structures of high stereoelectronic shape complementarity in order to achieve the goal of sophisticated supramolecular receptors and enzyme mimicry (Figure 58).

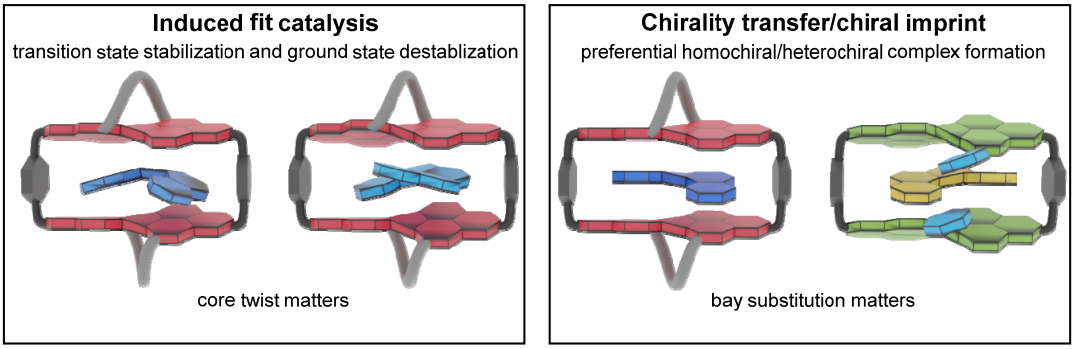

Figure 58. Schematic summary of the supramolecular concepts applied within this thesis to obtain an enzyme mimicking supramolecular catalyst (*Chapter 4* and *Chapter 5*) and a host-mediated chirality transfer, resulting in either homochiral or heterochiral host-guest complexes (*Chapter 3* and *Chapter 6*), depending on the molecular design.

Chapter 8

Zusammenfassung und Fazit

Seit den Anfängen der supramolekularen Chemie war die Entwicklung von maßgeschneiderten Kavitäten, die hochentwickelte natürliche Rezeptoren nachahmen, um spezifische Substratbindung zu ermöglichen, von großem Interesse. Dieses ehrgeizige Vorhaben kann durch das gezielte Design von Wirtmolekülen erreicht werden, um komplementäre nichtkovalente Wechselwirkungen zwischen Bindungsstelle und Gast zu ermöglichen. Die strukturelle Flexibilität von Perylen bietet die Möglichkeit, verdrillte, inhärent chirale Perylenbisimide durch eine geeignete Kernsubstitution herzustellen. Bisher diente jegliche Substitution in PBI basierten Cyclophanen lediglich der verbesserten Löslichkeit im organischen oder wässrigen Medium, wurde jedoch noch nicht genutzt, um neuartige chirale Bindungstaschen zu erhalten, die eine enantiospezifische Substraterkennung ermöglichen würden. Anknüpfend an die früheren Arbeiten über Perylenbisimid-Cyclophanwirte befasste sich diese Arbeit daher mit der Synthese und Untersuchung der ersten chiralen PBI-Cyclophankavitäten mit dem Ziel diese als supramolekulare Rezeptoren zu nutzen.

In *Kapitel 3* wird die Synthese von **1-*MM*** und **1-*PP*** vorgestellt (Abbildung 1a), sowie die Charakterisierung der Makrozyklen mit Hilfe von optischer Spektroskopie. Der synthetische Schlüsselschritt stellt eine kovalente Verknüpfung der 1,7-Buchtpositionen durch eine intramolekulare ringschließende Metathese dar, welche stabile chirale Perylene ergab. Eine anschließende Hydrierung der resultierenden olefinischen Doppelbindung, Verseifung, Imidisierung, chirale Auflösung durch HPLC und eine erneute Verseifung machten die Perylenebisanhydride **57-*M*** und **57-*P*** zugänglich. Die angestrebten Cyclophane **1-*PP*** und **1-*MM*** wurden in einer Makrozyklisierungsreaktion mit *para*-Xylylendiamin und dem enantiomerenreinen Perylenbisanhydrid **57** in der gewünschten Konfiguration synthetisiert.

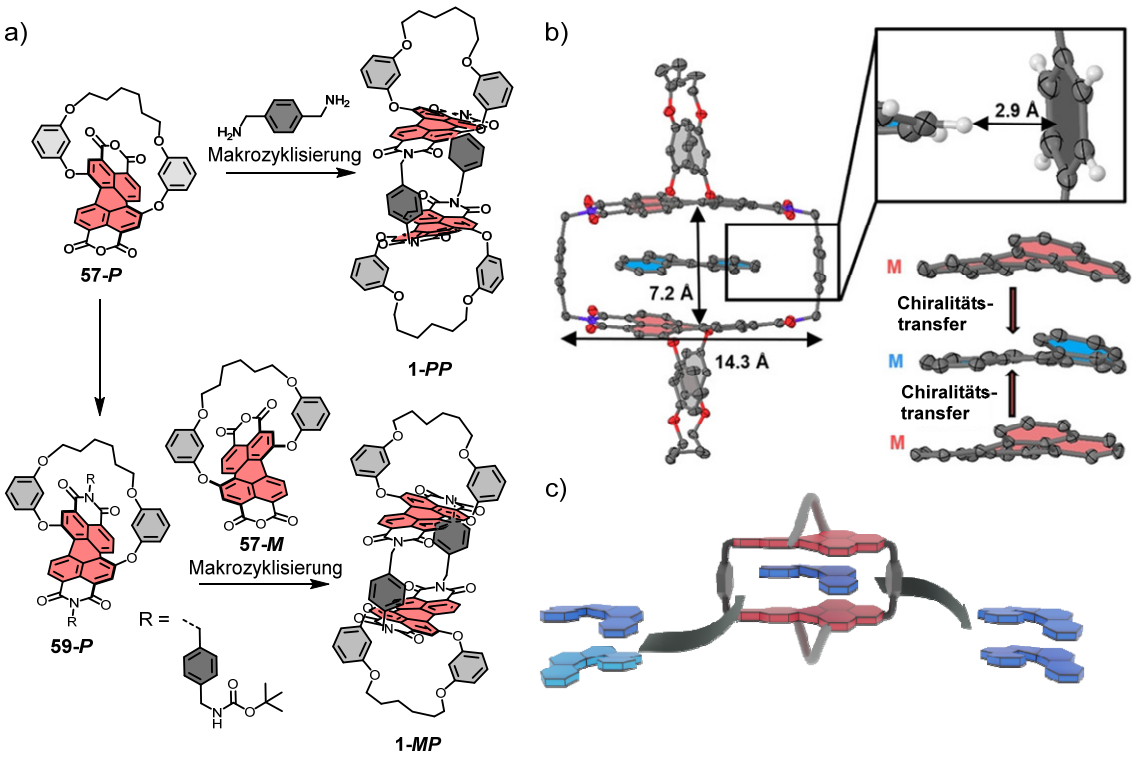

Abbildung 1. a) Synthese von **1-*PP*** (**1-*MM*** analog) und **1-*MP*** sowie b) die Röntgen-Einkristallstruktur von [4]Helicen⊂**1-*MM*** und c) die schematische Darstellung der Deracemisierung von [5]Helicen in der Gegenwart von **1-*PP***.

1-*MM* und **1-*PP*** bieten eine gut zugängliche chirale Kavität, die zur Komplexierung kleiner aromatischer Gäste durch π–π Stapelwechselwirkungen geeignet ist. Aufgrund der perfekten Formübereinstimmung zwischen den mäßig helikal verdrillten PBI-Chromophoren und [4]- und [5]-Helicen ergaben UV/vis- und Fluoreszenztitrationsstudien hohe Substratbindungsaffinitäten in Chloroform mit Assoziationskonstanten von bis zu 10^6 M^{-1} für die jeweiligen homochiralen Wirt-Gast Komplexe, welche im unpolaren Tetrachlormethan zu noch höheren Bindungsaffinitäten im nanomolaren Bereich gesteigert werden konnten. Die Strukturaufklärung des thermodynamisch stabilsten [4]Helicen-Einschlusskomplexes durch (2D)-NMR-Studien sowie dessen theoretische Modellierung unterstützten die vorgeschlagene 1:1 Bindung des zwischen den PBI-Einheiten eingeschlossenen Carbohelicens. Eine entsprechende Einkristallstrukturanalyse ergab, dass die Homochiralität des Wirts die Übertragung seiner Konfiguration auf [4]Helicen ermöglicht, was zu einem perfekt eingebetteten Helicensubstrat mit π–π und CH-π Wechselwirkungen zwischen Gast und Cyclophan führt (Abbildung 1b). Darüber hinaus ermöglichten die homochiralen Kavitäten die Anreicherung von *P*-

konfiguriertem [5]Helicen in Gegenwart von **1-*PP***, während *M*-[5]Helicen in Gegenwart von **1-*MM*** angereichert werden konnte. Experimentelle Beweise für den Wirt-vermittelten Chiralitätstransfer (Abbildung 1c) wurden durch zeitabhängige CD-Spektroskopie von *rac*-[5]Helicen in Gegenwart der Wirttemplate erhalten.

Neben den Untersuchungen zur Wirt-Gast-Bindung befasste sich diese Arbeit auch mit der katalytischen Wirkung von PBI-Cyclophanen auf die Isomerisierung von eingeschlossenen Gästen. Dabei wurde [5]Helicen als idealer Kandidat identifiziert, um tiefere Einblicke in den beobachteten Chiralitätstransfer zu gewinnen, da dieser Gast durch eine geeignete Enantiomerisierungskinetik, die auf der Zeitskala von Standardspektroskopiemethoden untersucht werden kann, charakterisiert ist. Dementsprechend wurde in *Kapitel 4* dieser Arbeit der Einfluss des chiralen Wirts **1-*PP*** auf die Enantiomerisierungsbarriere von [5]Helicen detailliert untersucht. Als Referenz wurde zusätzlich die meso-Verbindung **1-*MP*** in einer verbesserten zweistufigen Synthese durch Bildung eines *Boc*-geschützten Zwischenprodukts vor der Makrozyklisierung synthetisiert (Abbildung 1a). Eine entsprechende Fluoreszenz-Wirt-Gast-Titration in Tetrachlormethan ergab eine deutlich verringerte Bindungsaffinität von *rac*-[5]Helicen gegenüber **1-*MP*** im Vergleich zu *P*-[5]Helicen gegenüber **1-*PP*** um drei Größenordnungen auf $K_a = 2.0 \times 10^6\ M^{-1}$, was mit der berechneten Bindungsenergie übereinstimmte und auf die stereochemische Verschiedenartigkeit des Gastes und einer der PBI-Einheiten zurückgeführt werden konnte.

Zunächst wurden Tieftemperatur-NMR Untersuchungen durchgeführt, um die Existenz nur einer epimeren Komplexspezies bei der Bindung von [5]Helicen durch **1-*PP*** (d. h. *P*-[5]Helicen⊂**1-*PP***) in Lösung zu bestätigen. Dies konnte mit Hilfe einer Einkristallstrukturanalyse eines Co-Kristalls, der aus einem racemischen Gemisch des Gastes und **1-*PP*** gezogen wurde, weiter bekräftigt werden. Die Studien im Festkörper und in Lösung zeigten nicht nur eine wechselseitig induzierte Konformationsanpassung von Wirt und Gast, die sich durch ein komprimiertes [5]Helicen-Substrat und eine erhöhte Kernverdrillung der Chromophore bemerkbar machte. Darüber hinaus konnte eine dynamische Rotation von [5]Helicen entlang der *z*-Achse in der Kavität des Wirts beobachtet werden (Abbildung 2c). Diese dynamische Bewegung wurde mit Hilfe von temperaturabhängigen NMR-Studien sowie ^{1}H-^{1}H-EXSY NMR-Messungen bei niedriger Temperatur mit einer Barriere von ~54 kJ mol^{-1} quantifiziert.

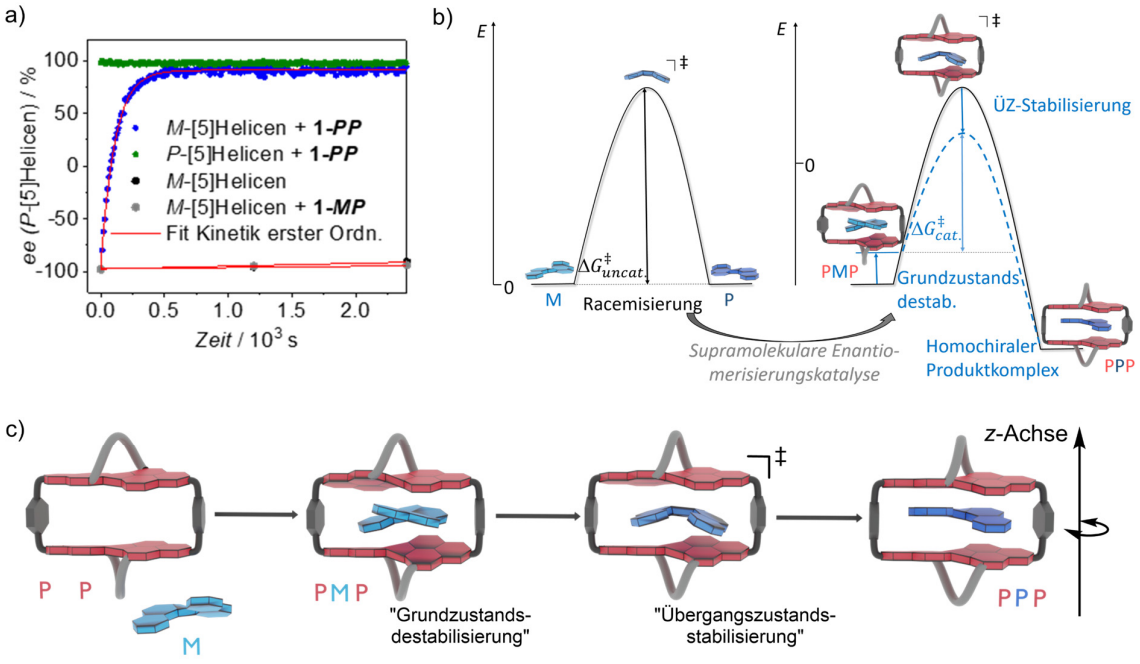

Abbildung 2. a) Darstellung des Enantiomerenüberschusses von *P*-[5]Helicen in Tetrachlormethan (*ee* = –100% entspricht enantiomerenreinem *M*-[5]Helicen). b) Schematische Potentialhyperfläche von [5]Helicen in Abwesenheit und Anwesenheit von **1-*PP***. c) Schematische Darstellung der durch induzierte Anpassung katalysierten *M*-[5]Helicen-Enantiomerisierung in Anwesenheit von **1-*PP***, sowie der Gastrotation im Produktkomplex.

Vor allem aber zeigten zeitabhängige CD-Studien in Tetrachlormethan (Abbildung 2a), dass der Enantiomerisierungsprozess von *M*-[5]Helicen zu *P*-[5]Helicen in Gegenwart von **1-*PP*** bei Raumtemperatur um einen Faktor von ~700 beschleunigt wird ($\Delta\Delta G^{\ddagger}$ = 15.9 kJ mol^{-1}), so dass das gleiche CD-Signal wie bei der entsprechenden homochiralen Wirt-Gast-Mischung innerhalb von Minuten erhalten wird. Dementsprechend ist die einzigartige Fähigkeit dieses Wirts, kleine Carbohelicengäste zu deracemisieren, mit der Fähigkeit gekoppelt, die entsprechende Enantiomerisierungsbarriere um einen signifikanten Faktor zu senken. Im Gegensatz dazu hat die meso-Verbindung fast keinen Einfluss auf den Gastinversionsprozess, wirkt im Gegenteil als leichter Inhibitor für die Enantiomerisierung von [5]Helicen ($\Delta\Delta G^{\ddagger}$ = –2.1 kJ mol^{-1}) und liefert nach Zugabe des enantiomerenreinen Gastes racemisches [5]Helicen innerhalb eines Zeitraums von mehr als einem Tag.

Um die beobachteten drastischen kinetischen Unterschiede, die auf scheinbar geringen strukturellen Diskrepanzen im Hohlraum zwischen **1-*PP*** und **1-*MP*** beruhen, zu erklären, wurden theoretische Rechnungen angestellt. Dabei wurden Energiezerlegungsanalysen (EDA) der relevanten Komplexstrukturen im Grundzustand und im Übergangszustand durchgeführt.

Die Aufschlüsselung der supramolekularen Wechselwirkungen deutete darauf hin, dass eine subtile Formübereinstimmung zwischen der Perylenkrümmung im homochiralen Wirt und der nicht planaren Übergangszustandsstruktur von [5]Helicen letztere hauptsächlich durch Dispersions- und elektrostatische Wechselwirkungen stabilisiert. Die Übergangszustandsstruktur von [5]Helicen ist dagegen laut Energiezerlegungsanalyse innerhalb von **1-*MP*** tatsächlich leicht destabilisiert, was die experimentellen Daten bestätigt.

Neben der Stabilisierung des Übergangszustands hat sich zudem gezeigt, dass die Destabilisierung des Grundzustands zur Senkung der Reaktionsbarriere der Gastenantiomerisierung in **1-*PP*** beiträgt. Dies beruht auf der Tatsache, dass [5]Helicen im Reaktandenkomplex (*M*-[5]Helicen⊂**1-*PP***) strukturell stärker verzerrt ist als im Übergangszustandskomplex, was auf die unterschiedliche Form zwischen der im Uhrzeigersinn und der gegen den Uhrzeigersinn gerichteten Helizität der Peryleneinheiten des Rezeptors bzw. des Gastes zurückzuführen ist. Diese Spannung im heterochiralen Komplex dient, bildlich gesprochen, als Energiespeicher, der dabei hilft die Reaktionsbarriere zu senken.

Erwähnenswert ist, dass die DFT-Berechnungen nicht nur eine strukturelle Verzerrung im Reaktandenkomplex zeigen, sondern eine konformationelle Anpassungsfähigkeit von Wirt und Gast während des gesamten Enantiomerisierungsprozesses beobachtet werden kann. All diese Beobachtungen deuten darauf hin, dass dieses System eine einzigartige artifizielle "Deracemase" darstellt, die dem Pauling-Jencks-Konzept der Enzymkatalyse folgt (Abbildung 2b,c). Darüber hinaus zeigte der Vergleich mit dem Referenzcyclophan **1-*MP***, wie empfindlich der Enantiomerisierungsprozess von [5]Helicen auf kleine geometrische Veränderungen in der Kavität reagiert und wie entscheidend die präzise Gestaltung von Bindungsstellen ist, um eine Übergangszustandsstruktur mit Hilfe von π–π Stapelwechselwirkungen zu stabilisieren.

In *Kapitel 5* wurde **1-*PP*** zunächst als Wirt für planare polyzyklische aromatische Kohlenwasserstoffe untersucht. Hierbei zeigte sich, dass die Bindungsenergien für die Bildung der entsprechenden Komplexe linear mit der Zahl der π-Elektronen der untersuchten Gäste antsteigen und so Bindungskonstanten von bis zu $K_a = 2.8 \times 10^8\ M^{-1}$ in Chloroform bei Raumtermperatur ermittelt werden konnten. Ähnlich wie in *Kapitel 4* konnten diese in Tetrachlormethan weiter erhöht werden, sodass sich für Coronen, eine Bidnungskonstante von etwa $10^{12}\ M^{-1}$ durch lineare Extrapolation der Bindungsenergien abschätzen lässt (Abbildung 3a). Im Gegensatz dazu liegt die Bindungsenergie für Corannulen deutlich unter der von anderen Gästen mit einer vergleichbaren Anzahl von π-Elektronen. Folglich scheint das

Konzept der "induzierten Anpassungskatalyse" auf die „Schale-zu-Schale“ Inversion von Corannulen in Gegenwart von **1-*PP*** gut anwendbar, da eine bevorzugte Bindung planarer Strukturen, wie etwa die Übergangszustandsstruktur von Corannulen, beobachtet werden kann. Dementsprechend wurde untersucht, welchen Einfluss die verdrillten PBI-Einheiten und die daraus resultierenden strukturellen Unterschiede der nicht-planaren Chromophore auf die Stabilisierung der planaren Übergangszustandsstruktur von Corannulen haben.

VT-NMR-Studien einer Mischung von **1-*PP*** und Ethylcorannulen, dessen Methylenprotonen für die Barriere der „Schale-zu-Schale“ Inversion charakteristisch sind, zeigten trotz der offenkundigen strukturellen Verschiedenheit eine um etwa 11.6 kJ mol^{-1} verringerte Inversionsbarriere. Der beobachtete katalytische Effekt konnte in Analogie zu den in *Kapitel 4* vorgestellten Studien den Konzepten der Übergangszustandsstabilisierung einerseits und der zusätzlichen Grundzustandsdestabilisierung andererseits als Folge des komprimierten Corannulengastes bei der Komplexierung, zugeordnet werden. Die DFT-Berechnungen der Komplexstruktur deuteten auf eine wechselseitige Strukturanpassung von Wirt und Gast im Übergangszustand hin, welche zu einer nicht-planaren Übergangszustandsstruktur von Corannulen führt.

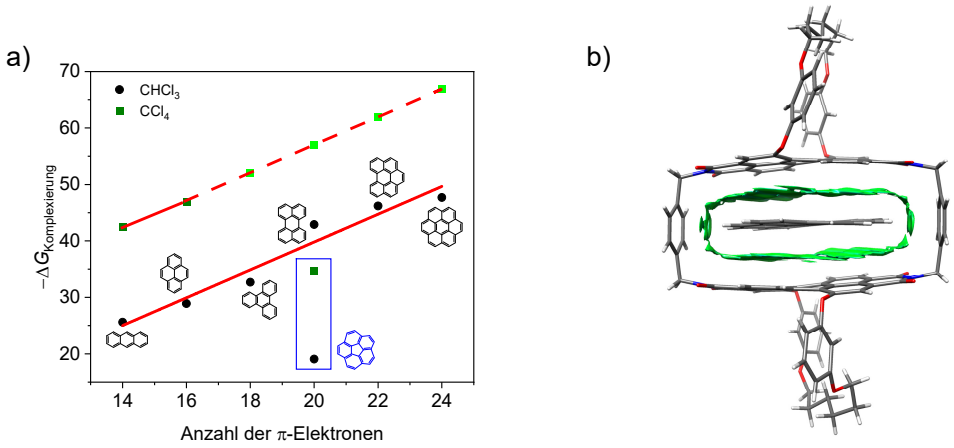

Abbildung 3. a) Gibbs Bindungsenergie der Komplexierung für verschiedene Gäste durch **1-*PP*** in Chloroform und Tetrachlormethan bei r.t. Die hellgrünen Symbole zeigen an, dass die Werte auf der Grundlage einer linearen Extrapolation abgeschätzt wurden. b) Nicht-kovalente Wechselwirkungsanalyse der Einkristall-Röntgenstruktur von Coronen⊂**1-*PP***.

Die berechnete Komplexstruktur wurde durch Einkristallstrukturanalyse von komplexiertem Coronen, einem qualitativen Übergangszustandsanalogon von Corannulen, weiter aufgeklärt und zeigte hierbei eine ähnliche Verzerrungen wie im berechnete Übergangszustandskomplex (Abbildung 3b). Wirt und Gast gehen also einen Kompromiss zwischen struktureller

Verzerrung und optimierten nicht-kovalenten Wechselwirkungen ein, um eine Übergangszustandsstabilisierung der „Schale-zu-Schale“ Inversion durch einen bestmöglichen π-Kontakt über einen induzierten Anpassungsmechanismus zu erreichen.

Eine andere Strategie zur Synthese chiraler Cyclophane auf PBI-Basis wird im letzten Teil dieser Arbeit (*Kapitel 6*) vorgestellt. Durch direkte Arylierung des PBI-Kerns wurde hierbei ein Cyclophan mit stark verdrillten Chromophoren erhalten (Abbildung 4a,b). Zu diesem Zweck wurde eine Suzuki-Miyaura-Kreuzkupplung in den 1,6,7,12-Positionen des Chromophors als Schlüsselschritt zur Synthese der PBI-Vorstufe *rac*-**40** durchgeführt, wobei sterisch anspruchsvolle 4-*tert*-Butylphenyl-Substituenten so ineinandergreifen, dass stabile Atropoenantiomere entstehen. Das entsprechende *para*-Xylylen-verbrückte Dimer *rac*-**2** wies eine ausgezeichnete chirale Auflösung auf und konnte durch verschiedene optisch-spektroskopische Methoden, darunter UV/vis-, CD-, Fluoreszenz- und CPL-Spektroskopie, charakterisiert werden.

UV/vis- und NMR-Titrationsstudien ergaben, dass der Gasteinschluss mit Bindungskonstanten von bis zu $10^3\ M^{-1}$ in Tetrachlormethan für mehrere polyzyklische aromatische Kohlenwasserstoffe trotz der verzerrten Natur des Wirts möglich ist. Die freie Enthalpie der Komplexierung für eine Reihe von Gästen mit unterschiedlicher Anzahl von π-Elektronen zeigte eine gewisse Spezifität dieses Cyclophans gegenüber flexiblen Substraten, die ihre Konformation an die Struktur der sie umgebenden Kavität anpassen können. Darüber hinaus deuteten (zeitabhängige) NMR-Studien sowie UV/vis-Titrationsstudien auf die bevorzugte Bindung von Gastmolekülen mit der entgegengesetzten Konfiguration im Vergleich zu den Chromophoren des Wirts hin.

Der Chiralitätstransfer vom Wirt auf [5]Helicen führte dementsprechend zu einer Anreicherung des heterochiralen epimeren Komplexes, d. h. *M*-[5]Helicen⊂**2**-***PP***. DFT-Berechnungen bestätigten diese experimentelle Beobachtung (Abbildung 4c) und zeigten, dass die bevorzugte heterochirale Bindung von flexiblen Gästen ein allgemeines Merkmal dieses Wirtes ist. Die berechneten Strukturen sowie die Röntgen-Einkristallstrukturanalyse für den 1,1'-Biphenyl⊂**2** Komplex erklärten diese unerwartete Präferenz, welche auf die sterisch anspruchsvolle Bucht-substitution, die die Substrate in die entgegengesetzte Konfiguration im Vergleich zu den benachbarten Perylenbisimiden des Wirts zwingt, zurückzuführen ist. In diesen Komplexen werden π–π Wechselwirkungen zwischen den Peryleneinheiten und den aromatischen Gästen durch stabilisierende CH-π Wechselwirkungen zwischen den Phenylsubstituenten der

Chromophore und der π-Elektronenwolke der Gastmoleküle ersetzt (Abbildung 4c,d). Durch die Feinjustierung der PBI-Buchtsubstitution kann demnach die bevorzugte Bildung homochiraler PBI-Cyclophaneinschlusskomplexe, wie in *Kapitel 3* vorgestellt, in heterochirale Komplexe umgewandelt werden (Abbildung 4e).

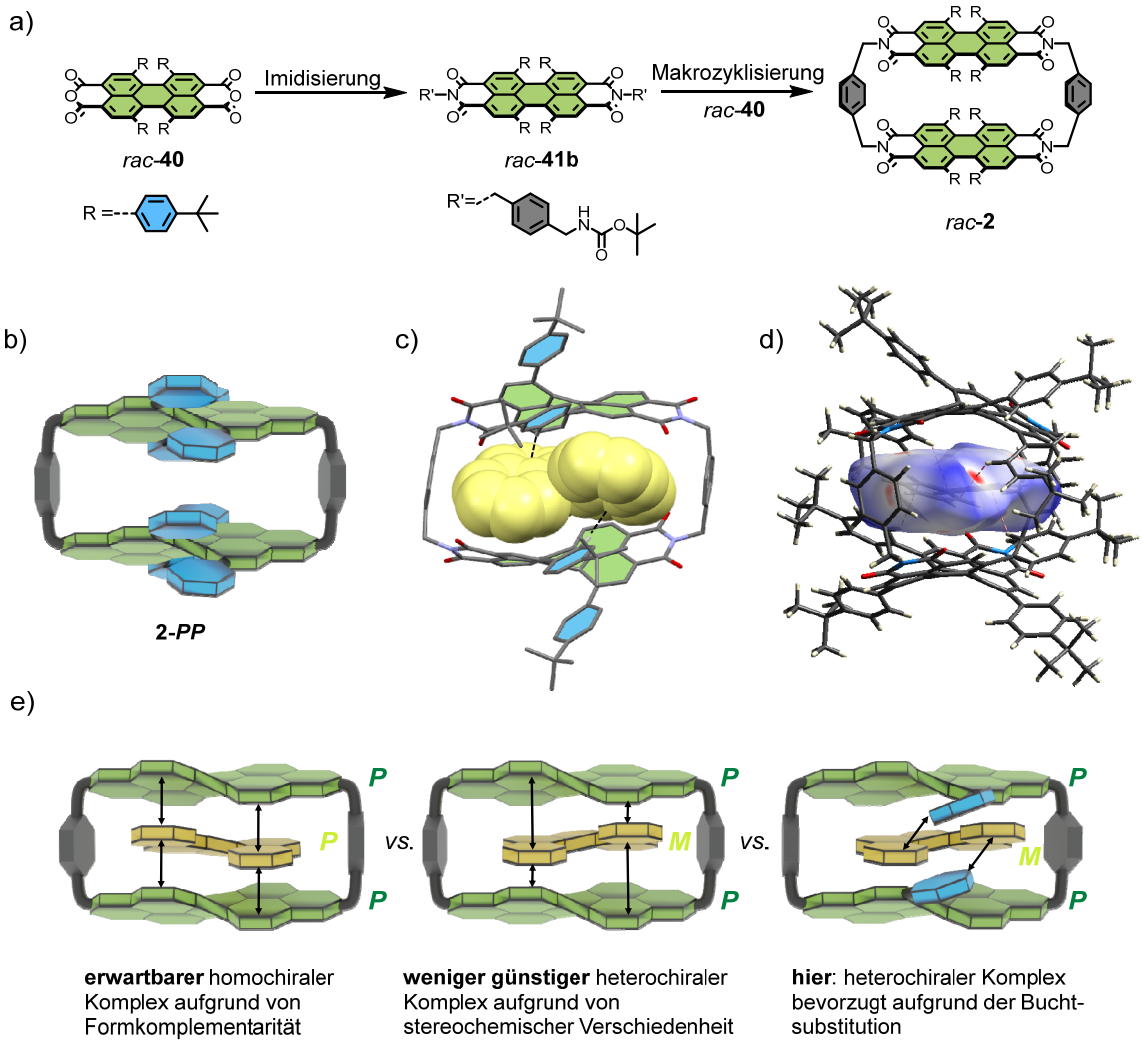

Abbildung 4. a) Synthese von *rac*-**2** durch Makrozyklisierung des tetraarylierten PBA *rac*-**40** und *rac*-**41b**. b) Schematische Darstellung von **2-*PP*** mit verzahnten Buchtsubstituenten. c) DFT-berechnete Struktur von *M*-[5]Helicen⊂**2-*PP***. d) Hirshfeld-Oberflächenanalyse einer Einkristall-Röntgenstruktur von 1,1'-Biphenyl⊂**2**. e) Allgemeines Konzept des Wechsels der bevorzugten homochiralen Gastbindung zu einer heterochiralen Gastbindung in chiralen *para*-xylylenverbrückten PBI-Cyclophanen.

Zusammenfassend zeigt diese Arbeit auf, wie durch die gezielte Konstruktion supramolekularer Kavitäten nicht nur hohe Bindungsaffinitäten aufgrund optimierter stereoelektronischer Formübereinstimmungen zwischen Wirt und Gast erreicht werden können (*Kapitel 3*), sondern auch, wie das molekulare Design der Bindungsstelle durch die genaue Einstellung der

Substitutionsperipherie der Kavität eine enantiospezifische Gasterkennung sowie einen Wirt-vermittelten Chiralitätstransfer ermöglicht (*Kapitel 3* und *Kapitel 6*). Darüber hinaus wurde ein Enzymimitat, welches dem Pauling-Jencks-Modell der Enzymkatalyse folgt, durch das intelligente Design eines PBI-Wirts, der aus moderat verdrillten Chromophoren besteht und die Substratinversion gemäß der Konzepte der Übergangszustandsstabilisierung und Grundzustandsdestabilisierung antreibt, realisiert (*Kapitel 4* und *Kapitel 5*). Die Ergebnisse dieser Arbeit tragen zu einem besseren Verständnis der strukturspezifischen Wechselwirkungen in Wirt-Gast-Komplexen sowie der entsprechenden thermodynamischen und kinetischen Eigenschaften bei und stellen eine attraktive Blaupause für das Design neuer künstlicher Komplexsysteme mit hoher stereoelektronischer Formkomplementarität dar, um das Ziel hochentwickelter supramolekularer Rezeptoren sowie Enzym-ähnlicher Katalyse zu realisieren (Abbildung 5).

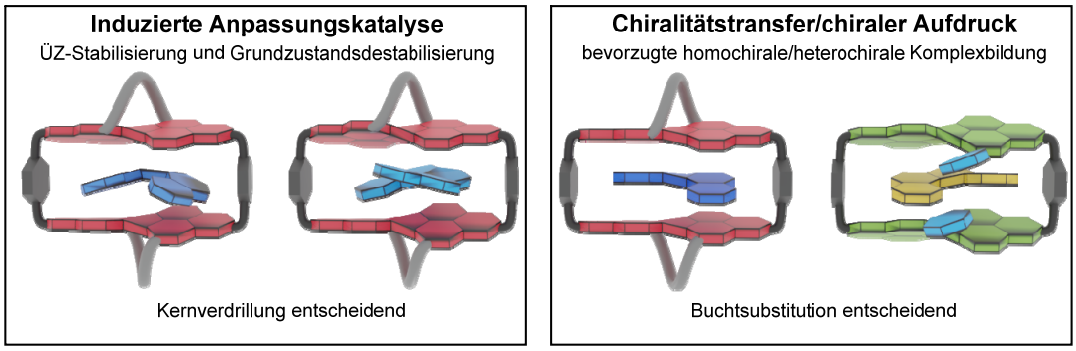

Abbildung 5. Schematische Zusammenfassung der in dieser Arbeit angewandten supramolekularen Konzepte zur Gewinnung eines Enzym-ähnlichen supramolekularen Katalysators (*Kapitel 4* und *Kapitel 5*) und eines Wirt-vermittelten Chiralitätstransfers, der je nach Moleküldesign entweder die Bildung homochiraler oder heterochiraler Wirt-Gast-Komplexe bevorzugt (*Kapitel 3* und *Kapitel 6*).

Chapter 9

Appendix

9.1 Appendix for Chapter 3: Deracemization of Carbohelicenes by a Chiral Perylene Bisimide Cyclophane Template

General Methods

Chemicals: All chemicals and solvents were purchased from commercial suppliers and used without further purification. 1,7-dibromoperylene-3,4,9,10-tetracarboxy tetrabutylester, 3-(but-3-en-1-yloxy)phenol and (*Z*)-1,2-di(naphthalen-2-yl)ethene were synthesized according to literature known procedures.[302-305] *Rac*-[5]helicene was synthesized in a similar procedure as reported in literature[302] with (*Z*)-1,2-di(naphthalen-2-yl)ethene (109 mg, 389 µmol) and iodine (32 mg, 126 µmol), dissolved in cyclohexane and irradiated with UV/vis light (λ = 254–575 nm) for 1 h. The resolution of the enantiomers of [5]helicene could be achieved by chiral HPLC (DCM/*n*-hexane 3:7, flow rate 6.5 mL/min). The enantiomeric excess was determined by analytical HPLC (Reprosil 100 Chiral-NR 8 µm, Trentec, *n*-hexane/DCM 9:1) with values of *ee* > 98%. Subsequently, the CD spectra of the enantiomers were recorded (Figure A46a) and compared to the ones in literature in order to assign the two isomers.[212] By rearrangement of equation A2 (see the part on "Deracemization Studies"), the $\Delta\varepsilon$ values of the enantiopure compound in chloroform were calculated and used for the calculation of the enantiomeric excess.

HPLC: Analytical HPLC was carried out on a JASCO system (PU 2080 PLUS) with a diode array detector (MD 2015), equipped with a ternary gradient unit (DG-2080-533) and inline-degasser (LG 2080-02). Recycling semipreparative HPLC was carried out on a JAI LC-9105. Chiral resolution was carried out using a Trentec Reprosil-100 Chiral-NR 8 µm-column.

GPC: Gel permeation chromatography (GPC) was performed on a Shimadzu Recycling GPC-System (LC-20AD Prominence Pump; SPDMA20A Prominence Diode Array Detector) with three or two preparative columns (Japan Analytical Industries Co., Ltd.; JAIGEL-1 H, JAIGEL-

For the sake of harmonization of all Supporting Information Chapters (Appendix), some modifications were made.

2H and JAIGEL-2.5 H) in chloroform (HPLC grade, stabilized with 0.1% EtOH) with a flow rate of 6.5 or 5.0 mL/min.

NMR spectroscopy: ^{1}H NMR and ^{13}C NMR spectra were recorded on a Bruker Avance III HD 400 spectrometer at 298 K. Chemical shift data are reported in parts per million (ppm, δ scale) downfield from tetramethylsilane and referenced internally to the residual proton (for proton NMR) in the solvent ($CDCl_3$: δ = 7.26; CD_2Cl_2: δ = 5.32; $C_2D_2Cl_4$ δ = 6.00) or to the carbon resonance ($CDCl_3$: δ = 77.16; CD_2Cl_2: δ = 53.84, $C_2D_2Cl_4$: δ = 74.20). The coupling constants are listed in Hertz.

Mass spectrometry: The MALDI-TOF mass spectra were measured with a Bruker Daltonics ultrafleXtreme mass spectrometer by using DCTB as a matrix. High-resolution ESI TOF spectra were acquired on a Bruker Daltonics micrOTOF focus spectrometer.

Melting points: Melting points were measured with an Olympus BX41 polarization microscope connected to a TP84 Linkam scientific temperature regulator.

Optical UV/vis absorption spectroscopy: All spectroscopic measurements were carried out under ambient conditions using solvents of spectroscopic grade. The absorption spectra were recorded on a JASCO V-770 or V-670 spectrometer equipped with a PAC-743R Peltier for temperature control.

Ciruclar dichroism (CD) spectroscopy: CD spectra were measured with a Jasco J-810 spectropolarimeter equipped with a JASCO CDF-426S Peltier temperature controller.

Steady-State fluorescence spectroscopy: Fluorescence spectra were recorded on an Edingburgh Instruments FLS981 fluorescence spectrometer. The quantum yields were determined by using the dilution method ($A < 0.05$) with *N,N'*-bis[2,6-diisopropylphenyl]perylene-3,4:9,10- bis(dicarboximide) (ϕ_F = 100% in chloroform)[306] as a reference compound.

Single crystal X-ray analysis: The diffraction images for X-ray crystallographic analysis were collected on a Bruker D8 Quest Kappa diffractometer with a Photon II CPAD area detector using Cu Kα radiation.

Synthetic Procedure

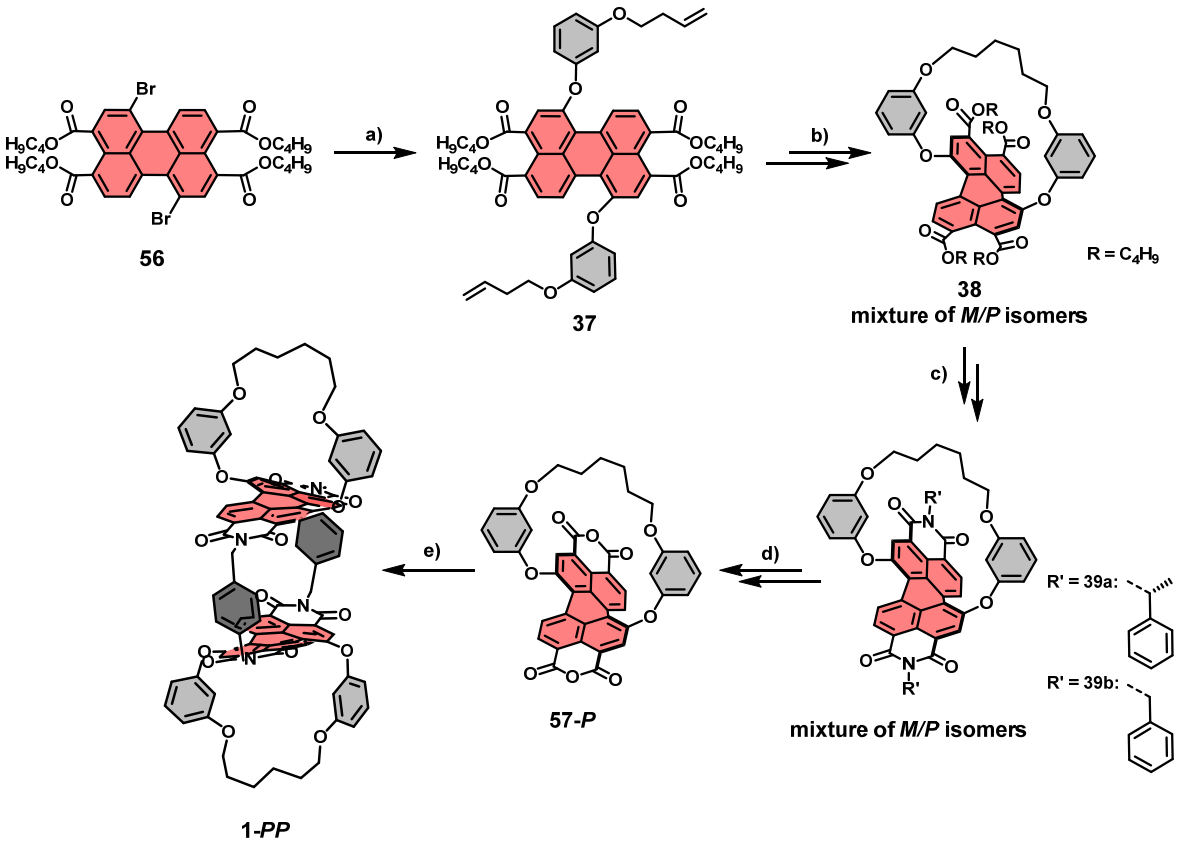

Scheme A1. Synthetic route to PBI cyclophane **1-*PP*** (route to **1-*MM*** analogous). In addition, the chemical structures of PBI dye **39b** is shown. Reaction conditions: a) 3-(but-3-en-1-yloxy)phenol, Cs_2CO_3, DMF, 100 °C, 7.5 h, 49%; b) 1. Grubbs II catalyst, DCM, reflux, 2 h, 82%; 2. H_2, Pd/C, EtOAc/MeOH (10:1), 2.5 h, 97%; c). 1. *p*-TsOH · H_2O, toluene, 140 °C, 17 h, quantitative, 2. **39a**: *R*-1-phenylethylamine, quinoline, $Zn(OAc)_2$, 140 °C, 5 h, 90% (diastereomeric mixture), d) 1. Chiral HPLC resolution of **39a**; 2. KOH, *tert*-butanol, 90 °C, 2 h, 72–90%; e) *para*-xylylenediamine, imidazole, toluene, 120 °C, 16 h, 17%.

1,7-Bis(3-(but-3-en-1-yloxy)phenoxy)-perylene-3,4,9,10-tetracarboxy tetrabutylester (37)

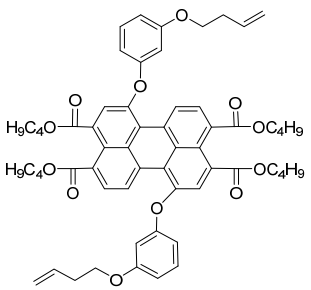

1,7-dibromoperylene-3,4,9,10-tetracarboxy tetrabutylester (**56**) (513 mg, 633 µmol), 3-(but-3-en-1-yloxy)phenol (408 mg, 2.48 mmol) and caesium carbonate (1.21 g, 3.73 mmol) were dissolved in dry DMF (21 mL) and stirred for 7.5 h at 100 °C under a nitrogen atmosphere. The mixture was cooled down to room temperature and DCM (100 mL) was added. Afterwards, the organic phase was washed with water (2 × 100 mL) and dried over Na_2SO_4. The solvent was removed under vacuum and the crude product purified by column chromatography (silica gel, DCM/cyclohexane 9:1 and then DCM/MeOH 99:1). **Yield**: 302 mg (309 µmol, 49%) of a red, waxy solid. **^{1}H NMR** (400 MHz, CD_2Cl_2): δ = 9.06 (d, ^3J = 8.1 Hz, 2H), 7.96 (d, ^3J = 8.1 Hz,

2H), 7.71 (s, 2H), 7.27–7.23 (m, 2H), 6.71 (ddd, ^3J = 8.5 Hz, ^4J = 2.3 Hz, ^4J = 0.9 Hz, 2H), 6.65–6.62 (m, 4H), 5.87 (ddt, ^3J = 17.3 Hz, ^3J = 10.2 Hz, ^3J = 6.8 Hz, 2H), 5.15–5.04 (m, 4 H), 4.24 (t, ^3J = 6.8 Hz, 4H), 4.19 (t, ^3J = 6.8 Hz, 4H), 3.97 (t, ^3J = 6.6 Hz, 4H), 2.50–2.48 (m, 4H), 1.73–1.63 (m, 8H), 1.45–1.33 (m, 8H), 0.95 (t, ^3J = 7.4 Hz, 6H), 0.89 (t, ^3J = 7.4 Hz, 6H). **^{13}C NMR** (101 MHz, CD_2Cl_2): δ = 168.6, 167.8, 161.0, 157.3, 152.1, 134.9, 132.3, 131.9, 131.5, 131.0, 130.1, 129.5, 127.6, 125.2, 125.1, 123.2, 117.2, 111.0, 110.5, 105.8, 67.9, 65.8, 65.6, 33.9, 31.0, 30.8, 19.6, 19.5, 13.94, 13.90. **HRMS** (ESI, positive, acetonitrile/chloroform): (*m/z*) [*M*+Na]$^+$, calcd. for $C_{60}H_{64}NaO_{12}^+$: 999.4290; found: 999.4289. **mp**.: 44–46 °C.

rac-(E/Z)-1,7-(3,3'-(hex-3-en-1,6-diylbis(oxy))diphenolate)-perylene 3,4,9,10-tetracarboxy tetrabutylester (58)

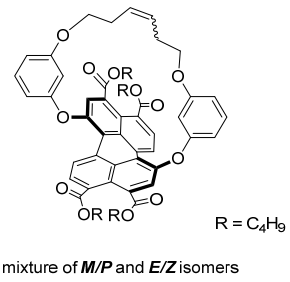

mixture of ***M/P*** and ***E/Z*** isomers

A solution of 2nd Generation Grubbs Catalyst (1,3-bis(2,4,6-trimethylphenyl)-2-imid-azolidinylidene)dichloro(phenylmethylene)-(tricyclohexylphosphine)ruthenium) (20.4 mg, 24.0 µmol, 9 mol%) in dry DCM (40 mL) was added to a mixture of 1,7-bis(3-(but-3-en-1-yloxy)phenoxy perylene-3,4:9,10-tetracarboxy tetrabutylester (**37**) (263.0 mg, 0.277 mmol) in dry DCM (90 mL). The resulting solution was stirred under a nitrogen atmosphere under reflux for 2 h. The solvent was evaporated under reduced pressure and the crude product was purified by column choromatography (silica gel, DCM). **Yield**: 216 mg (228 µmol, 82%) of a yellow solid. **^{1}H NMR** (400 MHz, CD_2Cl_2): δ = 9.06 (d, ^3J = 8.1 Hz, 2H), [8.99 (d, ^3J = 8.0 Hz, 0.17 H)], 7.97 (d, ^3J = 8.1 Hz, 2H), [7.92 (d, ^3J = 8.0 Hz, 0.18 H)], [7.81 (s, 0.17H)], 7.77 (s, 2H), 7.29 (t, ^3J = 8.2 Hz, 2H), 7.01 (ddd, ^3J = 8.2 Hz, ^4J = 2.3 Hz, ^4J = 0.8 Hz, 2H), 6.51 (ddd, ^3J = 8.2 Hz, ^4J = 2.3 Hz, ^4J = 0.8 Hz, 2H), 5.79 (t, ^4J = 2.3 Hz, 2H), 5.36–5.34 (m, 2H), 4.20–4.32 (m, 8H), 3.64 (t, ^3J = 6.3 Hz, 4H), 2.29–2.24 (m, 4H), 1.78–1.68 (m, 8H), 1.50–1.38 (m, 8H), 0.99–0.93 (m, 12H). [main isomer; *main:minor* ratio: *12*/*1*] Additional peaks with significant lower intensity are observed resulting from the presence of different isomers. **^{13}C NMR** (101 MHz, CD_2Cl_2): δ = 168.6, 167.8, 160.7, 158.4, 151.1, 132.43, 132.36, 131.1, 130.7, 130.4, 129.8, 128.8, 127.8, 127.7, 125.9, 125.2, 111.2, 108.4, 102.5, 67.4, 66.0, 65.8, 32.6, 31.0, 30.9, 19.63, 19.58, 13.95, 13.93. **HRMS** (ESI, positive, acetonitrile/chloroform): (*m/z*) [*M*+Na]$^+$, calcd. for $C_{58}H_{60}NaO_{12}^+$: 971.3977; found: 971.3963. **mp.**: 160–163 °C.

rac-1,7-(3,3'-(hexane-1,6-diylbis(oxy))diphenolate)-perylene-3,4,9,10-tetracarboxy tetrabu-tylester (38)

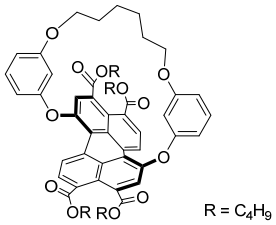

mixture of ***M/P*** isomers

Compound **58** (188 mg, 198 µmol) was dissolved in a solvent mixture of ethyl acetate and methanol (10:1, v:v, 130 mL) and then degassed for 15 min by bubbling argon through the solution. Afterwards, Pd/C (80 mg, 10% Pd) was added, the solution was again degassed for 15 min and finally stirred at room temperature for 2.5 h under a hydrogen atmosphere (atmospheric pressure). The catalyst was removed by filtration over celite and the solvent was removed under reduced pressure. **Yield**: 183 mg (192 µmol, 97%) of a yellow solid. **^{1}H NMR** (400 MHz, CD_2Cl_2): δ = 9.05 (d, ^3J = 8.1 Hz, 2H), 7.97 (d, ^3J = 8.1 Hz, 2H), 7.77 (s, 2H), 7.28 (t, ^3J = 8.2 Hz, 2H), 7.00 (ddd, ^3J = 8.2 Hz, ^4J = 2.3 Hz, ^4J = 0.9 Hz, 2H), 6.51 (ddd, ^3J = 8.3 Hz, ^4J = 2.3 Hz, ^4J = 0.9 Hz, 2H), 5.80 (t, ^4J = 2.3 Hz, 2H), 4.32–4.20 (m, 8H), 3.66–3.56 (m, 4H), 1.78–1.69 (m, 8H), 1.60–1.55 (m, 4H), 1.50–1.20 (m, 12H), 1.00–0.93 (m, 12H). **^{13}C NMR** (101 MHz, CD_2Cl_2): δ = 168.6, 167.9, 160.9, 158.3, 151.3, 132.4, 132.3, 131.1, 130.6, 130.3, 129.7, 127.8, 127.5, 125.8, 125.0, 111.2, 108.7, 102.6, 68.0, 66.0, 65.8, 31.0, 30.9, 29.4, 26.3, 19.63, 19.58, 13.95, 13.93. **HRMS** (ESI, positive, acetonitrile/chloroform): (*m/z*) $[M+Na]^+$, calcd. for $C_{58}H_{62}NaO_{12}^+$: 973.4134; found: 973.4111. **mp.**: 151–154 °C.

rac-1,7-(3,3'-(hexan-1,6-diylbis(oxy))diphenolate)-perylene-3,4:9,10-tetracarboxylic bisanhydride (57)

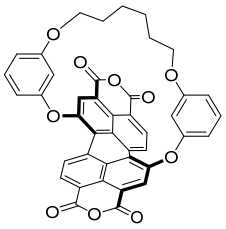
mixture of ***M/P*** isomers

Compound **38** (39.9 mg, 42.0 µmol) and *p*-TsOH · H_2O (89.4 mg, 470 µmol) were dissolved in toluene (7 mL) and stirred for 19 h at 100 °C. After cooling the mixture down to room temperature, the solvent was removed under reduced pressure. Water (10 mL) was added and the mixture sonicated for 5 min. The supernatant water was removed by centrifugation. The washing procedure was repeated twice to obtain a red solid, which was used without further purification. **Yield**: 29.0 mg (42.0 µmol, quant.) of a red solid. **^{1}H NMR** (400 MHz, $CDCl_3$): δ = 9.43 (d, ^3J = 8.2 Hz, 2H), 8.64 (d, ^3J = 8.2 Hz, 2H), 8.46 (s, 2H), 7.35 (t, ^3J = 8.3 Hz, 2H), 7.08 (ddd, ^3J = 8.3 Hz, ^4J = 2.3 Hz, ^4J = 0.9 Hz, 2H), 6.55 (ddd, ^3J = 8.3 Hz, ^4J = 2.3 Hz, ^4J = 0.9 Hz, 2H), 5.58 (t, ^4J = 2.3 Hz, 2H), 3.61–3.49 (m, 4H), 1.61–1.55 (m, 4H),

1.26–1.19 (m, 4H). **MS** (MALDI-Tof, positive, DCTB 1:3 in chloroform): (*m/z*) $[M]^+$, calcd. for $C_{42}H_{26}O_{10}^+$: 690.15260; found: 690.15214. **mp**.: 200 °C.

***(M/P)-R-N,N'*-(1-phenylethylamine)-1,7-(3,3'-(hexan-1,6-diylbis(oxy))diphenolate)-perylene-3,4:9,10-tetracarboxylic acid bisimide (39a)**

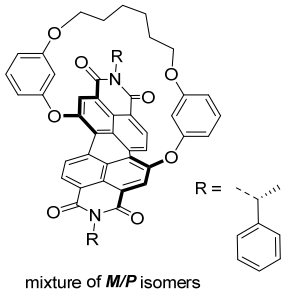

Racemic perylene bisanhydride **57** (164 mg, 237 µmol), *R*-phenylethylamine (1.50 mL, 1.44 g, 11.9 mmol) and $Zn(OAc)_2$ (117 mg, 638 µmol) were mixed together in freshly distilled quinoline (4.5 mL) and stirred for 5 h at 140 °C under a nitrogen atmosphere. After being cooled down to room temperature, the reaction mixture was diluted with DCM (50 mL) and washed with 1 M HCl (4 × 60 mL). The organic layer was dried over Na_2SO_4 and the solvent removed under reduced pressure. The crude product was purified by column chromatography (silica gel, DCM). The product was dissolved in a minimum amount of chloroform and precipitated by the addition of methanol. The precipitate was washed three times with *n*-hexane to give a red solid. The resulting diastereomers were separated by chiral HPLC (Reprosil, DCM:*n*-hexane 55:45, flow rate: 6.5 mL/min , see figure S28c)). **Yield**: 194 mg (216 µmol, 90%) of a red solid (isomeric mixture).

HRMS (ESI, positive, acetonitrile/chloroform): (*m/z*) $[M+Na]^+$, calcd. for $C_{58}H_{44}N_2NaO_8^+$: 919.29899; found: 919.29712. **Isomer 39a-*P***: Retention time (Trentec, Reprosil 100 chiral-NR, $\varnothing = 0.8$ cm, DCM/*n*-hexane (55:45), flow: 1.0 mL/min): 12.4 min; λ_{max} ($\Delta\varepsilon$): 528 nm (+ 46 M^{-1} cm^{-1}). **39a-*M***: Retention time (Trentec, Reprosil 100 chiral-NR, $\varnothing$ = 0.8 cm, DCM/*n*-hexane (55:45), flow: 1.0 mL/min): 13.6 min; λ_{max} ($\Delta\varepsilon$): 528 nm (– 48 M^{-1} cm^{-1}). The stereochemical assignment of the isolated diastereomers was achieved by comparison of the CD spectra with those of the previously reported, structurally similar, epimerically pure *P*- and *M*- configured macrocyclic PBIs.[179] **Isomer 39a-*P*: ^{1}H NMR** (400 MHz, CD_2Cl_2): $\delta = 9.37$ (d, $^3J = 8.3$ Hz, 2H), 8.52 (d, $^3J = 8.3$ Hz, 2H), 8.37 (s, 2H), 7.46–7.44 (m, 4H), 7.32–7.27 (m, 6H), 7.24–7.22 (m, 2H), 7.06 (ddd, $^3J = 8.2$ Hz, $^4J = 2.5$ Hz, $^4J = 0.9$ Hz, 2H), 6.50–6.47 (m, 4H), 5.66 (t, $^4J = 2.4$ Hz, 2H), 3.57–3.50 (m, 4H), 1.95 (d, $^3J = 7.1$ Hz, 6H), 1.56–1.5 (m, 4H), 1.21–1.16 (m, 4H). **^{13}C NMR** (101 MHz, CD_2Cl_2): δ = 163.2, 162.7, 160.5, 157.8, 153.3, 140.8, 132.5, 130.66, 130.57, 129.3, 129.0, 128.4, 128.1, 127.0, 126.9, 126.7, 126.4, 125.1, 123.1, 111.0, 108.6, 101.6, 67.6, 50.3, 28.9, 26.0, 16.0. **mp.:** 216–218 °C. **UV/vis** ($CHCl_3$, c_T = 10

µM, nm): λ_{max} (ε_{max}, M^{-1} cm^{-1}) = 528 (51000). **Fluorescence** ($CHCl_3$, nm): λ_{max} (λ_{ex}) = 548 (490). **CD** ($CHCl_3$, nm): λ_{max} ($\Delta\varepsilon_{max}$, M^{-1} cm^{-1}): 528 (47). **Isomer 39a-*M*: ^{1}H NMR** (400 MHz, CD_2Cl_2): δ = 9.31 (d, ^3J = 8.3 Hz, 2H), 8.52 (d, ^3J = 8.3 Hz, 2H), 8.27 (s, 2H), 7.45–7.43 (m, 4H), 7.30–7.26 (m, 6H), 7.21–7.19 (m, 2H), 7.03 (ddd, ^3J = 8.2 Hz, ^4J = 2.5 Hz, ^4J = 0.9 Hz, 2H), 6.50–6.44 (m, 4H), 5.57 (t, ^3J = 2.4 Hz, 2H), 3.51–3.44 (m, 4H), 1.94 (d, ^3J = 7.1 Hz, 6H), 1.50–1.48 (m, 4H), 1.14–1.10 (m, 4H). **^{13}C NMR** (101 MHz, CD_2Cl_2): δ = 163.3, 162.5, 160.4, 157.7, 153.2, 140.8, 132.4, 130.7, 129.1, 128.9, 128.3, 128.1, 127.1, 126.9, 126.6, 126.3, 125.1, 123.0, 111.0, 108.6, 101.5, 67.6, 50.3, 28.9, 25.9, 16.0. **mp.:** 204–207 °C. **UV/vis** ($CHCl_3$, c_T = 10 µM, nm): λ_{max} (ε_{max} M^{-1} cm^{-1}) = 528 (51000). **Fluorescence** ($CHCl_3$, nm): λ_{max} ($\lambda_{ex,\,nm}$) = 548 (490). **CD** ($CHCl_3$, nm): λ_{max} ($\Delta\varepsilon_{max}$, M^{-1} cm^{-1}): 528 (–48).

(*P/M*)-1,7-(3,3'-(hexane-1,6-diylbis(oxy))diphenolate) perylene-3,4:9,10-tetracarboxylic bisanhydride (57-*P*/57-*M*)

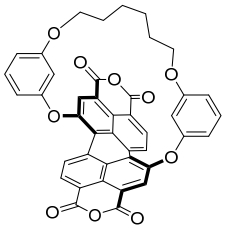

57-*P*: Perylenbisimide **39a-*P*** (152 mg, 169 µmol) was stirred together with KOH (488 mg, 8.70 mmol) in *tert*-butanol (32 mL) under a nitrogen atmosphere for 2 h at 90 °C. The reaction mixture was cooled down to room temperature. Subsequently, 1 M HCl (32 mL) was added to the mixture and it was stirred for 15 min. The supernatant solution was removed after centrifuging. **Yield**: 83.5 mg (121 µmol, 72%) of a red solid. **^{1}H NMR** (400 MHz, $CDCl_3$): δ = 9.43 (d, ^3J = 8.2 Hz, 2H), 8.64 (d, ^3J = 8.2 Hz, 2H), 8.46 (s, 2H), 7.35 (t, ^3J = 8.3 Hz, 2H), 7.08 (ddd, ^3J = 8.3 Hz, ^4J = 2.3 Hz, ^4J = 0.9 Hz, 2H), 6.55 (ddd, ^3J = 8.3 Hz, ^4J = 2.3 Hz, ^4J = 0.9 Hz, 2H), 5.58 (t, ^4J = 2.3 Hz, 2H), 3.61–3.49 (m, 4H), 1.61–1.55 (m, 4H), 1.26–1.19 (m, 4H). **^{1}H NMR** is in accordance with the spectral data obtained from the racemic compound **57**. **m.p.:** 201 °C.

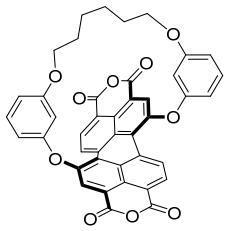

57-*M*: The synthesis was carried out analogue to the synthesis of **57-*P*** with perylenbisimide **39a-*M*** (118 mg, 132 µmol) and KOH (386 mg, 6.88 mmol) in *tert*-butanol (25 mL). **Yield**: 81.8 mg (118 µmol, 90%) of a red solid. **^{1}H NMR** (400 MHz, $CDCl_3$): δ = 9.43 (d, ^3J = 8.2 Hz, 2H), 8.64 (d, ^3J = 8.2 Hz, 2H), 8.46 (s, 2H), 7.35 (t, ^3J = 8.3 Hz, 2H), 7.08 (ddd, ^3J = 8.3 Hz, ^4J = 2.3 Hz, ^4J = 0.9 Hz, 2H), 6.55 (ddd, ^3J = 8.3 Hz, ^4J = 2.3 Hz, ^4J = 0.9 Hz, 2H), 5.58 (t,

^4J = 2.3 Hz, 2H), 3.61–3.49 (m, 4H), 1.61–1.55 (m, 4H), 1.26–1.19 (m, 4H). **^{1}H NMR** is in accordance with the spectral data obtained from the racemic compound **57**. **m.p.:** 200 °C.

rac-N,N'-benzylamine-1,7-(3,3'-(hexan-1,6-diylbis(oxy))diphenolate)-perylene-3,4:9,10-tetracarboxylic acid bisimide (39b)

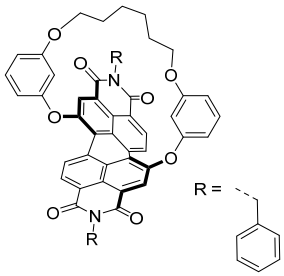

mixture of ***M/P*** isomers

Racemic perylene bisanhydride **57** (29.0 mg, 42.0 µmol), benzylamine (500 µL, 492 mg, 4.59 mmol) and $Zn(OAc)_2$ (27.0 mg, 147 µmol) were dissolved in freshly distilled quinolone (1.5 mL). The solution was stirred for 5.5 h at 140 °C under a nitrogen atmosphere. Afterwards, the reaction was cooled down to room temperature and DCM (80 mL) was added to the mixture, which was subsequently washed with 1 M HCl (2 × 100 mL). The organic layer was dried over Na_2SO_4 and the solvent removed under reduced pressure. The red solid was dissolved in a minimum amount of DCM and was precipitated upon the addition of methanol. The precipitate was separated from the supernatant by centrifuging the mixture and further purified by GPC ($CHCl_3$, flow rate: 6.4 mL min^{-1}). **Yield**: 13.0 mg (15.0 µmol, 36%) of a red solid. **^{1}H NMR** (400 MHz, TCE-d_2): δ = 9.35 (d, ^3J = 8.2 Hz, 2H), 8.60 (d, ^3J = 8.2 Hz, 2H), 8.42 (s, 2H), 7.54–7.52 (m, 4H), 7.35–7.28 (m, 8H), 7.08 (dd, ^3J = 8.3 Hz, ^4J = 2.2 Hz, 2H), 6.51 (dd, ^3J = 8.3 Hz, ^4J = 2.2 Hz, 2H), 5.59 (t, ^3J = 8.3 Hz, 2 H), 5.34 (s, 4H), 3.55–3.47 (m, 4H), 1.55–1.47 (m, 4H), 1.18–1.12 (m, 4H). **^{13}C NMR** (101 MHz, TCE-d_2): δ = 163.6, 163.0, 160.4, 157.8, 153.5, 137.0, 132.7, 131.3, 131.2, 129.4, 129.2, 129.1, 128.9, 128.0, 127.1, 126.3, 124.7, 122.8, 111.4, 109.3, 101.7, 67.9, 44.0, 29.0, 26.3. **HRMS** (ESI, positive, acetonitrile/chloroform): (*m/z*) $[M+Na]^+$, calc. for $C_{56}H_{40}N_2NaO_8^+$: 891.26769; found: 891.26888. **mp.:** >300 °C. **UV/vis** ($CHCl_3$, c_T = 10 µM, nm): λ_{max} (ε_{max}, M^{-1} cm^{-1}) = 530 (55000). **Fluorescence** ($CHCl_3$, nm): λ_{max} (λ_{ex}) = 550 (490).

Cyclophane 1-*PP*:

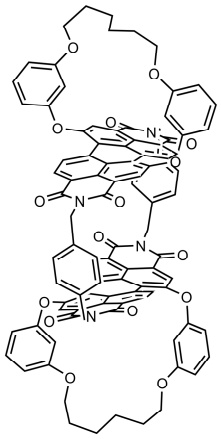

A mixture of perylene bisanhydride **57-*P*** (82.5 mg, 119 µmol), *para*-xylylenediamine (16.3 mg, 120 µmol) and imidazole (820 mg, 12.0 mmol) were stirred in toluene (200 mL) at 120 °C under a nitrogen atmosphere for 16 h. After cooling down to room temperature, the reaction mixture was washed with 1 M HCl (3 × 50 mL). The combined organic layers were dried over Na_2SO_4 and the organic solvent was removed under reduced pressure. The crude product was purified by column chromatography (chloroform/MeOH, 95.5:0.5) and GPC ($CHCl_3$, flow rate: 6.4 mL/min). The red solid was subsequently dissolved in a minimum amount of chloroform and precipitated by the addition of methanol. The suspension was centrifuged, the supernatant removed and the solid washed with *n*-hexane. **Yield**: 15.9 mg (10.1 µmol, 17%) of a red solid. **^{1}H NMR** (400 MHz, TCE-d_2): δ = 9.05–9.04 (br, 4H), 8.38–8.35 (m, 8H), 7.49 (s, 8H), 7.31 (t, ^3J = 8.1 Hz, 4H), 7.03 (dd, ^3J = 8.4 Hz, ^4J = 1.9 Hz, 4H), 6.52 (dd, ^3J = 8.4 Hz, ^4J = 1.9 Hz, 4H), 5.68 (t, ^3J = 2.1 Hz, 4H), 5.40 (d, ^3J = 13.2 Hz, 4H), 5.22 (d, ^3J = 13.3 Hz, 4H), 3.58–3.50 (m, 8H), 1.58–1.46 (m, 8H), 1.23–1.13 (m, 8H). **^{13}C NMR**: see enantiomeric form (*vide infra*) **HRMS** (ESI, positive, acetonitrile/chloroform): (*m/z*) $[M]^+$, calc. for $C_{100}H_{68}N_4O_{16}^+$: 1581.46639; found: 1581.47067. **mp.:** >300 °C.**UV/vis** ($CHCl_3$, c_T = 10 µM, nm): λ_{max} (ε_{max}, M^{-1} cm^{-1}) = 528 (75000). **Fluorescence** ($CHCl_3$, nm): λ_{max} (λ_{ex}) = 561 (490). **CD** ($CHCl_3$, nm): λ_{max} ($\Delta\varepsilon_{max}$, M^{-1} cm^{-1}): 530 (+94).

Cyclophane 1-*MM:*

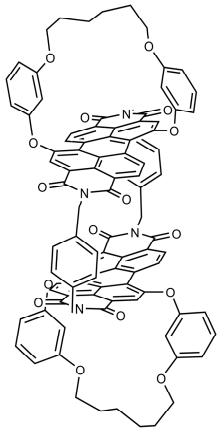

The synthesis was carried out analogue to the synthesis of **1-*PP*** with perylene bisanhydride **57-*M*** (81.4 mg, 118 µmol, (1eq.)), *para*-xylylenediamine (16.1 mg, 118 µmol, (1 eq.)) and imidazole (820 mg, 12.0 mmol) in toluene (200 mL). **Yield**: 16.0 mg (10.1 µmol, 17%) of a red solid. **^{1}H NMR (**400 MHz, TCE-d_2): δ = 9.04–9.03 (br, 4H), 8.38–8.35 (m, 8H), 7.49 (s, 8H), 7.31 (t, ^3J = 8.1 Hz, 4H), 7.03 (dd, ^3J = 8.4 Hz, ^4J = 1.9 Hz 4H), 6.52 (dd, ^3J = 8.4 Hz, ^4J = 1.9 Hz 4H), 5.68 (t, ^3J = 2.1 Hz, 4H), 5.40 (d, ^3J = 13.7 Hz, 4H), 5.22 (d, ^3J = 13.3 Hz, 4H), 3.60–3.48 (m, 8H), 1.60–1.44 (m, 8H), 1.23–1.13 (m, 8H). **^{13}C NMR** (101 MHz, TCE-d_2): δ = 162.8, 162.4, 160.5, 157.6, 153.7, 137.3, 132.4, 131.2, 130.7, 130.6, 129.2, 128.5, 128.3,

126.3, 125.7, 124.6, 122.6, 111.6, 109.5, 101.9, 68.0, 42.8, 29.0, 26.3. **HRMS** (ESI, positive, acetonitrile/chloroform): (*m/z*) $[M+Na]^+$, calc. for $C_{100}H_{68}N_4NaO_{16}^+$: 1603.45225; found: 1603.45260. **mp.:** >300 °C. **UV/vis** ($CHCl_3$, c_T = 10 µM, nm): λ_{max} (ε_{max}, M^{-1} cm^{-1}) = 528 (75000). **Fluorescence** ($CHCl_3$, nm): λ_{max} (λ_{ex}) = 561 (490). ϕ_{fl} ($CHCl_3$) = 0.2 **CD** ($CHCl_3$, nm): λ_{max} ($\Delta\varepsilon_{max}$, M^{-1} cm^{-1}): 530 (–89).

NMR Spectra

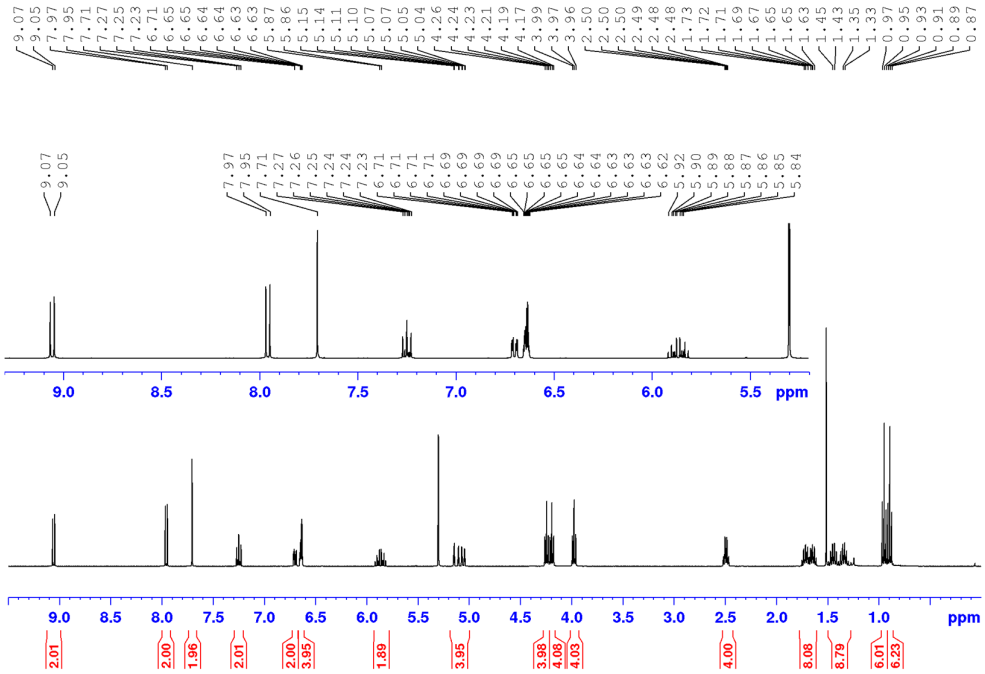

Figure A1. ^{1}H NMR (400 MHz) spectrum of compound **37** in CD_2Cl_2 at 298 K.

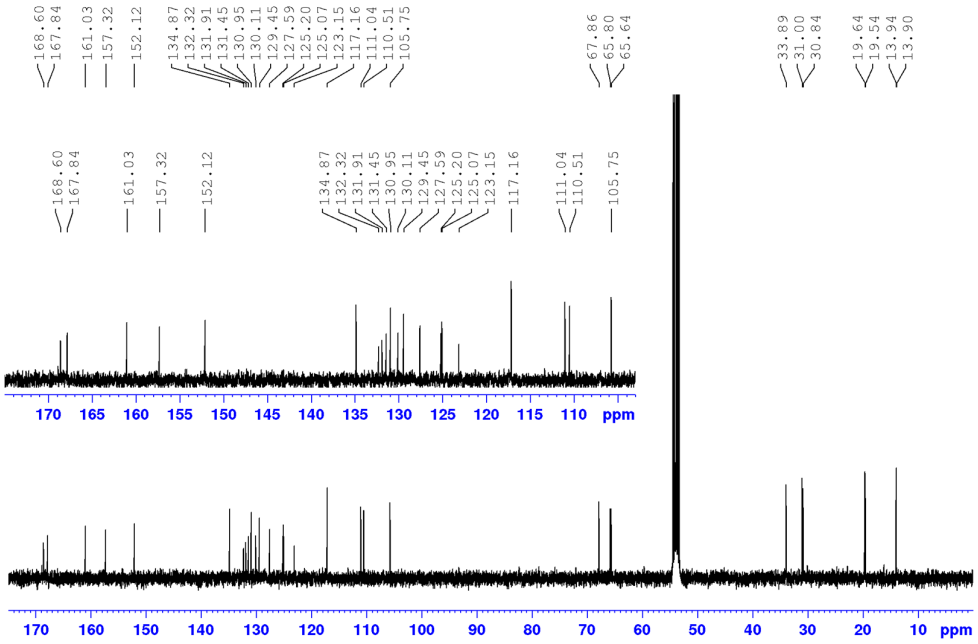

Figure A2. ^{13}C NMR (101 MHz) spectrum of compound **37** in CD_2Cl_2 at 298 K.

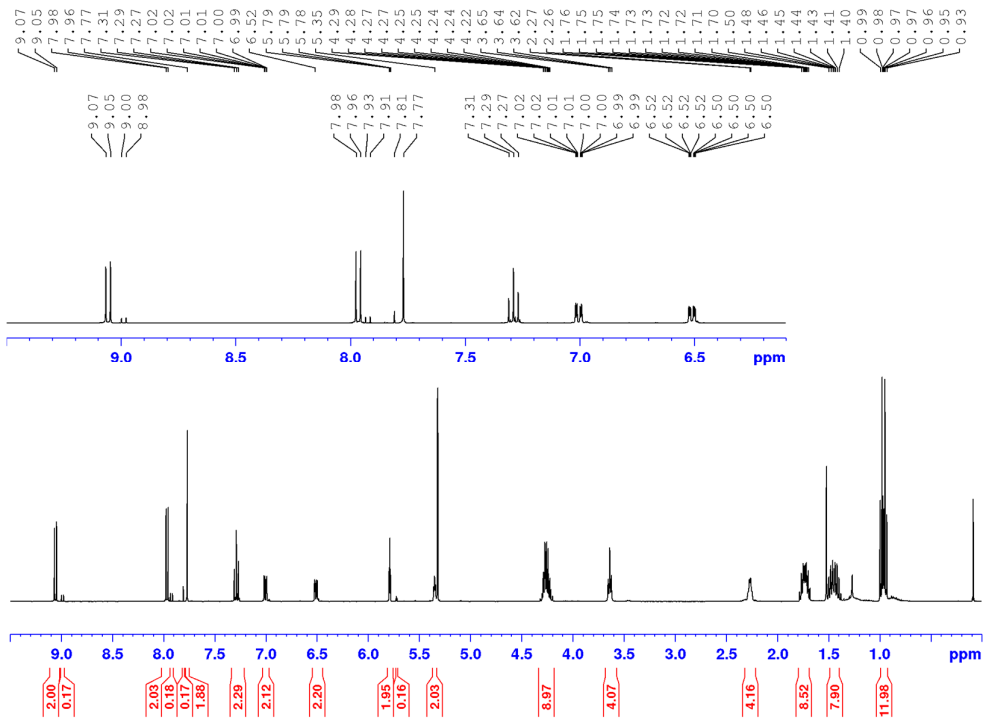

Figure A3. ^{1}H NMR (400 MHz) spectrum of compound **58** in CD_2Cl_2 at 298 K.

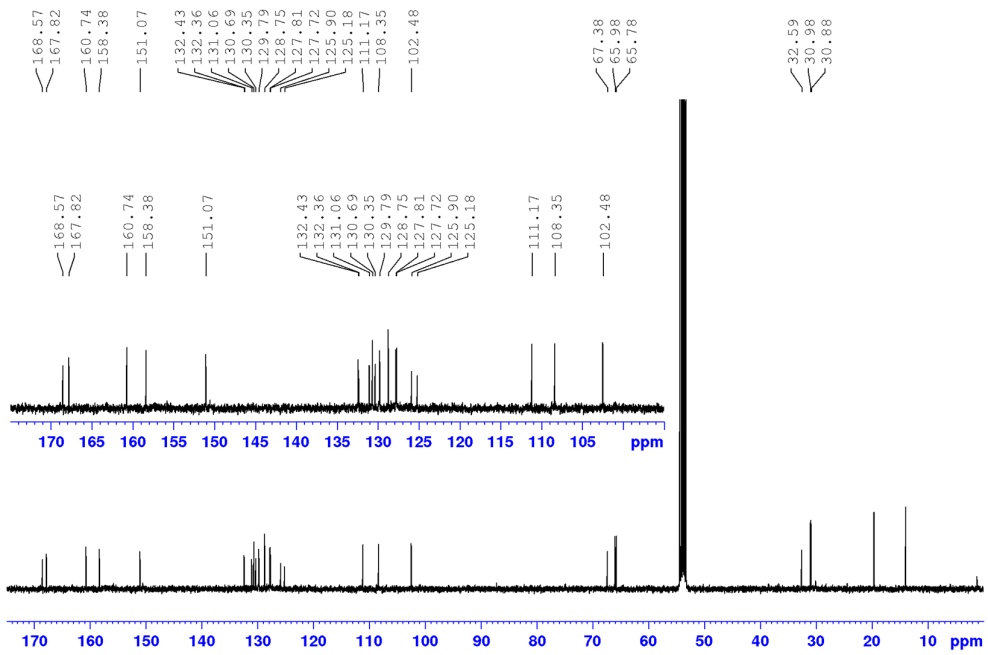

Figure A4. ^{13}C NMR (101 MHz) spectrum of compound **58** in CD_2Cl_2 at 298 K.

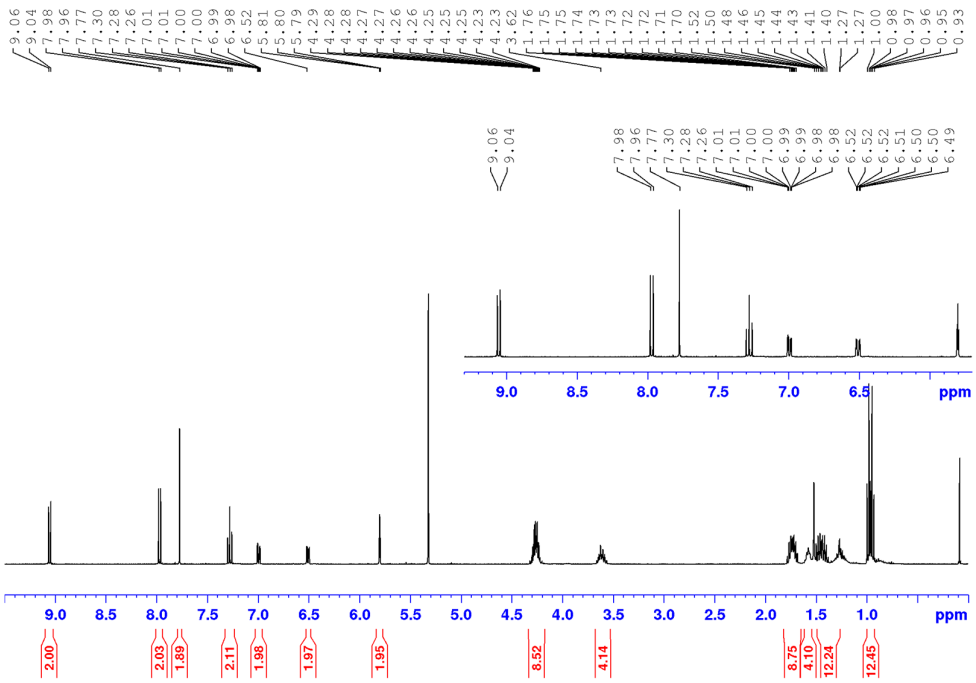

Figure A5. ^{1}H NMR (400 MHz) spectrum of compound **38** in CD_2Cl_2 at 298 K.

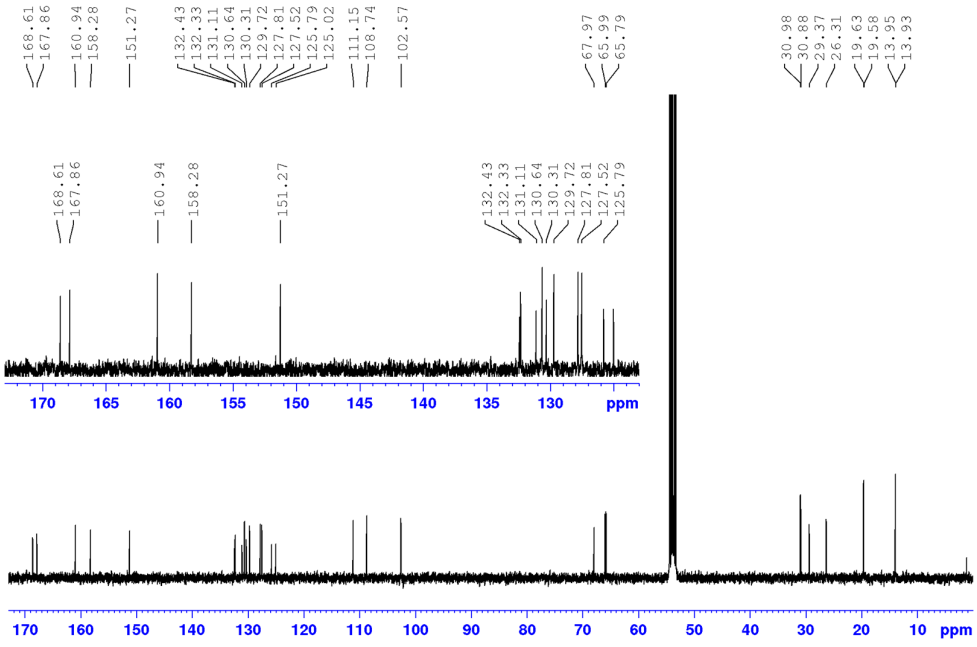

Figure A6. ^{13}C NMR (101 MHz) spectrum of compound **38** in CD_2Cl_2 at 298 K.

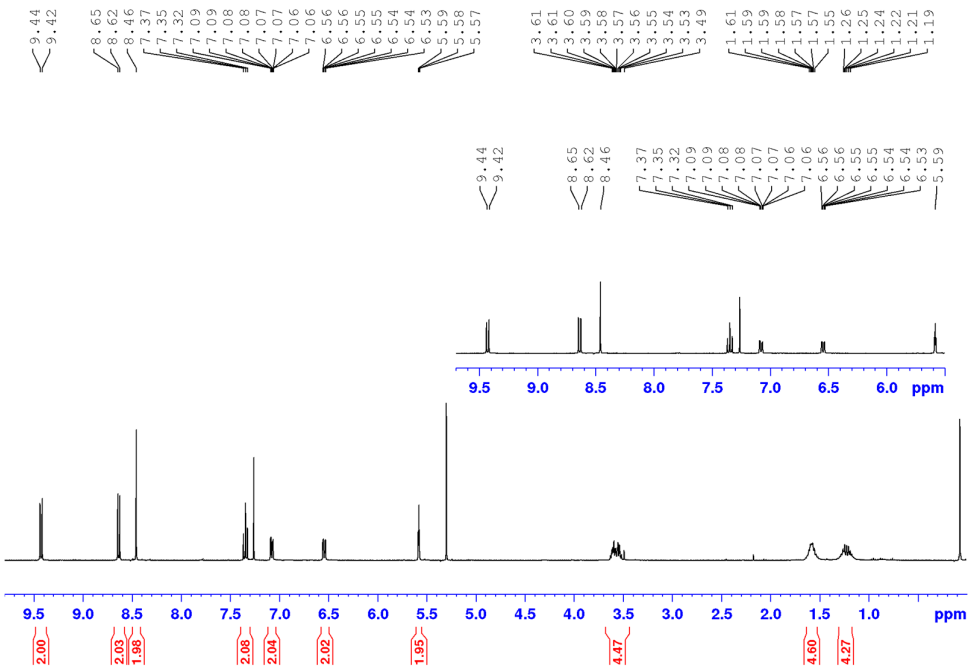

Figure A7. ^{1}H NMR (400 MHz) spectrum of compound **57** in CD_2Cl_2 at 298 K.

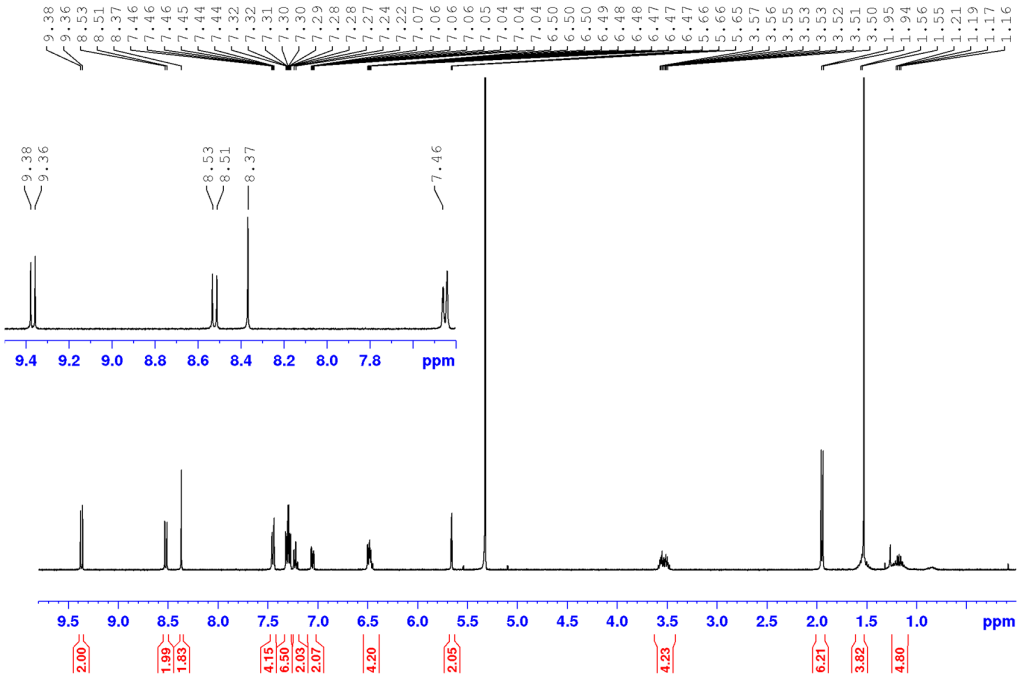

Figure A8. ^{1}H NMR (400 MHz) spectrum of compound **39a-*P*** in CD_2Cl_2 at 298 K.

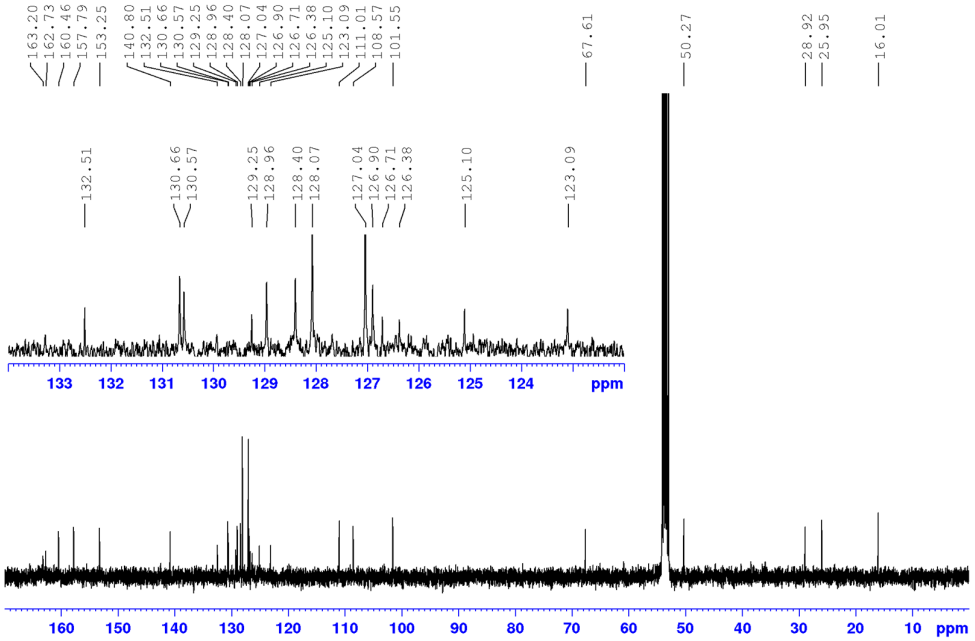

Figure A9. ^{13}C NMR (101 MHz) spectrum of compound **39a-*P*** in CD_2Cl_2 at 298 K.

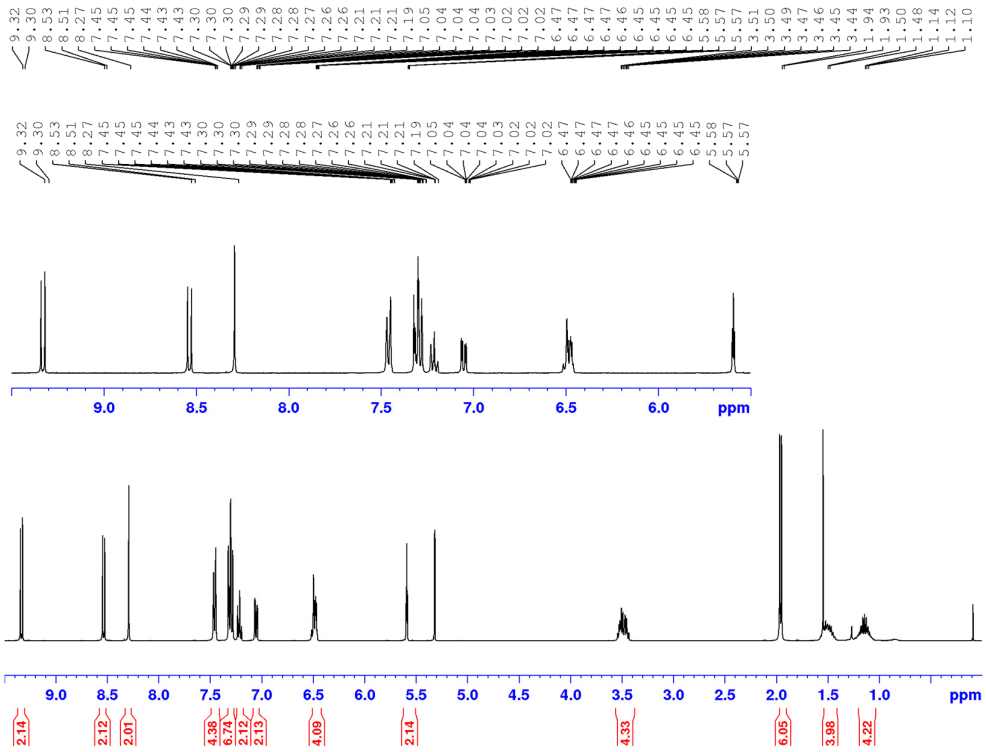

Figure A10. ^{1}H NMR (400 MHz) spectrum of compound **39a-*M*** in CD_2Cl_2 at 298 K.

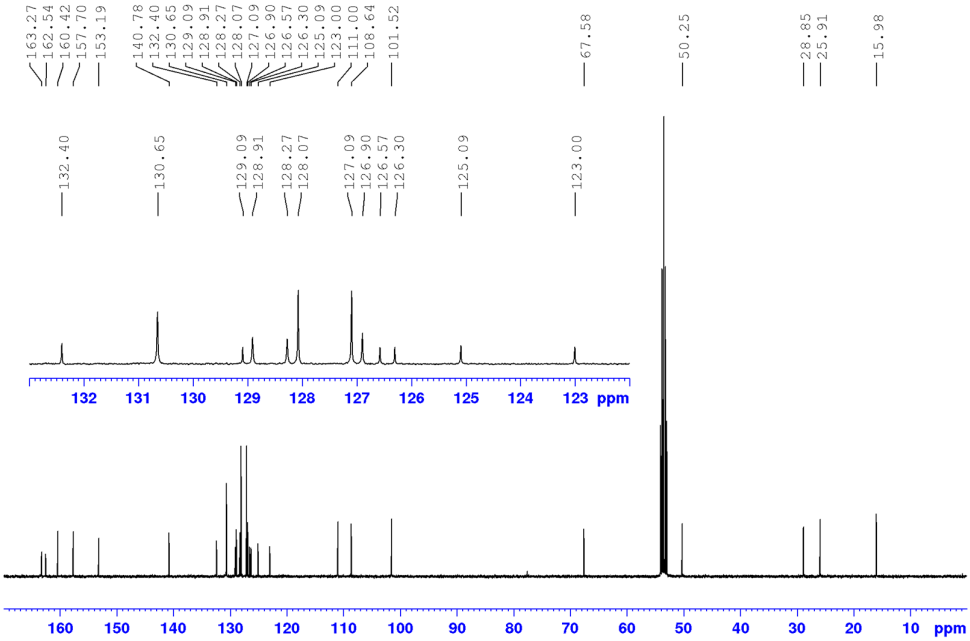

Figure A11. ^{13}C NMR (101 MHz) spectrum of compound **39a-*M*** in CD_2Cl_2 at 298 K.

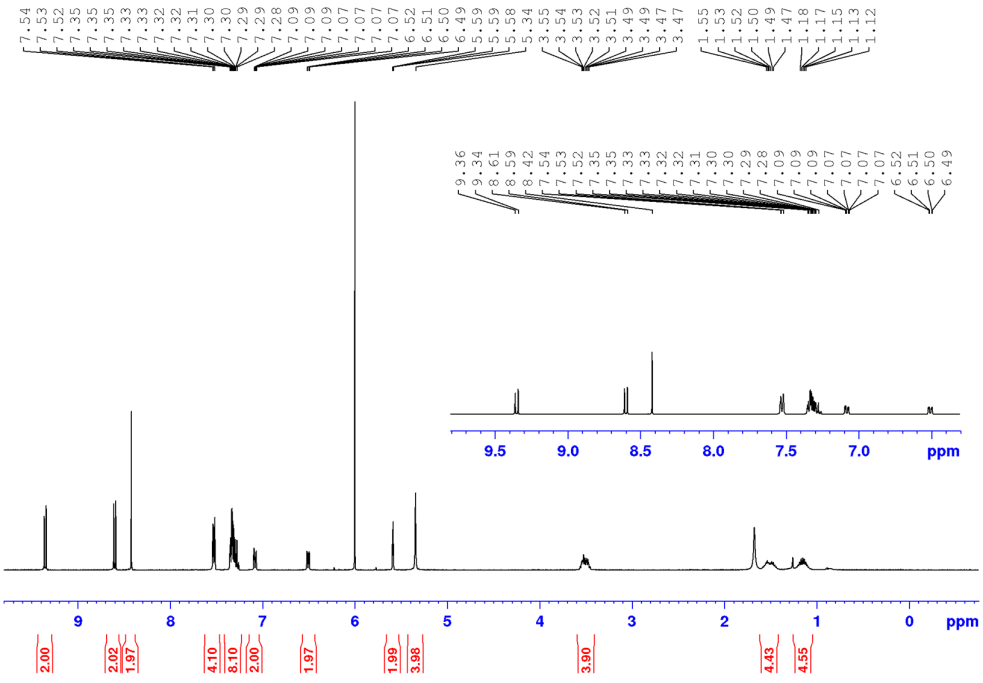

Figure A12. ^{1}H NMR (400 MHz) spectrum of compound **39b** in TCE-d_2 at 298 K.

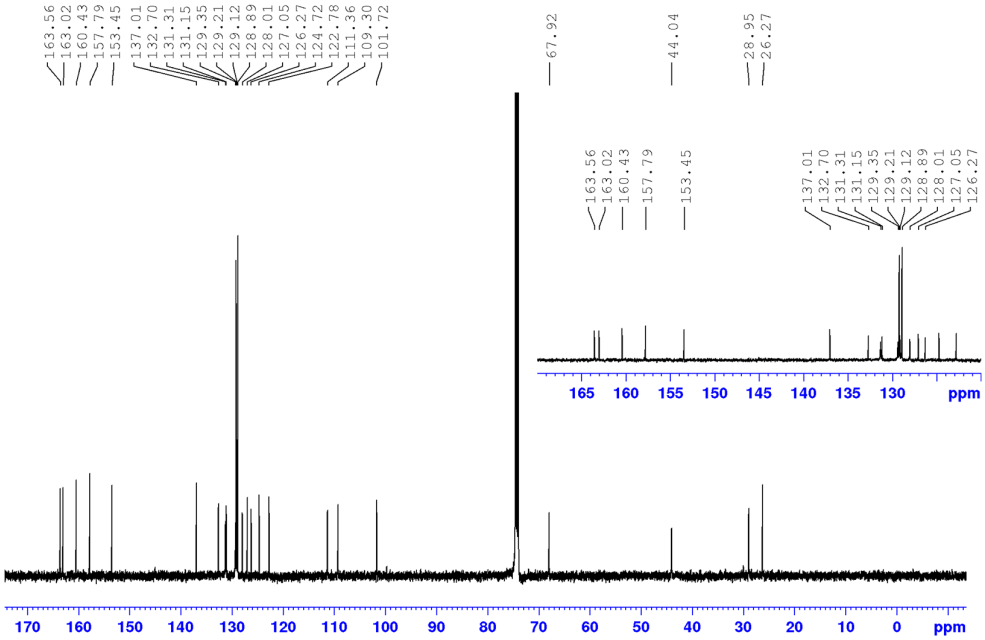

Figure A13. ^{13}C NMR (101 MHz) spectrum of compound **39b** in TCE-d_2 at 298 K.

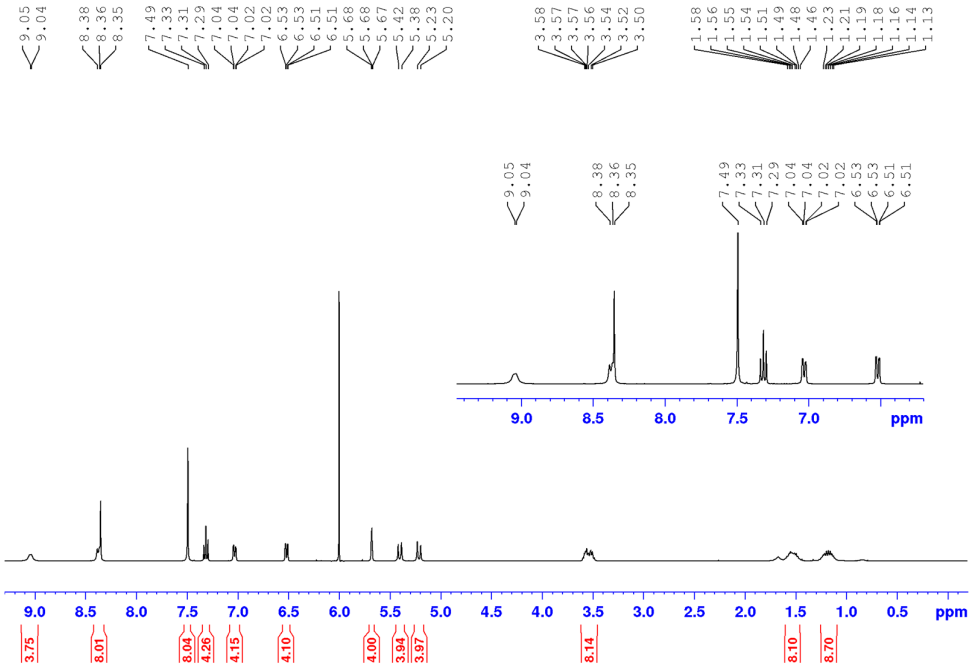

Figure A14. ^{1}H NMR (400 MHz) spectrum of compound **1-*PP*** in TCE-d_2 at 298 K.

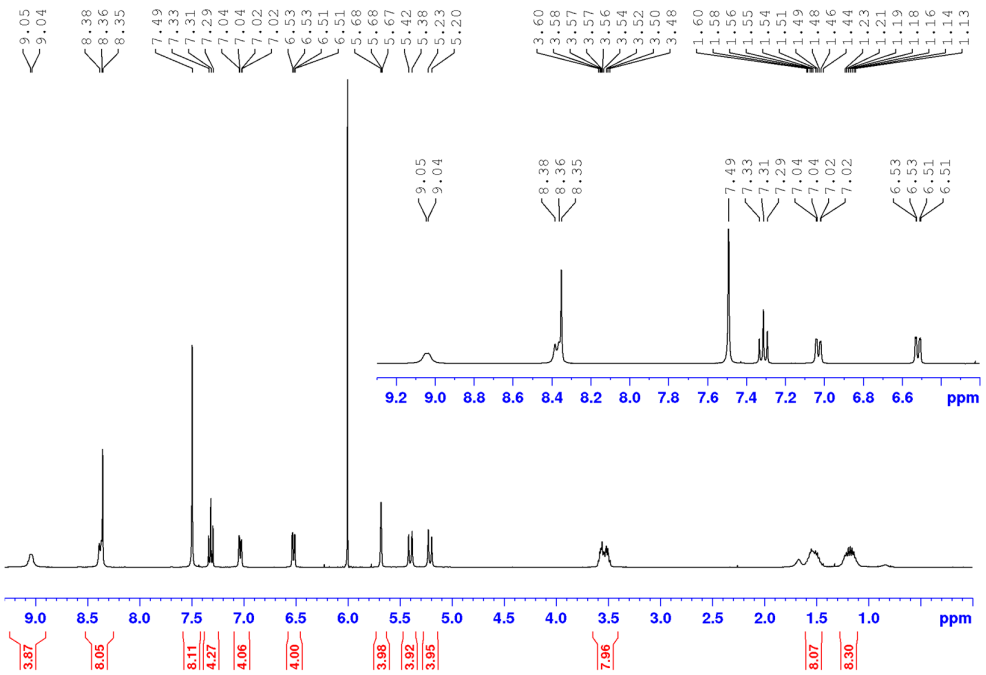

Figure A15. ^{1}H NMR (400 MHz) spectrum of compound **1-*MM*** in TCE-d_2 at 298 K.

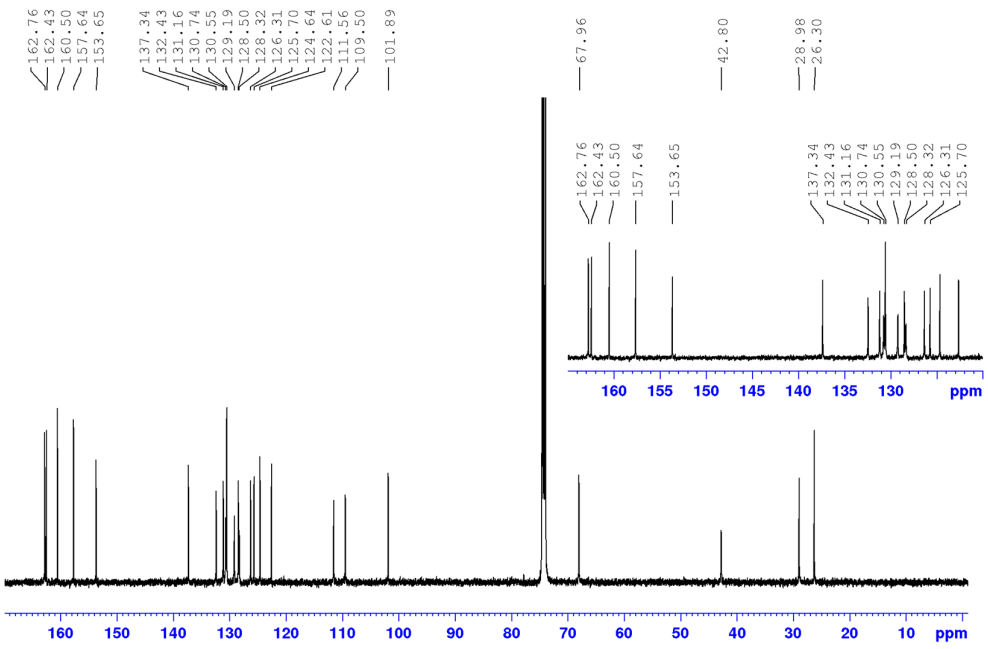

Figure A16. ^{13}C NMR (101 MHz) spectrum of compound **1-*MM*** in TCE-d_2 at 298 K.

Mass Spectra

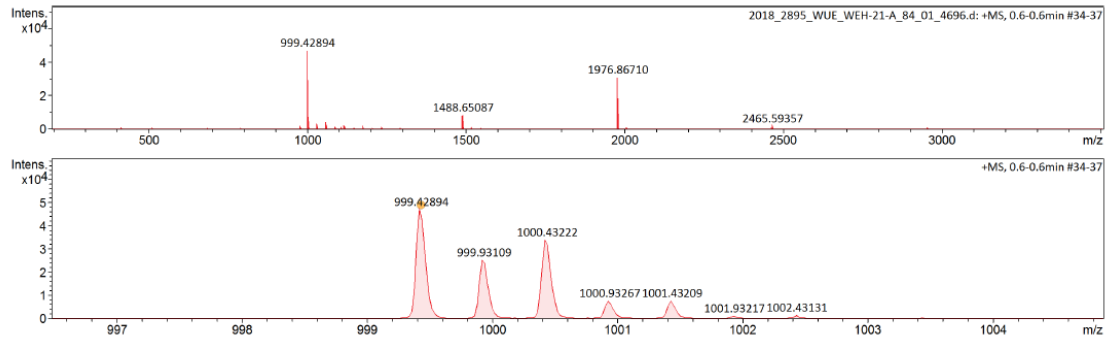

Figure A17. HRMS (ESI, positive, acetonitrile/chloroform) of compound **37**.

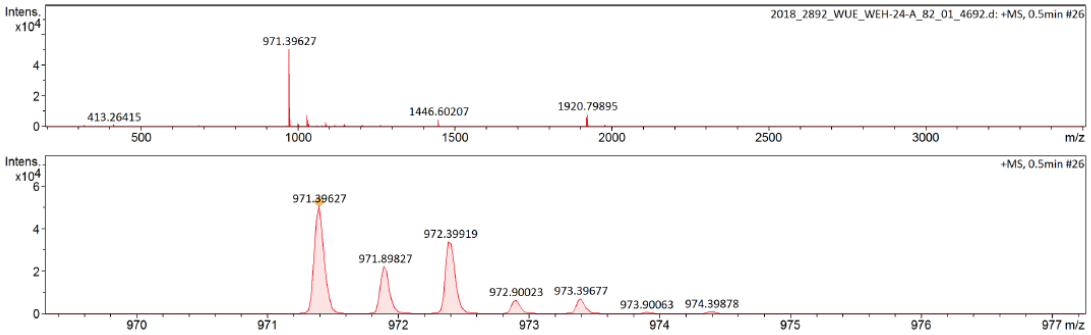

Figure A18. HRMS (ESI, positive, acetonitrile/chloroform) of compound **58**.

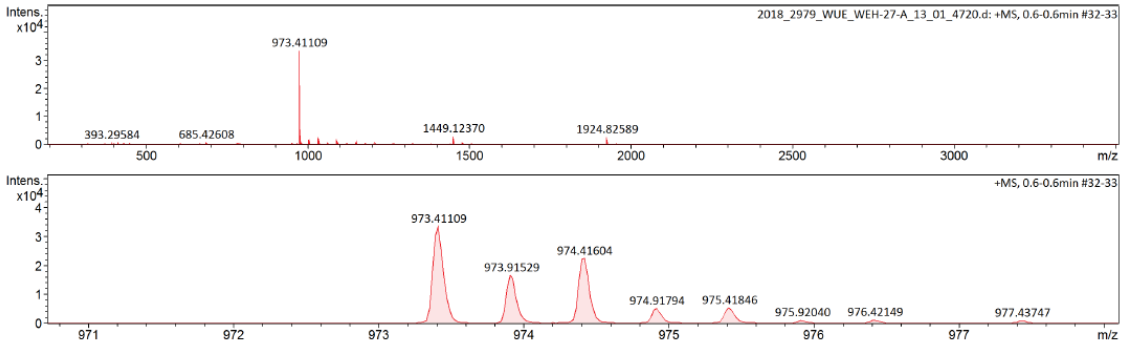

Figure A19. HRMS (ESI, positive, acetonitrile/chloroform) of compound **38**.

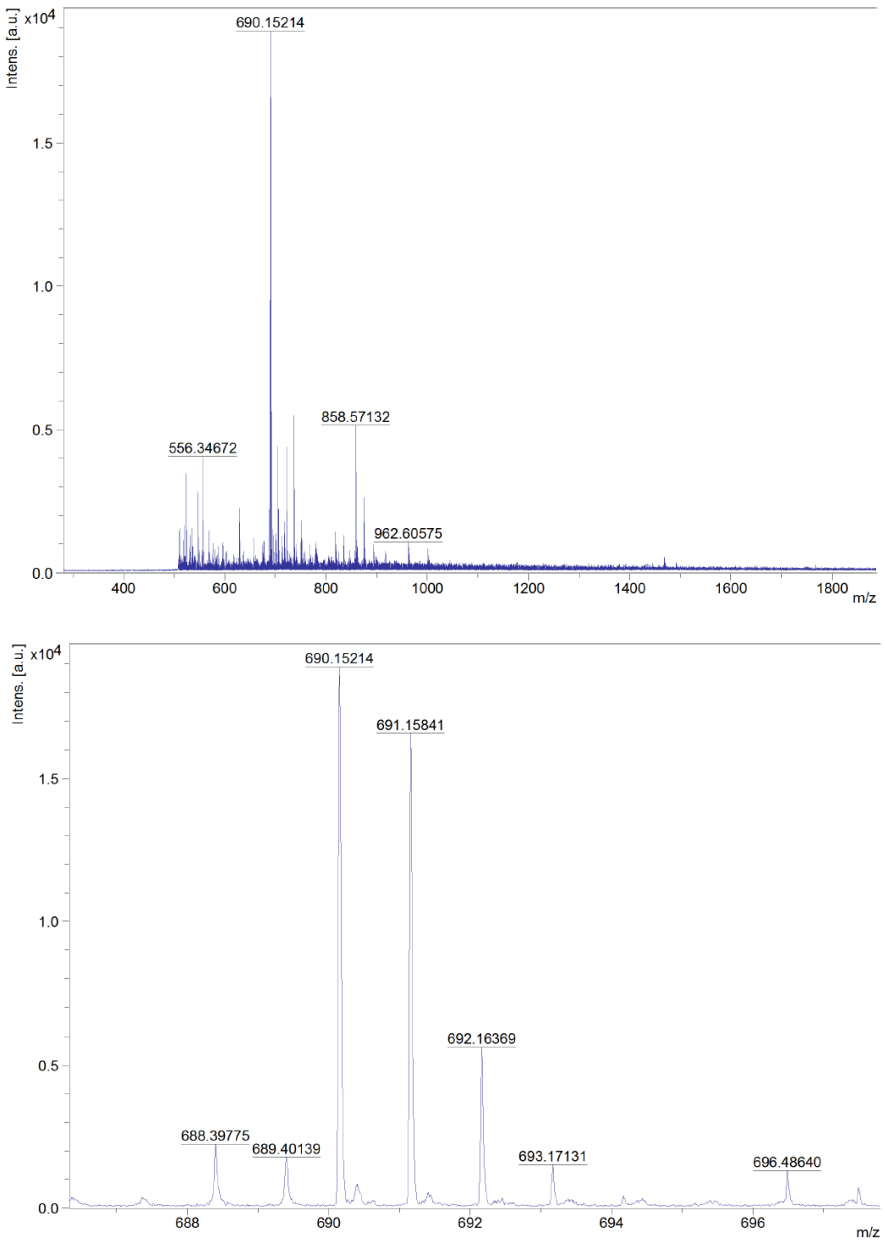

Figure A20. MALDI-TOF (positive, DCTB in chloroform) of compound **57**.

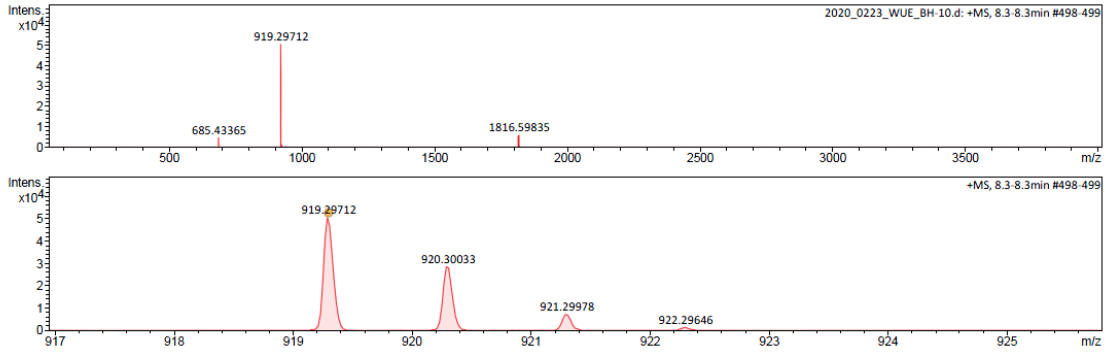

Figure A21. HRMS (ESI, positive, acetonitrile/chloroform) of compound **39a** (diastereomeric mixture).

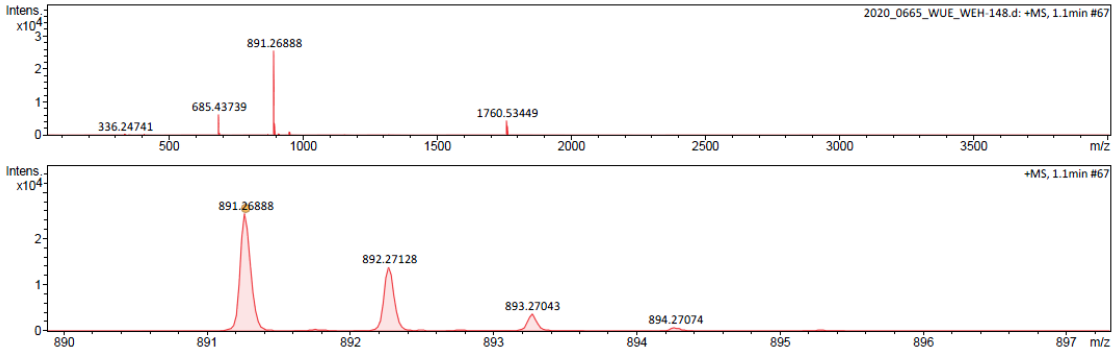

Figure A22. HRMS (ESI, positive, acetonitrile/chloroform) of compound **39b**.

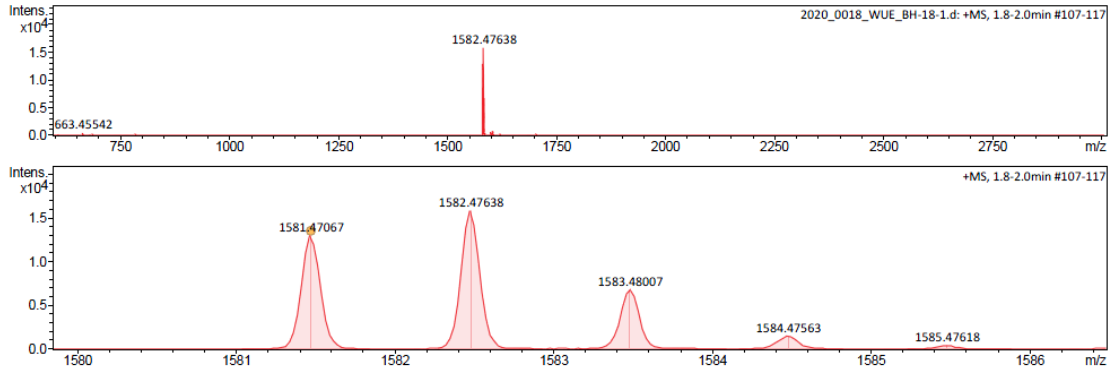

Figure A23. HRMS (ESI, positive, acetonitrile/chloroform) of compound **1-*PP*.**

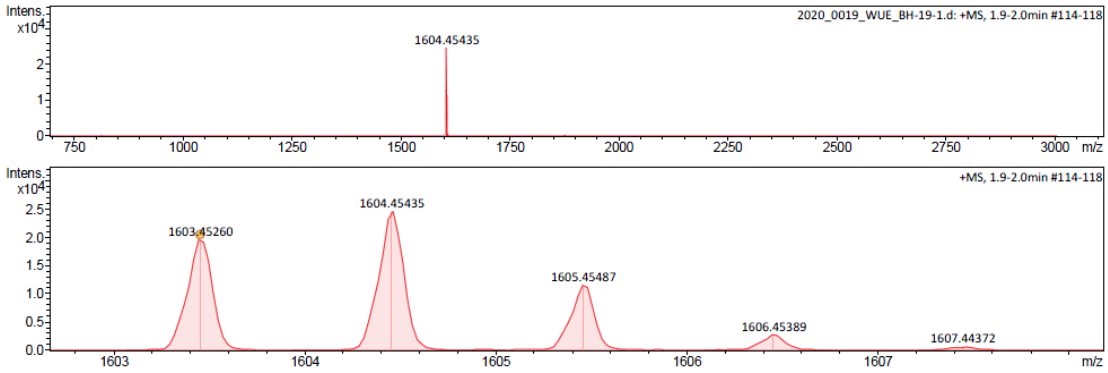

Figure A24. HRMS (ESI, positive, acetonitrile/chloroform) of compound **1-*MM***.

Separation of Diastereomers

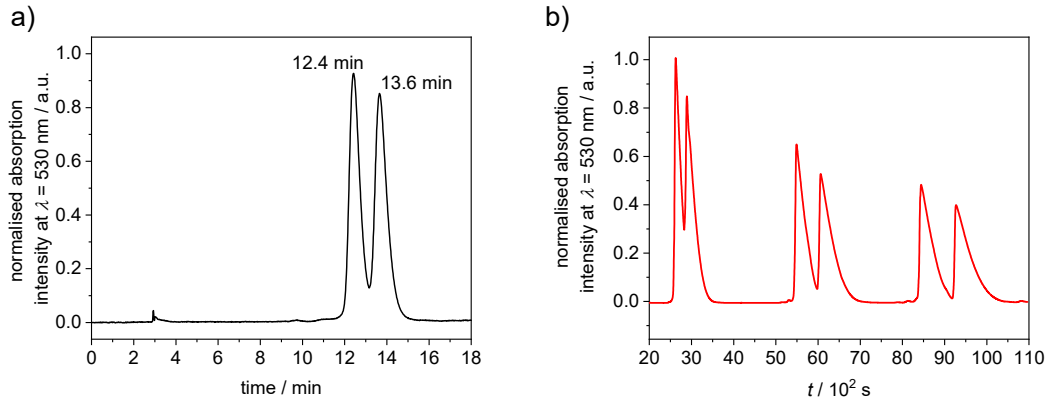

Figure A25. a) Analytical HPLC chromatogram of the separation of **39a-*M*** and **39a-*P*** (flow: 1 mL/min). b) Semipreparative HPLC chromatogram of the separation of **39a-*M*** and **39a-*P*** (flow: 6.5 mL/min). The HPLC was used on recycling mode (three cycles are shown here) with a DCM/*n*-hexane solvent mixture (55:45).

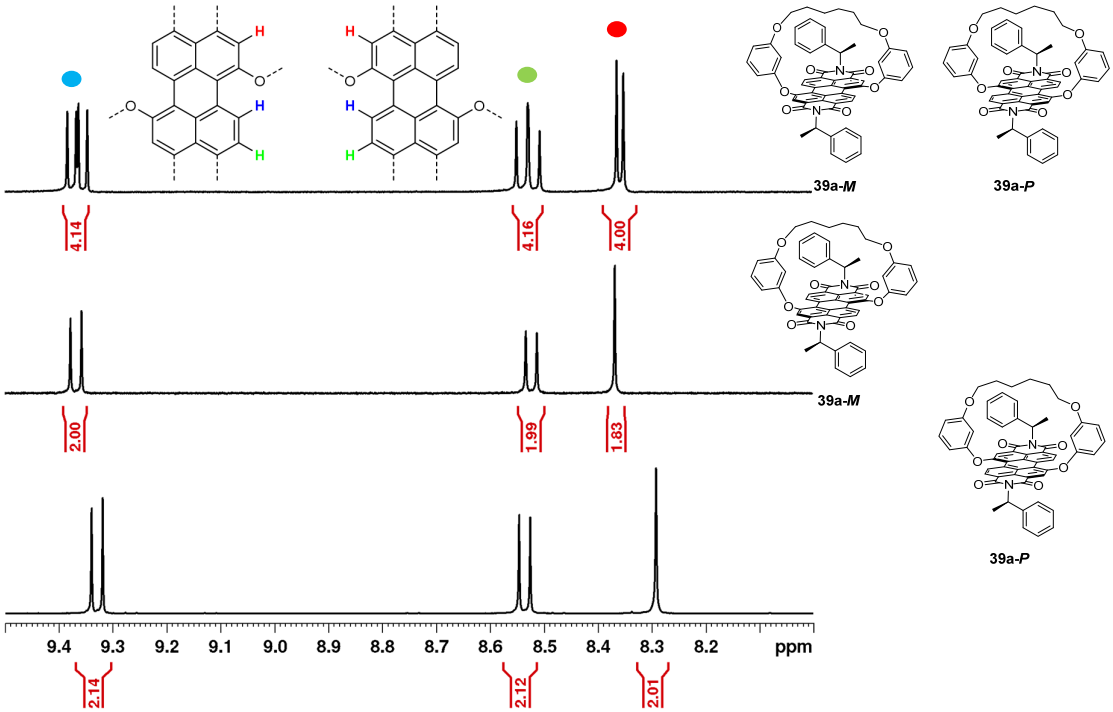

Figure A26. Excerpts of 400 MHz ^{1}H NMR spectrum of the diastereomeric mixture of **39a-*M*** and **39a-*P*** and of the respective isomerically pure compounds after HPLC separation (see Figure A25) at r.t. in $CDCl_3$. Shown are only the perylene protons.

Optical Spectroscopy

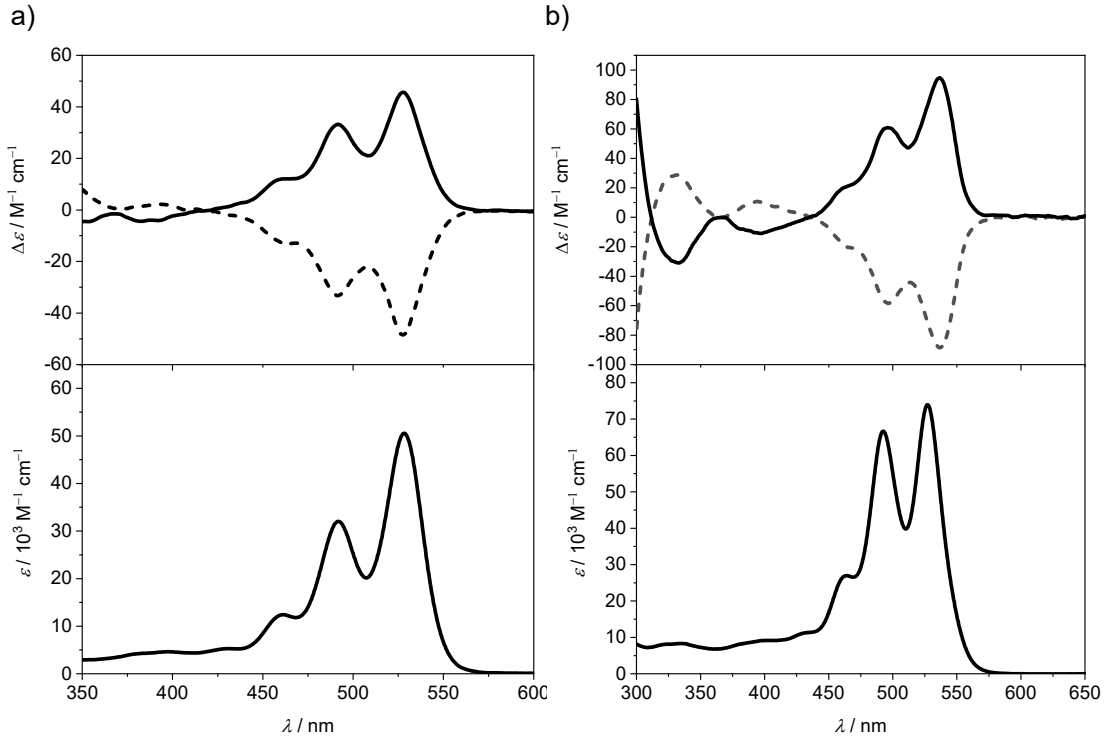

Figure A27. a) CD and UV/vis absorption spectra of **39a-*P*** (solid line) and **39a-*M*** (dashed line) in chloroform at r.t. (c = 30 µM). They behave like pseudo-enantiomers as the imide substituent does not contribute to the optical properties. b) CD and UV/vis absorption spectra of **1-*PP*** (solid lines) and **1-*MM*** (dashed line) in chloroform at r.t. (c = 10 µM).

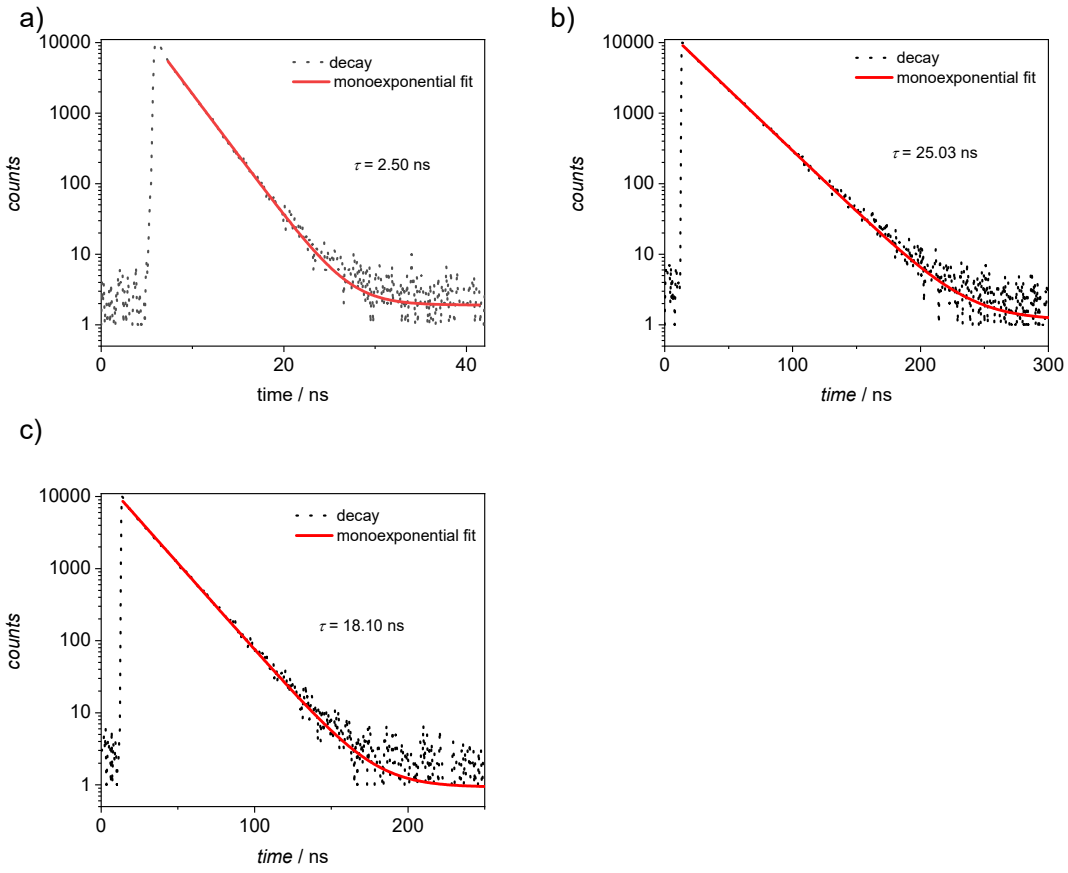

Figure A28. Lifetime measurement (black) of a) free cyclophane **1-*PP*** ($CHCl_3$, 295 K, λ_{ex} = 480 nm, λ_{em} = 545 nm), b) [4]helicene⊂**1-*PP*** ($CHCl_3$, 295 K, λ_{ex} = 480 nm, λ_{em} = 630 nm), c) [5]helicene⊂**1-*PP*** ($CHCl_3$, 295 K, λ_{ex} = 480 nm, λ_{em} = 650 nm). The monoexponential fits are shown in red.

Titration Studies

For the titration experiments, a solution of PBI cyclophane **1-*MM*** or **1-*PP*** and the respective guest in excess (see corresponding graphs for exact amount of the individual guest) was titrated to a solution of the pure cyclophane in the same solvent (mixture) of the same concentration keeping the host concentration constant during the experiment. The UV/vis and fluorescence (λ_{exc} = 490 nm) titration data were fitted to a 1:1 binding model (equation A1, with a_h, a_{hg} and a_{obs}, which are the absorption at a given wavelength of the free host, the host-guest complex and the measured absorption and c_h^0 and c_g^0 as total concentrations of the host and the guest and the variable K_a as binding constant.[143] Note that the conformational lability of [4]helicene allows a direct titration with the racemic mixture as the corresponding racemization barrier is low enough to allow an instantaneous conformational adaption to the cyclophane receptor while [5]helicene had to be used enantiomerically pure in order to avoid kinetic effects.

$$a_{obs} = a_h + \frac{a_{hg}-a_h}{2c_h^0}\left(c_h^0 + c_g^0 + \frac{1}{K_a} \pm \sqrt{\left(c_h^0 + c_g^0 + \frac{1}{K_a}\right)^2 - 4c_h^0 c_g^0}\right) \quad \text{(A1)}$$

For the competitive titration studies in CCl_4 a host solution of a defined concentration was prepared. Phenanthrene, whose binding constant could be determined by direct titration (K_i), was added to this solution in excess as a competitive guest. In order to keep the host concentration and the one of phenanthrene constant, the respective guest solution (with the guest of which the binding constant K_g had to be determined) was prepared from the host-phenanthrene-solution. After the stepwise titration, the obtained data were fitted for competitive systems by means of a nonlinear fit.[208] The script below can be directly implemented in *Origin*[307] to fit the data at a selected wavelength. For details on the parameters see the corresponding reference.[208]

```
double a = Ki*Kg;
double b = Ki+Kg+Ki*Kg*It+Ki*Kg*x-Ki*Kg*Ht;
double c = 1+Ki*It+Kg*x-(Ki+Kg)*Ht;
double d = -Ht;
double H = Ht;
for(double step=1.0; abs(step)>1E-15; H=H-step) {
        step = (a*H*H*H+b*H*H+c*H+d)/(3*a*H*H+2*b*H+c);
}
y=Eh*H+Ehi*(Ki*H/(1+Ki*H))*It+Ehg*(Kg*H/(1+Kg*H))*x;
```

1. Chloroform as solvent

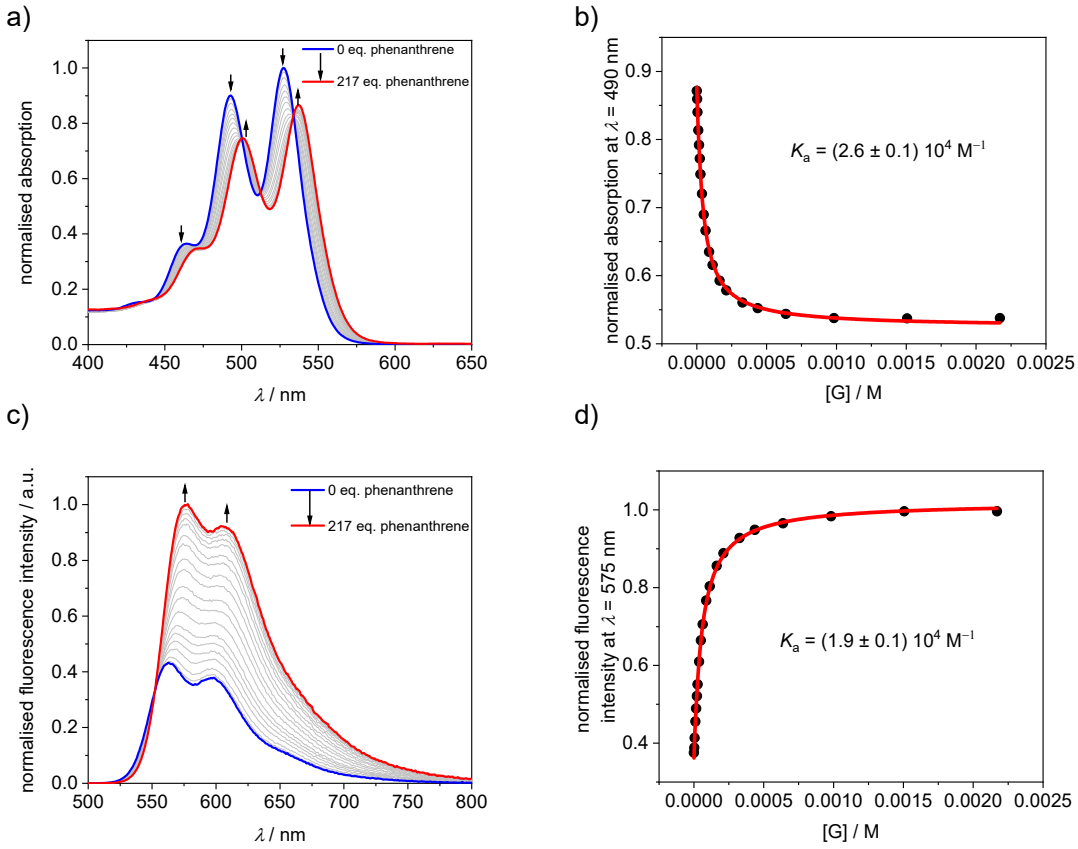

Figure A29. a) UV/vis spectra of cyclophane **1-*PP*** in $CHCl_3$ at 22 °C ($c = 10 \times 10^{-6}$ M) upon the addition of phenanthrene as a guest and b) the resulting plot of the absorption at $\lambda = 490$ nm with nonlinear curve fit (1:1 binding model, red curve). c) Fluorescence spectra of cyclophane **1-*PP*** in $CHCl_3$ at 22 °C ($c = 10 \times 10^{-6}$ M) upon the addition of phenanthrene as a guest and d) the resulting plot of fluorescence intensity at $\lambda = 575$ nm with nonlinear curve fit (1:1 binding model, red curve).

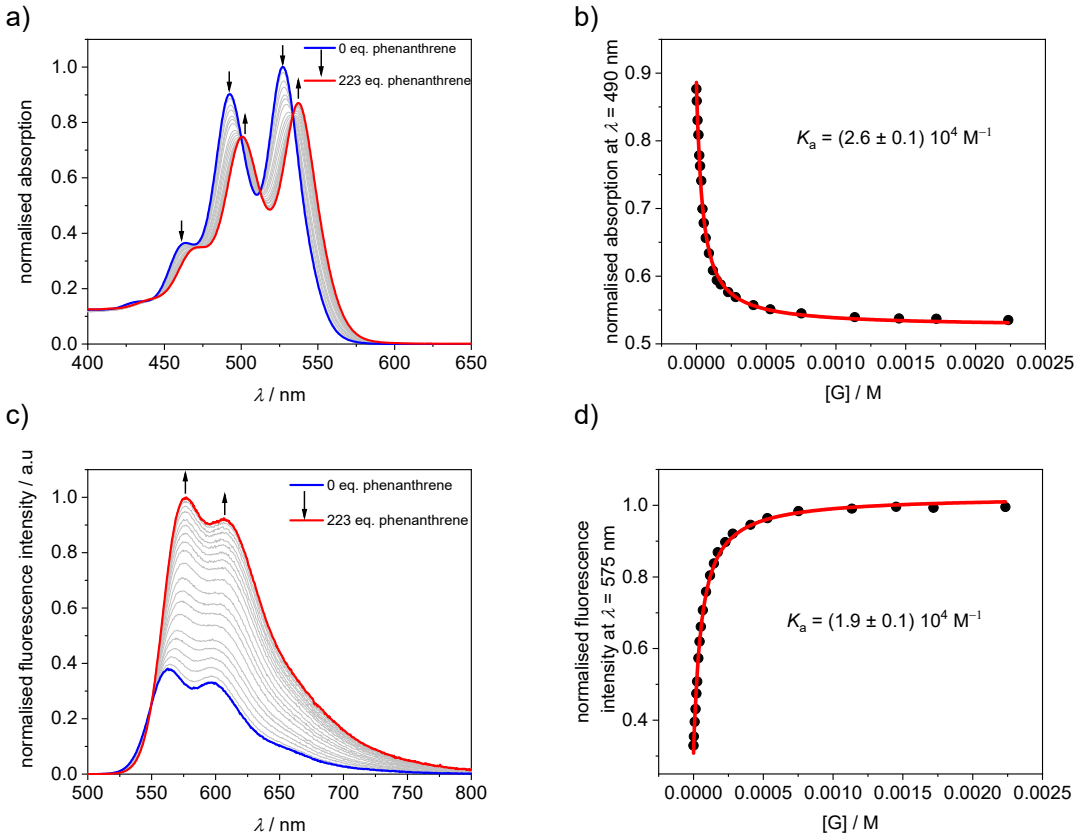

Figure A30. a) UV/vis spectra of cyclophane **1-*MM*** in $CHCl_3$ at 22 °C ($c = 10 \times 10^{-6}$ M) upon the addition of phenanthrene as a guest and b) the resulting plot of the absorption at $\lambda = 490$ nm with nonlinear curve fit (1:1 binding model, red curve). c) Fluorescence spectra of cyclophane **1-*MM*** in $CHCl_3$ at 22 °C ($c = 10 \times 10^{-6}$ M) upon the addition of phenanthrene as a guest and d) the resulting plot of fluorescence intensity at $\lambda = 575$ nm with nonlinear curve fit (1:1 binding model, red curve).

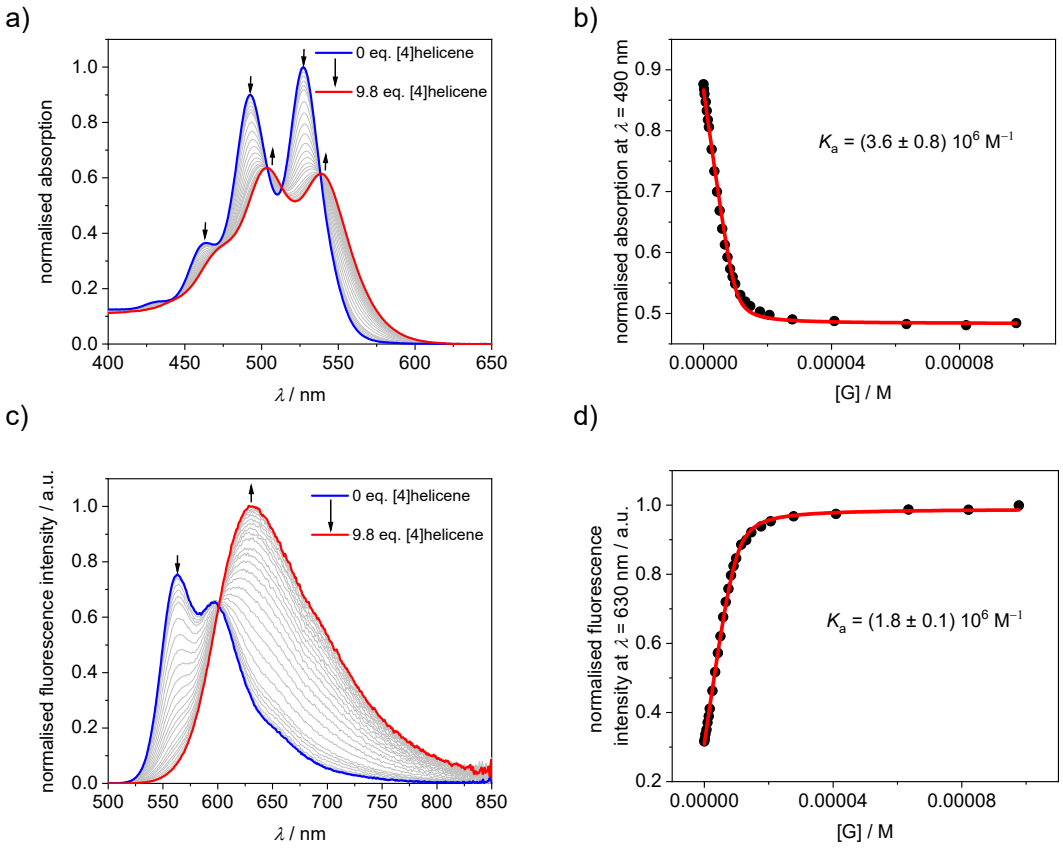

Figure A31. a) UV/vis spectra of cyclophane **1-*PP*** in $CHCl_3$ at 22 °C ($c = 10 \times 10^{-6}$ M) upon the addition of [4]helicene as a guest and b) the resulting plot of the absorption at $\lambda = 490$ nm with nonlinear curve fit (1:1 binding model, red curve). c) Fluorescence spectra of cyclophane **1-*PP*** in $CHCl_3$ at 22 °C ($c = 10 \times 10^{-6}$ M) upon the addition of [4]helicene as a guest and d) the resulting plot of fluorescence intensity at $\lambda = 630$ nm with nonlinear curve fit (1:1 binding model, red curve).

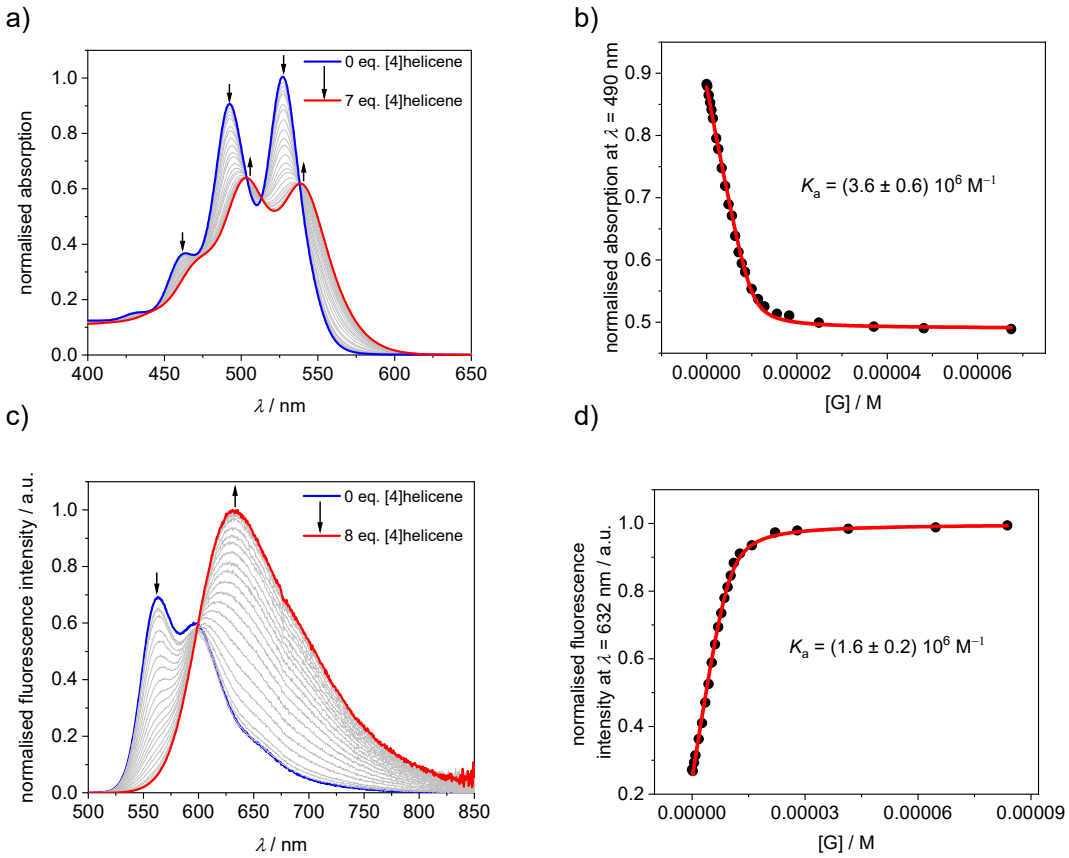

Figure A32. a) UV/vis spectra of cyclophane **1-*MM*** in $CHCl_3$ at 22 °C ($c = 10 \times 10^{-6}$ M) upon the addition of [4]helicene as a guest and b) the resulting plot of the absorption at $\lambda = 490$ nm with nonlinear curve fit (1:1 binding model, red curve). c) Fluorescence spectra of cyclophane **1-*MM*** in $CHCl_3$ at 22 °C ($c = 10 \times 10^{-6}$ M) upon the addition of [4]helicene as a guest and d) the resulting plot of fluorescence intensity at $\lambda = 632$ nm with nonlinear curve fit (1:1 binding model, red curve).

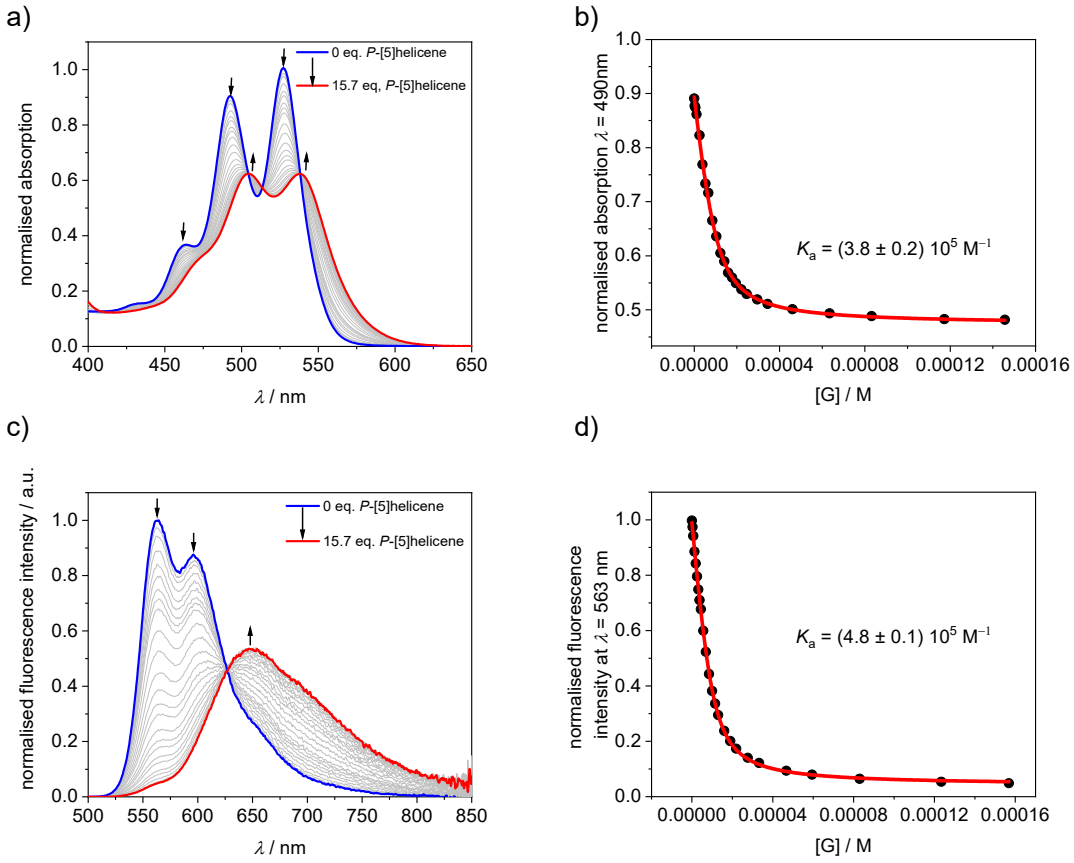

Figure A33. a) UV/vis spectra of cyclophane **1-*PP*** in $CHCl_3$ at 22 °C ($c = 10 \times 10^{-6}$ M) upon the addition of *P*-[5]helicene as a guest and b) the resulting plot of the absorption at $\lambda = 490$ nm with nonlinear curve fit (1:1 binding model, red curve). c) Fluorescence spectra of cyclophane **1-*PP*** in $CHCl_3$ at 22 °C ($c = 10 \times 10^{-6}$ M) upon the addition of *P*-[5]helicene as a guest and d) the resulting plot of fluorescence intensity at $\lambda = 563$ nm with nonlinear curve fit (1:1 binding model, red curve).

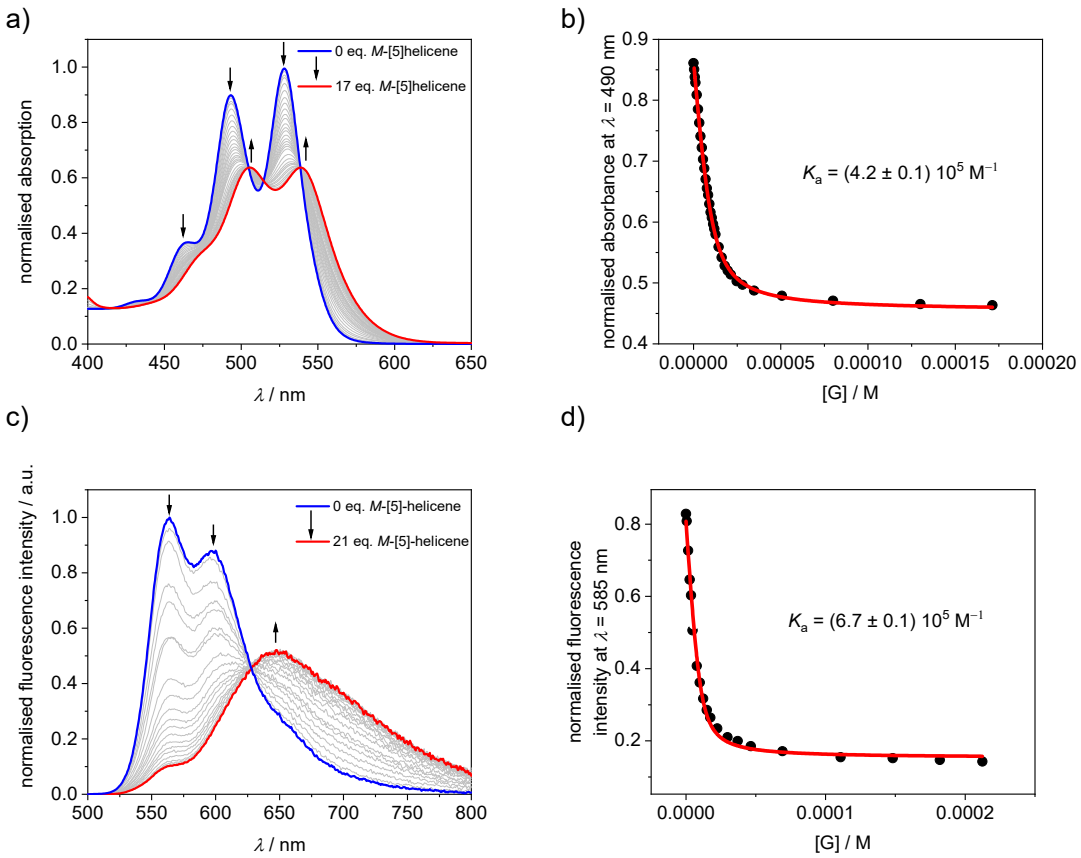

Figure A34. a) UV/vis spectra of cyclophane **1-*MM*** in $CHCl_3$ at 22 °C ($c = 10 \times 10^{-6}$ M) upon the addition of *M*-[5]helicene as a guest and b) the resulting plot of the absorption at $\lambda = 490$ nm with nonlinear curve fit (1:1 binding model, red curve). c) Fluorescence spectra of cyclophane **1-*MM*** in $CHCl_3$ at 22 °C ($c = 10 \times 10^{-6}$ M) upon the addition of *M*-[5]helicene as a guest and d) the resulting plot of fluorescence intensity at $\lambda = 585$ nm with nonlinear curve fit (1:1 binding model, red curve).

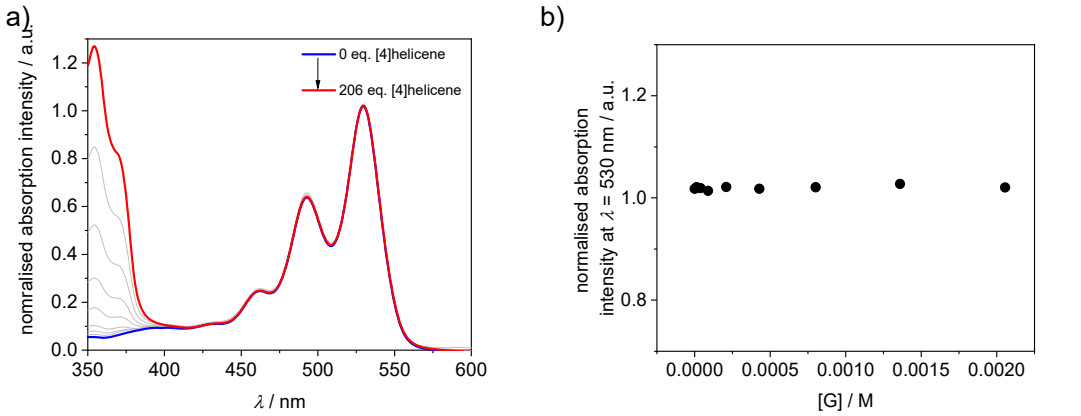

Figure A35. a) UV/vis titration spectra of *rac*-**39b** in $CHCl_3$ at 22 °C ($c = 10 \times 10^{-6}$ M) upon the addition of [4]helicene as a guest and b) the resulting plot of the absorption at $\lambda = 530$ nm.

2. Tetrachloromethane as a solvent

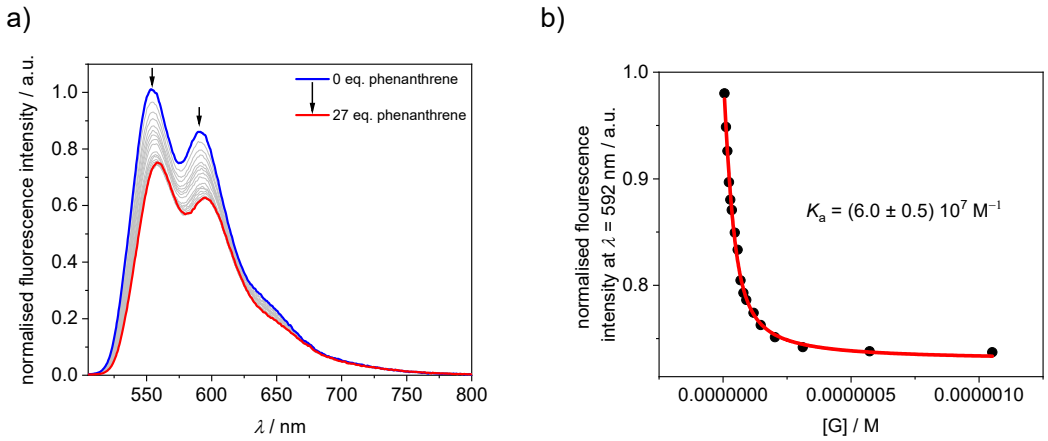

Figure A36. a) Fluorescence spectra of **1-*PP*** in CCl_4 at 22 °C ($c = 3.9 \times 10^{-8}$ M) upon the addition of phenanthrene as a guest and b) the resulting plot of the fluorescence intensity at $\lambda = 592$ nm with nonlinear curve fit (1:1 binding model, red curve).

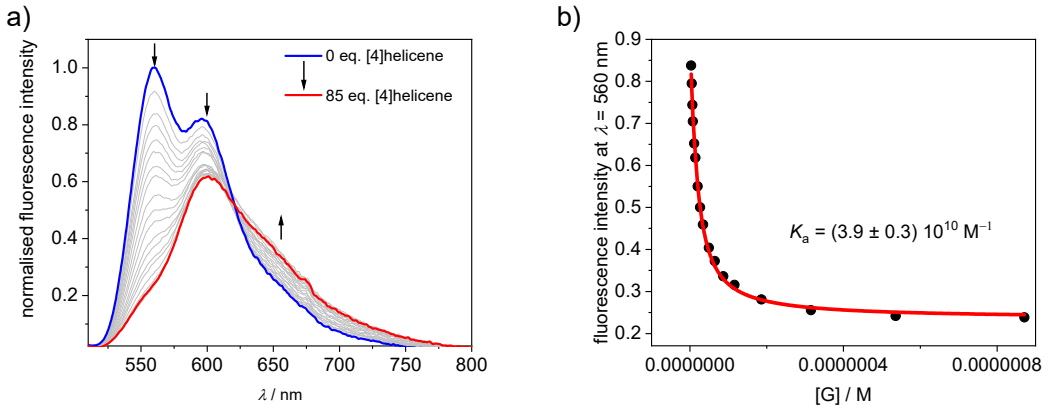

Figure A37. a) Fluorescence spectra of **1-*PP*** ($c = 1.3 \times 10^{-8}$ M) in the presence of phenanthrene ($c = 8.3 \times 10^{-6}$ M) in CCl_4 at 22 °C upon the addition of [4]helicene as a guest and b) the resulting plot of the fluorescence intensity at $\lambda = 560$ nm with competitive nonlinear curve fit (1:1 binding model, red curve).

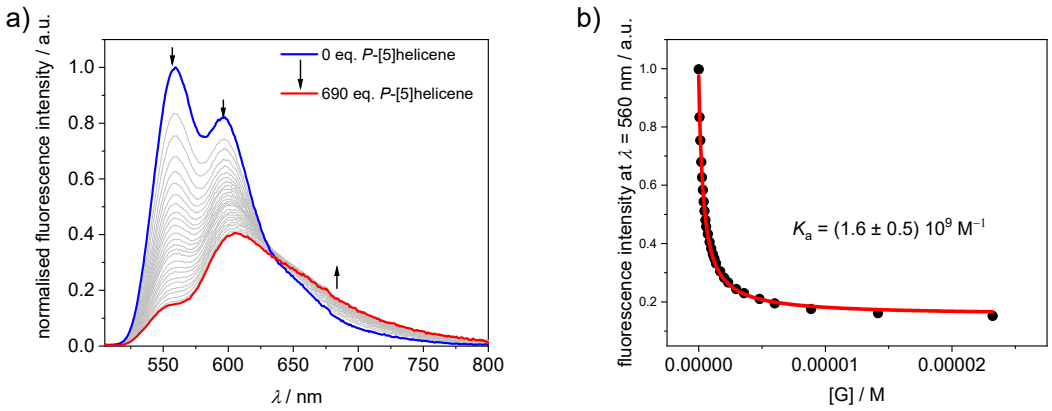

Figure A38. a) Fluorescence spectra of **1-*PP*** ($c = 3.4 \times 10^{-8}$ M) in the presence of phenanthrene ($c = 9.5 \times 10^{-6}$ M) in CCl_4 at 22 °C upon the addition of *P*-[5]helicene as a guest and b) the resulting plot of the fluorescence intensity at $\lambda = 560$ nm with competitive nonlinear curve fit (1:1 binding model, red curve).

DFT Calculations

Energy minimized structures of **39a-*M*** and **39a-*P*** were obtained by DFT calculations (Gaussian 09) with B3-LYP as functional and 6-31G* as basis set (Figure A39a,b). The optimized structures were used for the calculations of the CD spectra by TD-DFT calculations with CAM-B3-LYP as functional and 6-31G* as basis set (Figure A39c,d). Note that our TD-DFT calculations do not consider vibronic coupling. Therefore, our structures do not reproduce the fine structure present in the experimental spectra.

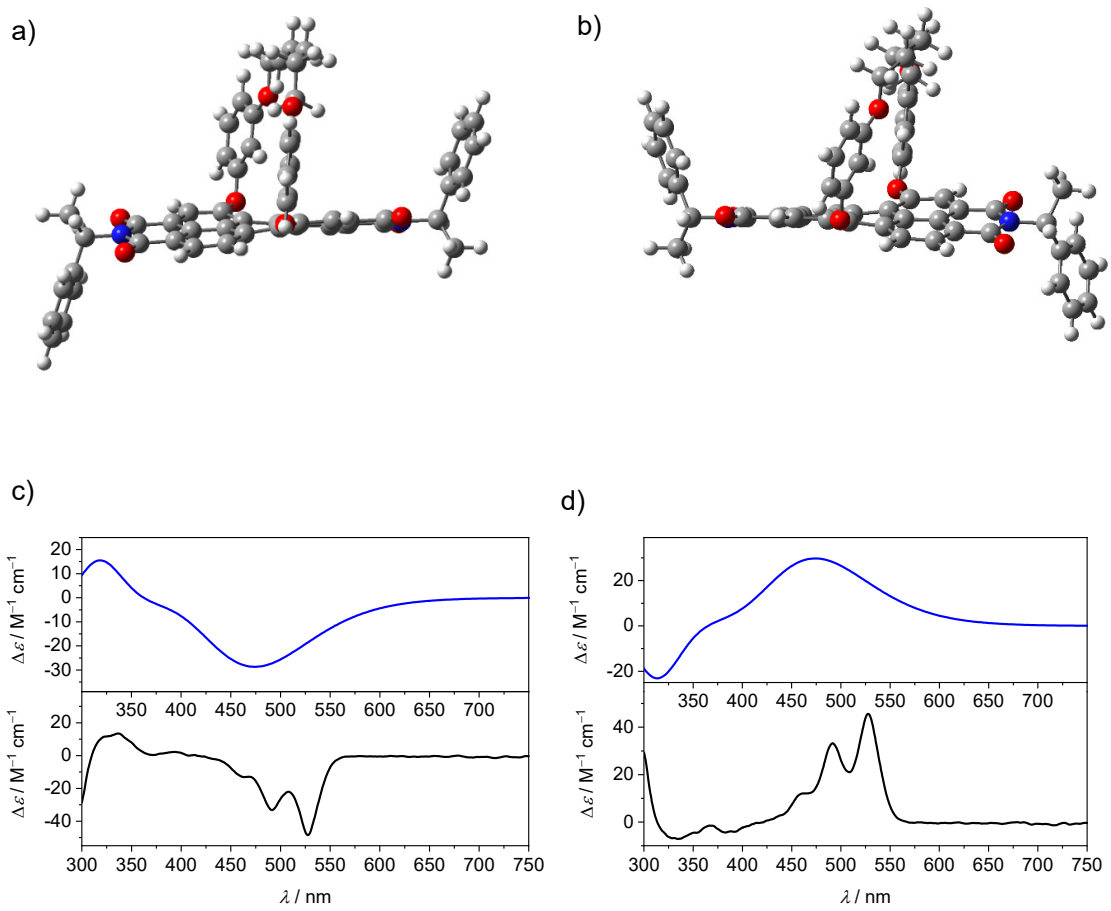

Figure A39. Energy minimized structures of a) **39a-*M*** and b) **39a-*P***. Calculated (blue solid line) and experimental (black solid line) CD spectra of c) **39a-*M*** and d) **39a-*P***.

Energy minimized structures of free [4]helicene and [4]helicene⊂**1**-***MM*** were obtained by DFT calculations (Gaussian 09) with B3-LYP-D3 as functional and 6-311G* as basis set (Figure A40).

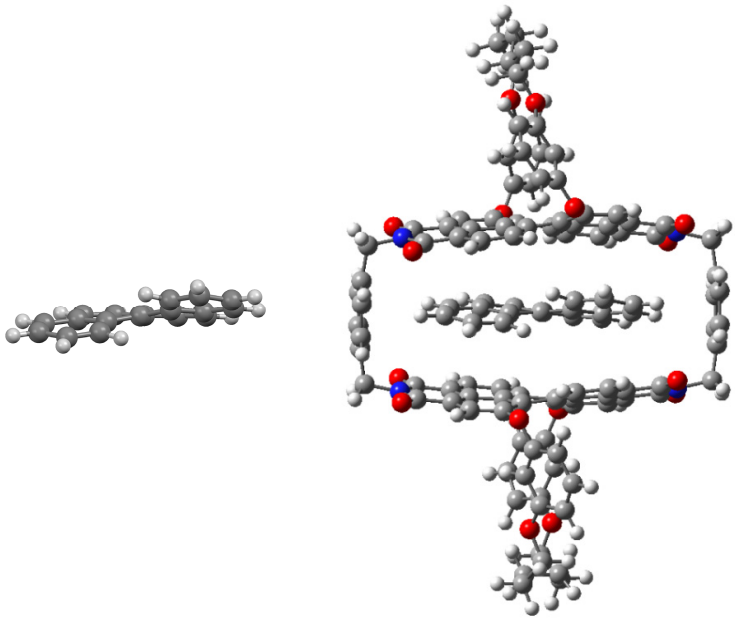

Figure A40. Energy minimized structures of [4]helicene and [4]helicene⊂**1**-***MM***.

2D NMR studies

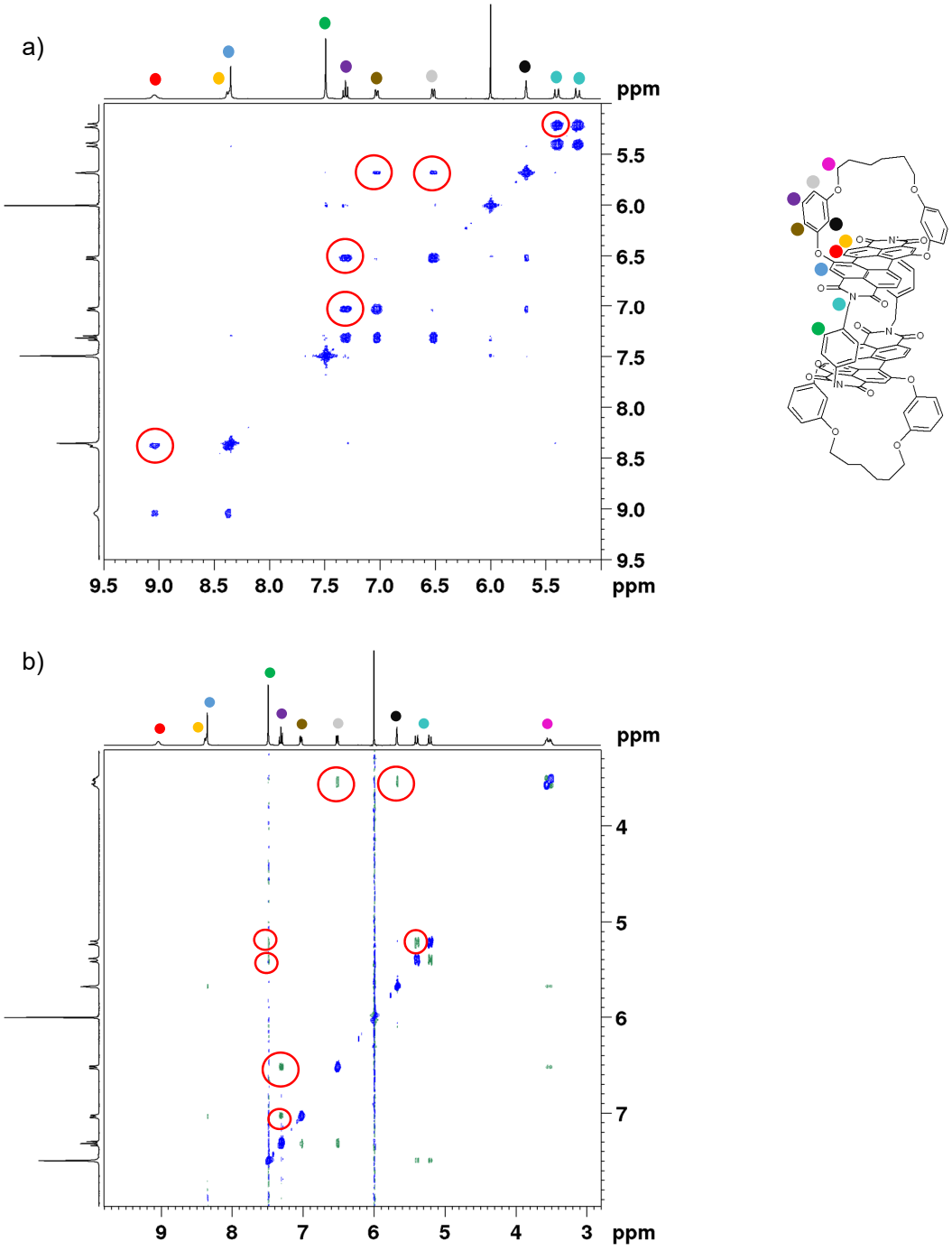

Figure A41. a) ^{1}H-^{1}H COSY NMR spectrum (400 MHz, 298 K) of free **1-*MM*** (c = 3.5 mol L^{-1}) in TCE-d_2. The important cross signals are marked in red. b) ^{1}H-^{1}H ROESY NMR spectrum (400 MHz, 298 K) of free **1-*MM*** (c = 3.5 mol L^{-1}) in TCE-d_2. The important cross signals are marked in red.

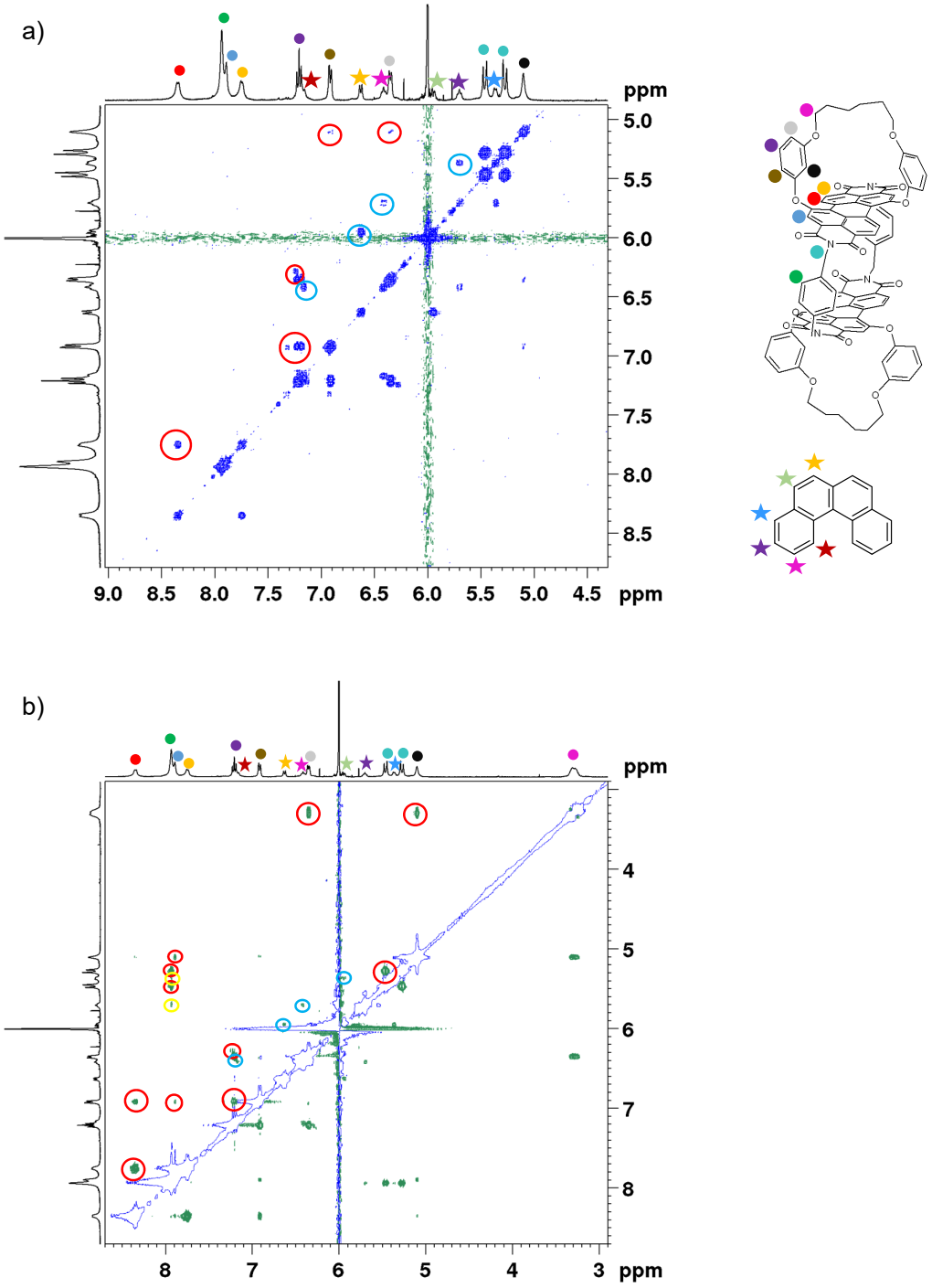

Figure A42. a) ^{1}H-^{1}H COSY NMR spectrum (400 MHz, 298 K) of [4]helicene⊂**1-*MM*** (c = 3.5 mol L^{-1}) in TCE-d_2. The important cross signals are marked in red (host) and blue (guest). b) ^{1}H-^{1}H ROESY NMR spectrum (400 MHz, 298 K) of [4]helicene⊂**1-*MM*** (c = 3.5 mol L^{-1}) in TCE-d_2. The important cross signals are marked in red (host), blue (guest) and yellow (host-guest).

Single Crystal X-ray Analysis

The co-crystal of **1-*MM*** and [4]helicene (~2.5 eq.) was grown in a borosilicate glass tube (10 mm × 75 mm) by slow diffusion of *n*-hexane into chlorobenzene and was obtained as a red, fluorescent block (Figure A43a):

a)

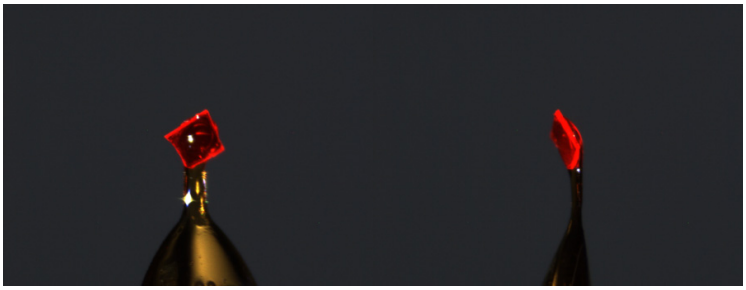

b)

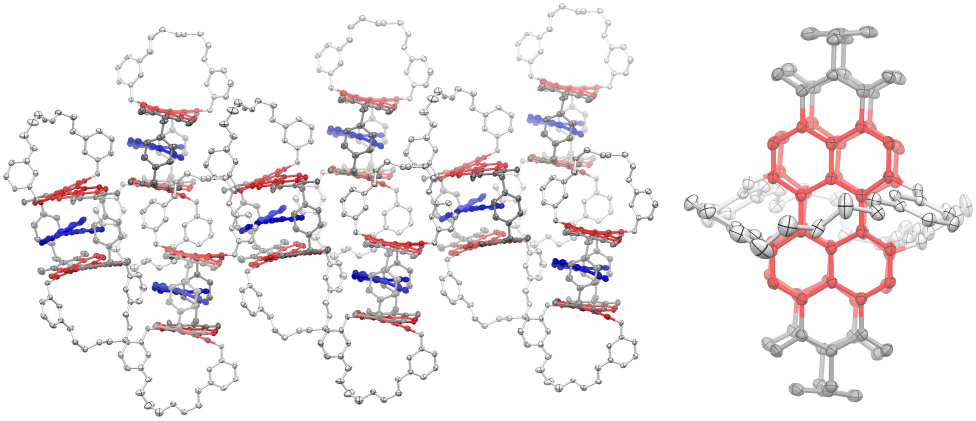

Figure A43. a) Images of the crystals of [4]helicene⊂**1-*MM***. b) Left: Packing of [4]helicene⊂**1-*MM*** in the solid state (solvent molecules and hydrogens are omitted for clarity). The perylene unit and the guest are highlighted in red and blue, respectively. Right: Top-view of the cyclophane (guest, solvent molecules and hydrogens are omitted for clarity).

Table A1. Single Crystal X-ray data for [4]helicene⊂**1**-***MM***.

CCDC number	2074804
Sum formula	$C_{154}H_{110}Cl_6N_4O_{16}$
M / g mol^{-1}	2485.16
Crystal size	0.221 × 0.217 × 0.029 mm
Temperature / K	100 (2)
Wavelength / Å	1.54178
Crystal description	Block
Crystal colour	Red
Crystal system	monoclinic
Space group	P 2_1
a / Å	16.9238 (8)
b / Å	18.6773 (9)
c / Å	19.9114 (9)
α / °	90
β / °	108.037 (2)
γ / °	90
V / Å^3	5984.5 (5)
Z	2
ρ_{cal} / g cm^{-3}	1.379
Absorption coefficient / mm^{-1}	1.902
F(000)	2584.0
Measurement range of θ / °	2.334 to 72.489
Limiting indices	–20 <= h <= 20, –23 <= k <= 22, –24 <=l <= 24
Reflections collected / unique	100934 / 23417 [R_{int} = 0.0381]
Completeness / %	100%
Absorption correction	Semi-empirical from equivalents
T_{min}, T_{max}	0.6371, 0.7536
Refinement method	Full-matrix least-squares on F^2
Data / restraints / parameters	23417 / 451 / 1693
Goodness of fit for F^2	1.024
R[l > 2s(l)]	R_1 = 0.0631, wR_2 = 0.1766
R(all data)	R_1 = 0.0668, wR_2 = 0.1811
Largest diff. peak and hole	1.390 and –0.867 e·Å^{-3}

Deracemization Experiments

For a typical deracemization experiments, a solution of **1-*MM*** or **1-*PP*** (63.3 µg, 0.04 µmol) in 4.0 mL chloroform or tetrachloromethane (c = 1.0 × 10^{-5} M) was prepared. Since the solubility in tetrachloromethane is comparatively poor, ultrasonic treatment and heating was used to dissolve the compound. Afterwards, one equivalent of *rac*-[5]helicene (11.1 µg, 0.04 µmol) was added as a solid to the solution and the time dependent CD measurement was started (Figure A45). When no changes were observed in the CD signal anymore, the formed host-guest complex was separated by GPC (6.5 mL/min, see Figure A44). For the experiments in chloroform, the solution could be directly used for separation by GPC, while in the case of tetrachloromethane the solvent was removed under reduced pressure at r.t.. The residue was then dissolved in chloroform and applied to the GPC separation.

The separated guest was collected and the solvent removed under reduced pressure at r.t.. A CD spectrum of the deracemized guest was measured and a UV/vis absorption spectrum was recorded to determine the concentration from the extinction coefficient, which was determined before from the racemic compound ($\varepsilon_{312\ nm}$ = 31600 M^{-1} cm^{-1}). The enantiomeric excess (*ee*) was calculated by equation A2,[80] where $\Delta\varepsilon_{312\ nm}$ is the experimental value for $\Delta\varepsilon$ at λ = 312 nm and $\Delta\varepsilon_{312\ nm,\ max}$ is the value for $\Delta\varepsilon$ at λ = 312 nm for the enantiopure compound.

$$ee = \frac{\Delta\varepsilon_{312\ nm}}{\Delta\varepsilon_{312\ nm,max}} \times 100\% \qquad \text{(A2)}$$

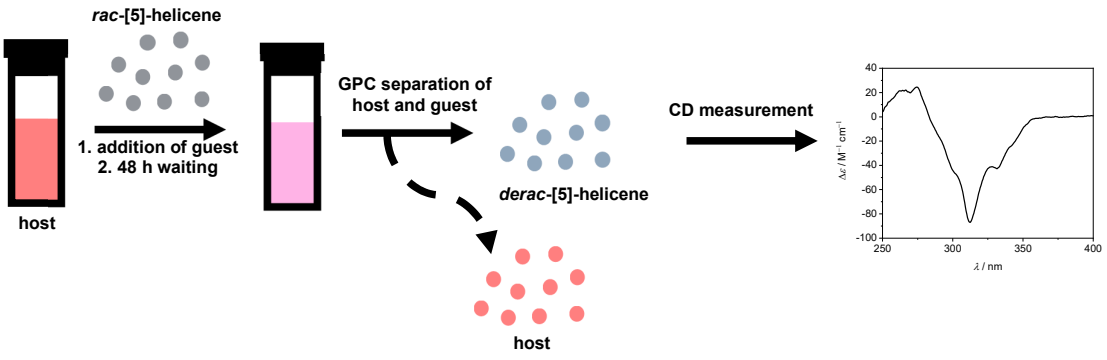

Figure A44. Schematic representation of the experimental protocol for the deracemization experiment of *rac*-[5]helicene by complexation with **1-*MM*** or **1-*PP***.

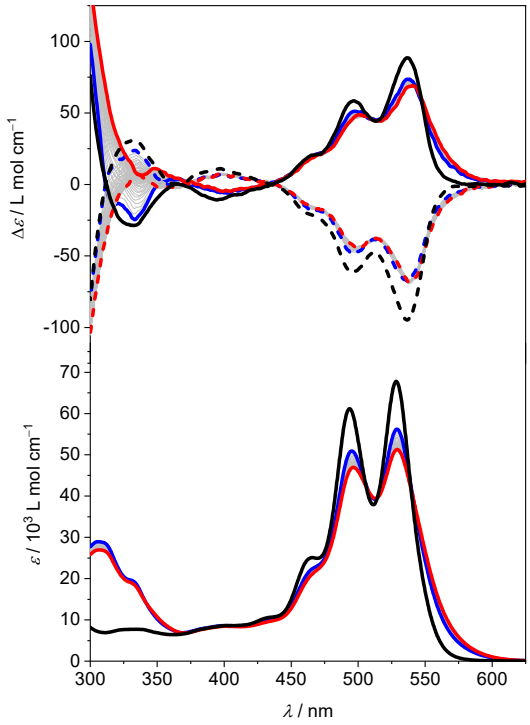

Figure A45. CD (top) and UV/vis (bottom) absorption spectra of **1-*PP*** (solid black line) and **1-*MM*** (dashed black line) and corresponding time dependent spectra after the addition of *rac*-[5]helicene (blue: first spectrum after the addition, red: after 32 h (no changes after 14 h)) in chloroform at r.t..

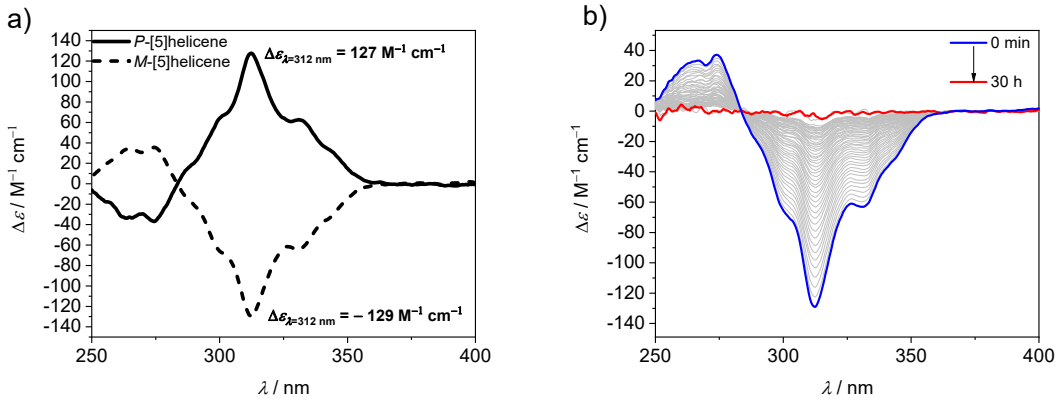

Figure A46. a) CD absorption spectra of *P*-[5]helicene and *M*-[5]helicene (*ee* > 98%) in chloroform at 22 °C and b) time dependent CD absorption spectrum of *M*-[5]helicene in chloroform at 22 °C (*c* = 30 µM).

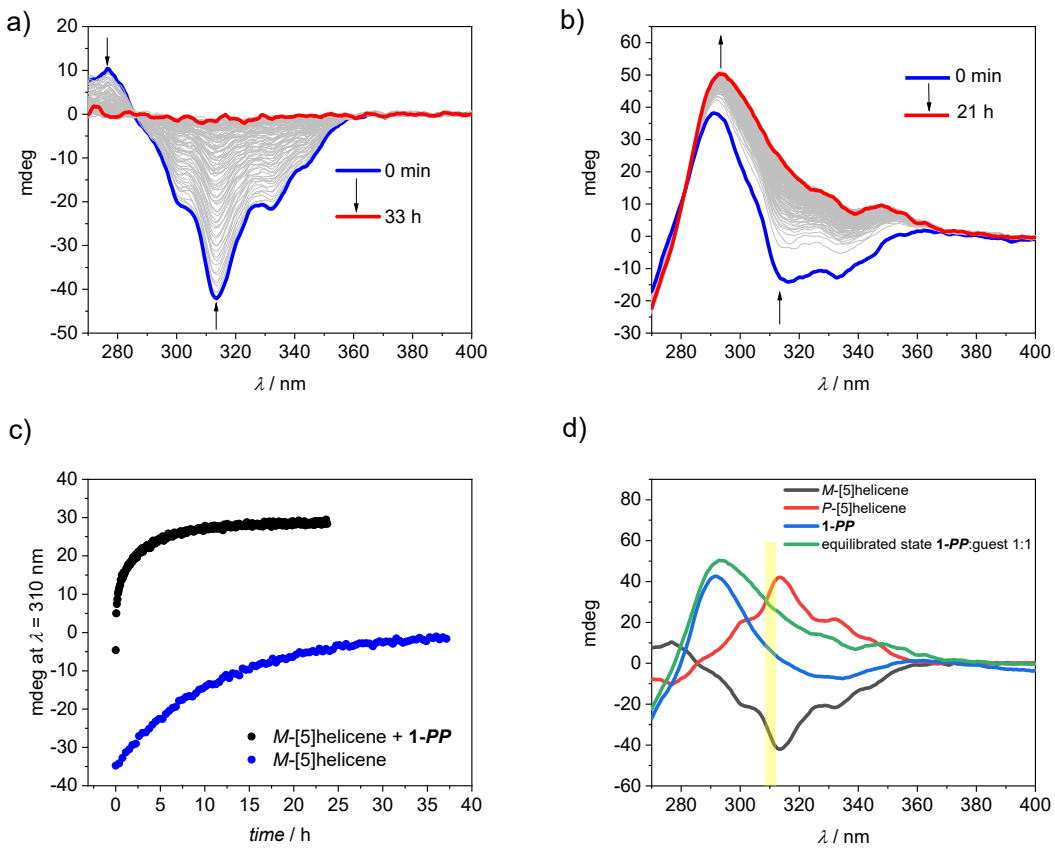

Figure A47. Time dependent CD absorption spectra of a) *M*-[5]helicene (*ee* > 98%) and b) *M*-[5]helicene (*ee* > 98%) with one equivalent of **1-*PP*** in tetrachloromethane at 22 °C (c = 10 µM). c) Time course of the CD spectral changes from Figures A47a and A47b at λ = 310 nm. d) CD spectra of the guest, the host and the equilibrated state from figure A47b in tetrachloromethane at 22 °C (c = 10 µM). At λ = 310 nm (highlighted in yellow) the contribution of **1-*PP*** to the CD spectrum is small (6 mdeg).

9.2 Appendix for Chapter 4: π–π Catalysis Made Asymmetric - Enantiomerization Catalysis Mediated by the Chiral π-System of a Perylene Bismide Cyclophane

General Methods

Chemicals: All chemicals and solvents were purchased from commercial suppliers and used without further purification. (*P/M*)-1,7-(3,3'-(hexane-1,6-diylbis(oxy))diphenolate) perylene-3,4:9,10-tetracarboxylic bisanhydride (**57**), *tert*-butyl (4-(aminomethyl)benzyl)carbamate and *rac*-[5]helicene were synthesized according to literature known procedures.[193, 308] The resolution of the enantiomers of [5]helicene could be achieved by chiral HPLC (DCM/*n*-hexane 3:7, flow rate 6.5 mL/min). The enantiomeric excess was determined by analytical HPLC (Reprosil 100 Chiral-NR 8µm, Trentec, *n*-hexane/DCM 9:1) and integration of the corresponding peaks with values of *ee* > 98%.

HPLC: Analytical HPLC was carried out on a JASCO system (PU 2080 PLUS) with a diode array detector (MD 2015), equipped with a ternary gradient unit (DG-2080-533) and inline-degasser (LG 2080-02). Recycling semipreparative HPLC was carried out on a JAI LC-9105. Chiral resolution was carried out using a Trentec Reprosil-100 Chiral-NR 8µm-column.

GPC: Gel permeation chromatography (GPC) was performed on a Shimadzu Recycling GPC-System (LC-20AD Prominence Pump; SPDMA20A Prominence Diode Array Detector) with three or two preparative columns (Japan Analytical Industries Co., Ltd.; JAIGEL-1 H, JAIGEL-2H and JAIGEL-2.5 H) in chloroform (HPLC grade, stabilized with 0.1% EtOH) with a flow rate of 6.5 or 5.0 mL/min.

NMR spectroscopy: ^{1}H NMR and ^{13}C NMR spectra were recorded on a Bruker Avance III HD 400 or 600 MHz spectrometer. Chemical shift data are reported in parts per million (ppm, δ scale) downfield from tetramethylsilane and referenced internally to the residual proton (for proton NMR) in the solvent ($CDCl_3$: $\delta = 7.26$; $C_2D_2Cl_4$: $\delta = 6.00$) or to the carbon resonance ($CDCl_3$: $\delta = 77.16$; $C_2D_2Cl_4$: $\delta = 74.20$). The coupling constants are listed in Hertz.

Mass spectrometry: The MALDI-TOF mass spectra were measured with a Bruker Daltonics ultrafleXtreme mass spectrometer by using DCTB as a matrix. High-resolution ESI TOF spectra were acquired on a Bruker Daltonics microTOF focus spectrometer.

Melting points: Melting points were measured with an Olympus BX41 polarization microscope connected to a TP84 Linkam scientific temperature regulator.

Optical UV/vis absorption spectroscopy: All spectroscopic measurements were carried out under ambient conditions using solvents of spectroscopic grade. The absorption spectra were recorded on a JASCO V-770 or V-670 spectrometer equipped with a PAC-743R Peltier for temperature control.

Ciruclar dichroism (CD) spectroscopy: CD spectra were measured with a JASCO J-810 spectropolarimeter equipped with a Jasco CDF-426S Peltier temperature controller.

Steady-State Fluorescence Spectroscopy: Fluorescence spectra were recorded on an Edingburgh Instruments FLS981 fluorescence spectrometer.

Single crystal X-ray analysis: Single crystal X-ray diffraction data for *P*-[5]helicene⊂**1-*PP*** were collected on a Bruker D8 Quest Kappa diffractometer with a Photon II CMOS detector and multi-layered mirror monochromated Cu Kα radiation. Single crystal X-ray diffraction data for **1-*MP*** were collected at the P11 beamline at DESY. The diffraction data were collected by a single 360 ° ϕ scan at 100 K. The diffraction data were indexed, integrated, and scaled using the XDS program package.[309] In order to compensate low completeness due to single-axis measurement two data sets were merged using the XPREP program from Bruker.[310] The structures were solved using SHELXT,[311] expanded with Fourier techniques and refined using the SHELX software package.[312] Hydrogen atoms were assigned at idealized positions and were included in the calculation of structure factors. All non-hydrogen atoms in the main residue were refined anisotropically. Disordered solvent molecules were modelled with constraints and restraints using standard SHELX commands EADP, FLAT, SAME, RIGU.

Synthetic Procedure

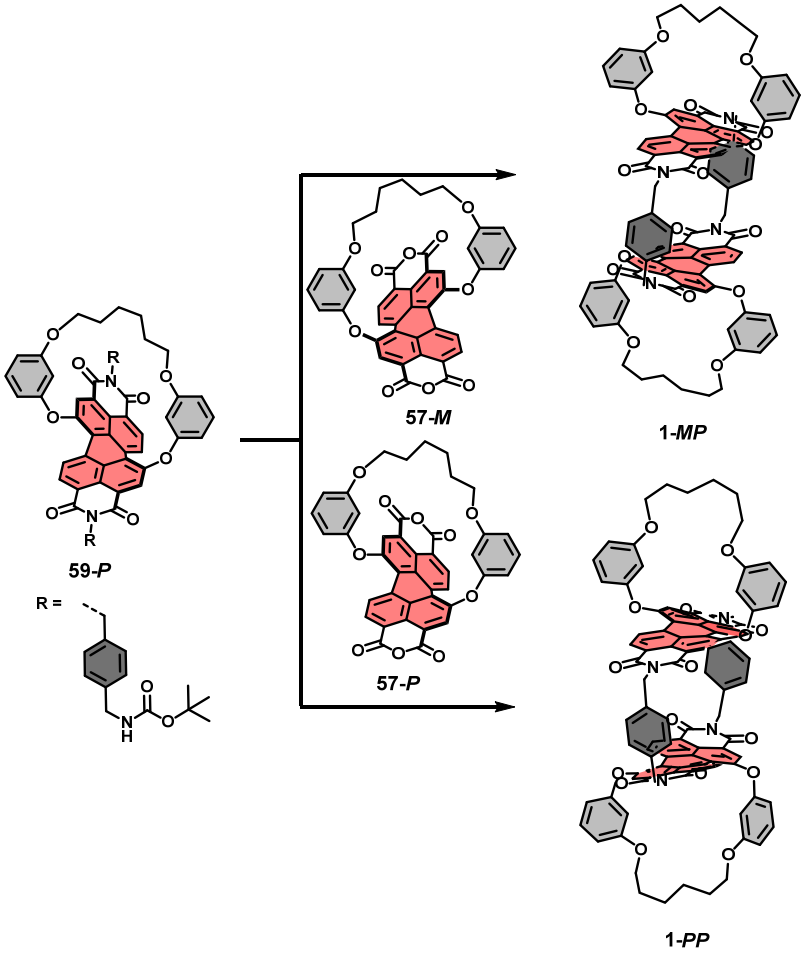

Scheme A2. Macrocyclization step for the cyclophane synthesis of **1-*MP*** and **1-*PP***.

Perylene Bisimide 59-*P*

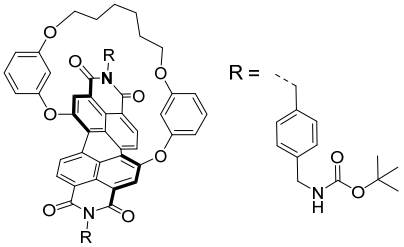

Perylene bisanhydride **57-*P*** (15.0 mg, 21.7 µmol, 1.0 eq.), *tert*-butyl (4-(aminomethyl)benzyl)carbamate (24.0 mg, 102 µmol, 4.7 eq.) and imidazole (190 mg) were mixed together in toluene (15 mL) and stirred for 16 h at 120 °C. After being cooled down to room temperature, toluene was removed under reduced pressure. The crude product was purified by column chromatography (DCM, 1% MeOH) and GPC ($CHCl_3$). **Yield**: 19.0 mg (16.9 µmol, 78%) of a red solid. **HRMS** (ESI, positive, acetonitrile/chloroform): (*m/z*) $[M]^+$,calcd. for $C_{78}H_{70}N_2NaO_4^+$: 1149.42564; found: 1149.42626. **^{1}H NMR** (400 MHz, $CDCl_3$): $\delta = 9.24$ (d, $^3J = 8.5$ Hz, 2H), 8.52 (d, $^3J = 8.5$ Hz, 2H), 8.30 (s, 2H), 7.50 (d, $^3J = 8.2$ Hz, 4H), 7.28 (t, $^3J = 8.3$ Hz, 2H), 7.19 (d, $^3J = 8.2$ Hz, 4H), 7.04 (ddd, $^3J = 8.2$ Hz, $^3J = 2.3$ Hz, $^4J = 0.7$ Hz 2H),

6.45 (ddd, ^3J = 8.2 Hz, ^3J = 2.3 Hz, ^4J = 0.7 Hz 2H), 5.44 (t, ^4J = 2.3 Hz, 2H), 5.27 (s, 4H), 4.75 (br, 2H), 4.21 (d, ^3J = 5.5 Hz, 4H), 3.51–3.43 (m, 4H), 1.53–1.45 (m, 4H), 1.42 (s, 18H), 1.18–1.09 (m, 4H). **^{13}C NMR** (101 MHz, $CDCl_3$): δ = 163.2, 162.6, 160.4, 157.6, 155.9, 153.3, 138.5, 136.1, 132.3, 131.0, 130.9, 129.7, 129.0, 128.9, 128.6, 127.8, 126.6, 126.1, 124.6, 122.6, 111.2, 108.9, 101.5, 79.6, 67.6, 44.5, 43.4, 28.9, 28.5, 26.2. **mp**.: 156–159 °C.

Perylene bisimide cyclophane 1-*MP*

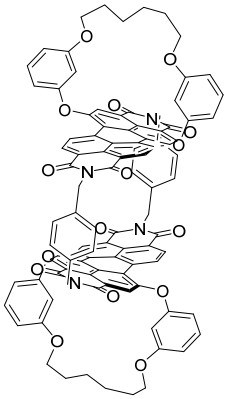

Perylene bisimide **59-*P*** (25.2 mg, 22.4 µmol) was dissolved in DCM (20 mL) and TFA (1.0 mL) was added to the solution. The mixture was stirred at room temperature for 1.5 h. The solvent was removed under reduced pressure, the remaining solid again dissolved in DCM and the latter again removed by rotary evaporation. Afterwards, perylene bisanhydride **57-*M*** (15.4 mg, 22.3 µmol) and imidazole (510 mg) were added and the solids dissolved in dry toluene (75 mL). The mixture was stirred under a nitrogen atmosphere at 120 °C for 16 h. The solution was cooled down to room temperature and the toluene was removed under reduced pressure. Subsequently, the solid was dissolved in DCM and the organic phase extracted with 1 M HCl. After drying over Na_2SO_4, the solvent was removed under reduced pressure and the crude product purified by column filtration (DCM, 1% MeOH), GPC ($CHCl_3$) and preparative TLC (DCM). The pure substance was dissolved in a minimum amount of $CHCl_3$ and precipitated upon the addition of MeOH. The precipitate was centrifuged and the solid washed with *n*-hexane to obtain the pure compound as a red solid. **Yield**: 3.00 mg (1.90 µmol, 8.5%) of a red solid. **HRMS** (MALDI, positive, DCTB): (*m/z*) $[M]^+$,calcd. for $C_{100}H_{68}N_4O_{16}^+$: 1581.46639; found: 1581.47019. **^{1}H NMR** (400 MHz, $C_2D_2Cl_4$): δ = 9.06 (d, ^3J = 8.3 Hz, 4H), 8.37 (d, ^3J = 8.3 Hz, 4H), 8.34 (s, 4H), 7.43 (s, 8H), 7.31 (t, ^3J = 8.3 Hz, 4H), 7.03 (dd, ^3J = 8.2 Hz, ^4J = 2.1 Hz, 4H), 6.51 (dd, ^3J = 8.2 Hz, ^4J = 2.1 Hz 4H), 5.65 (s, br, 4H), 5.58 (d, ^2J = 13.5 Hz, 4H), 5.04 (d, ^2J = 13.5 Hz, 4H), 3.58–3.47 (m, 8H), 1.57–1.45 (m, 8H), 1.23–1.13 (m, 8H). **^{13}C NMR** (101 MHz, $CDCl_3$): δ = 162.3, 162.2, 160.1, 157.2, 153.0, 136.8, 131.9, 131.0, 130.8, 129.8, 128.5, 128.2, 128.0, 126.0, 125.4, 124.1, 122.1, 120.2, 111.1, 109.1, 101.4, 67.5, 42.5, 28.6, 25.9. **mp**.: >300°C.

Perylene bisimide cyclophane 1-*PP*

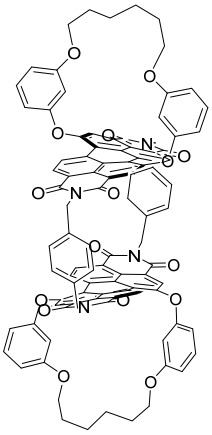

Perylene bisimide **59-*P*** (38.0 mg, 33.7 µmol) was dissolved in DCM (20 mL) and TFA (2.0 mL) was added to the solution. The mixture was stirred at room temperature for 2 h. The solvent was removed under reduced pressure, the remaining solid again dissolved in DCM and the latter again removed by rotary evaporation. Afterwards, perylene bisanhydride **57-*P*** (23.3 mg, 33.7 µmol) and imidazole (650 mg) were added and the solids dissolved in dry toluene (130 mL). The mixture was stirred under a nitrogen atmosphere at 120°C for 14 h. The solution was cooled down to room temperature and the toluene was removed under reduced pressure. Subsequently, the solid was dissolved in DCM and the organic phase extracted with 1 M HCl. After drying over Na_2SO_4, the solvent was removed under reduced pressure and the crude product purified by column chromatography (DCM, 2% MeOH) and GPC ($CHCl_3$). The pure substance was dissolved in a minimum amount of $CHCl_3$ and precipitated upon the addition of MeOH. The precipitate was centrifuged and the solid washed with *n*-hexane to obtain the pure compound as a red solid. **Yield**: 15.5 mg (9.80 µmol, 29%) of a red solid.

The obtained ^{1}H NMR spectrum was in accordance with the one from literature.[193]

NMR Spectra

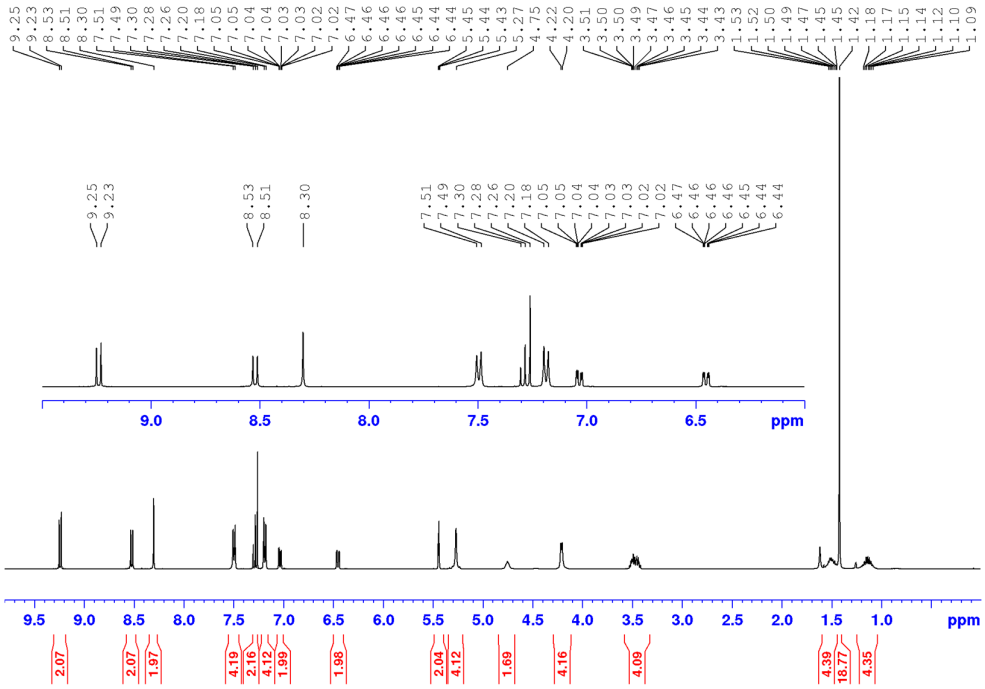

Figure A48. ^{1}H NMR (400 MHz) spectrum of compound **59-*P*** in $CDCl_3$ at 295 K.

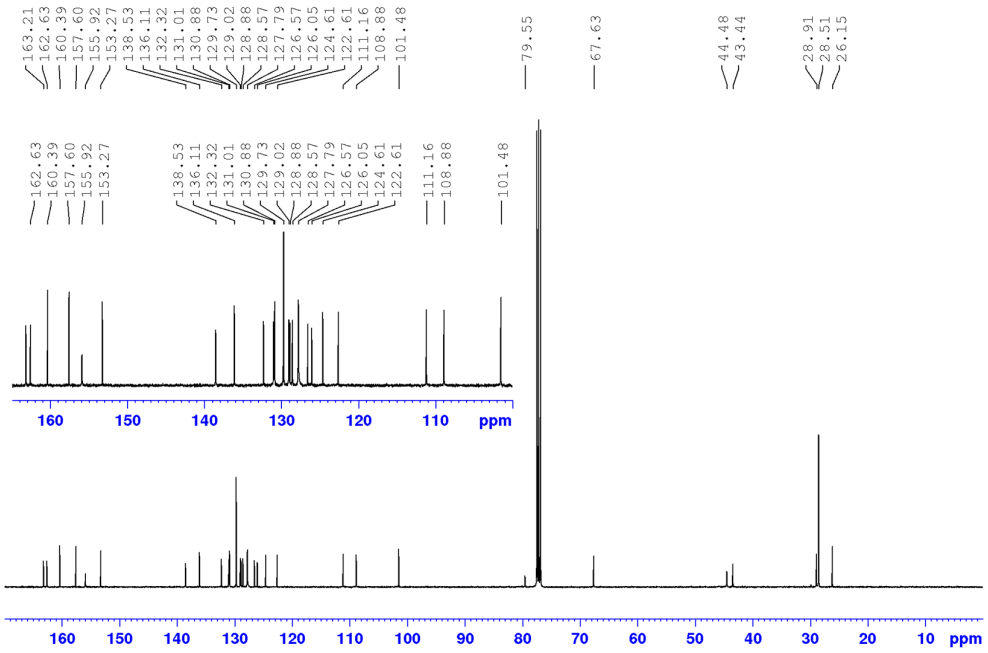

Figure A49. ^{13}C NMR (101 MHz) spectrum of compound **59-*P*** in $CDCl_3$ at 295 K.

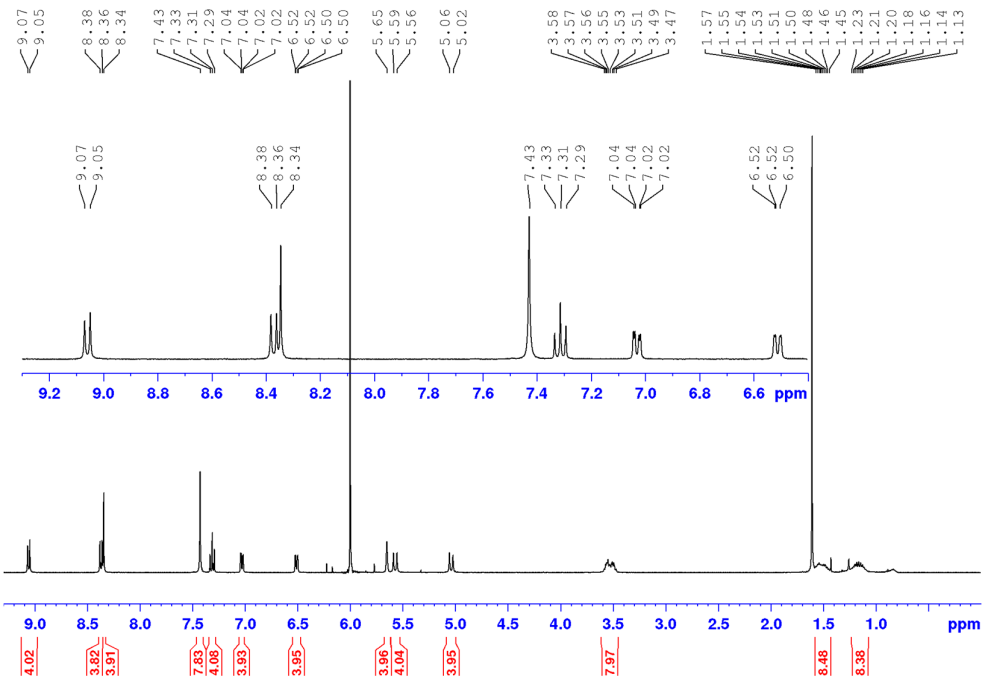

Figure A50. ^{1}H NMR (400 MHz) spectrum of compound **1-*MP*** in $C_2D_2Cl_4$ at 295 K.

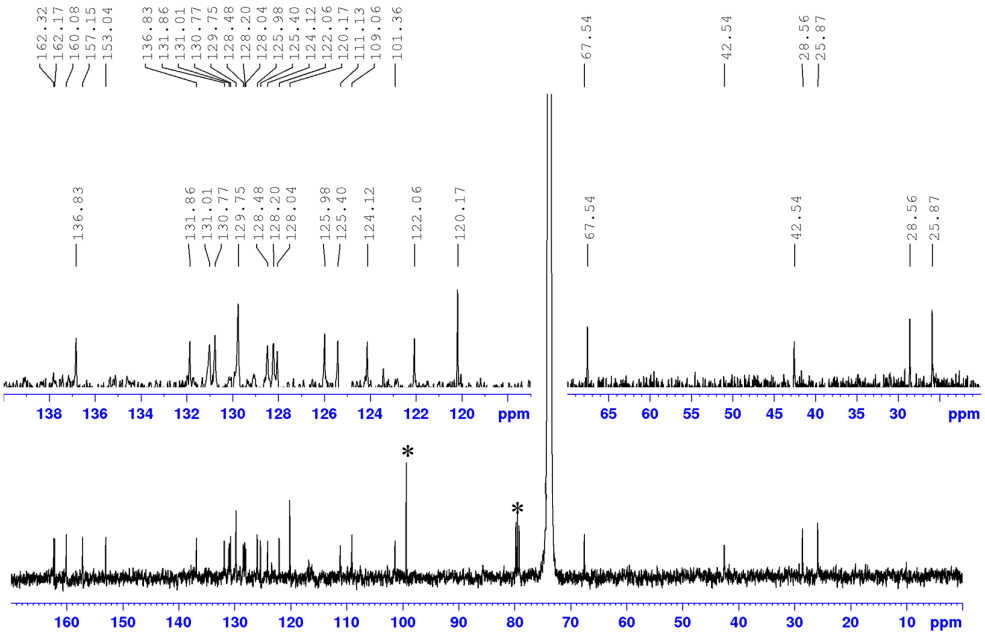

Figure A51. ^{13}C NMR (101 MHz) spectrum of compound **1-*MP*** in $C_2D_2Cl_4$ at 295 K. Asterisks mark solvent impurities (CCl_4 and $CDCl_3$) from the NMR solvent.

Mass Spectra

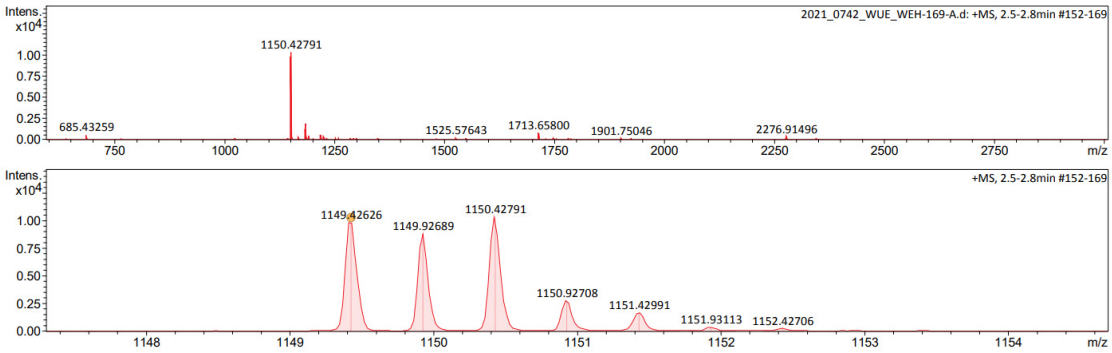

Figure A52. HRMS (ESI, positive, acetonitrile/chloroform) of compound **59-*P***.

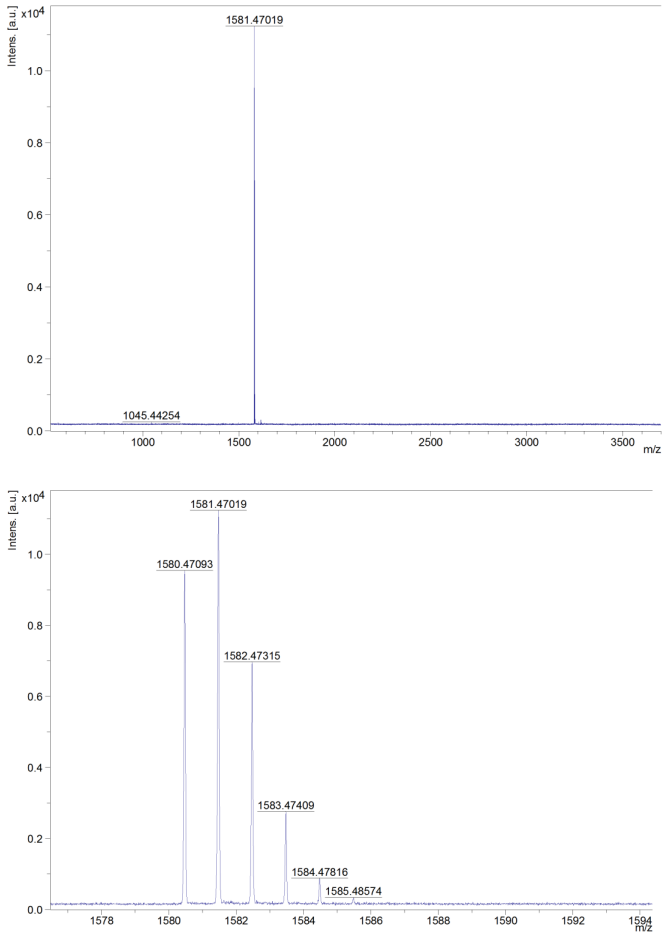

Figure A53. HRMS (MALDI, positive, DCTB) of compound **1-*MP***.

Fluorescence Titration

A solution of PBI cyclophane **1-*MP*** and an excess of *rac*-[5]helicene (see corresponding graphs for exact amount of the individual guest) was titrated to a solution of the pure cyclophane in the same solvent of the same concentration keeping the host concentration constant during the experiment. The fluorescence titration data was fitted to a 1:1 binding model.[143]

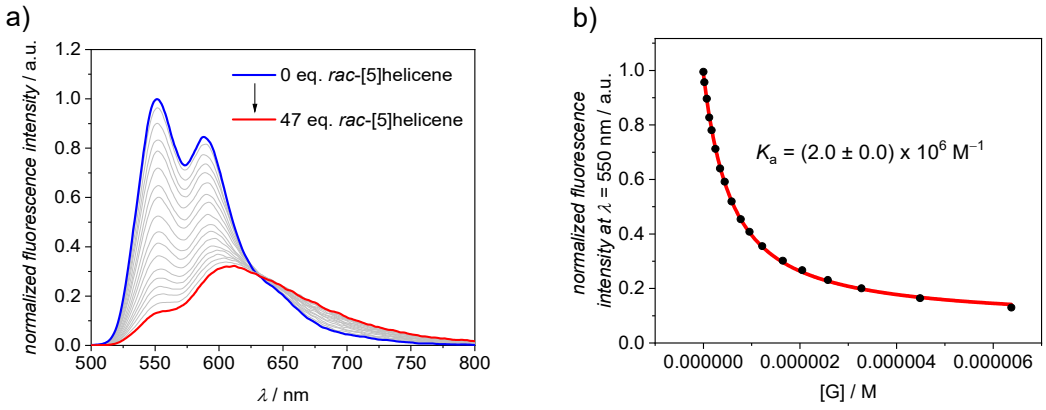

Figure A54. a) Fluorescence spectra (λ_{exc} = 470 nm) of cyclophane **1-*MP*** in CCl_4 at 22 °C (c = 1.3 x 10^{-7} M) upon the addition of *rac*-[5]helicene as a guest and b) the resulting plot of the fluorescence at λ = 550 nm with nonlinear curve fit (1:1 binding model, red curve).

Time Dependent CD Studies

For the rate analysis, a tetrachloromethane solution of *M*-[5]helicene was monitored by time-dependent CD spectroscopy. Subsequently, the time course and the integral from λ = 300–340 nm were fitted according to equation A3 under the assumption of pseudo-first-order kinetics.[313]

For the determination of the enantiomerization rate constants in the presence of the cyclophane templates, a solution of the host (**1-*PP*** or **1-*MP***) was prepared. The solution was transferred to a cuvette and equilibrated in the spectrometer at the corresponding temperature. The guest (*M*-[5]helicene) was dissolved in a particular volume of the solvent and added (~15–20 µL, depending on its concentration) to the host solution. The cuvette was quickly shaken, put back into the spectrometer and the measurement was immediately started. The obtained time courses and the integral in the characteristic absorption range of [5]helicene (λ = 300–320 nm in the presence of **1-*PP*** to obtain more data points for the fast process or λ = 300–340 nm in the presence of **1-*MP*** similar to the studies in the absence of host) were fitted according to equation A3.

$$A_t = \Delta A e^{-k_{obs}t} + A_\infty \quad \text{(A3)}$$

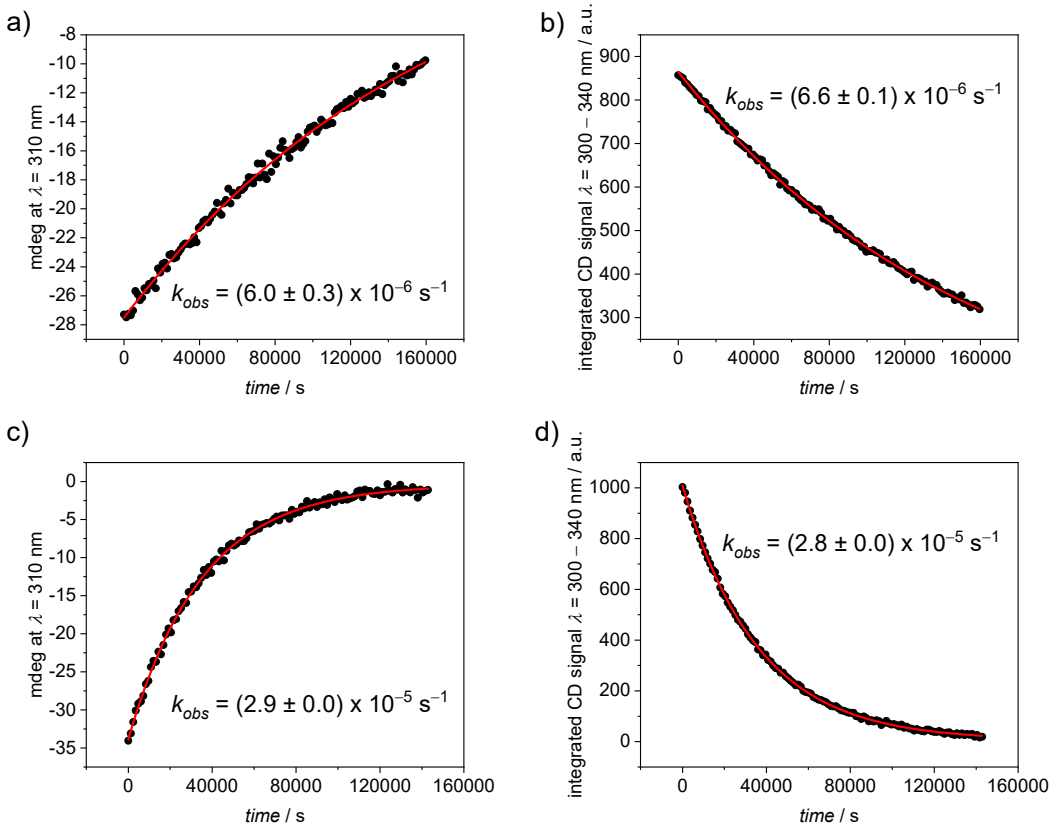

Figure A55. Time-dependent CD course (1 cm cuvette) and the corresponding integrated area from λ = 300 – 340 nm of *M*-[5]helicene in CCl_4 (c = 10 µM) at a)–b) 281 K and c)–d) 295 K.

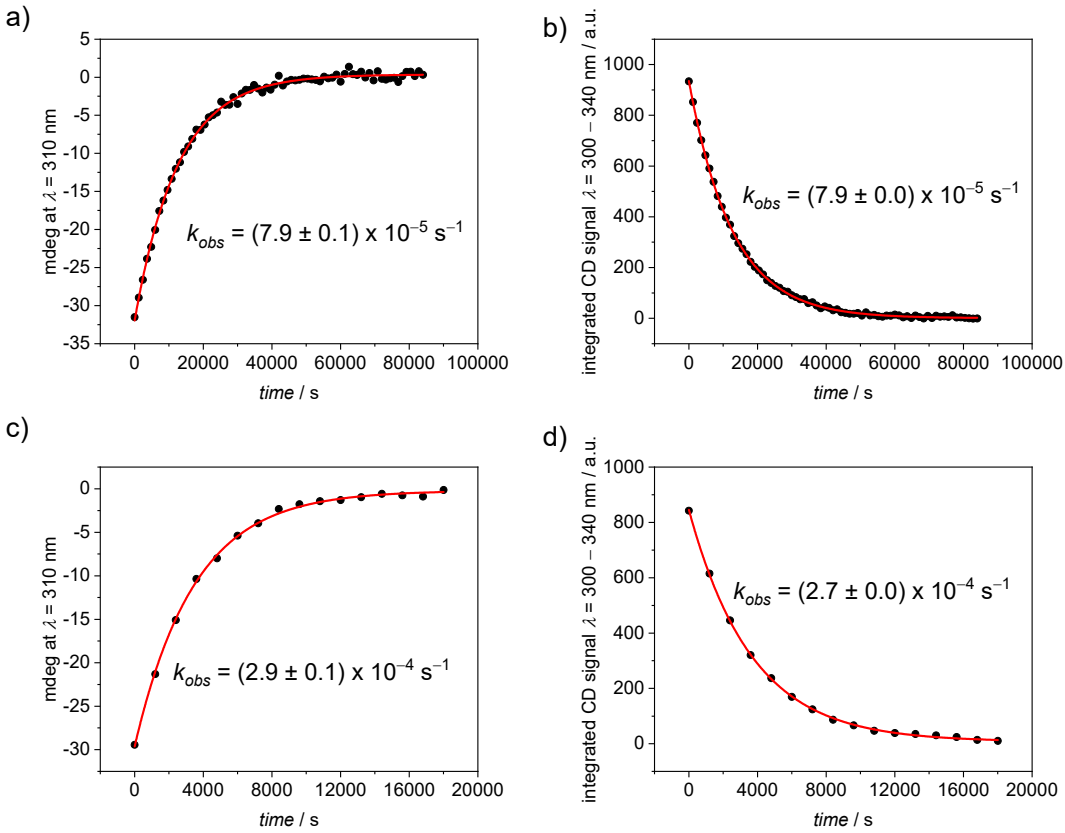

Figure A56. Time-dependent CD course (1 cm cuvette) and the corresponding integrated area from λ = 300 – 340 nm of *M*-[5]helicene in CCl_4 (c = 10 µM) at a)–b) 303 K and c)–d) 313 K.

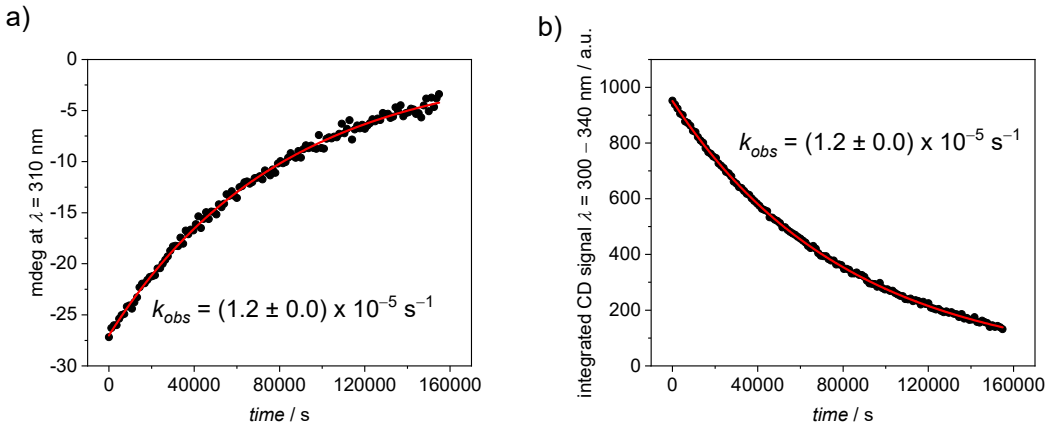

Figure A57. Time-dependent CD course (1 cm cuvette) and the corresponding integrated area from λ = 300 – 340 nm of *M*-[5]helicene (c = 10 µM) in the presence of two equivalents of **1-*MP*** in CCl_4 at 295 K.

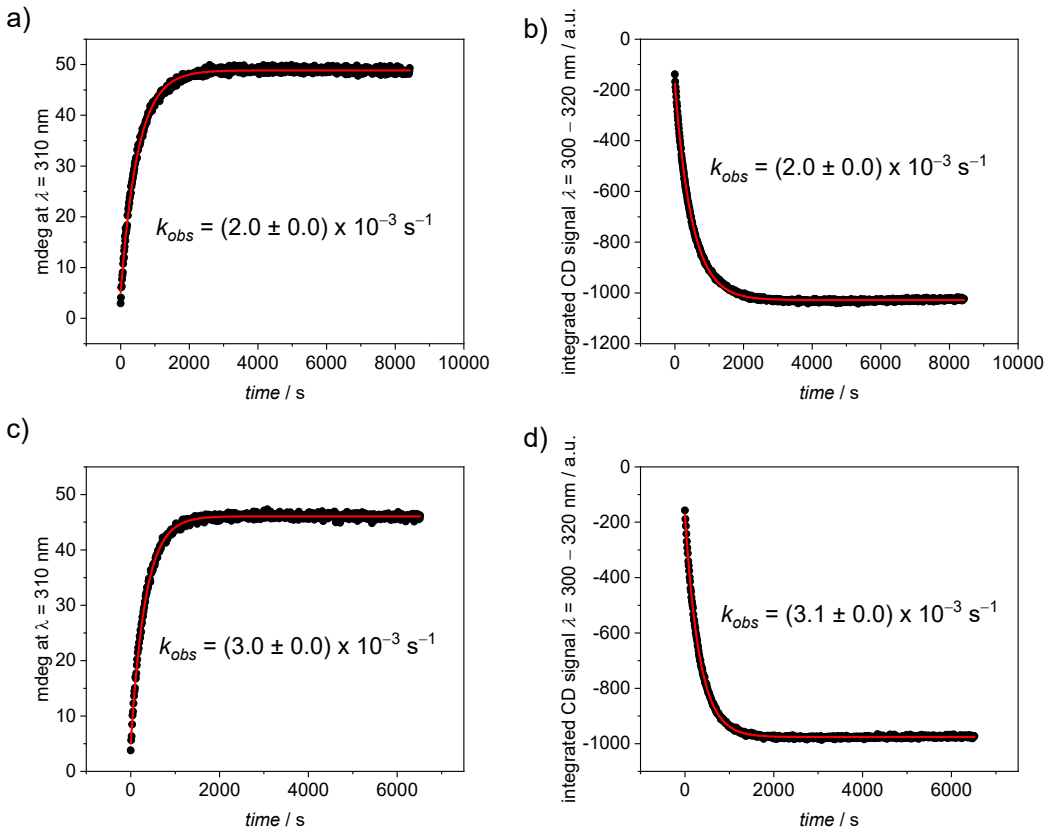

Figure A58. Time-dependent CD course (1 cm cuvette) and the corresponding integrated area from λ = 300 – 320 nm of *M*-[5]helicene (c = 10 µM) in the presence of two equivalents of **1-*PP*** in CCl_4 at a)–b) 279 K and c)–d) 283 K.

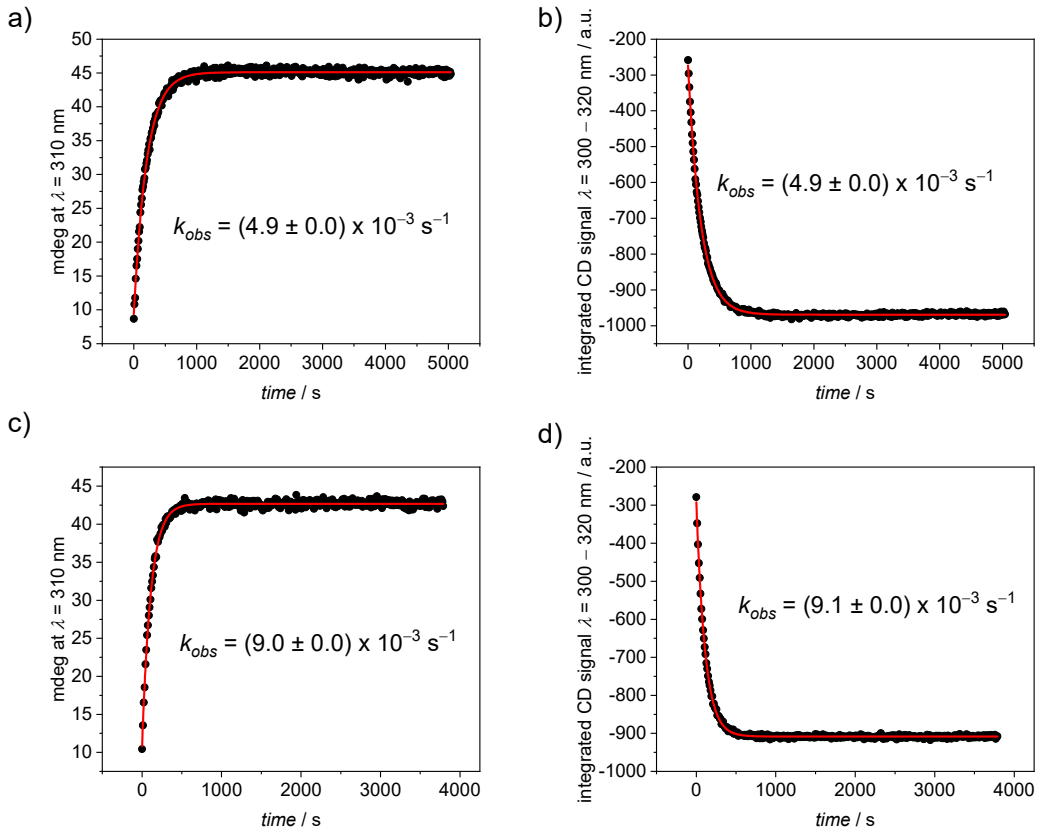

Figure A59. Time-dependent CD course (1 cm cuvette) and the corresponding integrated area from λ = 300 – 320 nm of *M*-[5]helicene (c = 10 µM) in the presence of two equivalents of **1-*PP*** in CCl_4 at a)–b) 288 K and c)–d) 295 K.

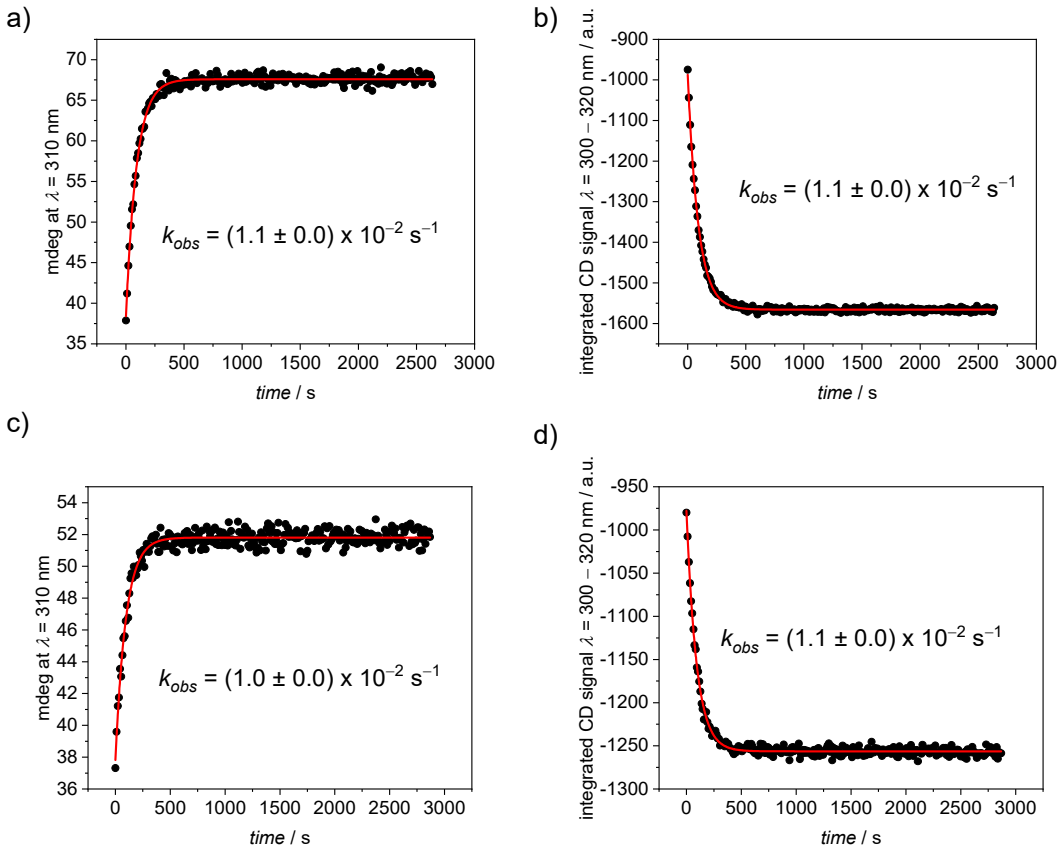

Figure A60. Time-dependent CD course and the corresponding integrated area from λ = 300 – 320 nm of *M*-[5]helicene in CCl_4 (c = 10 µM) in the presence of a)–b) five (1 cm cuvette) and c)–d) ten equivalents (0.5 cm cuvette) of **1-*PP*** in tetrachloromethane at 295 K.

The barriers for the enantiomerization process were calculated according to equation A4 with $k_{obs} = k_{rac} = 2k_e$ for pure *M*-[5]helicene and in the presence of **1-*MP***. For *M*-[5]helicene in the presence of **1-*PP*** $k_{obs} = k_e$.

$$\Delta G^{\ddagger} = -RT\ln(k_e h/k_b T) \tag{A4}$$

For the determination of the thermodynamic data, an Eyring analysis was carried out according to equation A5.

$$\ln\frac{k_e}{T} = -\left(\frac{\Delta H^{\ddagger}}{R}\right)\frac{1}{T} + \frac{\Delta S^{\ddagger}}{R} + ln\frac{k_b}{h} \tag{A5}$$

From the linear curve fit, one can determine the thermodynamic parameters.

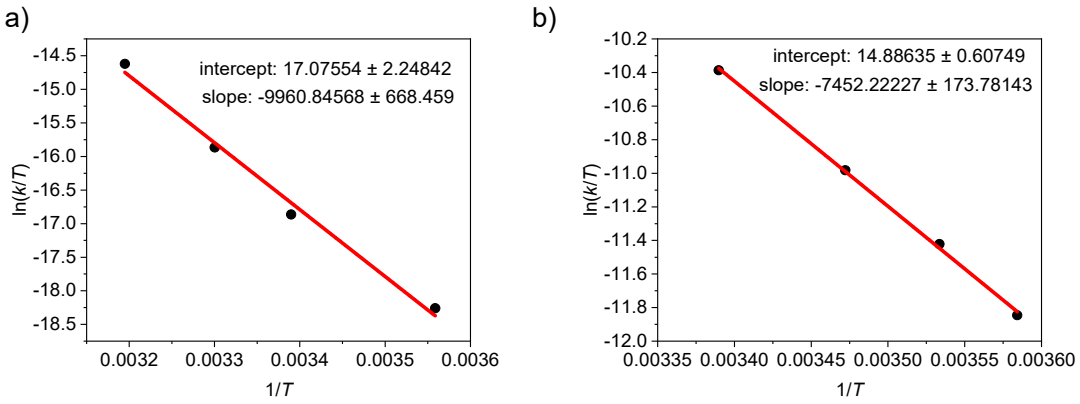

Figure A61. Eyring plot for the enantiomerization process of *M*-[5]helicene in the a) absence and b) presence of **1-*PP***. The enthalpy is calculated according to $\Delta H^{\ddagger} = -R \times$ slope. The entropy is calculated according to $\Delta S^{\ddagger} = R \times$ [(y-intercept)-ln(k_b/h)] with the Boltzmann constant k_b and Planck's constant h.

Table A2. Summary of thermodynamic data for catalyzed and uncatalyzed [5]helicene enantiomerization. Enthalpy and entropy were obtained from Eyring analysis (see Figure A61).

	$\Delta H^{\ddagger}$ [kJ mol^{-1}]	$\Delta S^{\ddagger}$ [J mol^{-1} K^{-1}]	$\Delta G^{\ddagger}$ (295 K)[a)] [kJ mol^{-1}]
M-[5]helicene	82.8	–55.6	99.2
M-[5]helicene + **1-*PP***	62.0	–73.8	83.8

a) Calculated according to $\Delta G^{\ddagger} = \Delta H^{\ddagger} - T\Delta S^{\ddagger}$ with T = 295 K.

NMR Studies

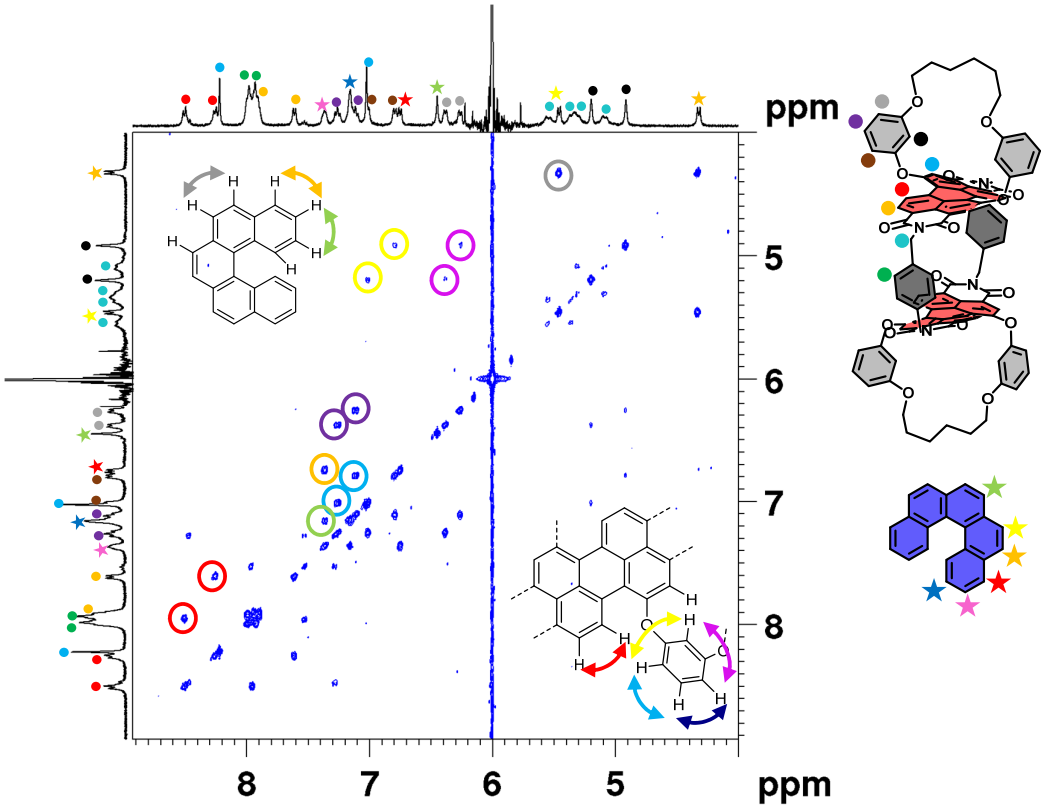

Figure A62. a) ^{1}H-^{1}H COSY NMR spectrum (600 MHz, 245 K) of [5]helicene⊂**1-*PP*** ($c \approx 1.0$ mM) in tetrachloroethane-d_2. The important cross signals are marked in the same colour as the arrows that indicate the corresponding coupling. The guest proton in the 1-position could not be resolved.

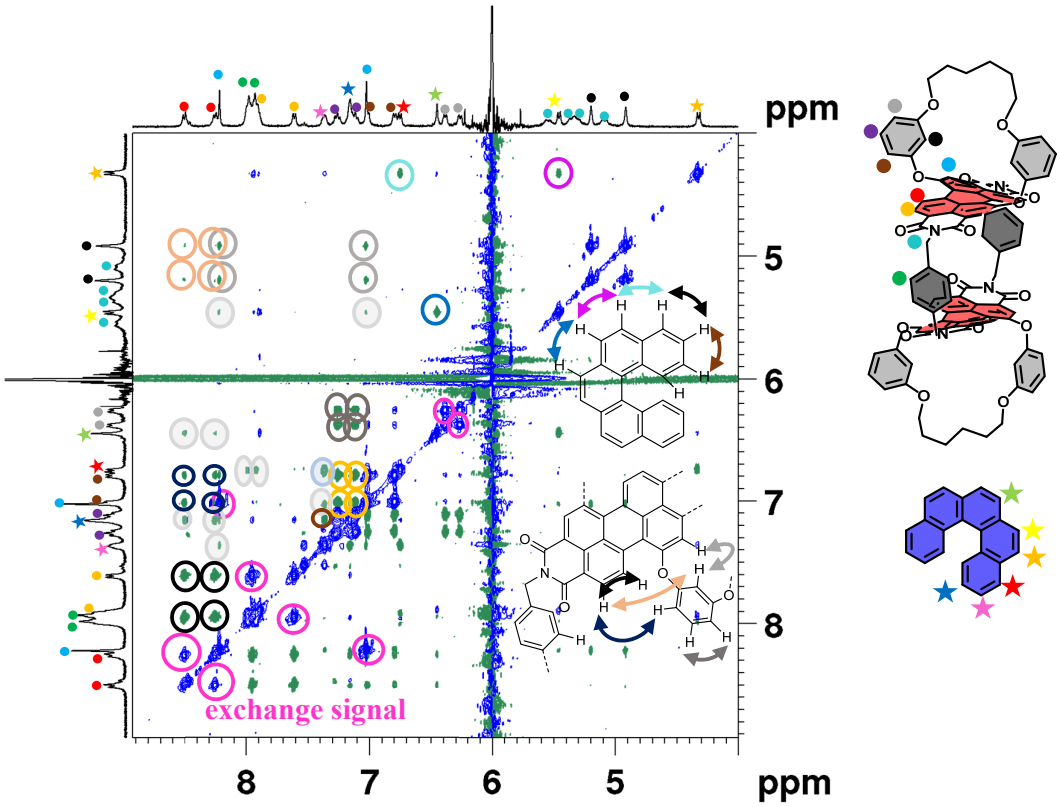

Figure A63. ^{1}H-^{1}H ROESY NMR spectrum (600 MHz, 245 K) of [5]helicene⊂**1-*PP*** ($c \approx 1.0$ mM) in tetrachloroethane-d_2. The important cross signals are marked in the same colour as the arrows that indicate the corresponding coupling. The host-guest through space correlations are marked with a filled grey circle. The guest proton in the 1-position could not be resolved.

Supporting note on guest rotation in the cyclophane

We could assign the dynamic conformational change observed in our NMR studies to a rotation of the guest within the cavity along an axis perpendicular to the chromophore plane as schematically illustrated in Figure A64.

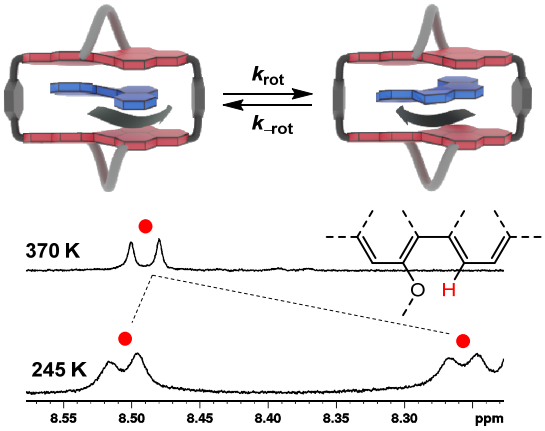

Figure A64. Schematic representation of the rotational motion by 180° around the *z*-axis of [5]helicene within the cavity of **1-*PP*** with an excerpt of the resulting ^{1}H NMR (400 MHz) at high and low temperatures.

Accordingly, we carried out variable temperature NMR studies in order to gain further insights into this rotational motion. As apparent from Figure A64 and Figure A65, the host protons, e.g. the bay protons in the 2 and 8 positions marked in red, which are split into two at low temperatures, give only one signal at 370 K. From the signal splitting at 245 K ($\Delta\nu$ = 100 Hz) and the coalescence temperature T_c = 279 K, we determined a barrier of $\Delta G^{\ddagger}$ = 55.6 kJ mol^{-1} for this process (see equation A6), corresponding to a rate constant $k_{rot} = k_{-rot}$ = 222 s^{-1} at the coalescence according to equation A7. A very similar barrier for this process was furthermore determined *via* ^{1}H-^{1}H EXSY NMR spectroscopy at 245 K (Figure A69) with the intensity of the cross and diagonal signals for two selected host protons according to equation A8. This explanation is also supported by the fact that no signal splitting at low temperatures can be observed for the smaller but structurally related carbohelicene congener [4]helicene (Figure A66), which is reasonable due to the lower steric demand of this guest and accordingly a lower barrier for the rotation. Hence, despite the structural and thermodynamic similarity of these two complexes,[193] we conclude a faster rotation of the smaller carbohelicene congener in the cyclophane cavity. We also compared the proton spectra of [4]- and [5]helicene in the presence of an excess of the host at low temperatures (Figure A67), which yielded two and three

sets of signals for our host, respectively. Hence, while the observed rotation of the guest is indeed slow for [5]helicene and fast for [4]helicene on the NMR time scale, we observe a slow guest exchange for both complexes, which rules out the guest exchange being the origin of the signal splitting of the 1:1 host:guest mixture. This outcome is also supported by a temperature series of a mixture with an excess of host, revealing an elevated coalescene temperature of around 313 K for the guest exhange (Figure A68) compared to the guest's rotational motion.

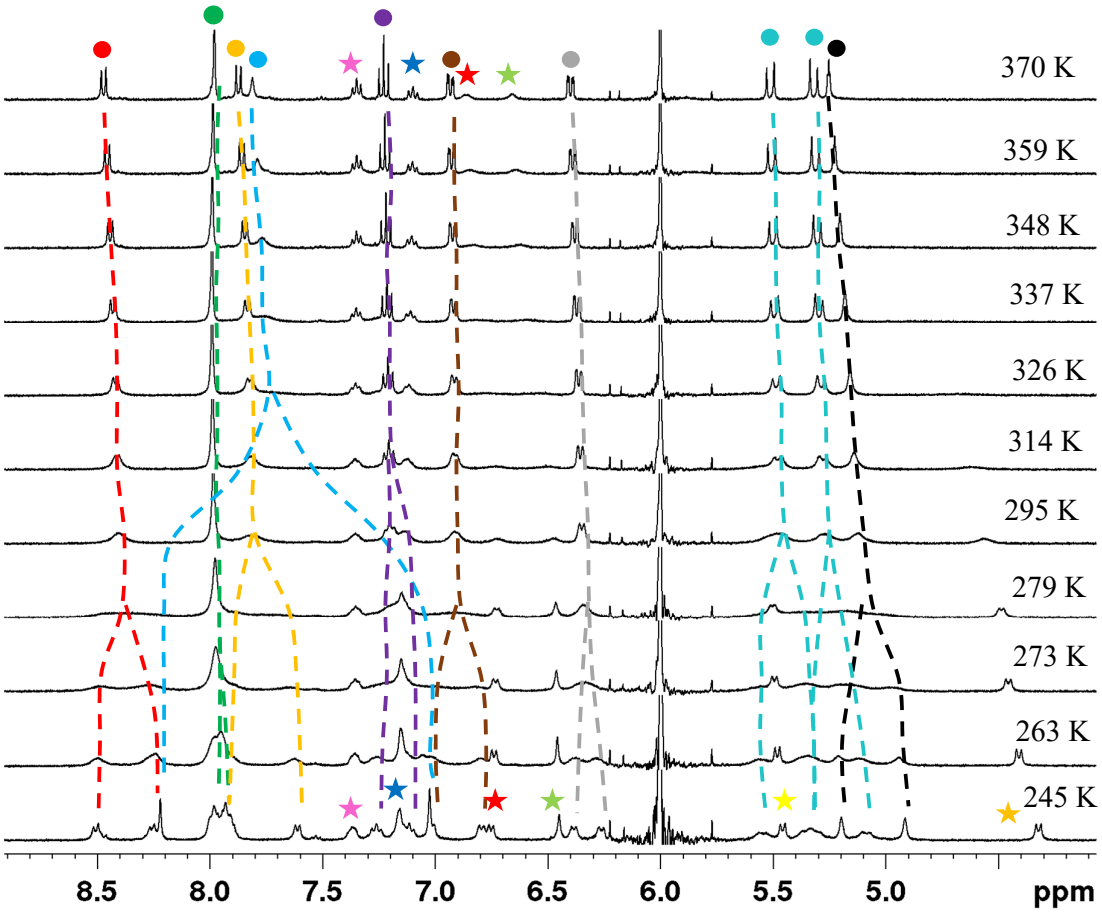

Figure A65. Variable-temperature NMR (400 MHz) study of **1-*PP*** in the presence of one equivalent of [5]helicene in TCE-d_2 (c (**1-*PP***) ≈ 1.0 mM). The proton signals marked with a yellow and orange star could not be resolved at higher temperatures.

The barrier for the rotational movement was calculated according to equation A6 with the ideal gas constant R, the coalescene temperature T_c (279 K) and the Avogadro constant N_A:[314]

$$\Delta G^{\ddagger} = RT_c \ln\left(\frac{RT_c\sqrt{2}}{\pi N_A h \Delta\nu}\right) \quad \text{(A6)}$$

At the coalescence temperature the rate constant k can be calculated according to:

$$k = \frac{\pi \Delta \nu}{\sqrt{2}} \quad \text{(A7)}$$

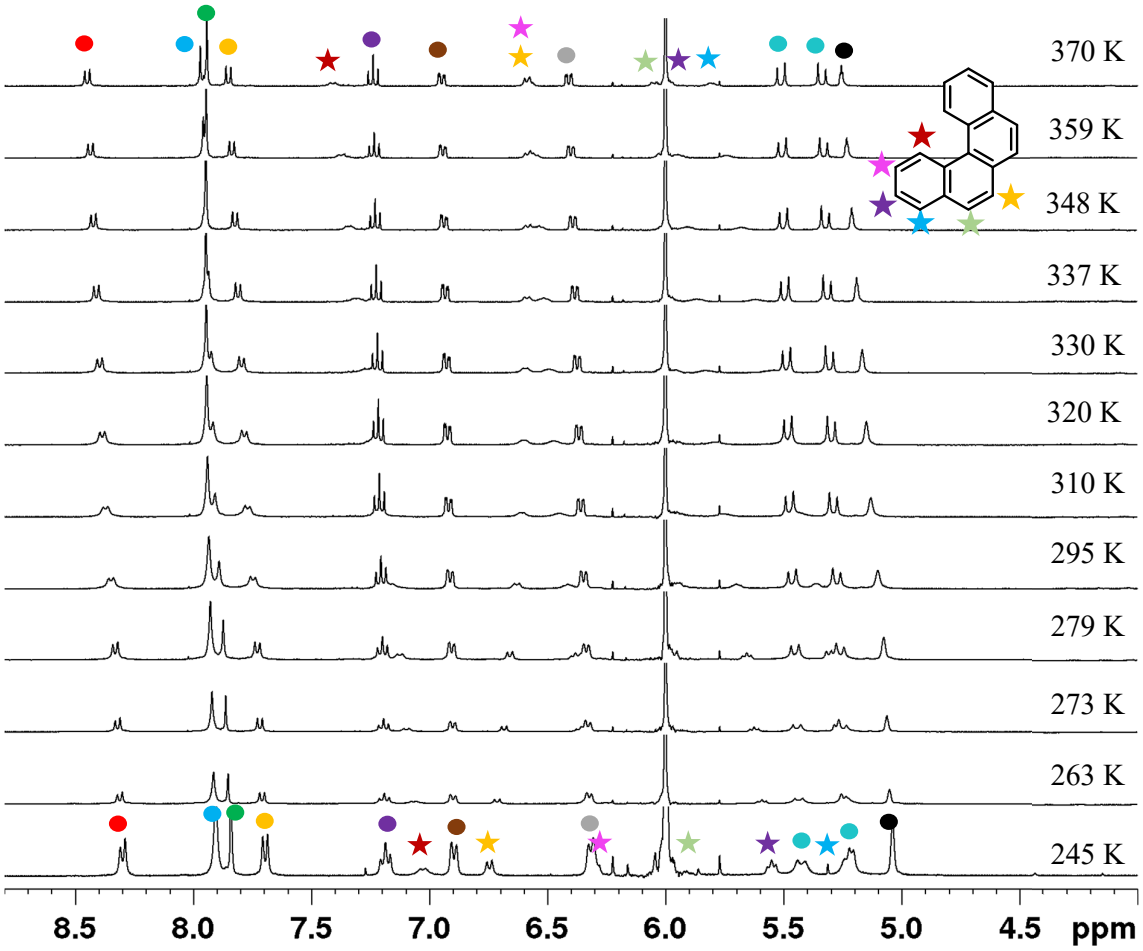

Figure A66. Variable-temperature NMR (400 MHz) study of **1-*PP*** in the presence of one equivalent of [4]helicene in TCE-d_2 (c (**1-*PP***) ≈ 3.0 mM).

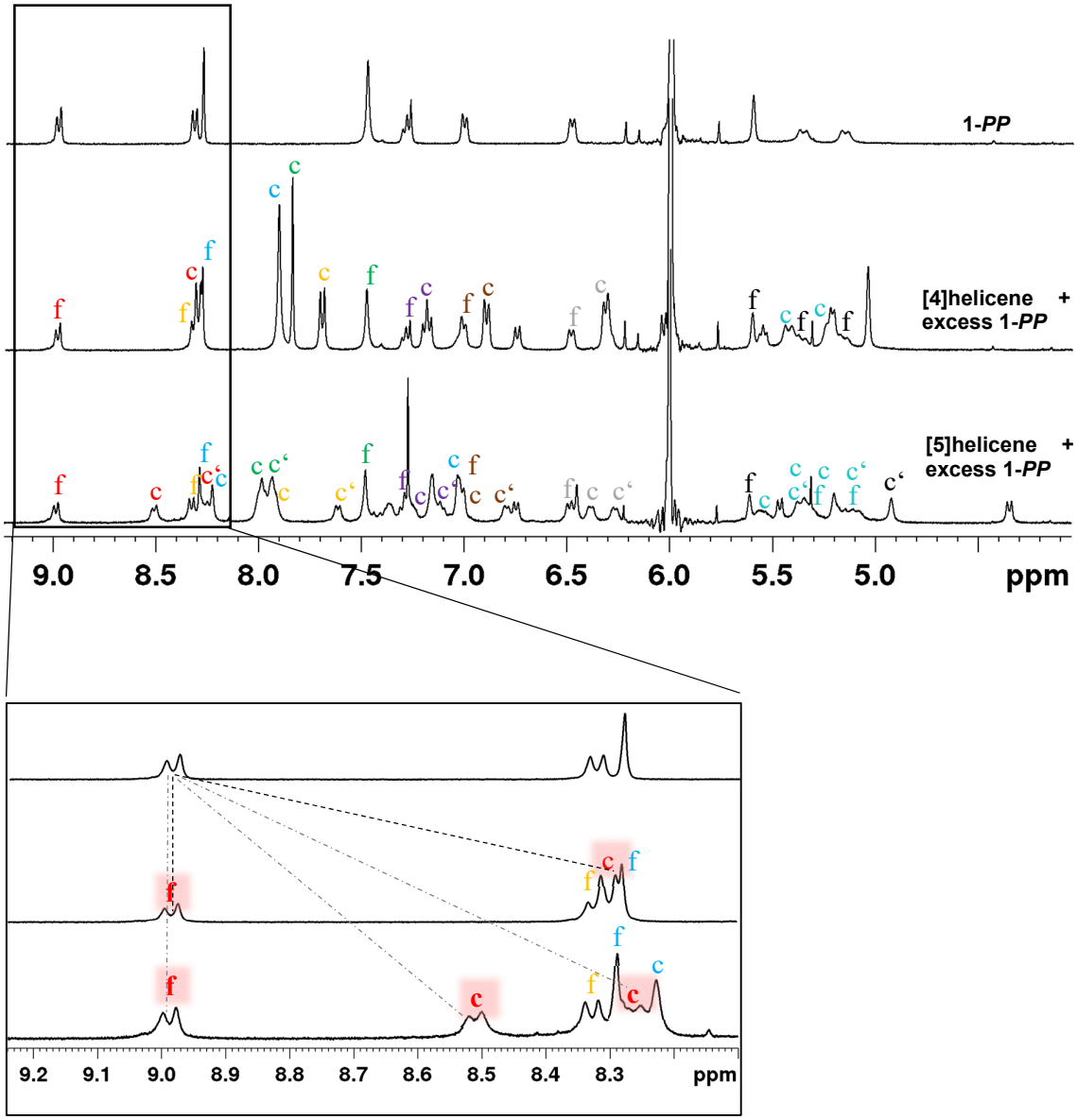

Figure A67. Low-temperature NMR (245 K, 400 MHz) spectrum of **1-*PP*** and of a mixture of [4]helicene and [5]helicene in the presence of an excess of **1-*PP*** in TCE-d_2. The letters "*f*" and "*c*" describe the signals as protons belonging to the free host (*f*) or to the complex (*c*).

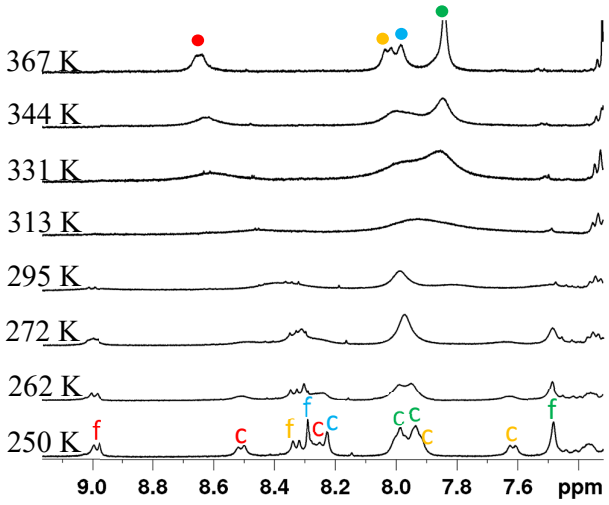

Figure A68. Excerpt of variable-temperature NMR (400 MHz) study of **1-*PP*** in the presence of 0.5 equivalent of [5]helicene in TCE-d_2 (c (**1-*PP***) ≈ 1.0 mM).

EXSY NMR Experiments[v]

All experiments were carried out with an equilibrated 1:1 host:guest (**1-*PP***:[5]helicene) mixture at 245 K, where the exchange observed in the standard proton NMR spectra is slow on the NMR time scale.

For the ^{1}H-^{1}H EXSY measurements, two host protons that split into two well separated signals were chosen in each case with defined cross and diagonal peaks that describe the exchange between them (Figure A69). Since the rotation of [5]helicene in the host can be approximated as an equally populated 2-site exchange (where the reaction and the backward reaction have the same barrier), explicit equations published for this case[315] that can be rearranged were used to obtain equation A8.

$$k_{rot} = -\ln[(D-C)/(D+C)]/(2\tau) \qquad \text{(A8)}$$

(D: average intensity of diagonal signal, C: average intensity of cross signal, τ = mixing time)

In addition, T_1 measurements were carried out to make sure that the spin-lattice relaxation times for the two split signals are similar, which is a prerequisite to apply equation A8 (for this purpose, a standard inversion recovery pulse sequence with a recycle delay time of at least 5 × T_1 was applied) and which turned out to be the case for the system under investigation.

[v] Performed by Dr. Matthias Grüne

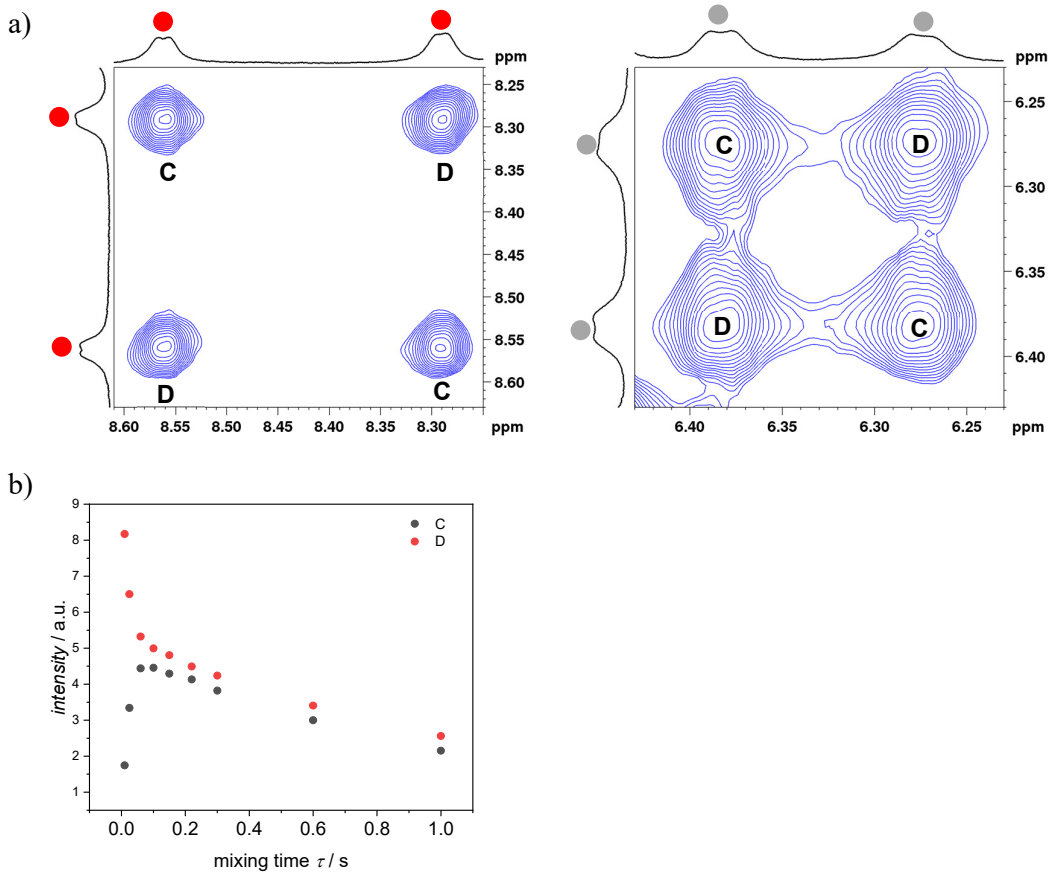

Figure A69. (a) Segments of a ^{1}H-^{1}H EXSY NMR spectrum (600 MHz) of an equilibrated 1:1 mixture of **1-*PP*** (c ≈ 0.5 mM) and [5]helicene at 245 K in $CDCl_3$ for τ = 300 ms. (b) Dependence of the averaged intensities of the diagonal (D) and cross (C) signals on the mixing time τ for the left segment of Figure A69a.

However, two assumptions for equation A8 are not fulfilled completely: (1.) In addition to the rotational exchange mechanism of [5]helicene within the host, a guest exchange exists which is, however, much slower (*vide supra*). (2.) The supposition of considering only isolated I = ½ spins[315] is not valid. In addition, the ratio of the cross and diagonal peak intensity only slightly deviates from one for long mixing times (Figure A69b) and thus becomes insensitive to the exchange rates. As a consequence, we quantitatively evaluated only the EXSY spectra with short mixing times (10–25 ms, initial rate approximation) to obtain an estimation of the rate constant.

The results are summarized in Table A3 and yield an average k_{rot} of 23.8 s^{-1} for the rotation of [5]helicene within the host at 245 K in $CDCl_3$ being a factor of about ten times smaller than at 279 K (coalescence temperature for this internal motion at 400 MHz resonance frequency) in

TCE-d_2. With equation A4 ($\Delta G^{\ddagger} = -RT\ln(k_{rot}h/k_bT)$) and the average of k_{rot}, a barrier of $\Delta G^{\ddagger} = 53.1$ kJ mol^{-1} is calculated for $CDCl_3$ as solvent at 245 K. This fits quite well with the result of $\Delta G^{\ddagger} = 55.6$ kJ mol^{-1} obtained for the solvent TCE-d_2 at 279 K calculated by equation A6.

Table A3. Overview over rate constants k_{rot}, determined from ^{1}H-^{1}H EXSY NMR at 245 K according to equation A8 for short mixing times τ.

mixing time τ [s]	k_{rot} [s^{-1}] (red proton)	k_{rot} [s^{-1}] (grey proton)
0.010	21.7	27.5
0.025	22.7	23.3
	average: 22.2	average: 25.4
	average: 23.8	

Single Crystal X-ray Analysis[vi]

The crystal of **1-*MP*** was grown in a borosilicate glass tube (10 mm × 75 mm) by slow diffusion of *n*-hexane into a chlorobenzene solution.

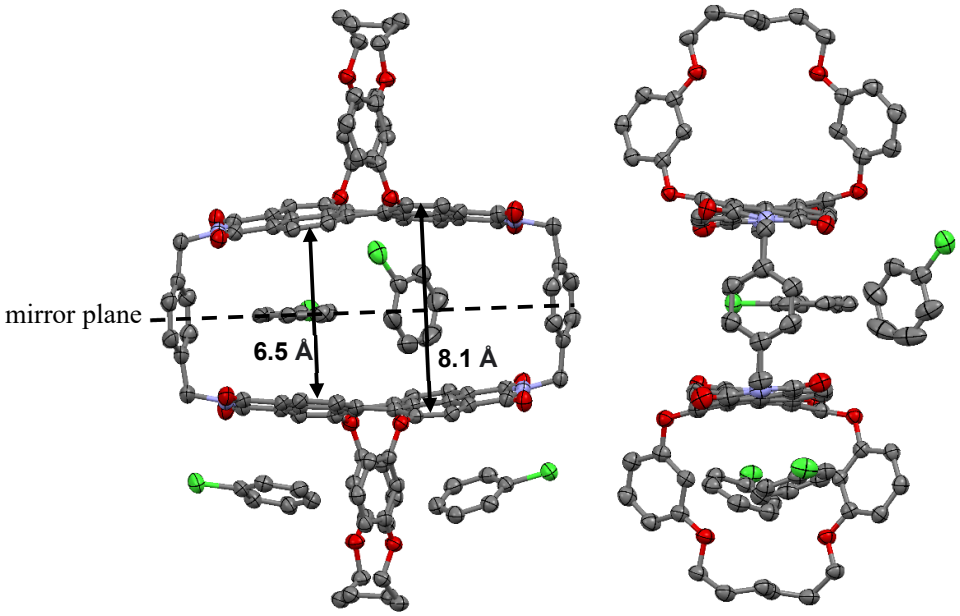

Figure A70. Molecular structure of **1-*MP*** from X-ray single crystal analysis (thermal ellipsoids set at 50% probability). Hydrogen atoms are omitted for clarity.

[vi] Perormed by Dr. Kazutaka Shoyama (see Individual Contribution)

Table A4. Single Crystal X-ray data for **1-*MP***.

Identification code	CCDC 2221170
Empirical formula	$C_{148}H_{108}Cl_8N_4O_{16}$
Formula weight	2482.21
Temperature	100(2) K
Wavelength	0.61991 Å
Crystal system	Triclinic
Space group	$P\bar{1}$
Unit cell dimensions	a = 12.895(2) Å
	b = 14.9380(19) Å
	c = 15.718(3) Å
Volume	2947.1(8) Å^3
Z	1
Density (calculated)	1.398 g/cm^3
Absorption coefficient	0.183 mm^{-1}
F(000)	1288.1
Crystal size	0.020 × 0.020 × 0.020 mm^3
Theta range for data collection	1.157 to 28.029°
Index ranges	$-19 \le h \le 19$, $-19 \le k \le 19$, $-21 \le l \le 20$
Reflections collected	106344
Independent reflections	16684 [R(int) = 0.0772]
Completeness to theta = 21.836°	99.1%
Absorption correction	None
Refinement method	Full-matrix least-squares on F^2
Data / restraints / parameters	16684 / 787 / 961
Goodness-of-fit on F^2	1.038
Final R indices [$I > 2\sigma(I)$]	R_1 = 0.0659, wR_2 = 0.1819
R indices (all data)	R_1 = 0.0884, wR_2 = 0.2026

The co-crystal of **1-*PP*** and [5]helicene (~5 eq.) was grown in a borosilicate glass tube (10 mm × 75 mm) by slow diffusion of *n*-hexane into a chlorobenzene solution and was obtained as a red, fluorescent block:

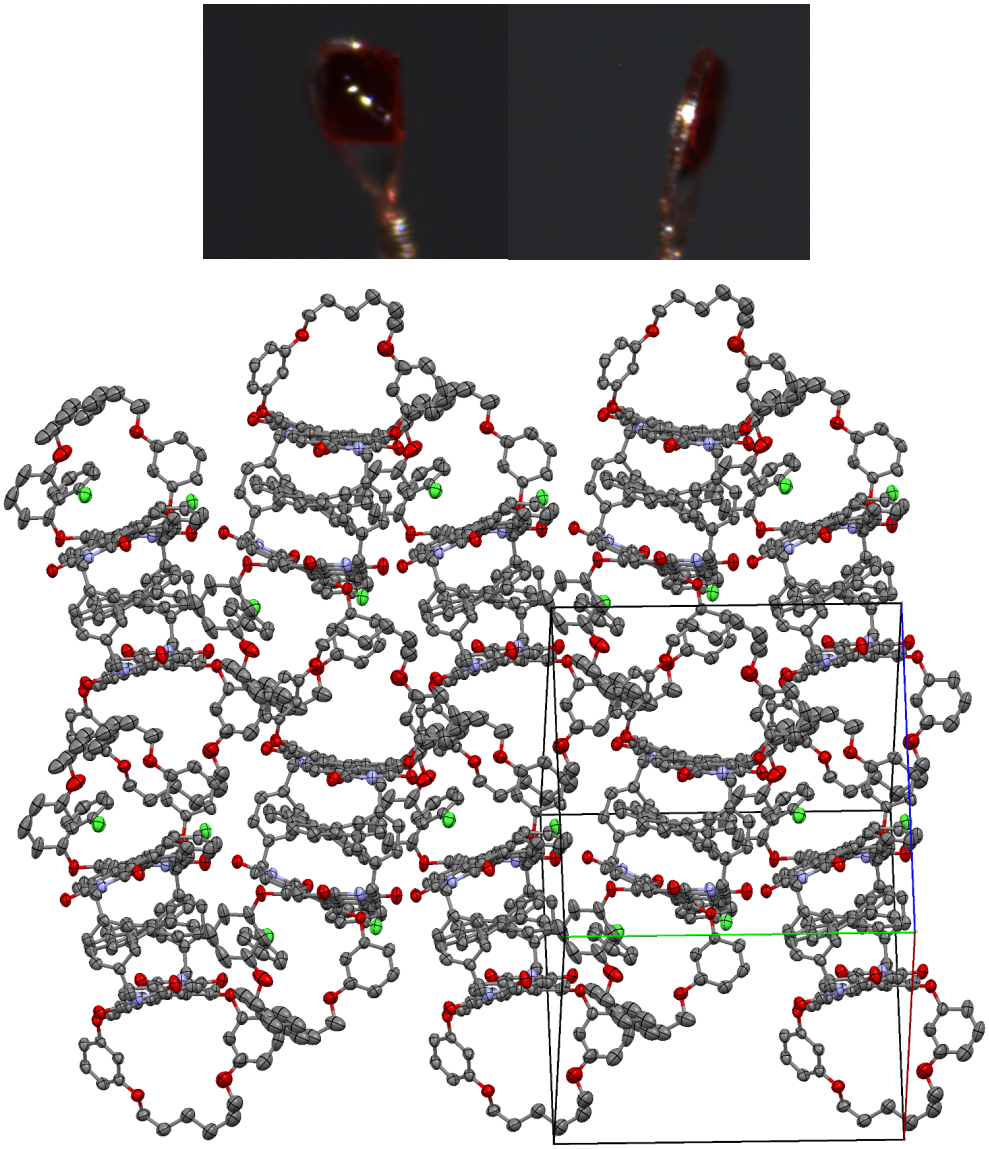

Figure A71. a) Images of the crystals of *P*-[5]helicene⊂**1-*PP***. b) Molecular structure of *P*-[5]helicene⊂**1-*PP*** from X-ray single crystal analysis (thermal ellipsoids set at 50% probability). Hydrogen atoms are omitted for clarity.

Table A5. Single Crystal X-ray data for *P*-[5]helicene⊂**1**-***PP***.

Identification code	CCDC 2221169
Empirical formula	$C_{134}H_{192}Cl_2N_4O_{16}$
Formula weight	2085.01
Temperature	100(2) K
Wavelength	1.54178 Å
Crystal system	Monoclinic
Space group	*P2* (1)
Unit cell dimensions	a = 16.6815(11) Å b = 19.2666(11) Å c = 19.9658(14) Å
Volume	6099.5(7) Å^3
Z	2
Density (calculated)	1.135 g/cm^3
Absorption coefficient	0.988 mm^{-1}
F(000)	2172
Crystal size	0.178 × 0.131 × 0.035 mm^3
Theta range for data collection	2.328 to 74.314°
Index ranges	$-20 \le h \le 20$, $-23 \le k \le 23$, $-24 \le l \le 24$
Reflections collected	73201
Independent reflections	23878 [R(int) = 0.0798]
Completeness to theta = 67.679°	100%
Absorption correction	Semi-empirical from equivalents
Refinement method	Full-matrix least-squares on F^2
Data / restraints / parameters	23878 / 417 / 1431
Goodness-of-fit on F^2	1.008
Final R indices [$I > 2\sigma(I)$]	R_1 = 0.0653, wR_2 = 0.1708
R indices (all data)	R_1 = 0.0927, wR_2 = 0.1930

Computational Methods[vii]

The geometries of equilibrium and transition structures along the PESs of interest were fully optimized at the B3LYP-D3(BJ)/def2-SVP level of theory.[240-242, 244-246, 316] Frequency calculations at the same level of theory were performed on all resulting structures to confirm them as equilibrium structures, having all real frequencies, or transition structures, having a single imaginary frequency along the reaction coordinate of the enantiomerization of interest. To further confirm the connectivities of the located transition structures to the reactant and product minima of interest, intrinsic reaction coordinate (IRC) calculations[317-318] were carried out at the B3LYP-D3(BJ)/def2-SVP level of theory. The resulting IRC paths are given in Figures A72–A74. To subsequently obtain more accurate enantiomerization barriers and supramolecular complexation energies, single point energy calculations were performed on the optimized structures at the PW6B95-D3(BJ)/def2-TZVPP level of theory.[244-247] In addition, corrections for bulk solvent effects of the experimentally used solvent tetrachloromethane were obtained using the SMD continuum solvation model[248] at the M05-2X/6-31G(d) level of theory as recommended in reference [248]. In order to obtain more detailed insights into the noncovalent interactions between hosts and guests, EDAs (energy decomposition analyses) were carried out using the second generation of the ALMO-EDA scheme[250] using the ωB97M-V functional[251] as recommended in reference [250] in conjunction with the Def2-SVP basis set.[244] All geometry optimizations, frequency, IRC and single point energy calculations were carried out using the Gaussian16 software package.[319] EDAs were performed using QChem 5.2.[320] 3D representations of optimized structures were generated using Mercury.[321]

[vii] Performed by Dr. Asja Kroeger

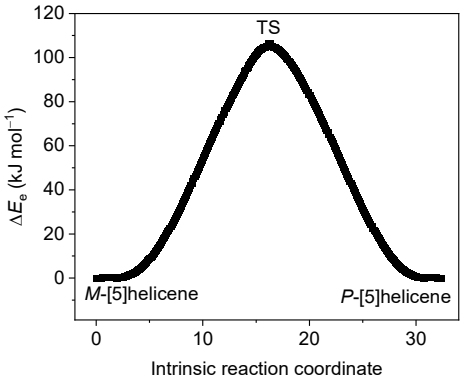

Figure A72. Intrinsic reaction coordinate for the uncatalyzed enantiomerization of [5]helicene, obtained at the B3LYP-D3(BJ)/Def2-SVP level of theory. Electronic energy (ΔE_e) is given relative to the energy of the optimized reactant.

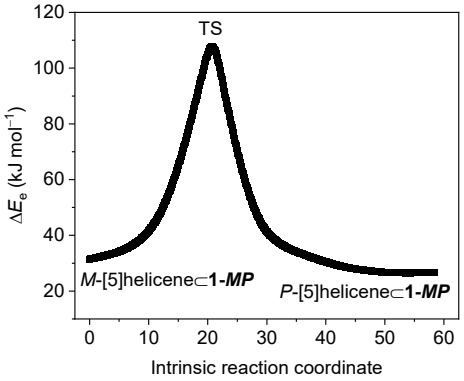

Figure A73. Intrinsic reaction coordinate for the enantiomerization of [5]helicene within **1-*MP***, obtained at the B3LYP-D3(BJ)/Def2-SVP level of theory. Electronic energy (ΔE_e) is given relative to the energy of the optimized reactant complex.

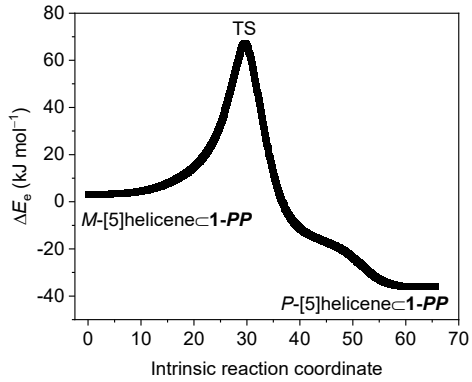

Figure A74. Intrinsic reaction coordinate for the enantiomerization of [5]helicene within **1-*PP***, obtained at the B3LYP-D3(BJ)/Def2-SVP level of theory. Electronic energy (ΔE_e) is given relative to the energy of the optimized reactant complex.

Table A6. Breakdowns of the intermolecular interaction energies (ΔE_{INT}) between the **1-*PP*** and **1-*MP*** hosts and [5]helicene guests in reactant, transition structure, and product complexes obtained from second generation ALMO-EDA at the ωB97MV/Def2-SVP level of theory in kJ mol^{-1}.

Structure	ΔE_{PAULI}	ΔE_{ELEC}	ΔE_{DISP}	ΔE_{POL}	ΔE_{CT}	ΔE_{INT}
M-[5]helicene⊂**1-*MP***	486.9	–307.0	–397.6	–11.7	–14.9	–244.4
[5]helicene⊂**1-*MP*** *(TS)*	481.8	–304.2	–389.1	–13.4	–16.9	–241.8
M-[5]helicene⊂**1-*PP***	455.8	–287.4	–377.2	–11.0	–14.4	–234.2
[5]helicene⊂**1-*PP*** *(TS)*	583.8	–370.7	–440.5	–15.0	–17.1	–259.4
P-[5]helicene⊂**1-*PP***	529.5	–335.5	–420.5	–12.8	–16.8	–256.0

Table A7. Differences in electronic energies between corresponding host and guest structures from free optimizations and from optimizations of reactant complexes (RC), transition structure complexes (TS), and product complexes (PC), as well as sums of destabilizations calculated for each complex in kJ mol^{-1}.

	RC$_{host}$	**RC$_{guest}$**	**TS$_{host}$**	**TS$_{guest}$**	**PC$_{host}$**	**PC$_{guest}$**	**∑RC**	**∑TS**	**∑PC**	**RC-TS**
1-*PP*	2.2	14.6	1.9	9.8	0.8	7.0	16.8	11.7	7.8	5.1
1-*MP*	7.1	9.1	4.5	11.2	7.1	9.1	16.2	15.7	16.2	0.5

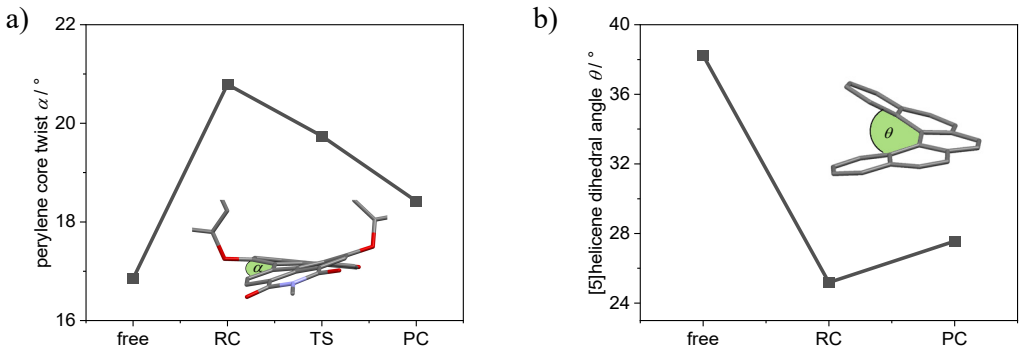

Figure A75. Plot of a) average core twist of the two PBI units in the cyclophane **1-*PP*** and b) the dihedral angle that the outer naphthalene units of [5]helicene span, obtained from the DFT calculated structures.

9.3 Appendix for Chapter 5: Mutual Induced Fit Transition Structure Stabilization of Corannulene's Bowl-to-Bowl Inversion

General Methods

Chemicals: All chemicals and solvents were purchased from commercial suppliers and used without further purification. **1-*PP*** and ethylcorannulene were synthesized according to literature known procedures.[50, 193, 322]

NMR spectroscopy: ^{1}H NMR spectra were recorded on a Bruker Avance III HD 600 MHz spectrometer. Chemical shift data are reported in parts per million (ppm, δ scale) downfield from tetramethylsilane and referenced internally to the residual proton (for proton NMR) in the solvent (CD_2Cl_2: $\delta = 5.32$).

UV/vis absorption spectroscopy: All spectroscopic measurements were carried out under ambient conditions using solvents of spectroscopic grade. The absorption spectra were recorded on a JASCO V-770 or V-670 spectrometer equipped with a PAC-743R Peltier for temperature control.

Steady-State Fluorescence Spectroscopy: Fluorescence spectra were recorded on an Edinburgh Instruments FLS981 fluorescence spectrometer.

Single crystal X-ray analysis: The diffraction images for X-ray crystallographic analysis were collected on a Bruker D8 Quest Kappa diffractometer with a Photon II CMOS detector and multi-layered mirror monochromated Cu Kα radiation.

DFT calculations: The geometries of equilibrium and transition structures along the PESs of interest were fully optimized at the B3LYP-D3(BJ)/def2-SVP level of theory.[240-242, 244-246, 316] Frequency calculations at the same level of theory were performed on all resulting structures to confirm them as equilibrium structures, having all real frequencies, or transition structures, having a single imaginary frequency along the reaction coordinate of the enantiomerization of interest. To further confirm the connectivities of the located transition structures to the reactant and product minima of interest, intrinsic reaction coordinate (IRC) calculations[317-318] were carried out at the B3LYP-D3(BJ)/def2-SVP level of theory. To subsequently obtain more accurate isomerization barriers and supramolecular complexation energies, single point energy calculations were performed on the optimized structures at the PW6B95-D3(BJ)/def2-TZVPP level of theory.[244-247] In addition, corrections for bulk solvent effects of the experimentally

used solvent tetrachloromethane were obtained using the SMD continuum solvation model[248] at the M05-2X/6-31G(d) level of theory as recommended in reference [248]. All geometry optimizations, frequency, IRC and single point energy calculations were carried out using the Gaussian16 software package.[319]

Titration Studies

For the titration experiments, a solution of PBI cyclophane **1-*PP*** and the respective guest in excess (see corresponding graphs for exact amount of the individual guest) was titrated to a solution of the pure cyclophane in the same solvent (mixture) of the same concentration keeping the host concentration constant during the experiment. The UV/vis or fluorescence titration data were fitted to a 1:1 binding model.[143] Data evaluation was furthermore performed by using *bindfit*.[323]

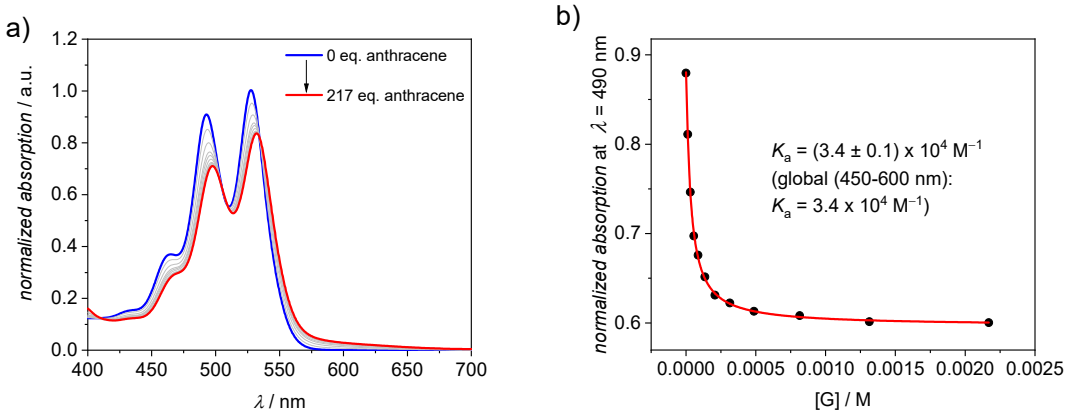

Figure A76. a) UV/vis spectra of cyclophane **1-*PP*** in $CHCl_3$ at 22 °C (c = 10 x 10^{-6} M) upon the addition of anthracene as a guest and b) the resulting plot of the absorption at λ = 490 nm with nonlinear curve fit (1:1 binding model, red curve).

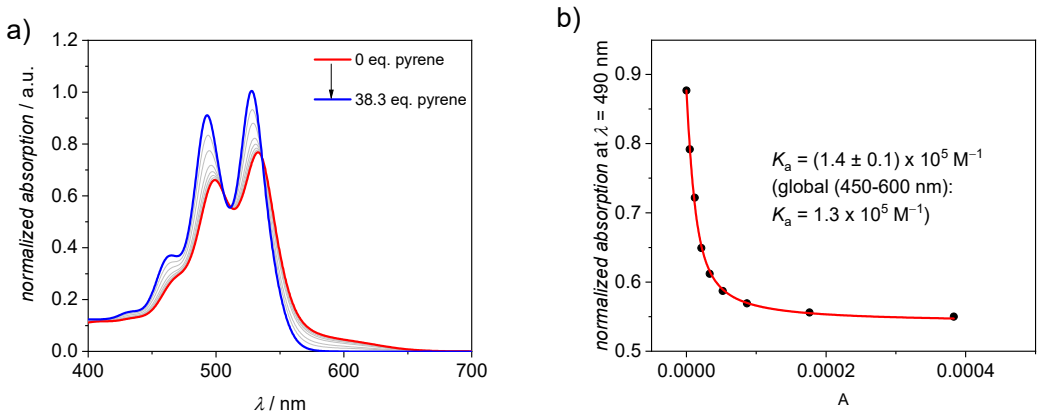

Figure A77. a) UV/vis spectra of cyclophane **1-*PP*** in $CHCl_3$ at 22 °C (c = 10 x 10^{-6} M) upon the addition of pyrene as a guest and b) the resulting plot of the absorption at λ = 490 nm with nonlinear curve fit (1:1 binding model, red curve).

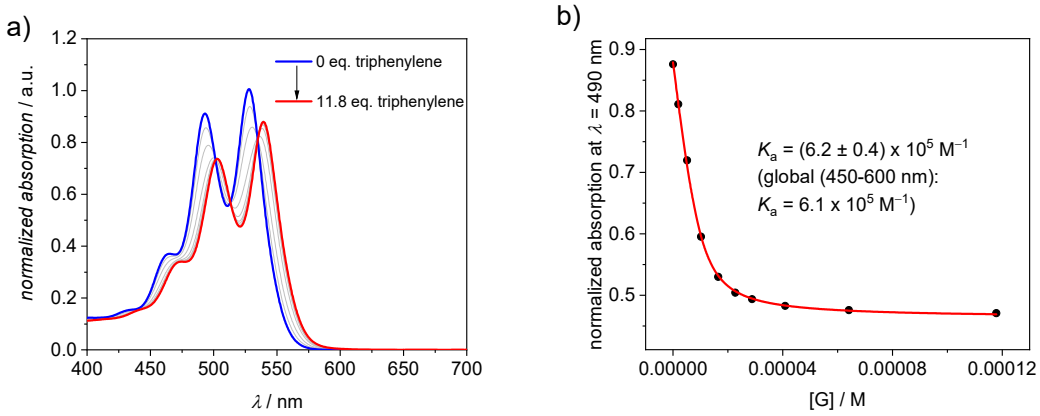

Figure A78. a) UV/vis spectra of cyclophane **1-*PP*** in $CHCl_3$ at 22 °C (c = 10 x 10^{-6} M) upon the addition of triphenylene as a guest and b) the resulting plot of the absorption at λ = 490 nm with nonlinear curve fit (1:1 binding model, red curve).

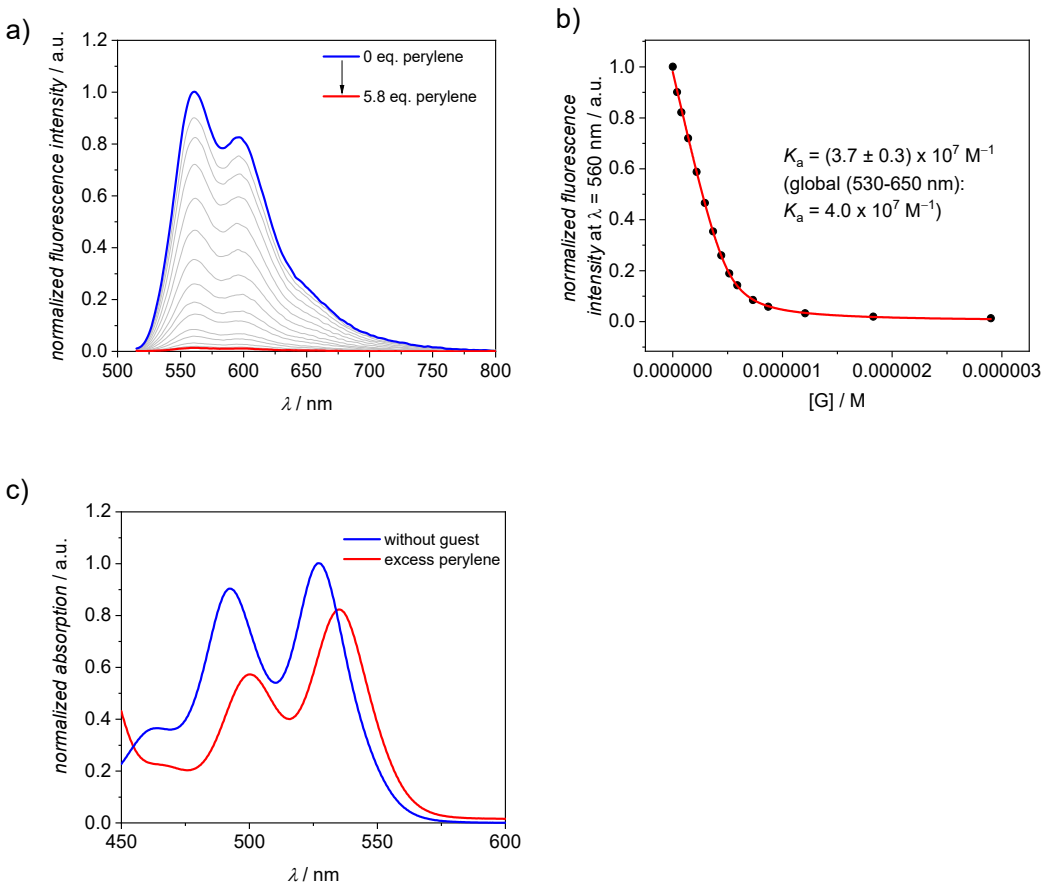

Figure A79. a) Fluorescence spectra (λ_{exc} = 507 nm) of cyclophane **1-*PP*** in $CHCl_3$ at 22 °C (c = 5 x 10^{-7} M) upon the addition of perylene as a guest and b) the resulting plot of the fluorescence at λ = 560 nm with nonlinear curve fit (1:1 binding model, red curve). c) UV/vis spectrum of free **1-*PP*** and perylene⊂**1-*PP*** in chloroform at 22 °C.

b)

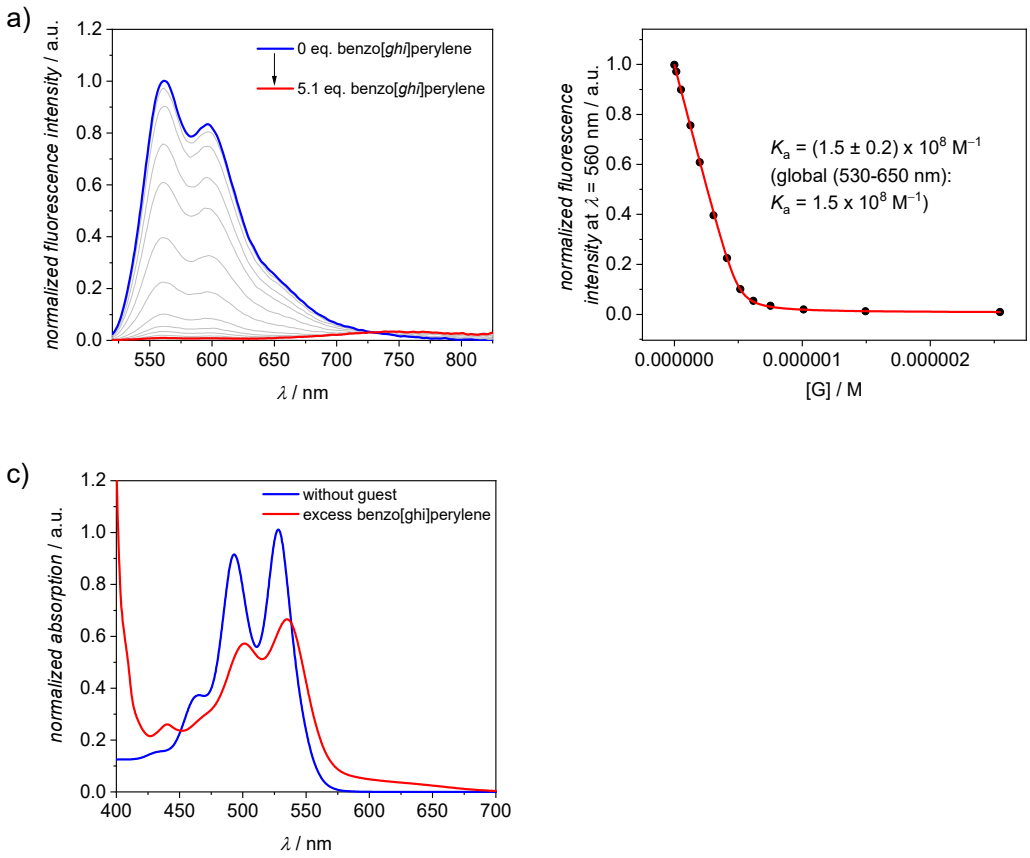

Figure A80. a) Fluorescence spectra (λ_{exc} = 510 nm) of cyclophane **1-*PP*** in $CHCl_3$ at 22 °C (c = 5 x 10^{-7} M) upon the addition of benzo[*ghi*]perylene as a guest and b) the resulting plot of the fluorescence at λ = 560 nm with nonlinear curve fit (1:1 binding model, red curve). c) UV/vis spectrum of free **1-*PP*** and benzo[*ghi*]perylene⊂**1-*PP*** in chloroform at 22 °C.

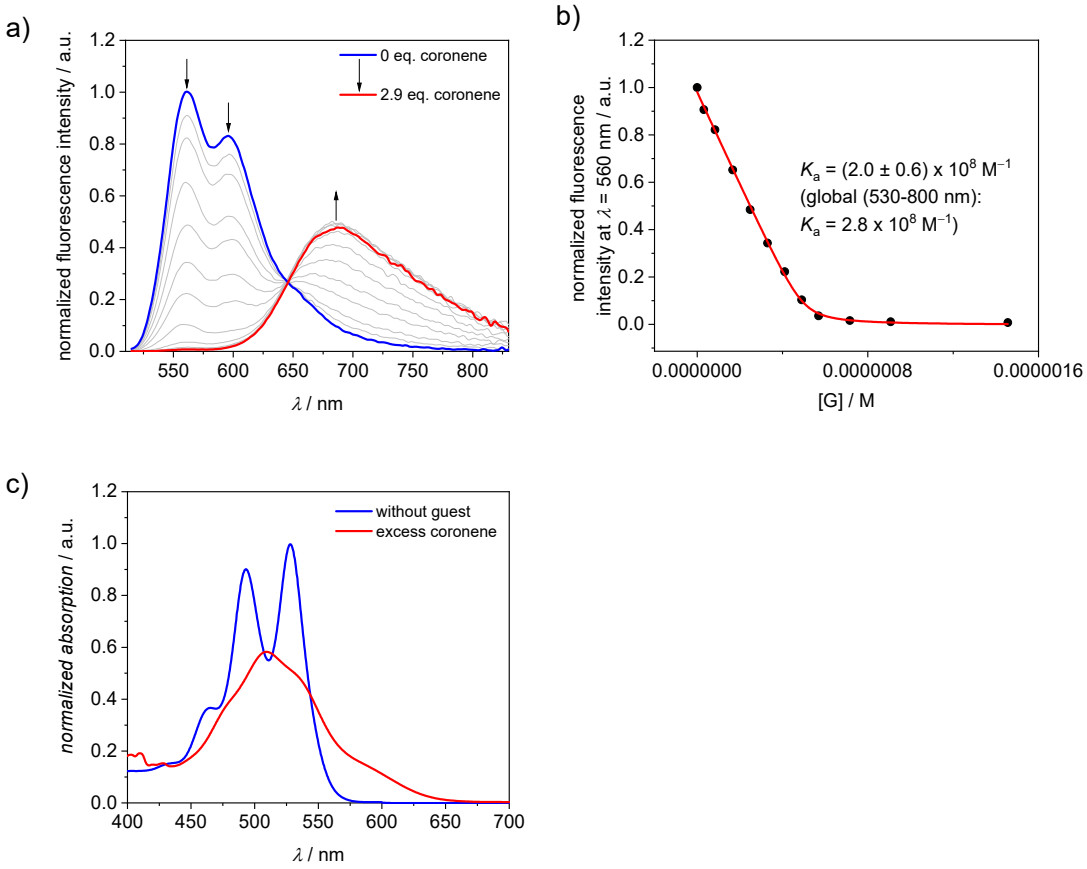

Figure A81. a) Fluorescence spectra (λ_{exc} = 507 nm) of cyclophane **1-*PP*** in $CHCl_3$ at 22 °C (c = 5 x 10^{-7} M) upon the addition of coronene as a guest and b) the resulting plot of the fluorescence at λ = 560 nm with nonlinear curve fit (1:1 binding model, red curve). c) UV/vis spectrum of free **1-*PP*** and coronene⊂**1-*PP*** in chloroform at 22 °C.

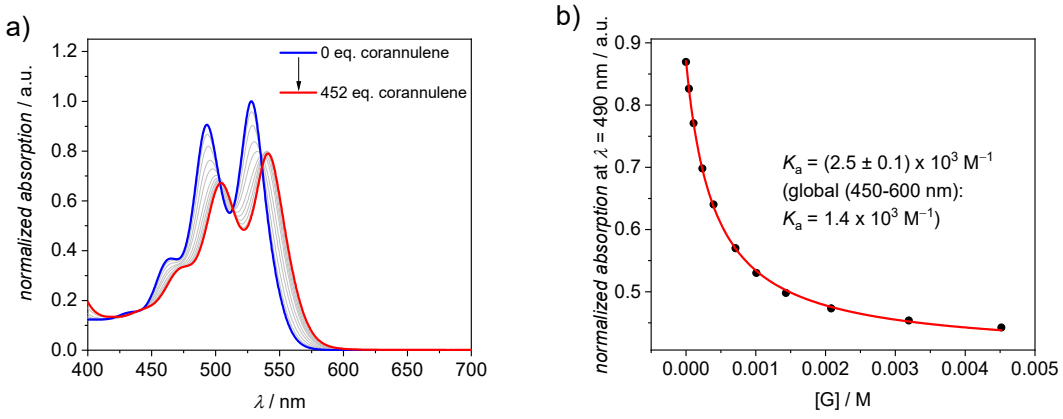

Figure A82. a) UV/vis spectra of cyclophane **1-*PP*** in $CHCl_3$ at 22 °C (c = 10 x 10^{-6} M) upon the addition of corannulene as a guest and b) the resulting plot of the absorption at λ = 490 nm with nonlinear curve fit (1:1 binding model, red curve).

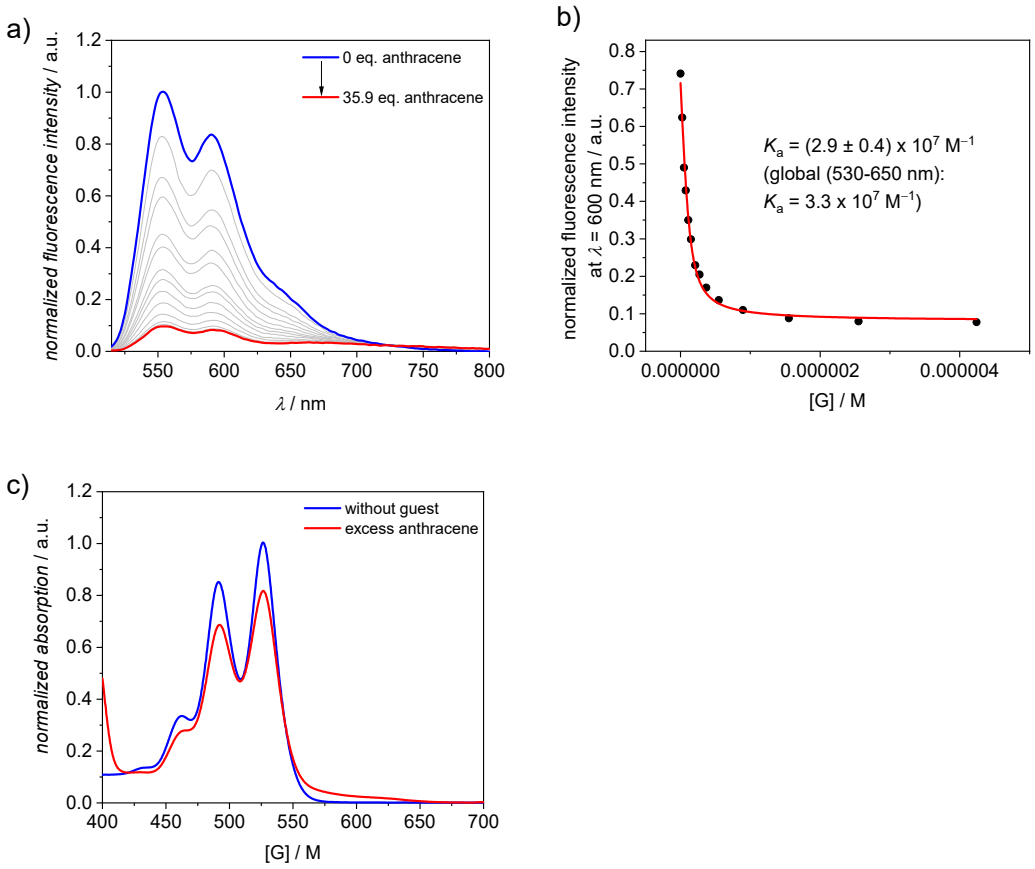

Figure A83. a) Fluorescence spectra (λ_{exc} = 507 nm) of cyclophane **1-*PP*** in CCl_4 at 22 °C (c = 1.2 x 10^{-7} M) upon the addition of anthracene as a guest and b) the resulting plot of the fluorescence at λ = 600 nm with nonlinear curve fit (1:1 binding model, red curve). c) UV/vis spectrum of free **1-*PP*** and anthracene⊂**1-*PP*** in tetrachloromethane at 22 °C.

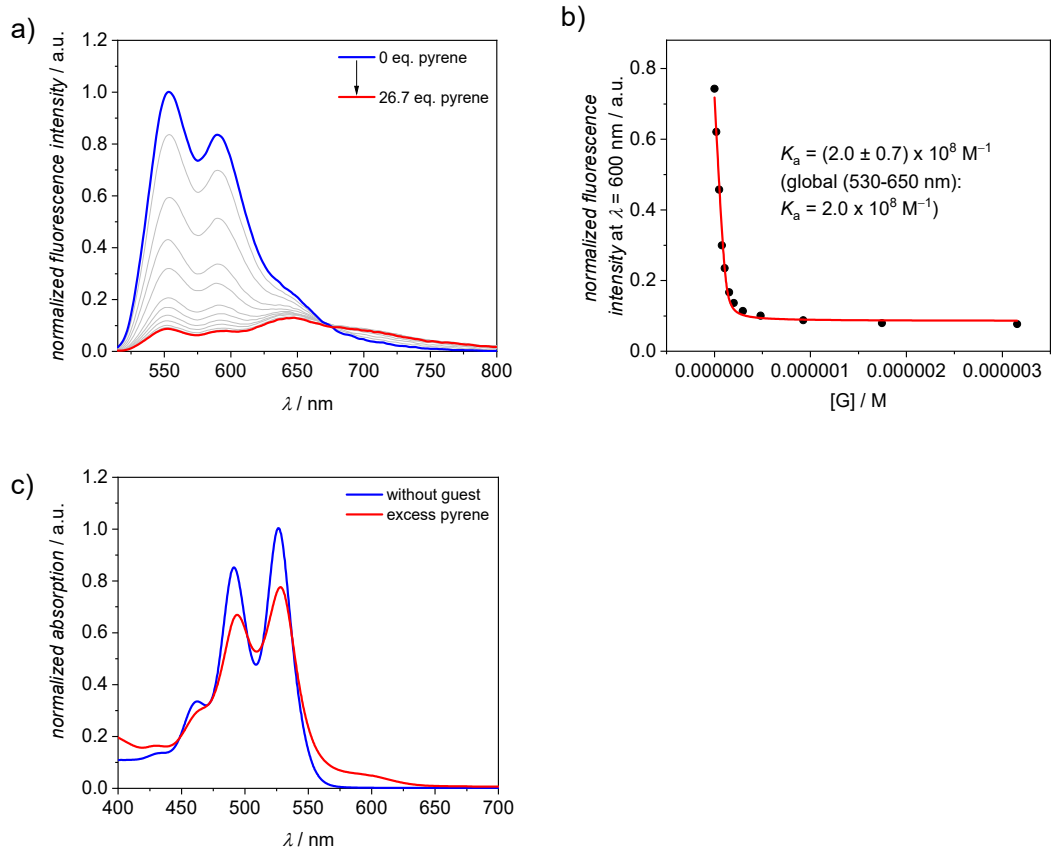

Figure A84. a) Fluorescence spectra (λ_{exc} = 503 nm) of cyclophane **1-*PP*** in CCl_4 at 22 °C (c = 1.2 x 10^{-7} M) upon the addition of pyrene as a guest and b) the resulting plot of the fluorescence at λ = 600 nm with nonlinear curve fit (1:1 binding model, red curve). c) UV/vis spectrum of free **1-*PP*** and pyrene⊂**1-*PP*** in tetrachloromethane at 22 °C.

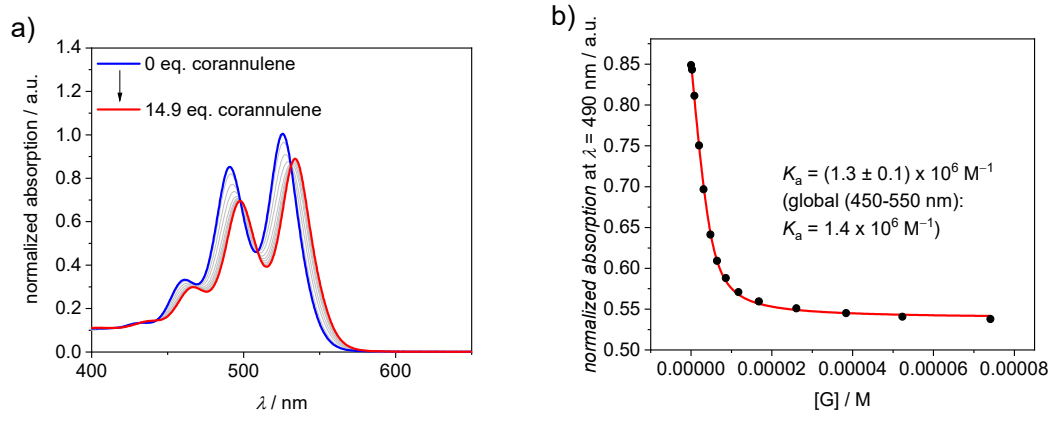

Figure A85. a) UV/vis spectra of cyclophane **1-*PP*** in CCl_4 at 22 °C (c = 5.0 x 10^{-6} M) upon the addition of corannulene as a guest and b) the resulting plot of the absorption at λ = 490 nm with nonlinear curve fit (1:1 binding model, red curve).

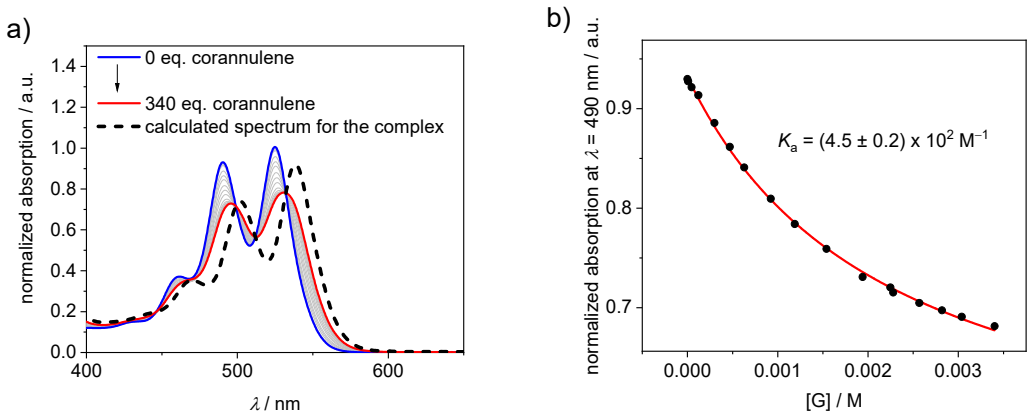

Figure A86. a) UV/vis spectra of cyclophane **1-*PP*** in CH_2Cl_2 at 22 °C (c = 10 x 10^{-6} M) upon the addition of corannulene as a guest. The spectrum of the 1:1 complex (dashed line) was calculated from the titration data. b) The resulting plot of the absorption at λ = 490 nm with nonlinear curve fit (1:1 binding model, red curve).

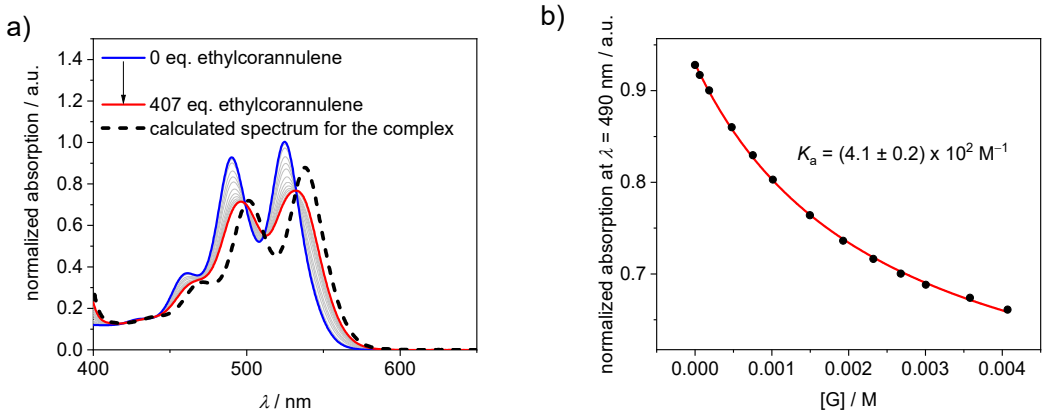

Figure A87. a) UV/vis spectra of cyclophane **1-*PP*** in CH_2Cl_2 at 22 °C (c = 10 x 10^{-6} M) upon the addition of ethylcorannulene as a guest. The spectrum of the 1:1 complex (dashed line) was calculated from the titration data. b) The resulting plot of the absorption at λ = 490 nm with nonlinear curve fit (1:1 binding model, red curve).

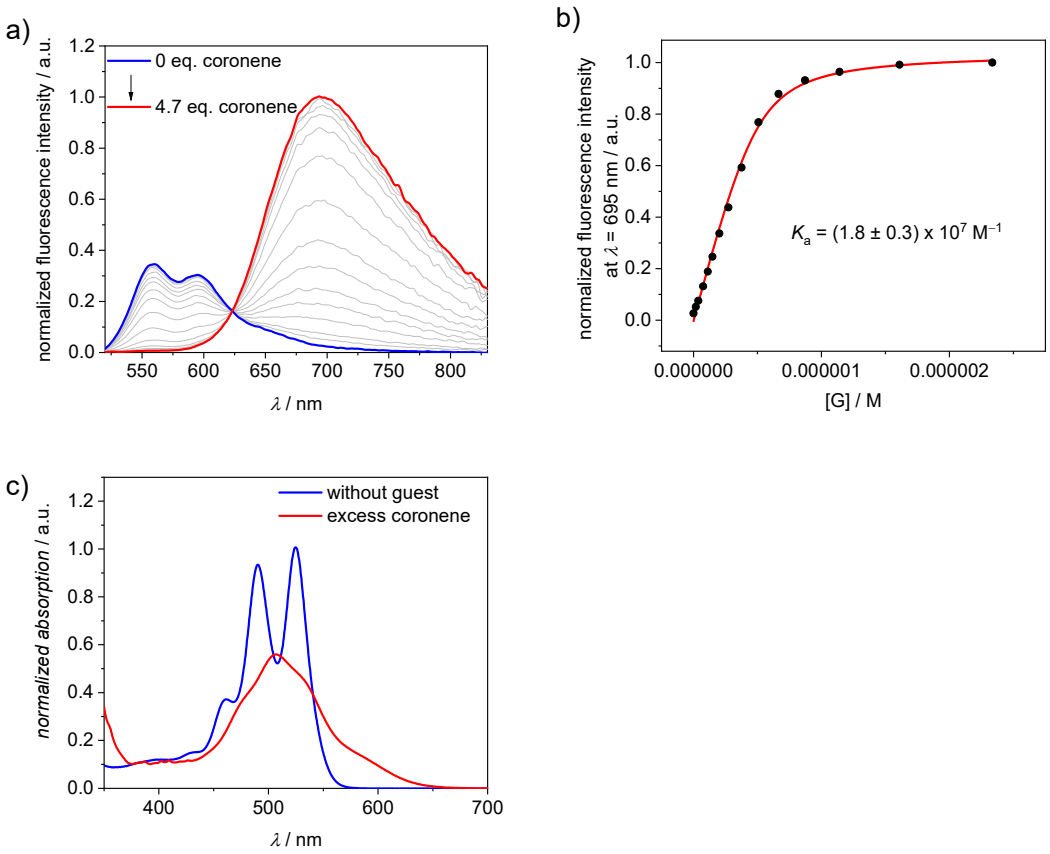

Figure A88. Fluorescence spectra (λ_{exc} = 505 nm) of cyclophane **1-*PP*** in CH_2Cl_2 at 22°C (c = 5.0 x 10^{-7} M) upon the addition of coronene as a guest and the resulting plot of the absorption at λ = 695 nm with nonlinear curve fit (1:1 binding model, red curve). c) UV/vis spectrum of free **1-*PP*** and coronene⊂**1-*PP*** in dichloromethane at 22 °C.

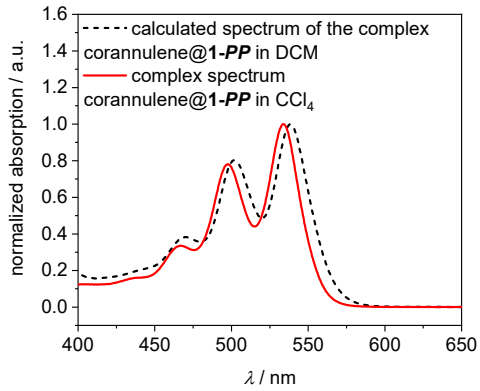

Figure A89. UV/vis spectrum of corannulene⊂**1-*PP*** in CCl_4 and the corresponding calculated spectrum in DCM. The spectrum of the 1:1 complex (dashed line) was calculated from the titration data.

Variable-temperature NMR Studies

From the coalescence temperature and the signal splitting of the methylene protons at the lowest measured temperature, the corresponding barrier for the bowl-to-bowl inversion can be determined according to equation S1 with the universal gas constant R, the coalescence temperature T_c, the Avogadro constant N_A, Planck's constant h and the signal splitting at the lowest measured temperature $\Delta\nu$.

$$\Delta G^{\ddagger} = RT_C \ln\left(\frac{RT_C\sqrt{2}}{\pi N_A h \Delta\nu}\right) \quad \text{(A9)}$$

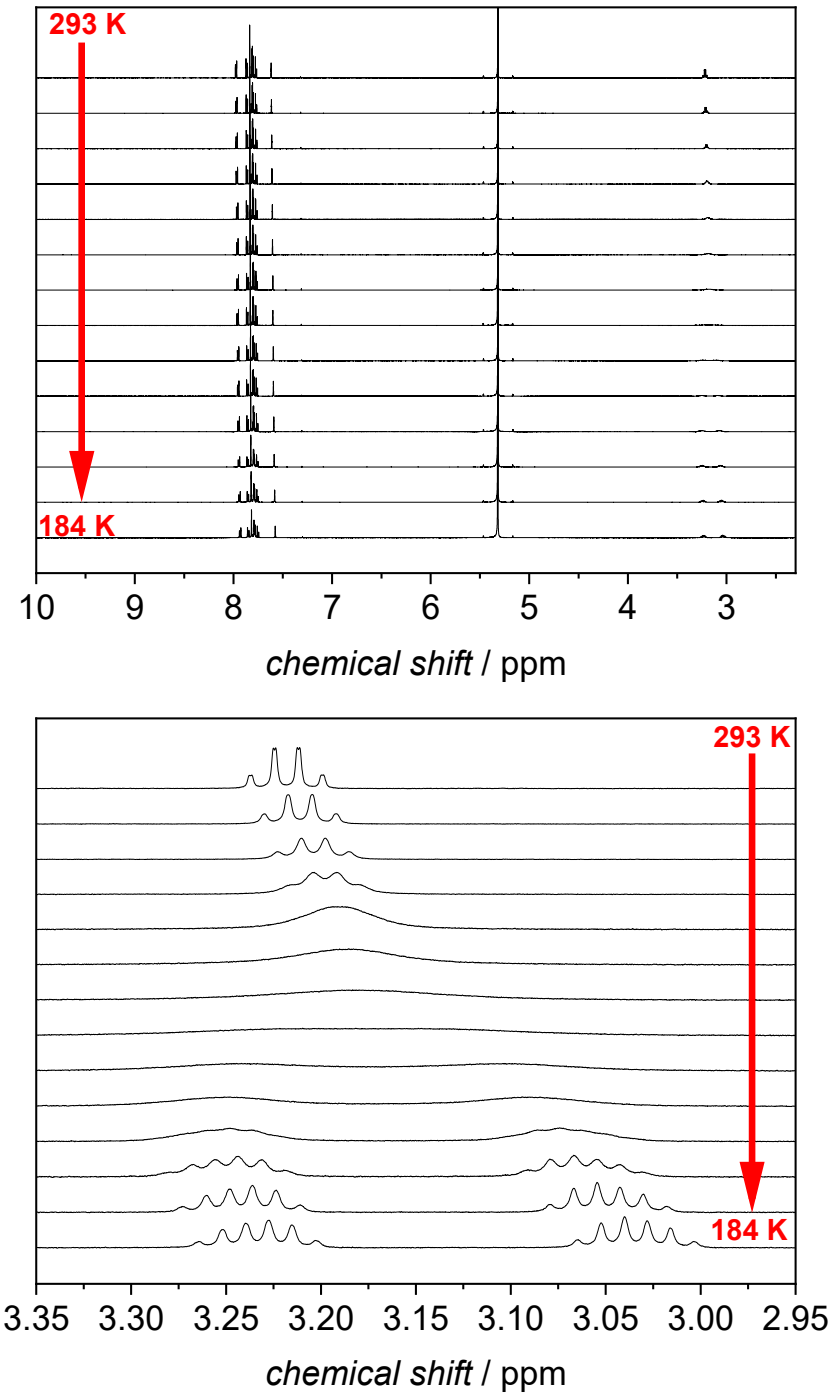

Figure A90. Variable-temperature NMR (600 MHz) study of ethylcorannulene in DCM-d_2 (c ≈ 1 mM).

Tc = (233 ± 2) K

Δν = (120 ± 5) Hz

$\Delta G^{\ddagger}$= (45.8 ± 0.5) kJ mol^{-1}

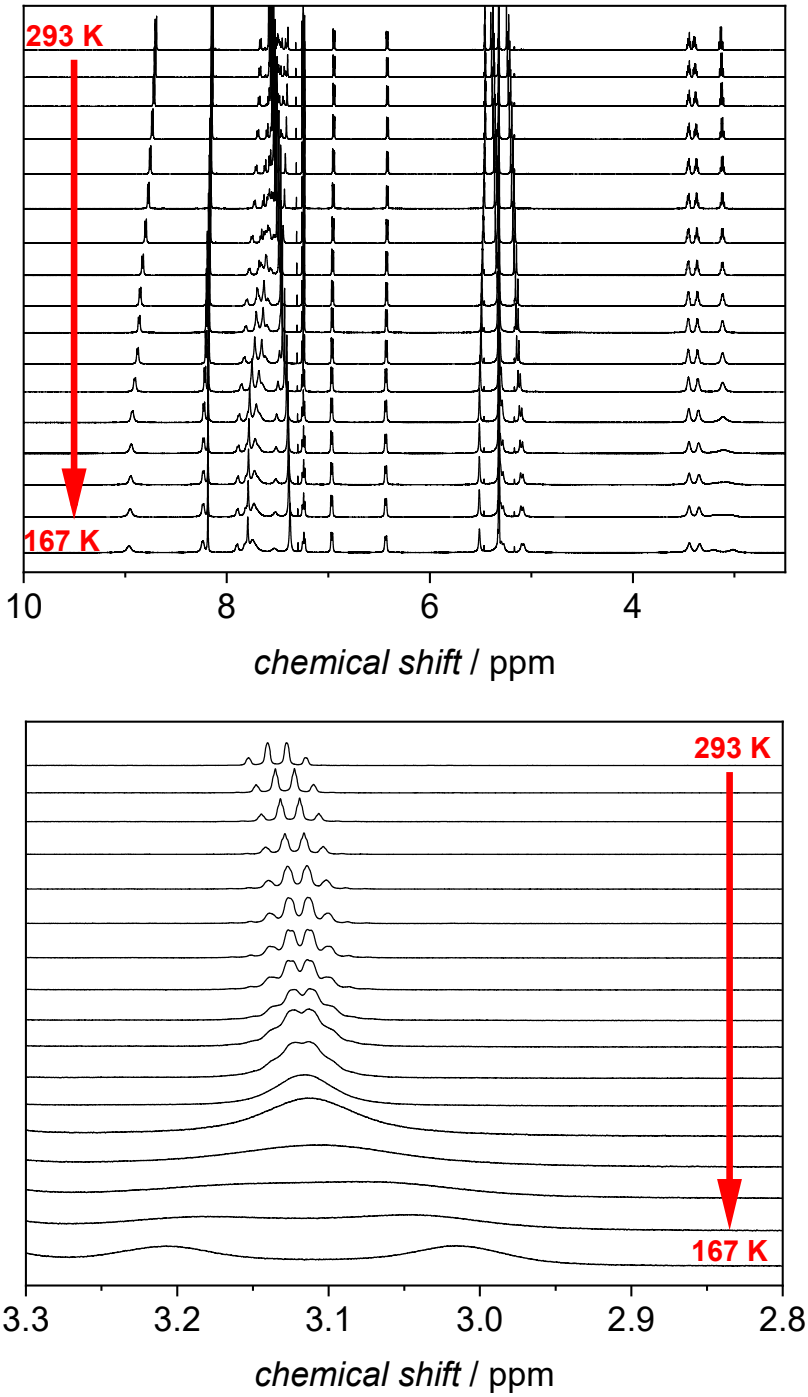

Figure A91. Variable-temperature NMR (600 MHz) study of ethylcorannulene in the prescenc of 0.5 equivalents of **1-*PP*** in DCM-d_2 (c (**1-*PP***) ≈ 1 mM). At room temperature, 20% of guest are bound under these conditions.

Tc = (176 ± 2) K

Δν = (116 ± 5) Hz

$\Delta G^{\ddagger}$= (34.2 ± 0.4) kJ mol^{-1}

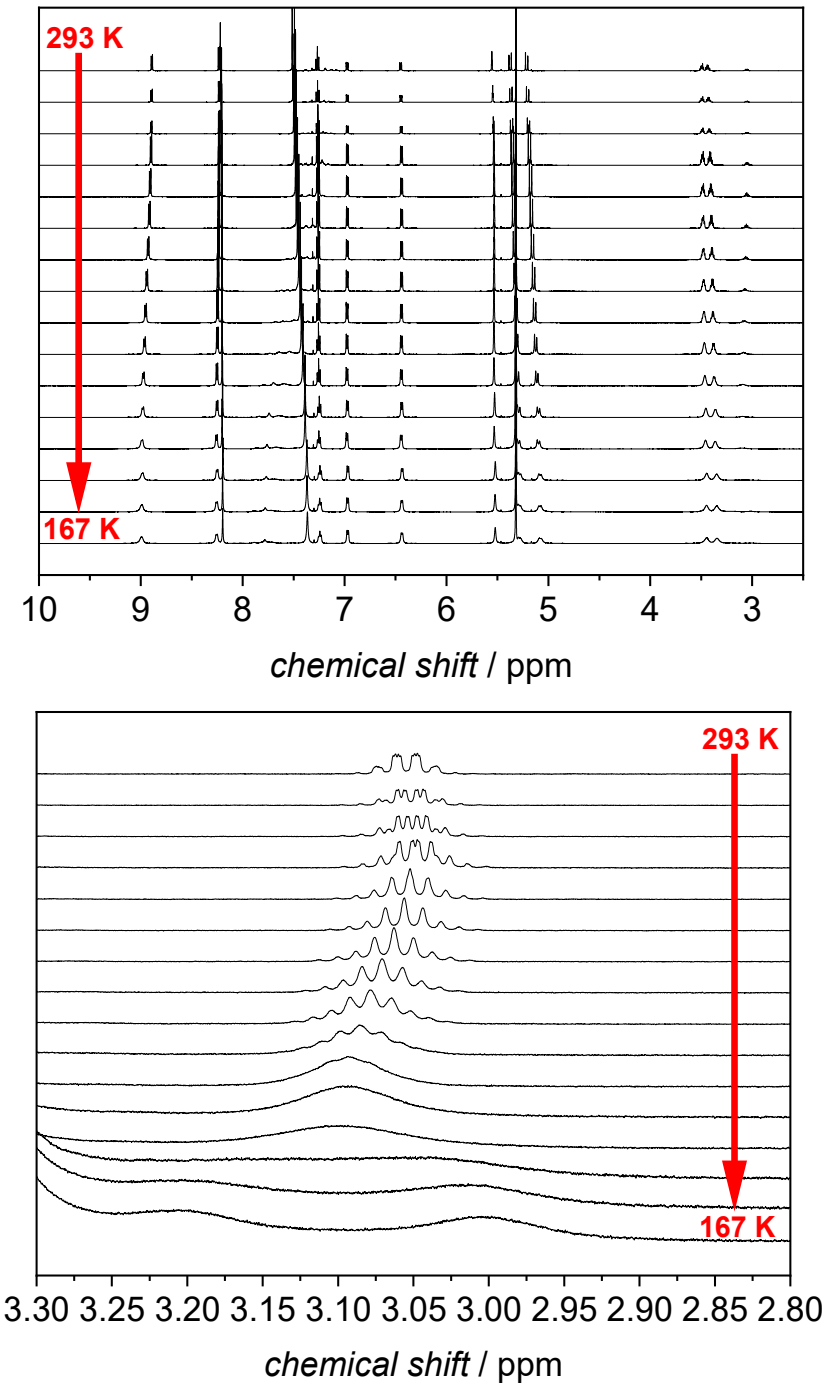

Figure A92. Variable-temperature NMR (600 MHz) study of ethylcorannulene in the prescenc of two equivalents of **1-*PP*** in DCM-d_2 (c (**1-*PP***) ≈ 2 mM). At room temperature, 40% of guest are bound under these conditions.

Tc = (174 ± 2) K

Δν = (122 ± 5) Hz

$\Delta G^{\ddagger}$= (33.7 ± 0.4) kJ mol^{-1}

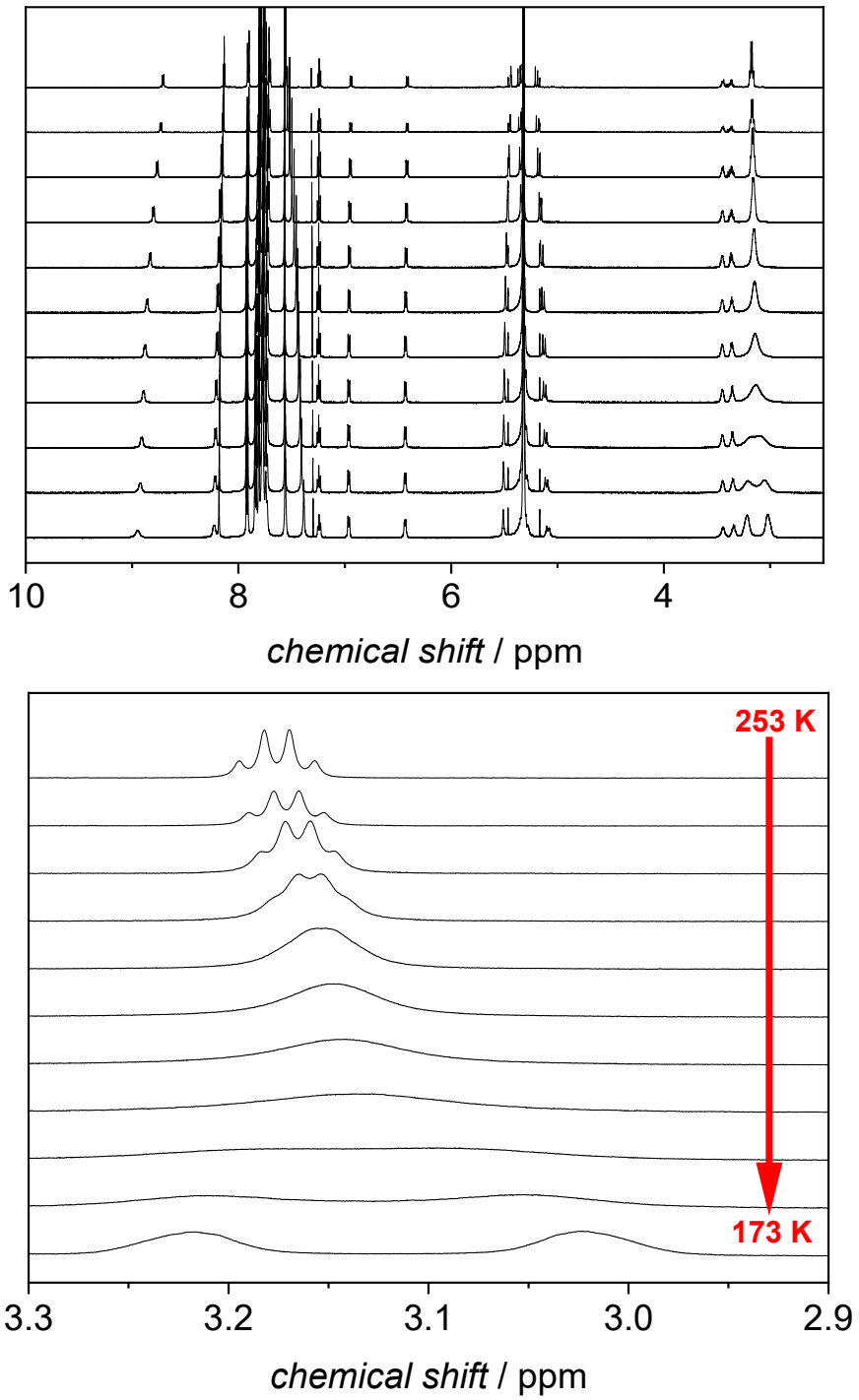

Figure A93. Variable-temperature NMR (600 MHz) study of ethylcorannulene in the prescenc of 0.1 equivalents of **1-*PP*** in DCM-d_2 (c (**1-*PP***) ≈ 0.2 mM). At room temperature, 4% of guest are bound under these conditions.

Tc = (189 ± 2) K

Δν = (117 ± 5) Hz

$\Delta G^{\ddagger}$= (36.8 ± 0.5) kJ mol^{-1}

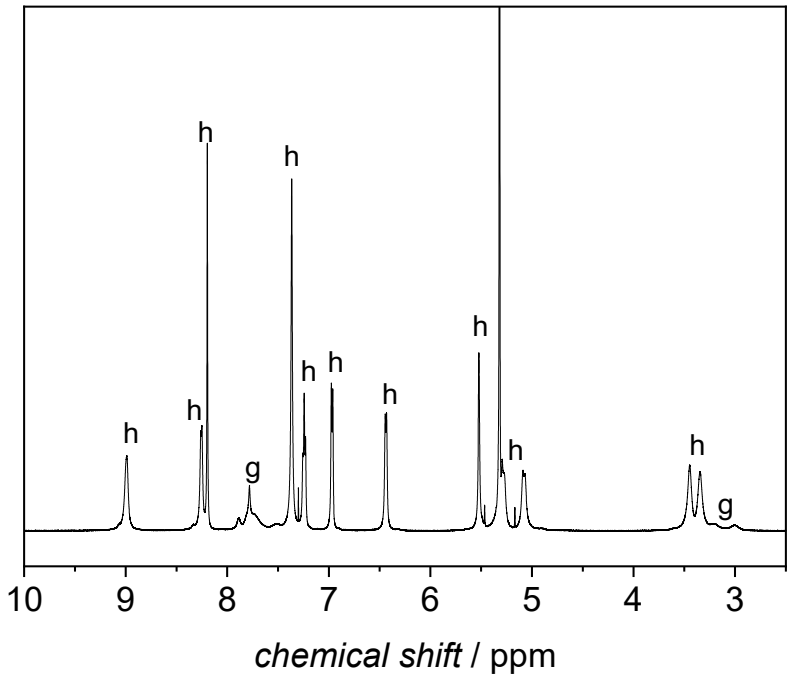

Figure A94. Low-temperature NMR (167 K, 600 MHz) of ethylcorannulene in the prescenc of two equivalents of a) **1-*PP*** ($c \approx 2$ mM). One set of host protons are visible (signals of host are marked with "h" and signals of guest with "g").

Single Crystal X-ray Analysis[viii]

The crystals of coronene⊂**1-*PP*** were grown from a host-guest mixture in chlorobenzene by slow evaporation of *n*-hexane into the solution and were obtained as red blocks.

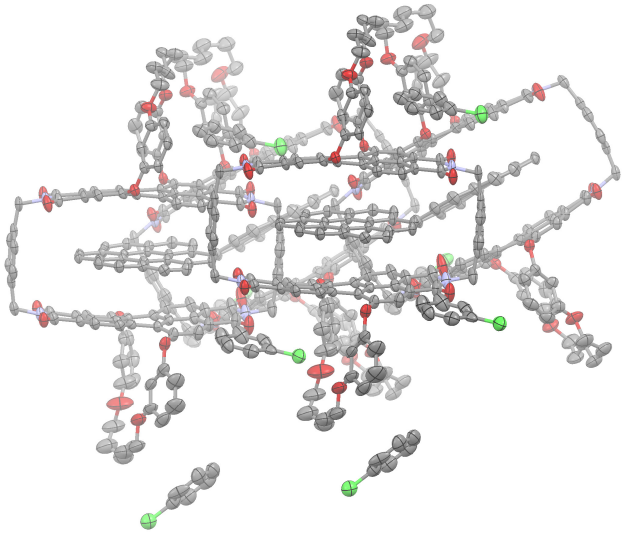

Figure A95. Packing of coronene⊂**1-*PP*** in the crystalline state, obtained by single crystal X-ray analysis (thermal ellipsoids set at 50% probability). Hydrogen atoms are omitted for clarity.

[viii] Performed by Olga Anhalt

Table A8. Crystal data and structure refinement for coronene⊂**1-*PP***.

Identification code	coronene⊂**1-*PP***
Empirical formula	$C_{136}H_{90}Cl_2N_4O_{16}$
Formula weight	2107.01
Temperature	100(2) K
Wavelength	1.54178 Å
Crystal system	Triclinic
Space group	*P1*
Unit cell dimensions	*a* = 13.2705 (10) Å
	b = 21.6957 (16) Å
	c = 22.1130 (17) Å
Volume	5394.3 (7) $Å^3$
Z	2
Density (calculated)	1.297 g/cm^3
Absorption coefficient	1.124 mm^{-1}
F(000)	2192
Crystal size	0.256 × 0.190 × 0.095 mm^3
Theta range for data collection	2.280 to 72.599°
Index ranges	$-16 \le h \le 16$, $-26 \le k \le 26$, $-27 \le l \le 27$
Reflections collected	435202
Independent reflections	41430 [*R*(int) = 0.0355]
Completeness to theta = 67.679°	100%
Absorption correction	Semi-empirical from equivalents
Refinement method	Full-matrix least-squares on F^2
Data / restraints / parameters	41430 / 2756 / 3240
Goodness-of-fit on F^2	1.015
Final *R* indices [$I > 2\sigma(I)$]	R_1 = 0.0503, wR_2 = 0.1461
R indices (all data)	R_1 = 0.0515, wR_2 = 0.1478
Absolute structure parameter	0.053 (3)
Largest diff. peak and hole	1.087 and -0.589 $e \cdot Å^{-3}$

Computational Methods[ix]

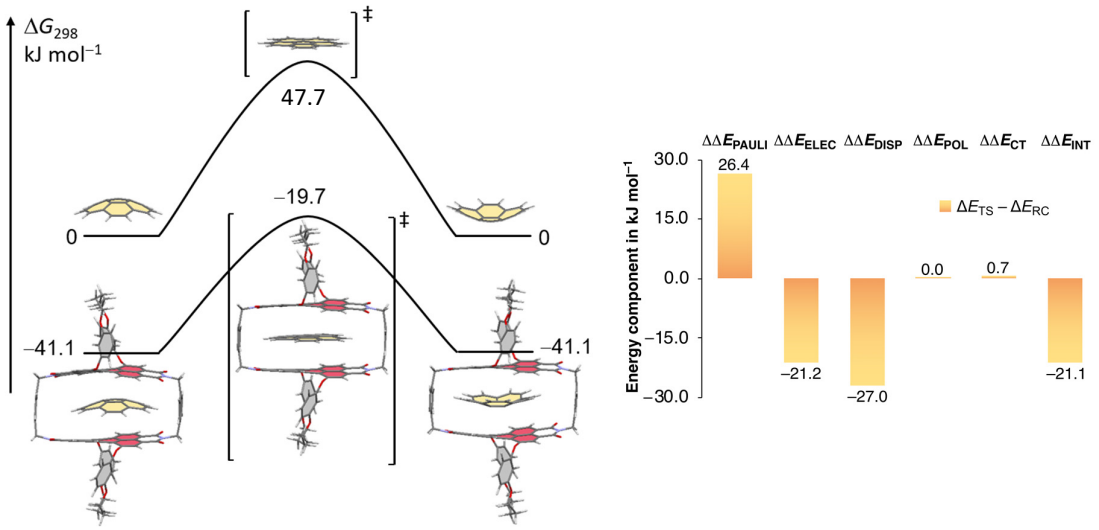

Figure A96. Schematic potential energy surface (PES) of the uncatalyzed and the catalyzed bowl-to-bowl inversion of corannulene in the absence and the presence of **1-*PP*** (left). Breakdowns of relative noncovalent stabilizations and destabilizations of TS obtained from EDAs, calculated as $\Delta\Delta E = \Delta E_{TS} - \Delta E_{RC}$. (RC = reactant complex, PC = product complex; geometries and energies were obtained at the SMD-(CCl_4)-PW6B95-D3(BJ)/def2-TZVPP//B3LYP-D3(BJ)/def2-SVP level of theory,[244-248] while ALMO-EDA-II analyses were performed using ωB97M-V/def2-SVP) (right).[244, 251]

Table A9. Core twist of the calculated complex structures with corannulene as a guest.

structure	average core twist (and core twist of the two chromophores)
1-*PP*	18.1° (17.4° and 18.7°)
corannulene⊂**1-*PP***	15.4° (12.3° and 18.5°)
[corannulene⊂**1-*PP***]‡	11.6° (12.4° and 10.7°)

Table A10. Summary of ground state destabilization of host and substrate for ground state (GS) and transition state (TS) structures given as difference in electronic energies in kJ mol^{-1}.

GS_{host}	GS_{guest}	TS_{host}	TS_{guest}	∑GS	∑TS	GS-TS[a)]
2.5	7.7	1.9	0.5	10.2	2.4	7.8

a) Corresponds to the effective ground state destabilization that contributes to catalysis.

[ix] Performed by Dr. Asja Kroeger

9.4 Appendix for Chapter 6: Preferential Molecular Recognition of Heterochiral Guests within a Cyclophane Receptor

General Methods: Chemicals and solvents were purchased from commercial suppliers and used without further purification. Precursor **40**, [5]helicene and *N*-boc-4-(aminomethyl)benzylamine were synthesized according to literature known procedures.[192-193, 300] The separation of the enantiomers of [5]helicene was achieved by chiral HPLC (DCM/*n*-hexane 3:7, flow rate 6.5 mL/min) with enantiomeric excess of > 95%. Analytical HPLC was perfomed on a JASCO device (PU 2080 PLUS) with a diode array detector (MD 2015), equipped with a ternary gradient unit (DG-2080-533). Semipreparative HPLC was performed on a JAI LC-9105 using a Trentec Reprosil-100 Chiral-NR 8µm-column for chiral resolution. For the Gel permeation chromatography (GPC) we used a Shimadzu Recycling GPC-System (LC-20AD Prominence Pump; SPDMA20A Prominence Diode Array Detector) with three or two preparative columns (Japan Analytical Industries Co., Ltd.; JAIGEL-1 H, JAIGEL-2H and JAIGEL-2.5 H) in chloroform (HPLC grade, stabilized with 0.1% EtOH) with a flow rate of 6.5 or 5.0 mL/min. NMR spectra were recorded on a Bruker Avance III HD 400 spectrometer at 295 K. Chemical shift data are reported in parts per million (ppm, δ scale) and are calibrated to the residual proton (for proton NMR) in the solvent ($CDCl_3$: δ = 7.26; $C_2D_2Cl_4$: δ = 6.00, CCl_4/C_7D_{14} 3:1 (v:v): δ = 1.62 (most downfield shifted signal)) or to the carbon resonance ($CDCl_3$: δ = 77.16). High-resolution ESI TOF spectra of all literature unknown compounds were acquired on a Bruker Daltonics microTOF focus spectrometer.

Optical spectroscopy: All spectroscopic measurements were carried out under ambient conditions. The UV/vis absorption spectra were recorded on a JASCO V-770 or V-670 spectrometer equipped with a PAC-743R Peltier for temperature control. CD spectroscopic measurements were performed with a JASCO J-810 spectropolarimeter equipped with a Jasco CDF-426S Peltier temperature controller or with a customised JASCO CPL-300/J-1500 hybrid spectrometer. CPL spectra were recorded with a customised JASCO CPL-300/J-1500 hybrid spectrometer. Fluorescence spectroscopic measurements were performed on an Edinburgh Instruments FLS981 fluorescence spectrometer. The quantum yields were determined under highly dilute conditions (A < 0.05) relative to Oxazine 1 (ϕ_F = 11% in ethanol)[324] as a reference compound.

DFT calculations: Energy minimized structures were obtained by DFT calculations (Gaussian 16)[325] on the B3LYP-D3/6-31G(d) level of theory. Frequency calculations at the

same level of theory were performed on all optimized structures to confirm them as equilibrium structures. Second-generation ALMO energy decomposition analysis[250] was applied to the optimized structures of *M*-[5]helicene⊂**2-*PP*** and *P*-[5]helicene⊂**2-*PP*** to decompose the noncovalent interaction energy (E_{int}) into electrostatics (E_{elec}), dispersion (E_{disp}), polarization (E_{pol}), charge-transfer (E_{CT}) and Pauli repulsion ($E_{Pauli\text{-}rep}$) contributions with the B3LYP-D3/6-311G(d) level of theory. For the calculation of the CD spectra by TD-DFT we used the CAM-B3LYP functional and 6-31G(d) as a basis set (scrf: chloroform). We note that our TD-DFT calculations do not consider vibronic coupling.

Single crystal X-ray analysis: The diffraction images for X-ray crystallographic analysis of *rac*-**2** were collected on a Bruker D8 Quest Kappa diffractometer with a Photon II CMOS detector and multi-layered mirror monochromated Cu Kα radiation. Single crystal X-ray diffraction data for 1,1'-biphenyl⊂*rac*-**2** were collected at the P11 beamline at DESY. The diffraction data were collected by a single 360 ° ϕ scan at 100 K. The diffraction data were indexed, integrated, and scaled using the XDS program package.[309] In order to compensate low completeness due to single-axis measurement two data sets were merged using the XPREP program from Bruker.[310] The structure was solved using SHELXT,[311] expanded with Fourier techniques and refined using the SHELX software package.[312] Hydrogen atoms were assigned at idealized positions and were included in the calculation of structure factors. All non-hydrogen atoms in the main residue were refined anisotropically. Disordered solvent molecules were modelled with restraints using standard SHELX commands DFIX, SAME, SADI, DELU, SIMU, CHIV, ISDOR, and RIGU. Because the refinement for 1,1'-biphenyl⊂*rac*-**2** was not stable presumably due to pseudo-symmetry between two crystallographic isomers, the DAMP command of SHELX was applied to converge refinement. Hirshfeld surface analysis[326] was done using Crystal Explorer 21.5 on the X-ray crystal structure of 1,1'-biphenyl⊂*rac*-**2**.

Complexation studies: For the titration experiments, a mixture of PBI cyclophane *rac*-**2** and the corresponding guest in excess was titrated to a solution of the pure cyclophane in the same solvent (or solvent mixture) of the same concentration to keep the host concentration constant during the experiment. The UV/vis and NMR titration data were fitted to a 1:1 binding model.[143, 207] In addition we also carried out a global fit analysis with the program *bindfit*[323] in a suitable spectral range. For the titration studies with enantiopure [5]helicene, several host-guest solutions of different stoichiometric ratios were prepared and measured immediately after guest dissolution to avoid kinetic effects due to guest racemization.

Synthetic Procedure

Perylene bisimide *rac*-41a

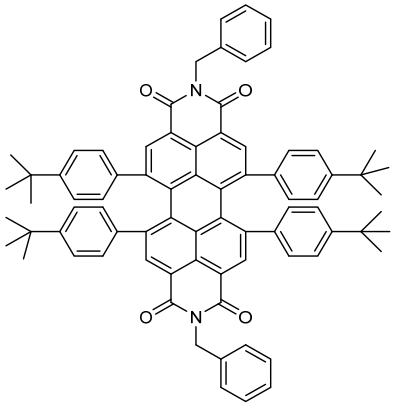

Racemic perylene bisanhydride *rac*-**40** (7.00 mg, 7.60 µmol, 1 eq.), benzylamine (500 mg, 4.67 mmol, 614 eq.) and imidazole (530 mg) were dissolved in dry toluene (5.0 mL) and stirred for 6 h at 120 °C under a nitrogen atmosphere. After being cooled down to room temperature, the solvent was removed under reduced pressure. The remaining solid was diluted with DCM and washed with 1 M HCl. The organic layer was dried over Na_2SO_4 and the solvent was removed under reduced pressure. The crude product was purified by preparative TLC (silica gel, DCM/cyclohexane 7:6), GPC (chloroform, 6.5 mL/min) and precipitation in DCM upon the addition of methanol. The supernatant was subsequently removed by centrifuging the mixture. **Yield**: 8.30 mg (7.55 µmol, 99%) of a green solid. **HRMS** (ESI, positive, acetonitrile/chloroform): (*m/z*) $[M]^+$, calcd. for $C_{78}H_{70}N_2NaO_4^+$: 1121.52333; found: 1121.51796. **^{1}H NMR** (400 MHz, $CDCl_3$): δ = 8.30 (s, 4H), 7.64–7.62 (m, 4H), 7.39–7.28 (m, 6H), 7.04 (s, br, 8H), 6.58 (m, br, 8H), 5.54 (d, ^3J = 13.9 Hz, 2H), 5.33 (d, ^3J = 13.9 Hz, 2H), 1.36 (s, 36H). **^{13}C NMR** (101 MHz, $CDCl_3$): δ = 164.0, 150.6, 142.1, 137.7, 137.5, 134.1, 132.2, 131.5, 129.4, 128.7, 128.2, 127.8, 126.0, 122.1, 43.8, 34.7, 31.4. **mp**.: >300 °C.

Perylene bisimide *rac*-41b

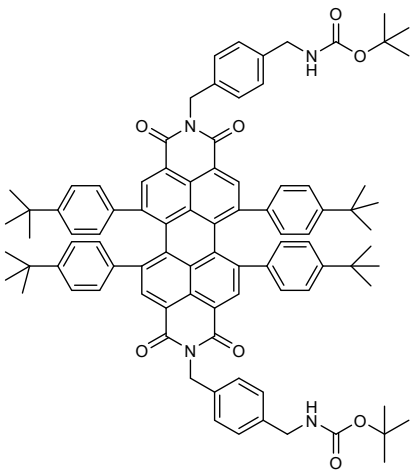

Racemic perylene bisanhydride **40** (141 mg, 153 µmol, 1 eq.), *N*-boc-4-(aminomethyl)-benzylamine (164 mg, 694 µmol, 4.5 eq.) and imidazole (2.20 g) were dissolved in dry toluene (140 mL) and stirred for 5.5 h at 120 °C under a nitrogen atmosphere. After being cooled down to room temperature, the solvent was removed under reduced pressure, the remaining solid was diluted with DCM and washed with 1 M HCl. The organic layer was dried over Na_2SO_4 and the solvent removed under reduced pressure. The crude product was purified by column chromatography (silica gel, DCM → DCM, 2% MeOH). **Yield**: 189 mg (139 µmol, 91%) of a green solid. **HRMS** (ESI,

positive, acetonitrile/chloroform): (*m/z*) $[M]^+$, calcd. for $C_{90}H_{92}N_4O_8^+$: 1356.69152; found: 1356.68400. **^{1}H NMR** (400 MHz, $C_2D_2Cl_4$): δ = 8.28 (s, 4H), 7.56 (d, ^3J = 8.3 Hz, 4H), 7.29 (d, ^3J = 8.3 Hz, 4H), 7.05 (d, br, ^3J = 11.2 Hz, 8H), 6.70 (s, br, 4H), 6.49 (s, br, 4H), 5.54 (d, ^3J = 14.0 Hz, 2H), 5.27 (d, ^3J = 14.0 Hz, 2H), 4.95 (t, ^3J = 5.4 Hz, 2H), 4.31 (d, ^3J = 5.9 Hz, 4H), 1.44 (s, 18H), 1.36 (s, 36H). **^{13}C NMR** (101 MHz, $CDCl_3$): δ = 164.0, 156.0, 150.6, 142.1, 138.6, 137.7, 136.6, 134.1, 132.2, 131.5, 129.7, 128.2, 127.8, 126.0, 122.0, 44.5, 43.5, 34.7, 31.4, 28.5. **mp**.: 136–138 °C (decomposition).

Racemate of perylene bisimide cyclophanes 2-*MM* and 2-*PP*

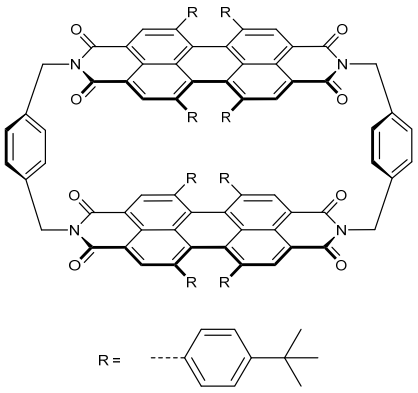

Perylene bisimide *rac*-**41b** (200 mg, 147 µmol, 1 eq.) was dissolved in DCM (30 mL). Subsequently, TFA (6 mL) was added and the mixture was stirred for 1 h at r.t.. The solvent was removed under reduced pressure and the residual solid was dissolved in DCM again. Subsequently, the solvent was again removed under reduced pressure in order to fully eliminate the remaining TFA. Next, racemic perylene bisanhydride **40** (136 mg, 148 µmol, 1 eq.) and imidazole (3.80 g) were added, the resulting mixture was dissolved in dry toluene (650 mL) and stirred for 28 h at 120 °C under a nitrogen atmosphere. After being cooled down to r.t., the solvent was removed under reduced pressure, the remaining solid was diluted with DCM and afterwards washed with 1 M HCl. The organic layer was dried over Na_2SO_4 and the solvent was removed under reduced pressure. The crude product was purified by column filtration (silica gel, DCM, 5% MeOH) and by GPC (chloroform, 6.5 mL/min). The pure compound was precipitated from chloroform upon the addition of methanol and the supernatant removed by centrifuging the mixture. **Yield**: 60.0 mg (29.4 µmol, 20 %) of a green solid. **HRMS** (ESI, positive, acetonitrile/chloroform): (*m/z*) $[M+Na]^+$, calcd. for $C_{144}H_{128}N_4NaO_8^+$: 2063.96244; found: 2063.97050. **^{1}H NMR** (400 MHz, $CDCl_3$): δ = 8.18 (s, 4H), 7.79 (s, 4H), 7.55 (s, 8H), 6.92 (s, br, 8H), 6.74 (dd, ^3J = 8.1 Hz, ^4J = 1.9 Hz, 4H), 6.64 (dd, ^3J = 8.1 Hz, ^4J = 1.9 Hz, 8H, overlapping with broad signal), 6.40 (s, br, 4H), 5.85 (dd, ^3J = 8.1 Hz, ^4J = 2.0 Hz, 4H), 5.65–5.61 (m, 8H), 5.18 (d, ^2J = 13.4 Hz, 4H), 1.36 (s, 36H), 1.28 (s, 36H). **^{13}C NMR** (101 MHz, $CDCl_3$): δ = 164.0, 163.5, 150.8, 149.2, 142.0, 141.5, 137.5, 137.1, 136.5, 134.3, 132.4, 132.3, 131.4, 131.1, 130.6, 127.9, 127.6, 127.3, 125.6, 124.1, 122.4, 121.6, 42.8, 34.61, 34.58,

31.46, 31.3. **mp**.: >300 °C. **UV/vis** ($CHCl_3$, c_T = 30 µM, nm): λ_{max} (ε_{max}, M^{-1} cm^{-1}) = 304 (77×10^3), 477 (33×10^3), 620 (31×10^3). **Fluorescence** ($CHCl_3$, nm): λ_{max} (λ_{ex}) = 705 (580).

The resulting enantiomers were separated by chiral HPLC (Reprosil, DCM)

2-*PP*: Retention time (Trentec, Reprosil 100 chiral-NR, $\varnothing$ = 0.8 cm, DCM, flow: 1.0 mL/min): 3.2 min; λ_{max} ($\Delta\varepsilon$): 304 nm (+ 81 M^{-1} cm^{-1}). **2-*MM***: Retention time (Trentec, Reprosil 100 chiral-NR, $\varnothing$ = 0.8 cm, DCM, flow: 1.0 mL/min): 4.3 min; λ_{max} ($\Delta\varepsilon$): 304 nm (– 90 M^{-1} cm^{-1}). The stereochemical assignment of the isolated diastereomers was achieved by comparison of the CD spectra with those of the previously reported enantiomerically pure *P*- and *M*-configured bay-tetraphenyl-substituted PBIs.[173] **2-*PP***: **CD** ($CHCl_3$, nm): λ_{max} ($\Delta\varepsilon_{max}$, M^{-1} cm^{-1}): 304 (+ 199), 334 (+ 277), 375 (+ 62), 459 (+ 31), 619 (+ 69). **2-*MM***: **CD** ($CHCl_3$, nm): λ_{max} ($\Delta\varepsilon_{max}$, M^{-1} cm^{-1}): 304 (– 200), 334 (– 274), 375 (– 67), 459 (– 32), 619 (– 67).

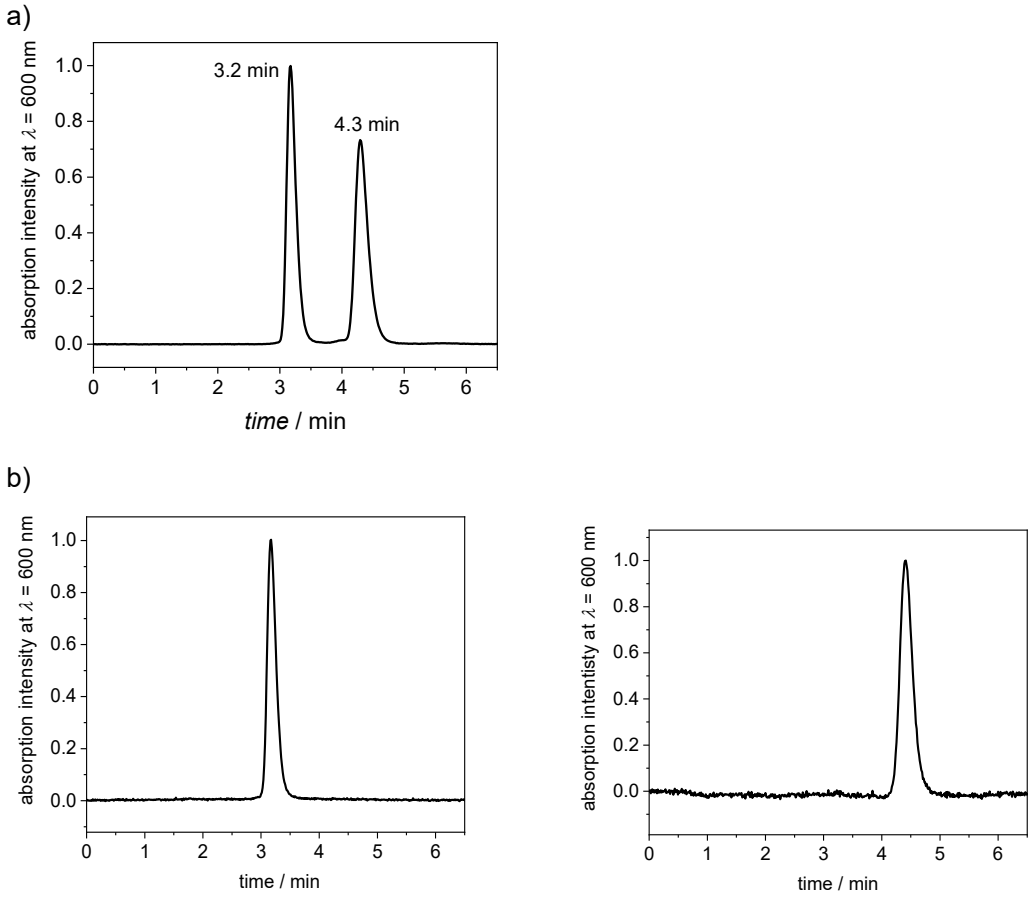

Figure A97. Analytical HPLC chromatogram a) for the separation of **2-*MM*** and **2-*PP*** and b) of the corresponding enantiomerically pure compounds which were separated by semipreparative chiral HPLC (DCM, flow: 1 mL/min).

Appendix Note

The enantiomeric excess (*ee*) values were calculated by equation A10, where *a(peak1)* and *a(peak2)* refer to the integrals of the peaks for the first and second eluted isomer, respectively. For both enantiomers, *ee* values of >99% could be determined.

$$ee = \frac{a(peak\ 1) - a(peak2)}{a(peak\ 1) + a(peak2)} \times 100\% \qquad \text{(A10)}$$

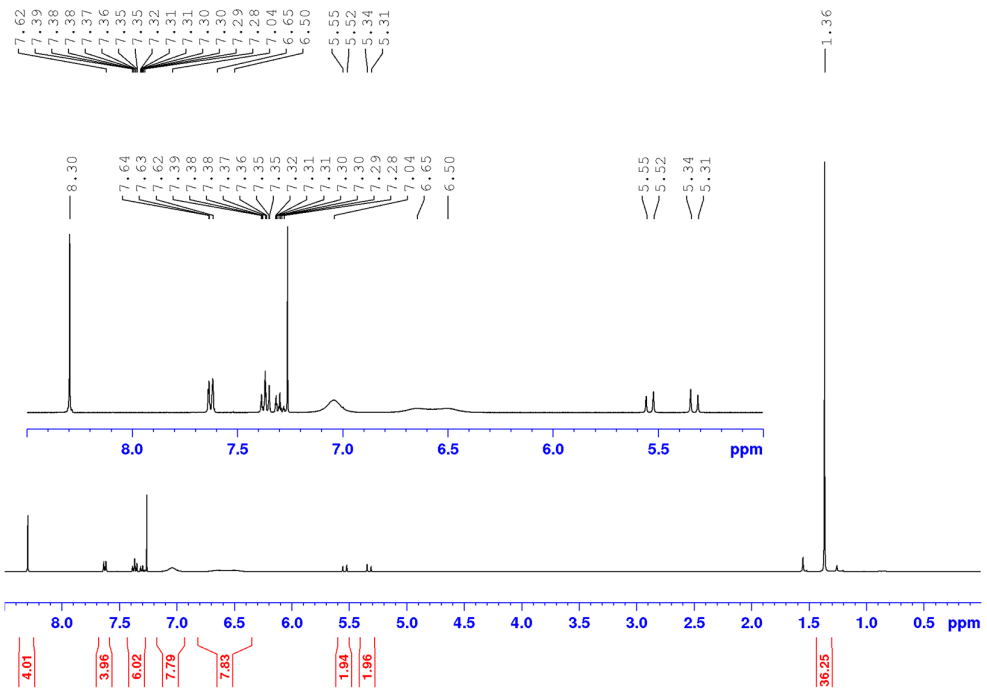

Figure A98. ^{1}H NMR (400 MHz) spectrum of compound *rac*-**41a** in $CDCl_3$ at 295 K.

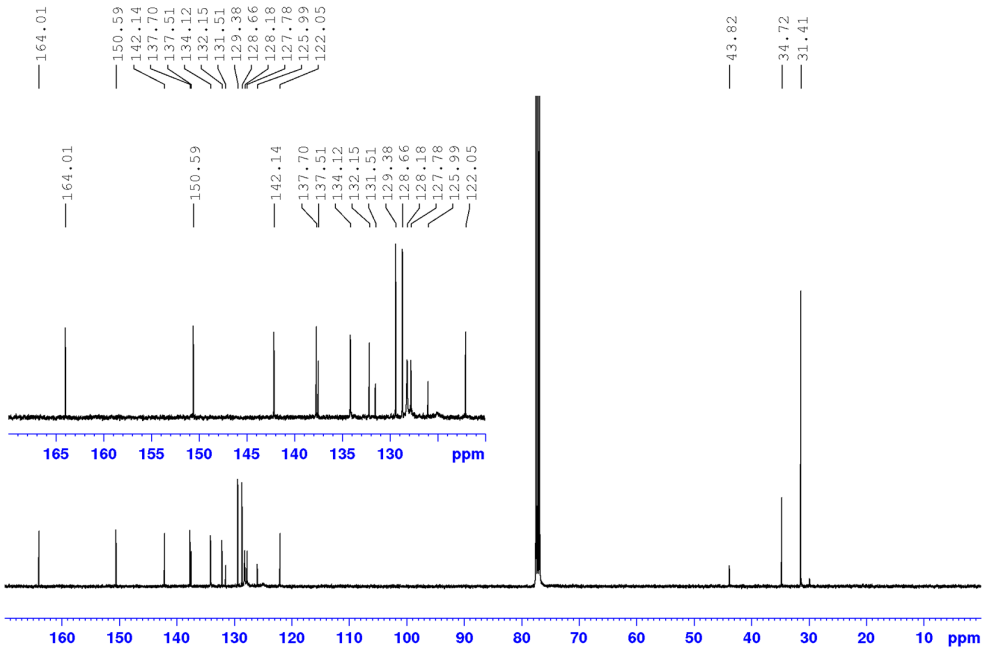

Figure A99. ^{13}C NMR (101 MHz) spectrum of compound *rac*-**41a** in $CDCl_3$ at 295 K.

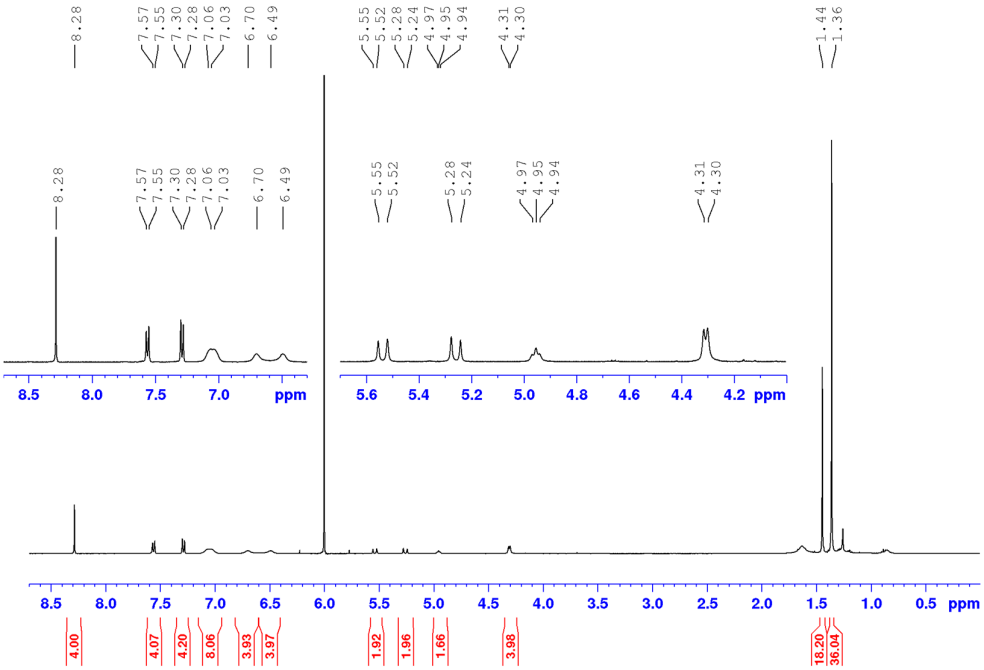

Figure A100. ^{1}H NMR (400 MHz) spectrum of compound *rac*-**41b** in $C_2D_2Cl_4$ at 295 K.

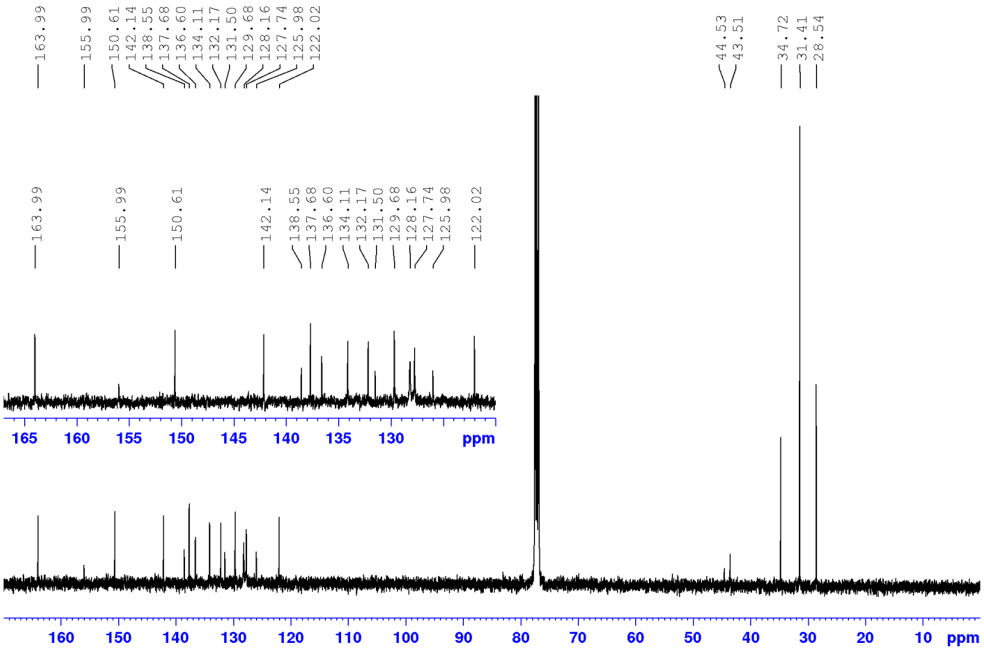

Figure A101. ^{13}C NMR (101 MHz) spectrum of compound *rac*-**41b** in $CDCl_3$ at 295 K.

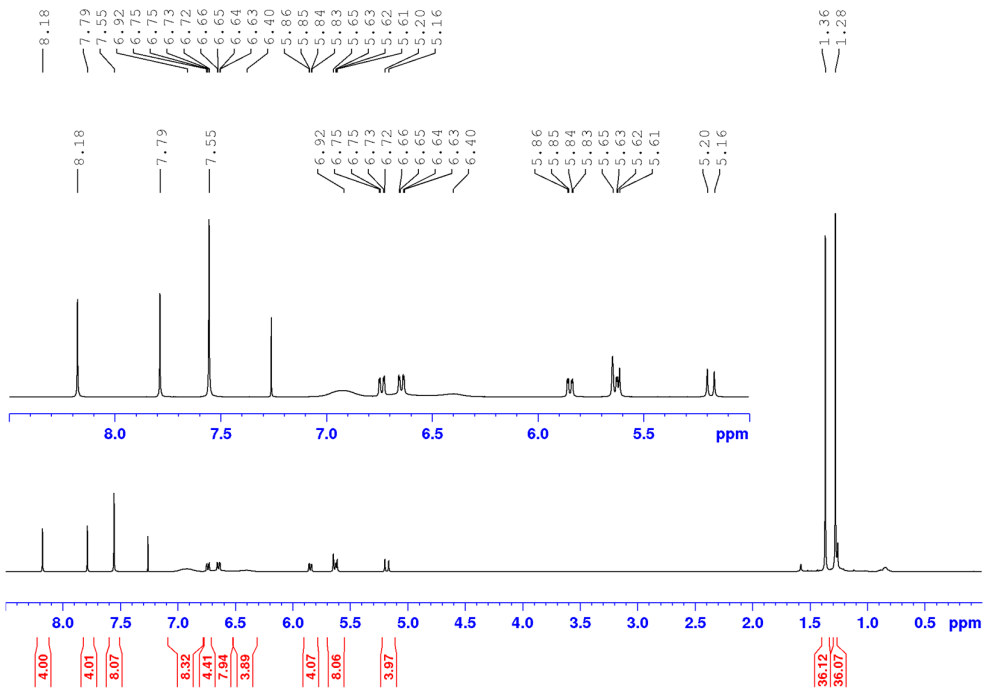

Figure A102. ^{1}H NMR (400 MHz) spectrum of compound *rac*-**2** in $CDCl_3$ at 295 K.

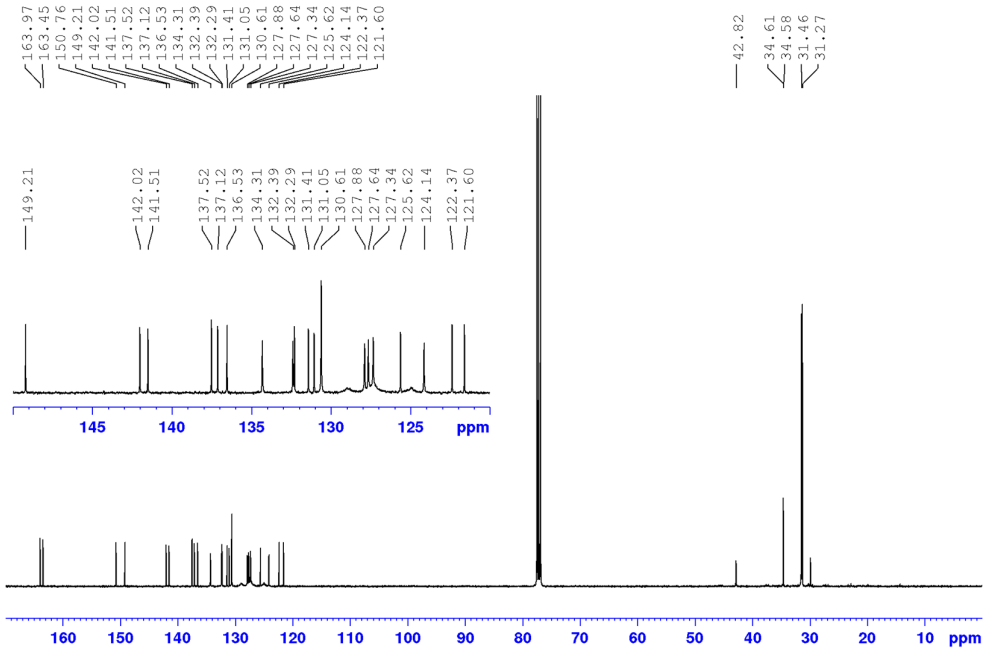

Figure A103. ^{13}C NMR (101 MHz) spectrum of compound *rac*-**2** in $CDCl_3$ at 295 K.

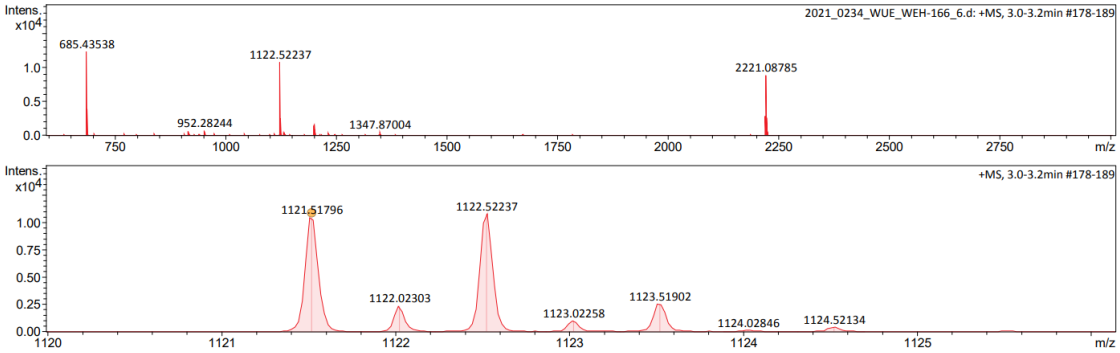

Figure A104. HRMS (ESI, positive, acetonitrile/chloroform) of compound *rac*-**41a**.

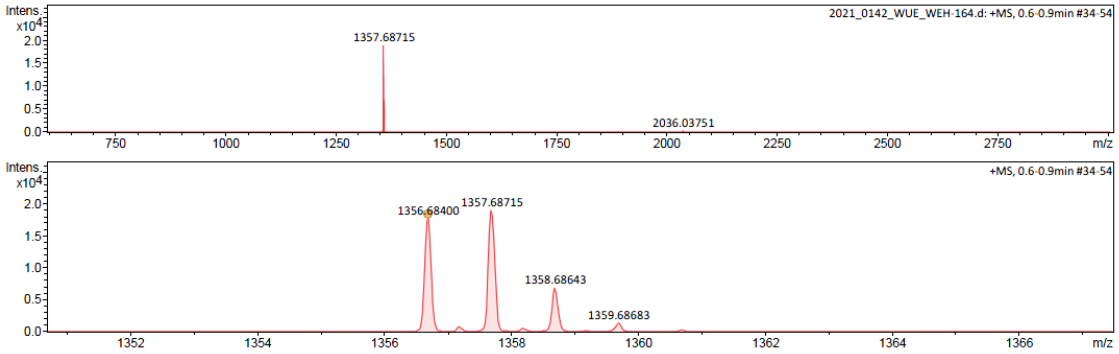

Figure A105. HRMS (ESI, positive, acetonitrile/chloroform) of compound *rac*-**41b**.

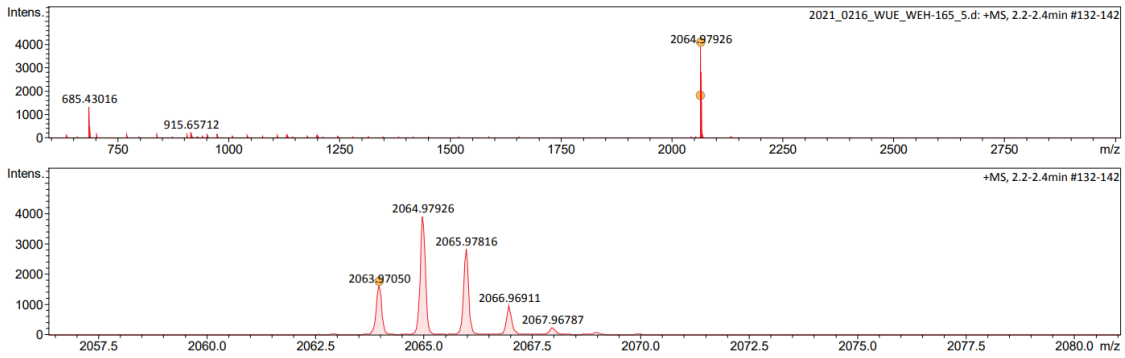

Figure A106. HRMS (ESI, positive, acetonitrile/chloroform) of compound *rac*-**2**.

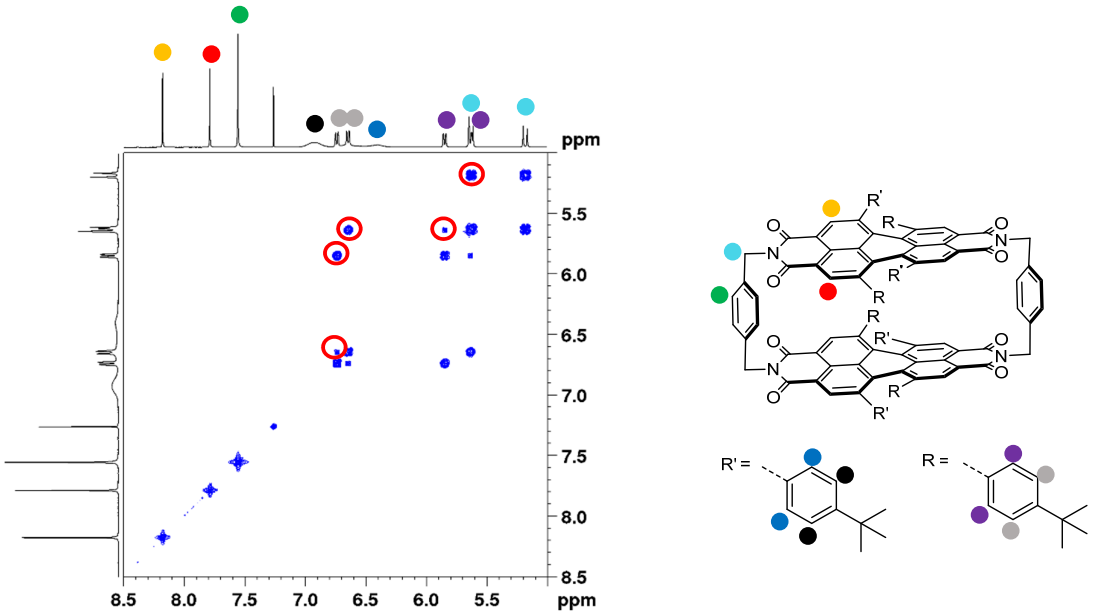

Figure A107. ^{1}H-^{1}H COSY NMR spectrum (400 MHz, 295 K) of *rac*-**2** in $CDCl_3$. The important cross signals are marked in red.

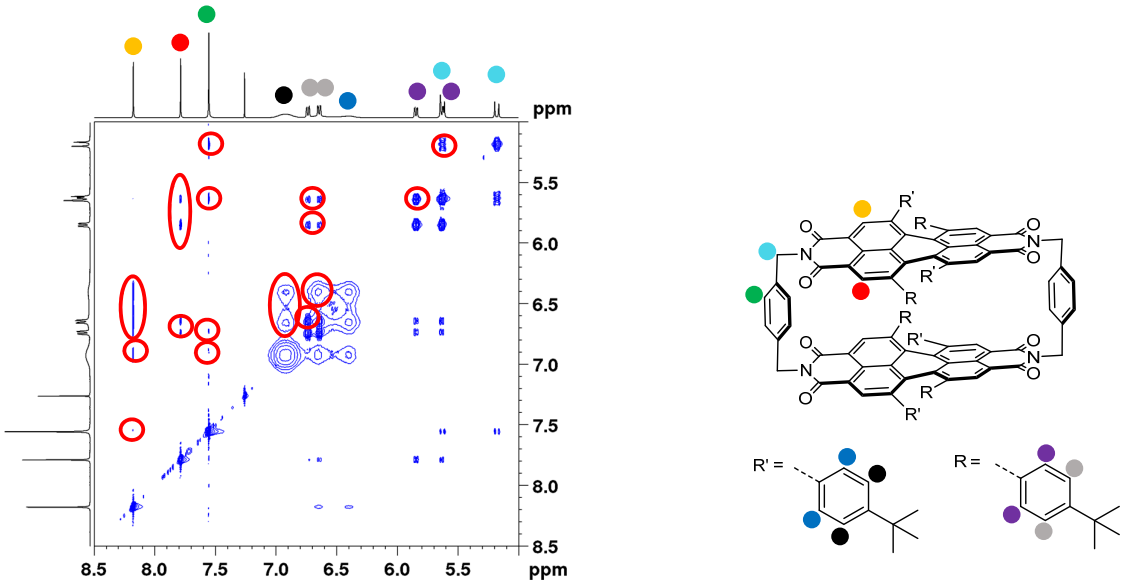

Figure A108. ^{1}H-^{1}H NOESY NMR spectrum (400 MHz, 295 K) of *rac*-**2** in $CDCl_3$. The important cross signals are marked in red.

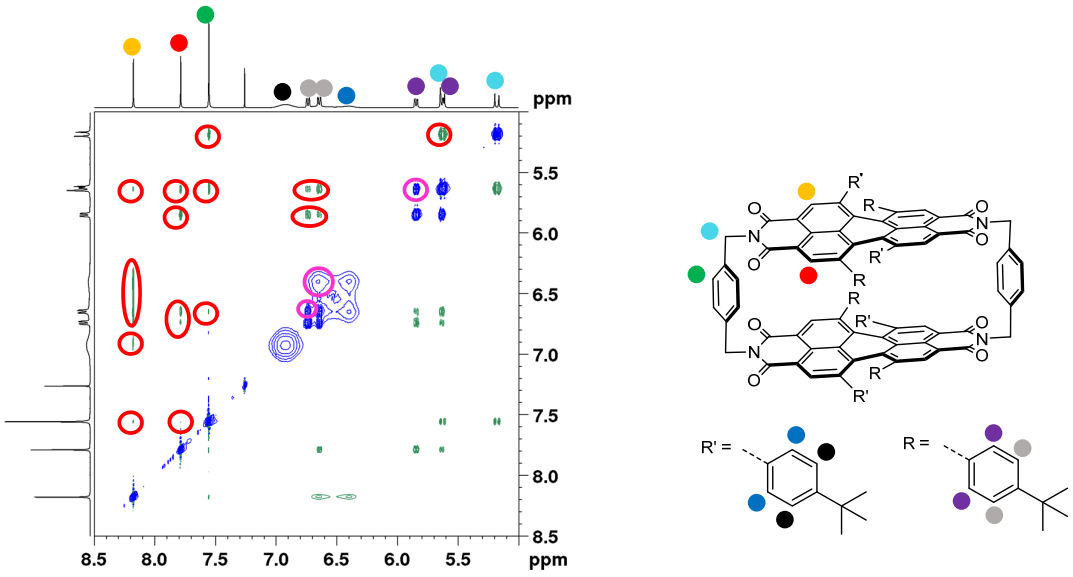

Figure A109. ^{1}H-^{1}H ROESY NMR spectrum (400 MHz, 295 K) of *rac*-**2** in $CDCl_3$. The important cross signals are marked in red. The exchange signals are marked in pink.

Appendix Note

Compound *rac*-**2** shows the expected singlet for the aromatic *para*-xylylene spacer protons (green), whose close proximity to the diastereotopic methylene protons (turquoise) can be seen from cross signals in the ^{1}H-^{1}H NOESY and ROESY spectra. The *ortho* protons of the PBI chromophore (red and orange) show two singlets in the proton NMR due to two different environments, i.e. one position that is more inside the cavity and one that points away from the cavity. The adjacent bay substituents can be easily assigned as they show through space correlations of different intensities to the *ortho* protons. Accordingly, the chemically and magnetically non-equivalent aromatic protons of the bay substituents (blue/black and purple/grey), which show spin-spin coupling signals in the ^{1}H-^{1}H COSY NMR, can be distinguished by different intensities of ^{1}H-^{1}H ROESY and NOESY cross signals (blue and purple are more intense than black and grey) with the protons marked in red and orange. In order to assign the *ortho* protons and their neighbouring bay substituents to the position that points outwards and towards the cyclophane cavity, we compared the shape of the aromatic bay substituents' proton signals. Both substituents show a rotation along the single bond to the PBI core with distinct exchange signals in the ^{1}H-^{1}H ROESY spectrum. While half of the substituents have broad signals, comparable to the monomeric reference dyes (Figure A98 and Figure A100), the rest is characterized by sharp signals. Accordingly, we conclude that the "outer" substituents have a similar rotational barrier as in the case of the monomeric references,

while the substituents that point towards the cavity are sharpened due to a more frozen rotation. Thus, the orange *ortho* proton must point away from the inner of the cyclophane while the red one is in close proximity to the cavity.

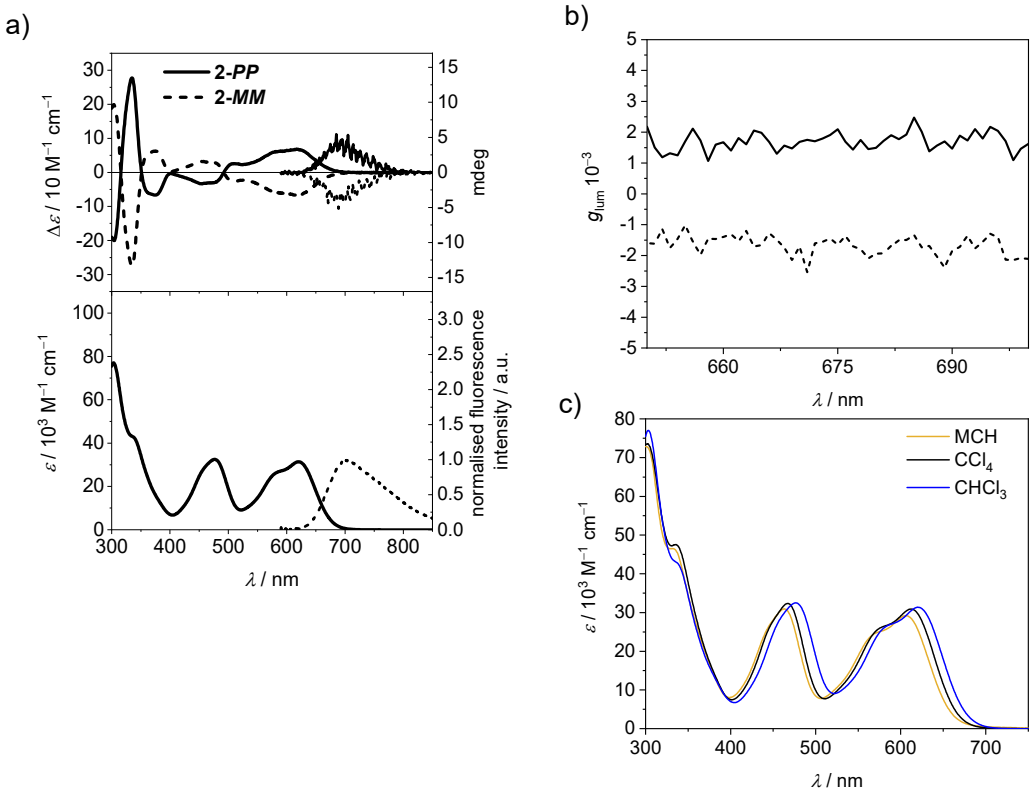

Figure A110. a) CD absorption spectra of **2-*PP*** and **2-*MM*** and UV/vis absorption spectrum of **2-*PP*** in chloroform at 295 K (c = 30 µM). Furthermore, the corresponding CPL (OD = 0.1) and fluorescence spectra (OD < 0.05) are shown. b) Plot of the dissymmetry factor g_{lum} of **2-*PP*** and **2-*MM*** in $CHCl_3$. c) UV/vis absorption spectra of *rac*-**2** in different solvents (c = 30 µM).

Table A11. Fluorescence quantum yields of *rac*-**2** in different solvents, determined relative to Oxazin 1 ([7-(diethylamino)-phenoxazin-3-ylidene]-diethylazanium) in ethanol.

solvent	**$CHCl_3$**	**CCl_4**	**MCH**
quantum yield ϕ_f	0.23	0.41	0.38
k_r [10^7 s^{-1}]	2.0	2.8	2.6
k_{nr} [10^7 s^{-1}]	6.7	4.0	4.3

(rate constants determined according to $k_r = \phi / \tau$, $k_{nr} = 1/\tau - k_r$)

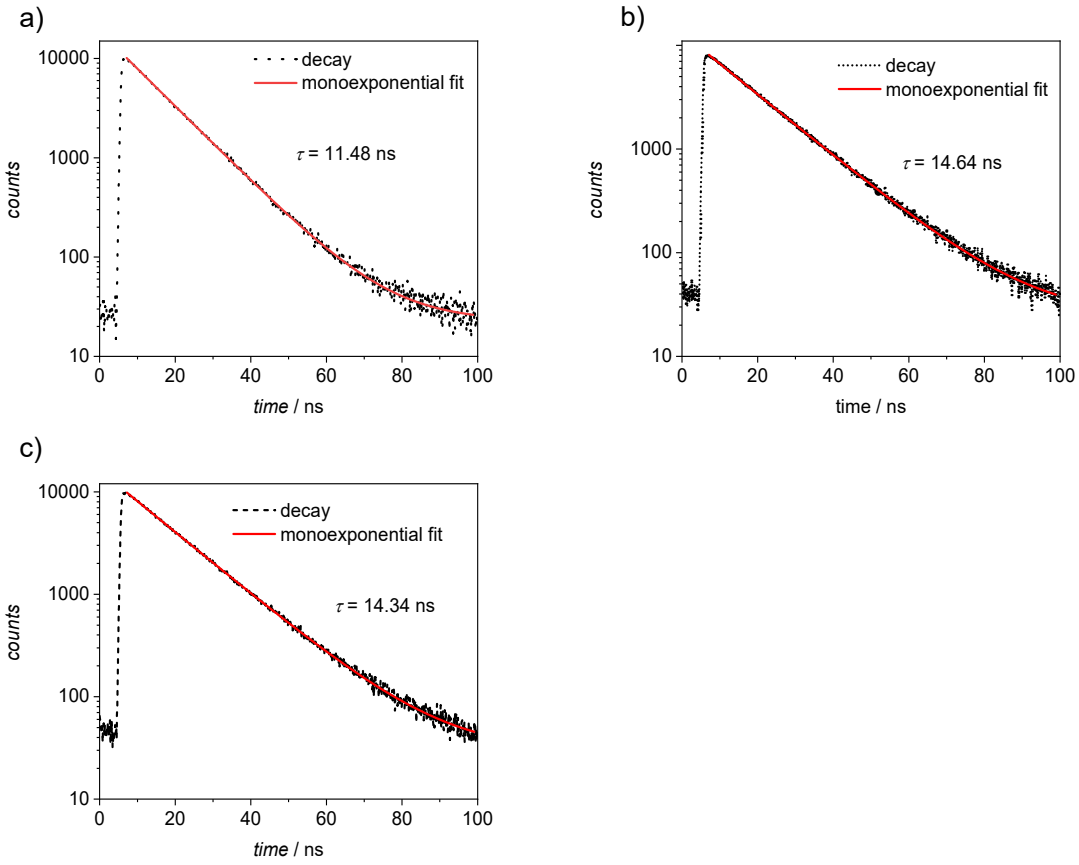

Figure A111. Lifetime measurement (black) of *rac*-**2** in a) $CHCl_3$ and b) tetrachloromethane and c) methylcyclohexane at 295 K (λ_{ex} = 635 nm, λ_{em} = 700 nm). The monoexponential fits are shown in red.

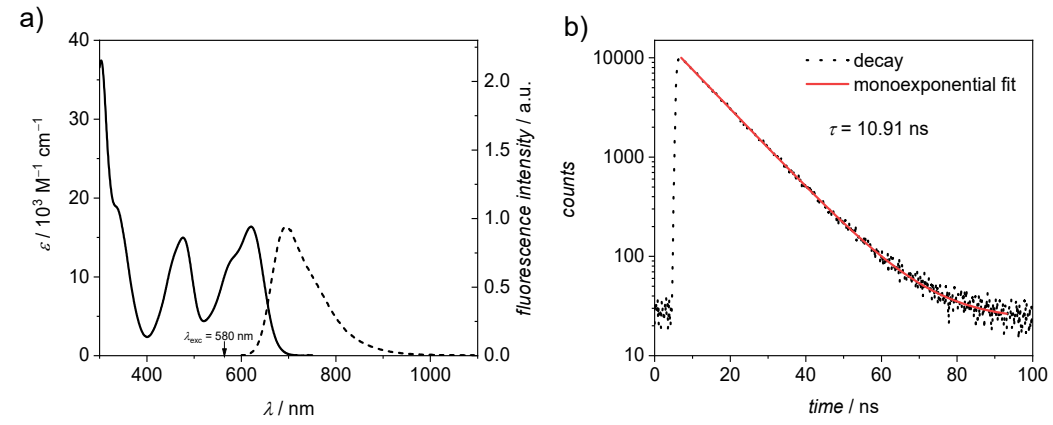

Figure A112. a) UV/vis absorption (c = 30 µM, solid line) and fluorescence (dashed line) spectra of *rac*-**41a** in chloroform and b) lifetime measurement (black) of *rac*-**41a** in $CHCl_3$ at 295 K (λ_{ex} = 635 nm, λ_{em} = 700 nm). The monoexponential fit is shown in red.

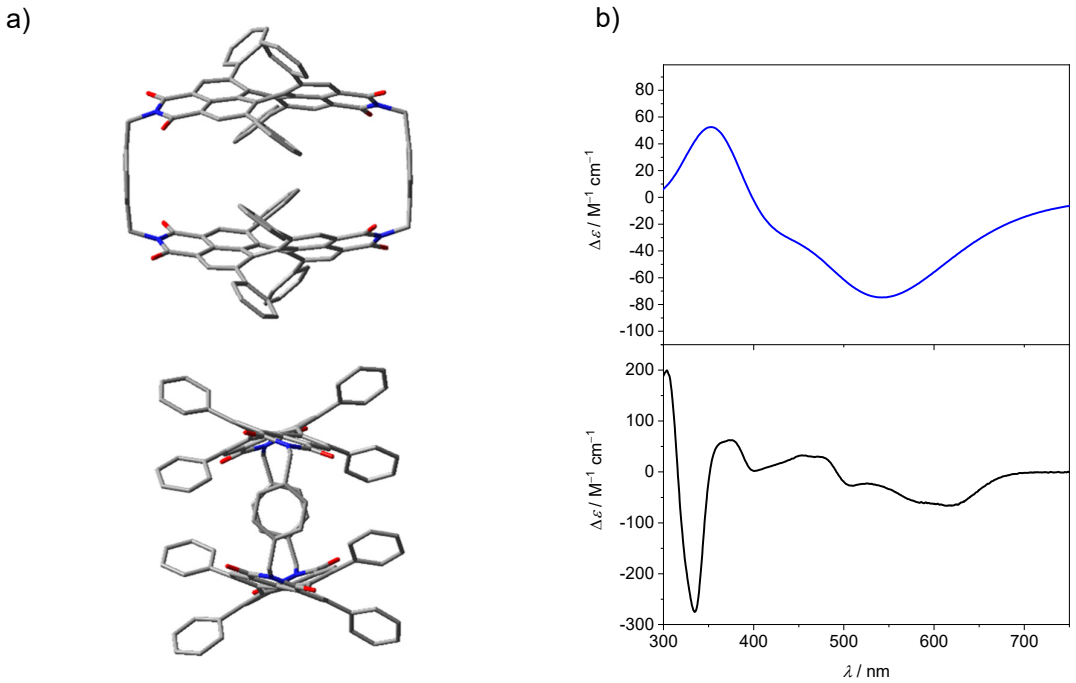

Figure A113. a) Energy minimized structures of **2-*MM*** (*tert*-butyl groups were removed for the calculation; hydrogen atoms are omitted for clarity). b) Calculated (blue solid line) and experimental (black solid line) CD spectra of the optimized structure and **2-*MM***.

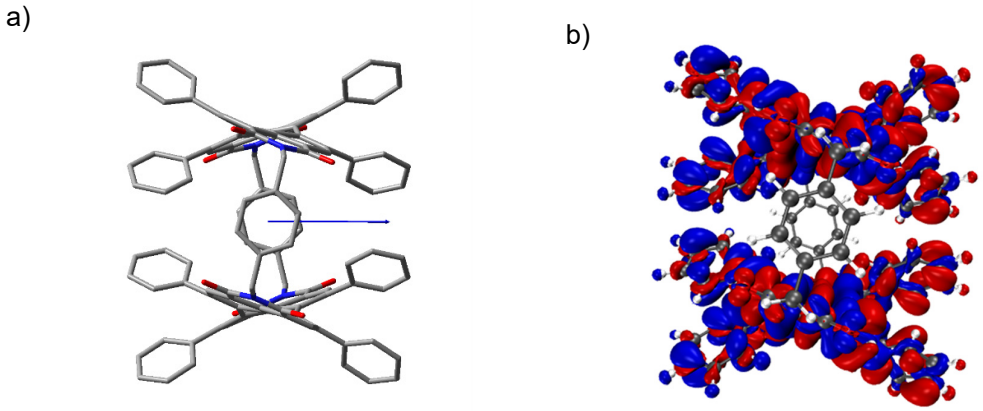

Figure A114. Energy minimized structure of **2-*MM*** (*tert*-butyl groups were removed for the calculation; hydrogen atoms are omitted for clarity) with a) transition dipole moment of the $S_0 \rightarrow S_2$ transition obtained by TD-DFT calculation (charge distribution vector × 0.5 from center of mass). b) Plotted transition densities for the $S_0 \rightarrow S_2$ transition.

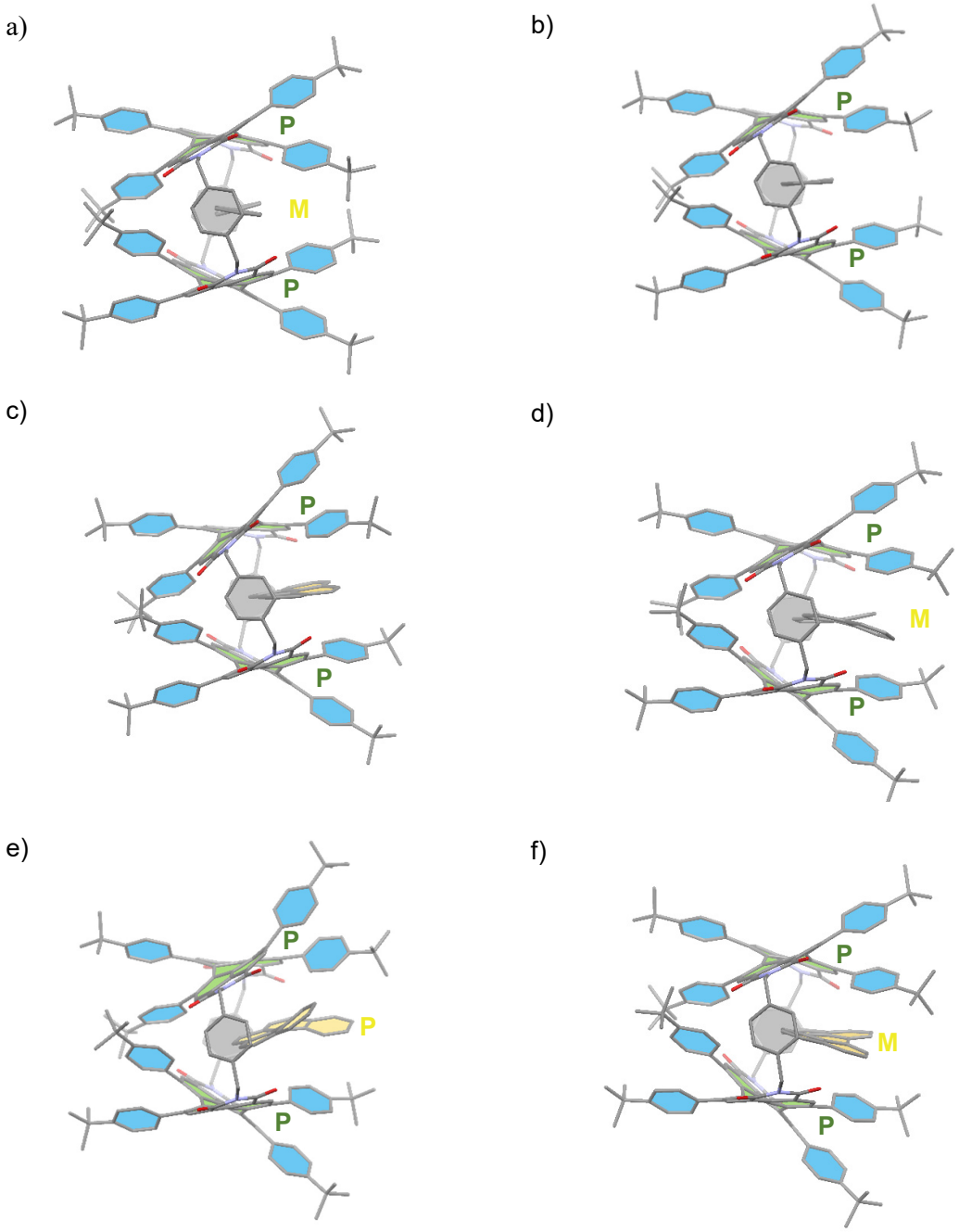

Figure A115. Front view of energy minimized complex structures of a) 1,1'-biphenyl⊂**2-*PP***, b) anthracene⊂**2-*PP***, c) pyrene⊂**2-*PP***, d) [4]helicene⊂**2-*PP*** e) *P*-[5]helicene⊂**2-*PP*** and f) perylene⊂**2-*PP*** (hydrogen atoms are omitted for clarity, the perylene units, the substituents, spacer units and the guests are highlighted in green, blue, grey and yellow).

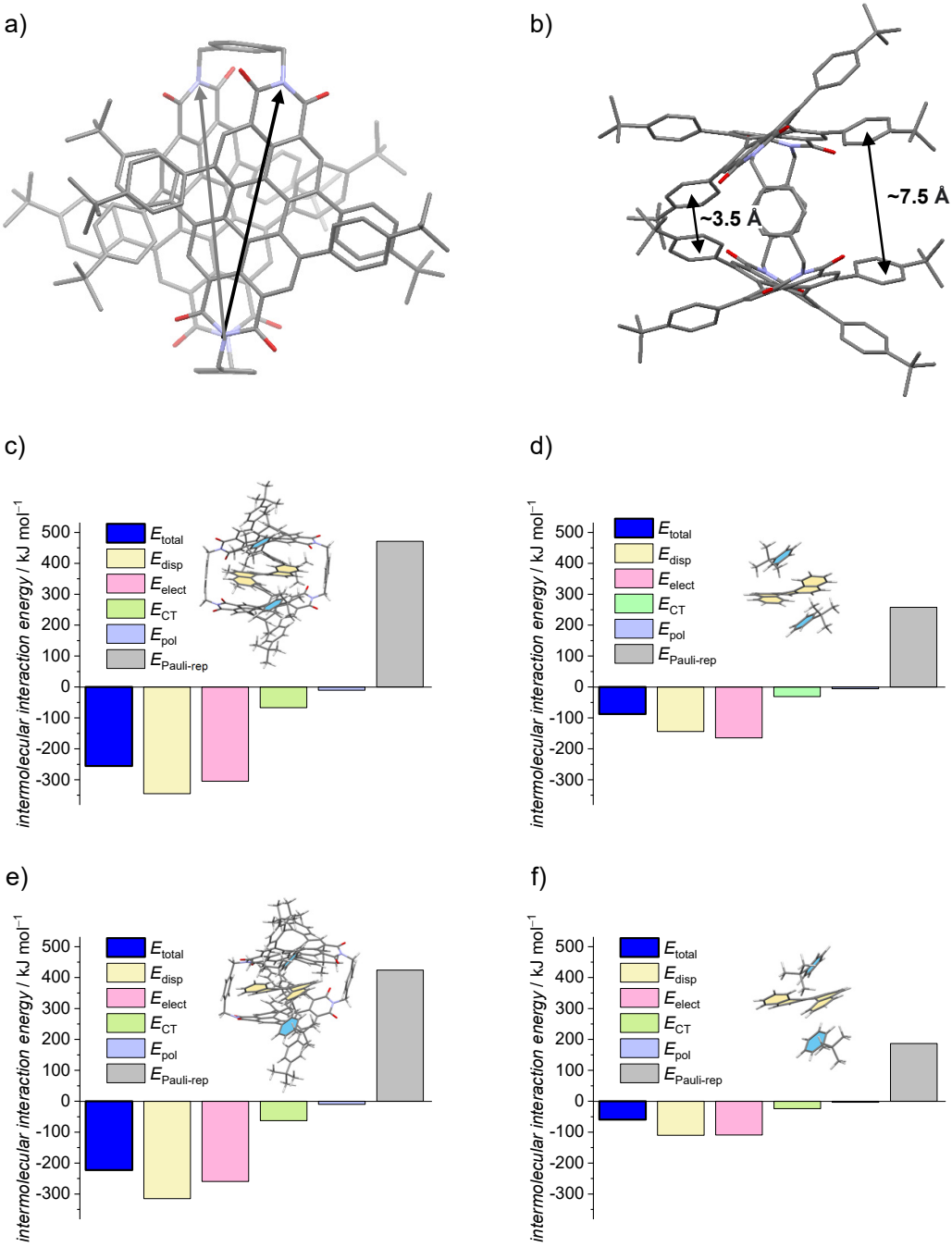

Figure A116. a) Top and b) front view of energy minimized complex structures of *M*-[5]helicene⊂**2-*PP***. The guest is omitted for clarity. c)-d) ALMO energy decomposition analysis performed on DFT optimized structure of *M*-[5]helicene⊂**2-*PP*** and a cutout of the complex structure (guest and the relevant bay substituent in close proximity as depicted in the inset). e)-f) ALMO energy decomposition analysis performed on DFT optimized structure of *P*-[5]helicene⊂**2-*PP*** and a cutout of the complex structure (guest and the relevant bay substituent in close proximity as depicted in the inset).

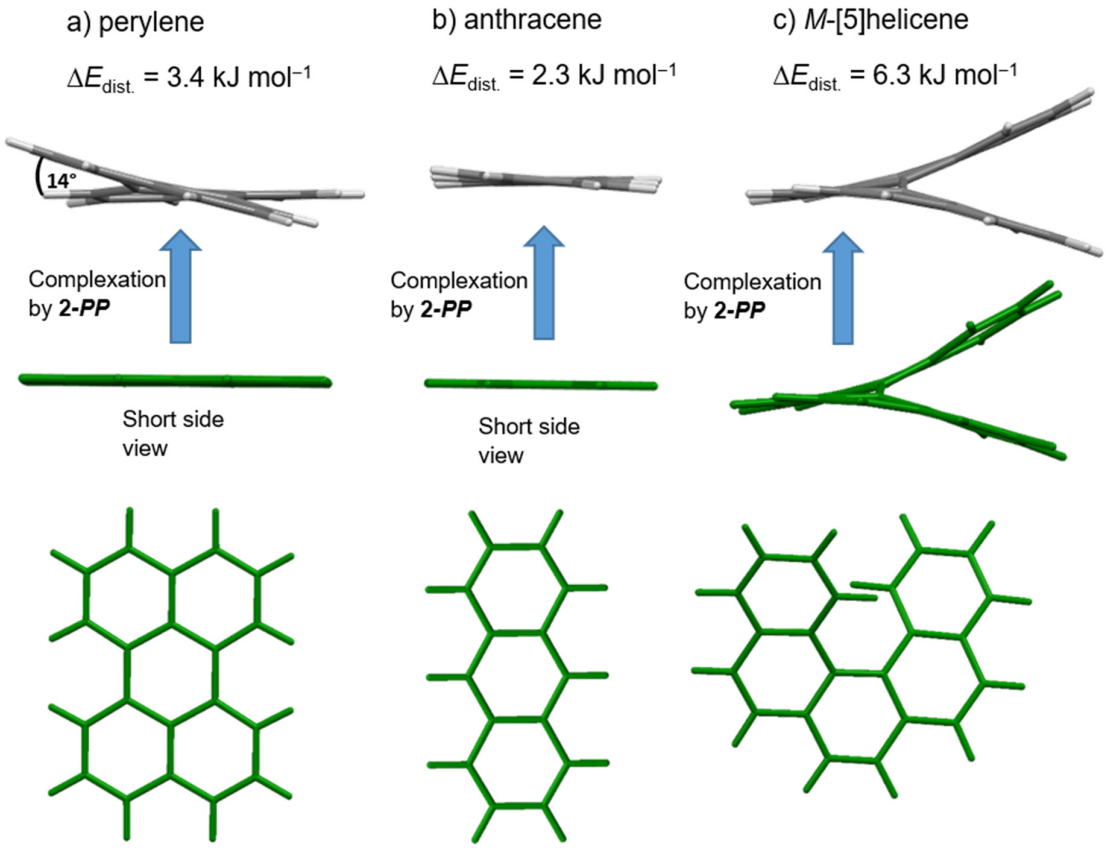

Figure A117. Geometric and energetic differences (SCF energies) between the free substrate (green) and the complexed substrate (grey) by **2-*PP***, given for a) perylene, b) anthracene and c) *M*-[5]helicene. The difference in SCF energies ($\Delta E_{dist.}$) shows that indeed only little energy is needed to distort perylene ($\Delta E_{dist.}$ = 3.4 kJ mol^{-1}) at the central benzene unit to significant dihedral angles of ~ 14° whilst for the other two examples similar or even higher energies are needed for more modest distortions.

Figure A118. Images of the crystals of *rac*-**2**. The crystals of *rac*-**2** were grown from a chloroform by slow diffusion of methanol into the solution.

Table A12. Crystal data and structure refinement for *rac*-**2**.

Identification code	CCDC 2207897
Empirical formula	$C_{145.76}H_{129.76}Cl_{15.29}N_4O_8$
Formula weight	2252.97
Temperature	100(2) K
Wavelength	1.54178 Å
Crystal system	monoclinic
Space group	C2/c
Unit cell dimensions	a = 31.824(2) Å
	b = 18.5816(12) Å
	c = 25.739(3) Å
Volume	12722.4(18) Å^3
Z	4
Density (calculated)	1.176 g/cm^3
Absorption coefficient	1.551 mm^{-1}
F(000)	4745
Crystal size	0.092 × 0.088 × 0.040 mm^3
Theta range for data collection	2.901 to 72.771°
Index ranges	$-39 \le h \le 39$, $-22 \le k \le 22$, $-31 \le l \le 31$
Reflections collected	94333
Independent reflections	12508 [R(int) = 0.1182]
Completeness to theta = 21.836°	99.6%
Absorption correction	Semi-empirical from equivalents
Refinement method	Full-matrix least-squares on F^2
Data / restraints / parameters	12508 / 19 / 789
Goodness-of-fit on F^2	1.137
Final R indices [$I > 2\sigma(I)$]	R_1 = 0.0893, wR_2 = 0.1911
R indices (all data)	R_1 = 0.1109, wR_2 = 0.2013

The crystals of 1,1'-biphenyl⊂*rac*-**2** were grown from a saturated and filtered host and guest solution in methylcyclohexane in a borosilicate glass tube (10 mm × 75 mm), which was put into a closed vial filled with methanol.

Table A13. Crystal data and structure refinement for1,1'-biphenyl⊂*rac*-**2**.

Identification code	CCDC 2207898
Empirical formula	$C_{198.73}\ H_{175.02}\ N_4\ O_8$
Formula weight	2747.23
Temperature	100(2) K
Wavelength	0.61992 Å
Crystal system	Triclinic
Space group	$P\bar{1}$
Unit cell dimensions	a = 20.835(4) Å α = 87.655(3)°
	b = 24.770(5) Å β = 79.275(8)°
	c = 31.712(5) Å γ = 72.772(13)°
Volume	15357(5) Å^3
Z	4
Density (calculated)	1.188 g/cm^3
Absorption coefficient	0.055 mm^{-1}
F(000)	5837.6
Crystal size	0.100 × 0.100 × 0.100 mm^3
Theta range for data collection	0.570 to 27.993°.
Index ranges	$-27 \le h \le 27$, $-37 \le k \le 37$, $-48 \le l \le 47$
Reflections collected	590152
Independent reflections	85764 [R(int) = 0.0920]
Completeness to theta = 21.836°	99.0 %
Absorption correction	None
Refinement method	Full-matrix least-squares on F^2
Data / restraints / parameters	85764 / 4753 / 4684
Goodness-of-fit on F^2	1.028
Final R indices [$I > 2\sigma(I)$]	R_1 = 0.0996, wR_2 = 0.2656
R indices (all data)	R_1 = 0.1615, wR_2 = 0.3232
Extinction coefficient	n/a
Largest diff. peak and hole	0.658 and –0.328 e·Å^{-3}

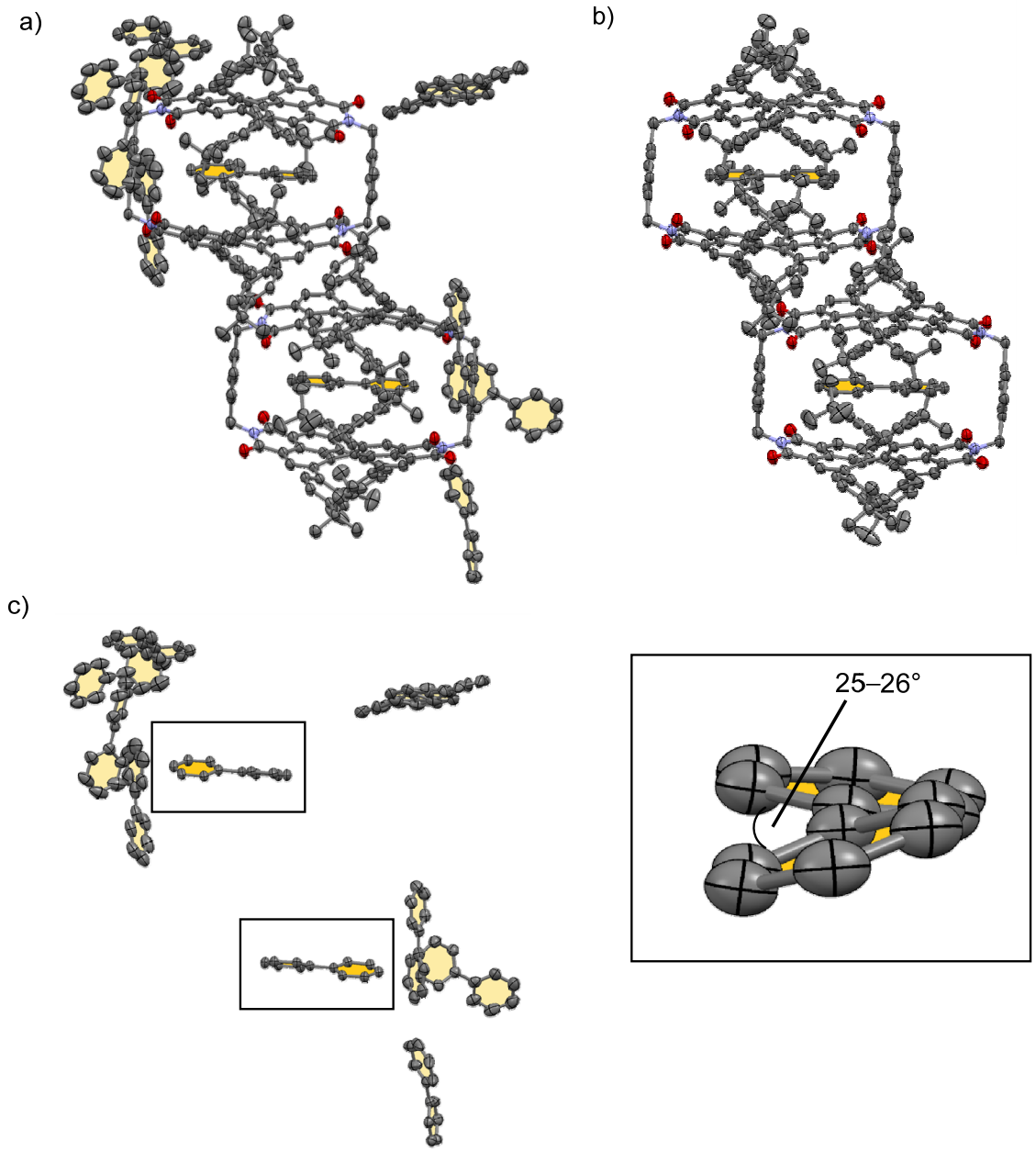

Figure A119. Side view of the packing of 1,1'-biphenyl⊂ *rac*-**2** in the solid state, obtained by single crystal X-ray analysis a) with and b) without the surrounding 1,1'-biphenyl matrix. c) Solid state structure of 1,1'-biphenyl⊂ *rac*-**2** without host molecules and zoom-in of the complexed 1,1'-biphenyl guests within the host cavities.

Appendix Note

From the solid state structure of the host-guest complex, the importance of guest flexibility investigated in the first part of this article also becomes apparent. While the rigidity of the PBI units is manifested in an unchanged core twist of 34–37° as in the solid state structure of the free host (Figure 48), we can clearly see how the angle, that the two planes of the phenyl units of the 1,1'-biphenyl guest spans, adapt to the host cavity. Thus, the twist of the phenyl moieties of the host-embedded 1,1'-biphenyl amounts to an angle of 25–26° (Figure A119), which is in good accordance with the result from our DFT calculation (23°, Figure A115a), while most of the surrounding biphenyl molecules in this crystal show either a twist angle of around 40° or planarity.

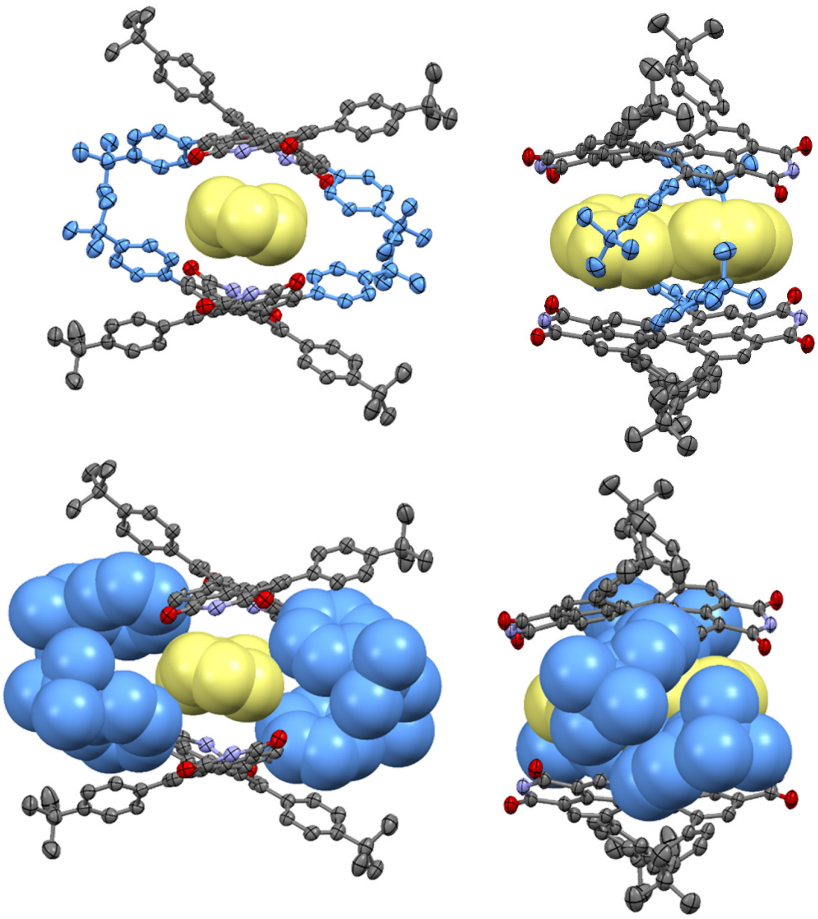

Figure A120. Front and side view of 1,1'-biphenyl⊂**2-*PP*** in the solid state, obtained by single crystal X-ray analysis and a depiction of the structure with the relevant bay substituents and the guest in the space filling model in order to visualize the origin of the heterochiral guest recognition. The guest molecule and the relevant bay substituents are highlighted in yellow and blue respectively. The *para*-xylylene spacer and hydrogens are omitted for clarity.

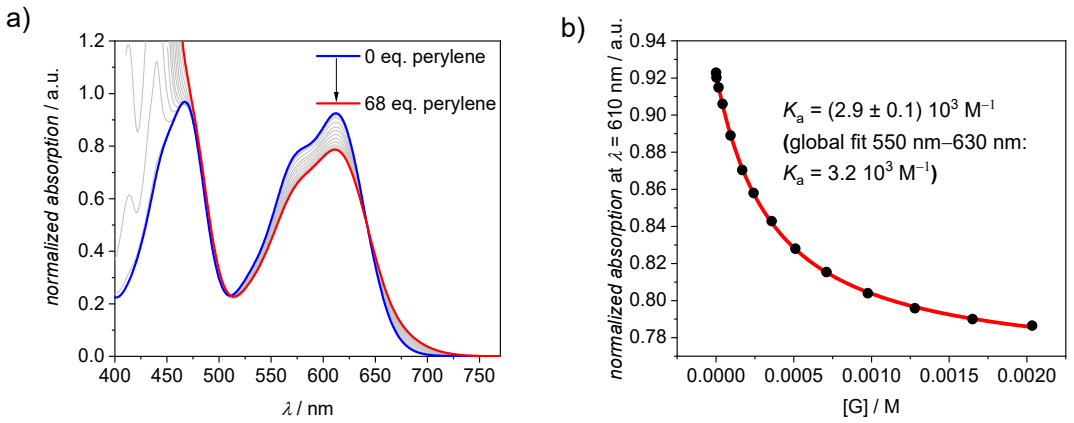

Figure A121. a) UV/vis spectra of cyclophane *rac*-**2** in CCl_4 at 22 °C (c = 30 × 10^{-6} M) upon the addition of perylene as a guest and b) the resulting plot of the absorption at λ = 610 nm with nonlinear curve fit (1:1 binding model, red curve) and binding constants obtained from this curve fit as well as a global fit for the whole $S_0 \rightarrow S_1$ absorption band of the PBI.

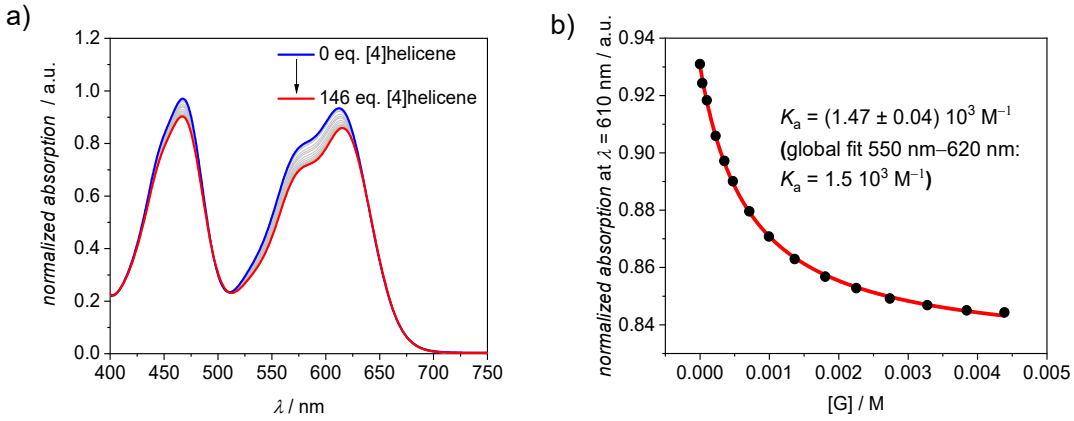

Figure A122. a) UV/vis spectra of cyclophane *rac*-**2** in CCl_4 at 22 °C (c = 30 × 10^{-6} M) upon the addition of [4]helicene as a guest and b) the resulting plot of the absorption at λ = 610 nm with nonlinear curve fit (1:1 binding model, red curve) and binding constants obtained from this curve fit as well as a global fit for the whole $S_0 \rightarrow S_1$ absorption band of the PBI.

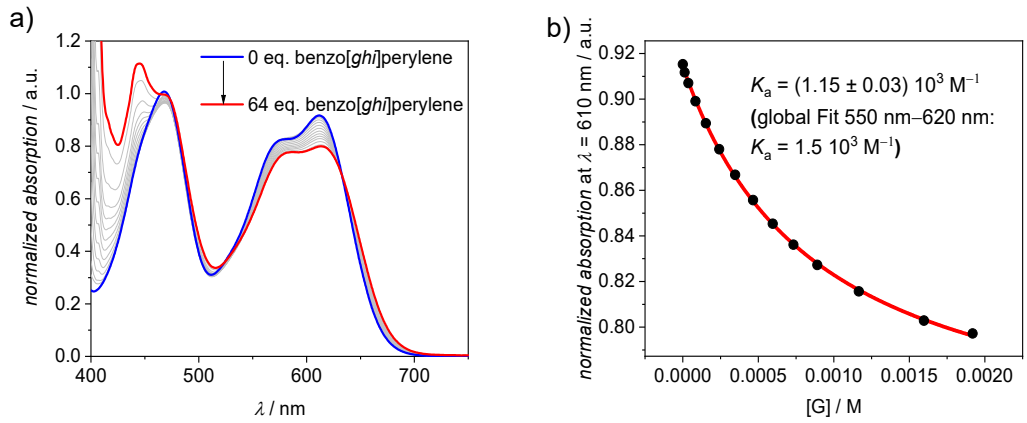

Figure A123. a) UV/vis spectra of cyclophane *rac*-**2** in CCl_4 at 22 °C ($c = 30 \times 10^{-6}$ M) upon the addition of benzo[*ghi*]perylene as a guest and b) the resulting plot of the absorption at $\lambda = 610$ nm with nonlinear curve fit (1:1 binding model, red curve) and binding constants obtained from this curve fit as well as a global fit for the whole $S_0 \rightarrow S_1$ absorption band of the PBI.

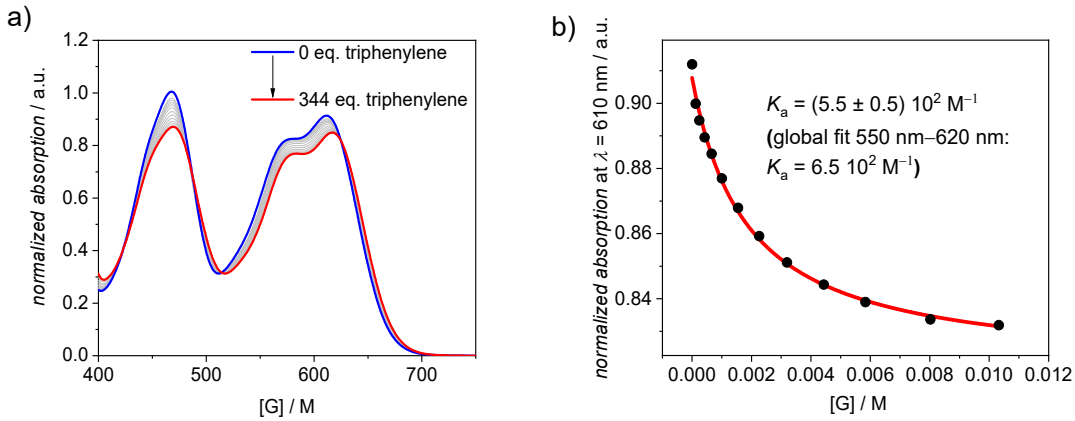

Figure A124. a) UV/vis spectra of cyclophane *rac*-**2** in CCl_4 at 22 °C ($c = 30 \times 10^{-6}$ M) upon the addition of triphenylene as a guest and b) the resulting plot of the absorption at $\lambda = 610$ nm with nonlinear curve fit (1:1 binding model, red curve) and binding constants obtained from this curve fit as well as a global fit for the whole $S_0 \rightarrow S_1$ absorption band of the PBI.

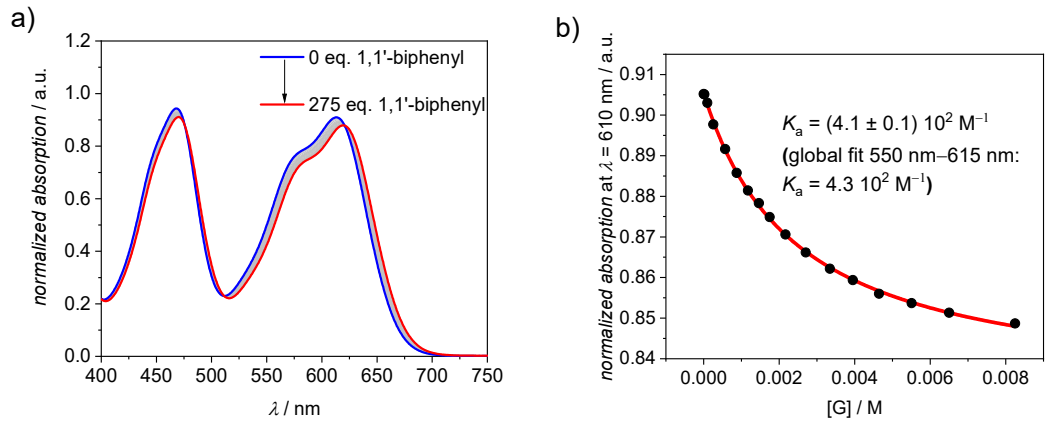

Figure A125. a) UV/vis spectra of cyclophane *rac*-**2** in CCl_4 at 22 °C (c = 30 × 10^{-6} M) upon the addition of 1,1'-biphenyl as a guest and b) the resulting plot of the absorption at λ = 610 nm with nonlinear curve fit (1:1 binding model, red curve) and binding constants obtained from this curve fit as well as a global fit for the whole $S_0 \rightarrow S_1$ absorption band of the PBI.

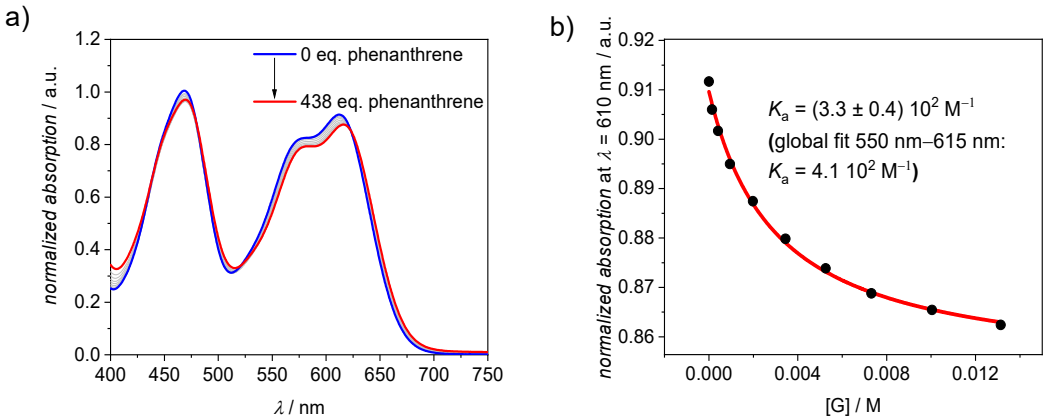

Figure A126. a) UV/vis spectra of cyclophane *rac*-**2** in CCl_4 at 22 °C (c = 30 × 10^{-6} M) upon the addition of phenanthrene as a guest and b) the resulting plot of the absorption at λ = 610 nm with nonlinear curve fit (1:1 binding model, red curve) and binding constants obtained from this curve fit as well as a global fit for the whole $S_0 \rightarrow S_1$ absorption band of the PBI.

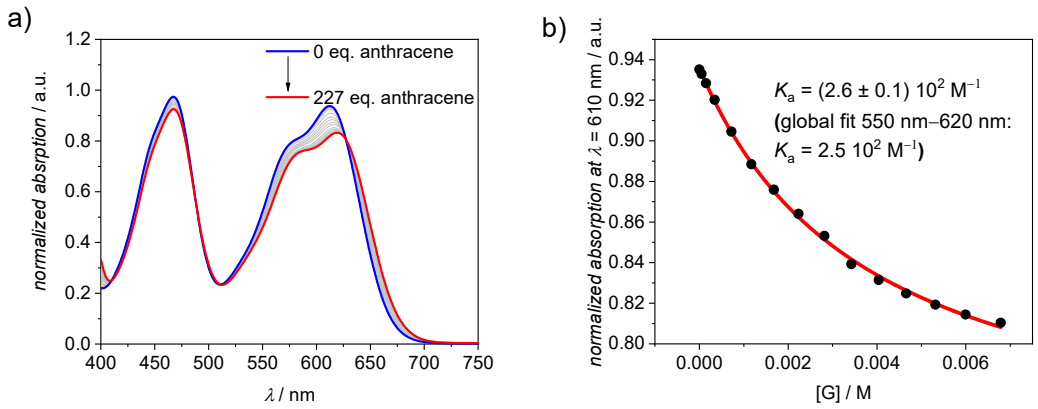

Figure A127. a) UV/vis spectra of cyclophane *rac*-**2** in CCl_4 at 22 °C ($c = 30 \times 10^{-6}$ M) upon the addition of anthracene as a guest and b) the resulting plot of the absorption at $\lambda = 610$ nm with nonlinear curve fit (1:1 binding model, red curve) and binding constants obtained from this curve fit as well as a global fit for the whole $S_0 \rightarrow S_1$ absorption band of the PBI.

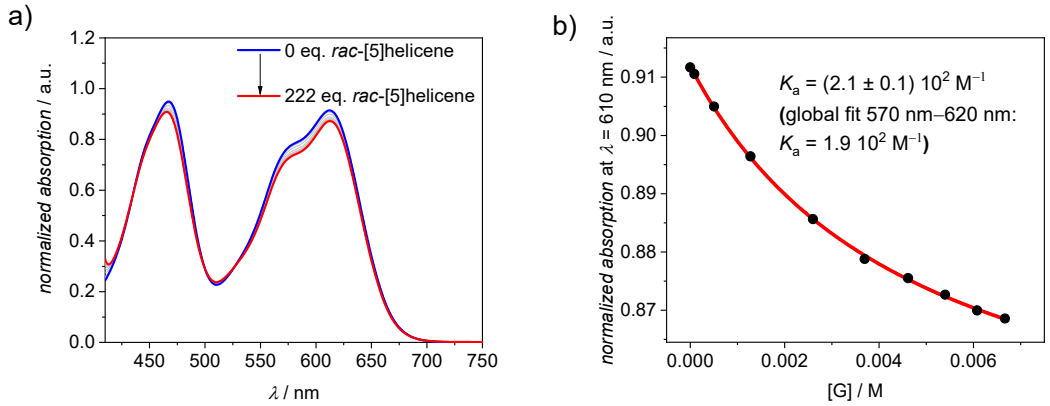

Figure A128. a) UV/vis spectra of cyclophane *rac*-**2** in CCl_4 at 22 °C ($c = 30 \times 10^{-6}$ M) upon the addition of [5]helicene as a guest and b) the resulting plot of the absorption at $\lambda = 610$ nm with nonlinear curve fit (1:1 binding model, red curve) and binding constants obtained from this curve fit as well as a global fit for the whole $S_0 \rightarrow S_1$ absorption band of the PBI.

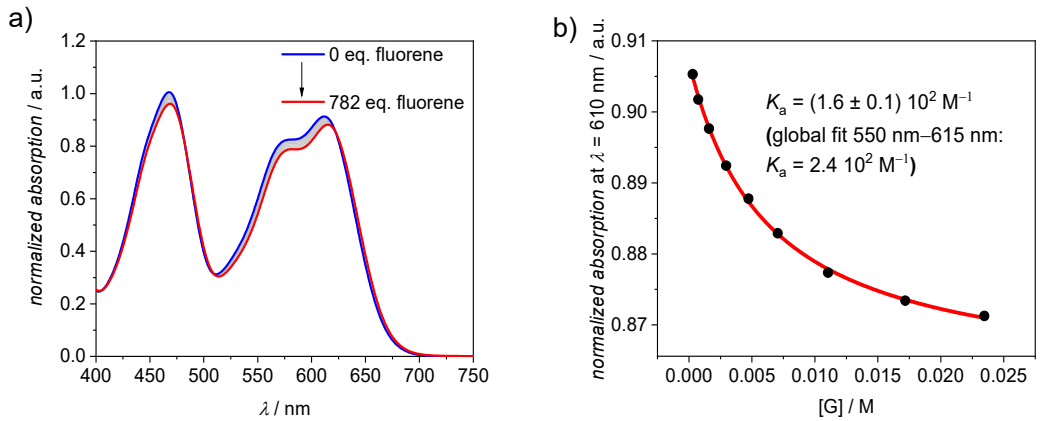

Figure A129. a) UV/vis spectra of cyclophane *rac*-**2** in CCl_4 at 22 °C ($c = 30 \times 10^{-6}$ M) upon the addition of fluorene as a guest and b) the resulting plot of the absorption at $\lambda = 610$ nm with nonlinear curve fit (1:1 binding model, red curve) and binding constants obtained from this curve fit as well as a global fit for the whole $S_0 \rightarrow S_1$ absorption band of the PBI.

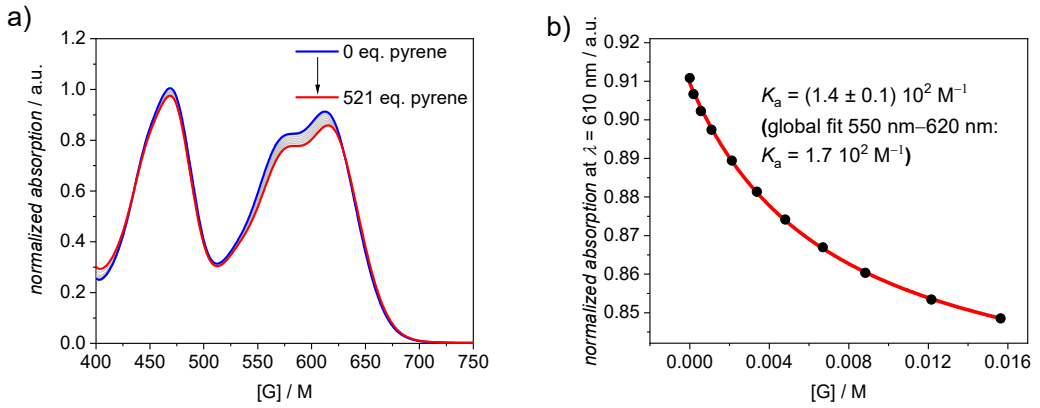

Figure A130. a) UV/vis spectra of cyclophane *rac*-**2** in CCl_4 at 22 °C ($c = 30 \times 10^{-6}$ M) upon the addition of pyrene as a guest and b) the resulting plot of the absorption at $\lambda = 610$ nm with nonlinear curve fit (1:1 binding model, red curve) and binding constants obtained from this curve fit as well as a global fit for the whole $S_0 \rightarrow S_1$ absorption band of the PBI.

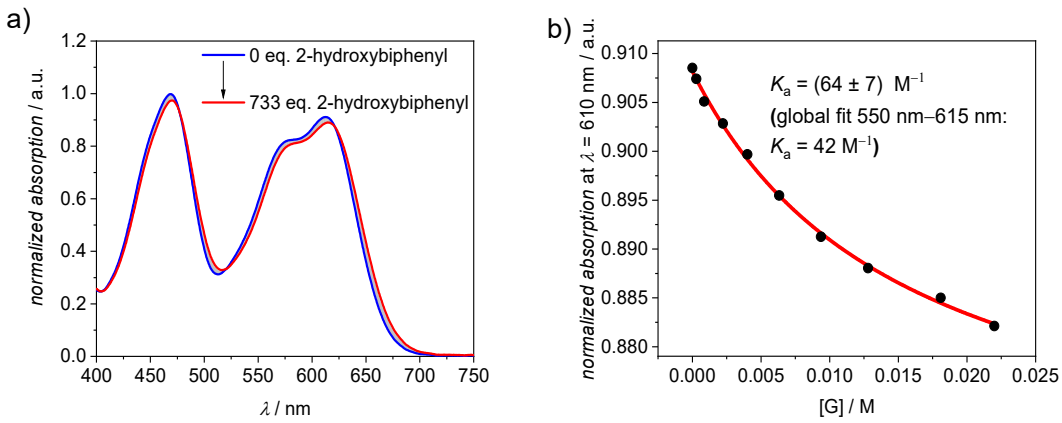

Figure A131. a) UV/vis spectra of cyclophane *rac*-**2** in CCl_4 at 22 °C ($c = 30 \times 10^{-6}$ M) upon the addition of 2-hydroxybiphenyl as a guest and b) the resulting plot of the absorption at $\lambda = 610$ nm with nonlinear curve fit (1:1 binding model, red curve) and binding constants obtained from this curve fit as well as a global fit for the whole $S_0 \rightarrow S_1$ absorption band of the PBI.

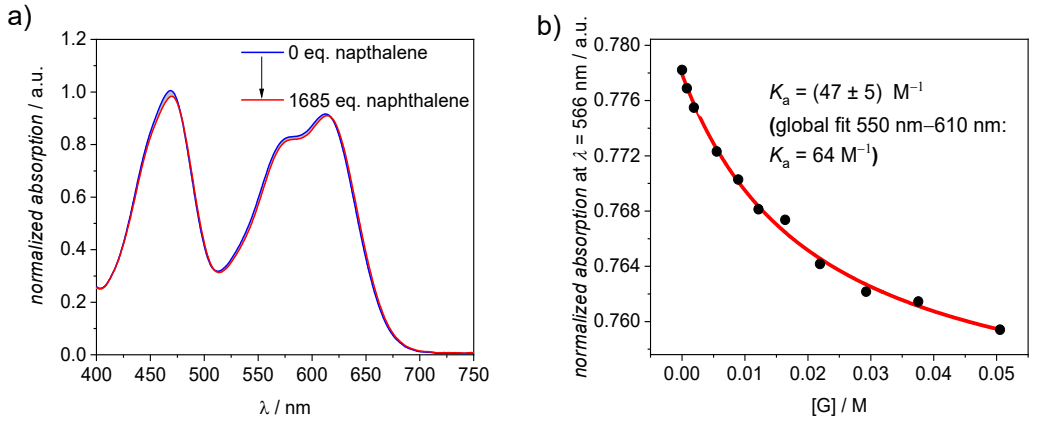

Figure A132. a) UV/vis spectra of cyclophane *rac*-**2** in CCl_4 at 22 °C ($c = 30 \times 10^{-6}$ M) upon the addition of naphthalene as a guest and b) the resulting plot of the absorption at $\lambda = 566$ nm with nonlinear curve fit (1:1 binding model, red curve) and binding constants obtained from this curve fit as well as a global fit for the whole $S_0 \rightarrow S_1$ absorption band of the PBI.

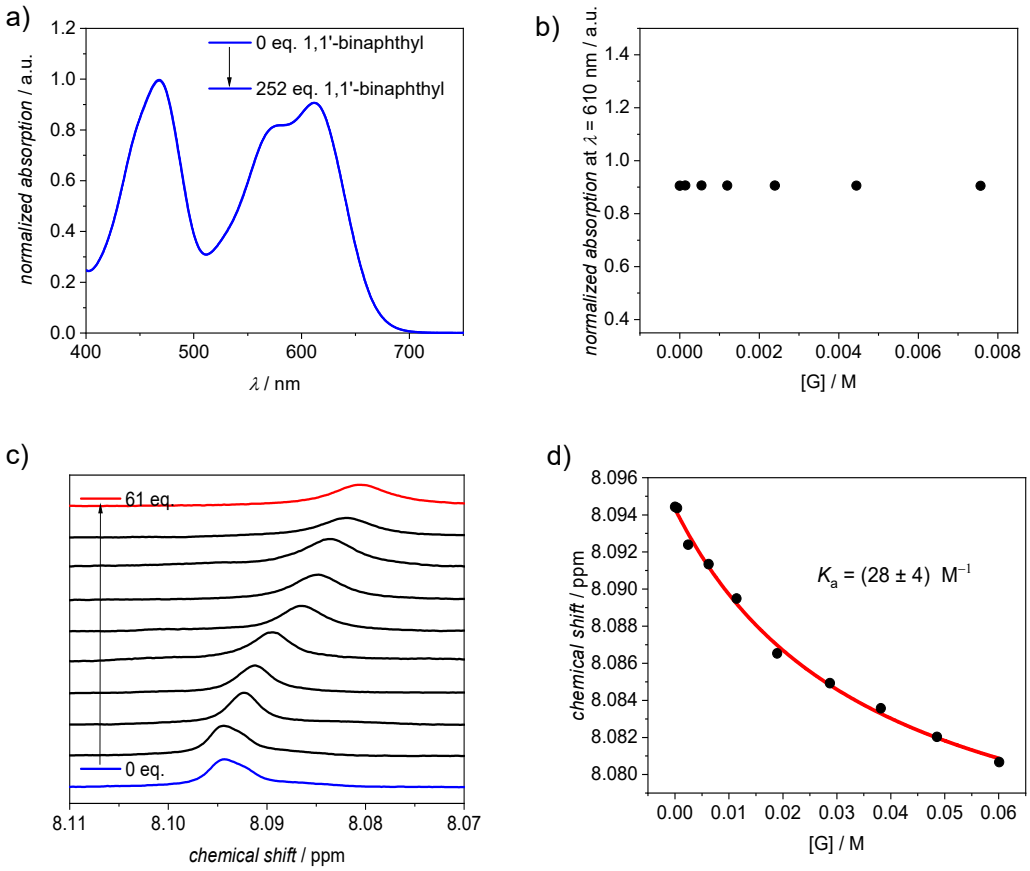

Figure A133. a) UV/vis spectra of cyclophane *rac*-**2** in CCl_4 at 22 °C ($c = 30 \times 10^{-6}$ M) upon the addition of 1,1'-binaphthyl as a guest and b) the resulting plot of the absorption at $\lambda = 566$ nm. c) Excerpt of ^{1}H NMR (CCl_4/MCH-d_{14} 3:1 (v:v), c (*rac*-**2**) = 1.0×10^{-3} M, 295 K) titration experiment of host *rac*-**2** with 1,1'-binaphthyl and d) the nonlinear curve fit of the obtained chemical shift versus guest concentration according to the 1:1 binding model.

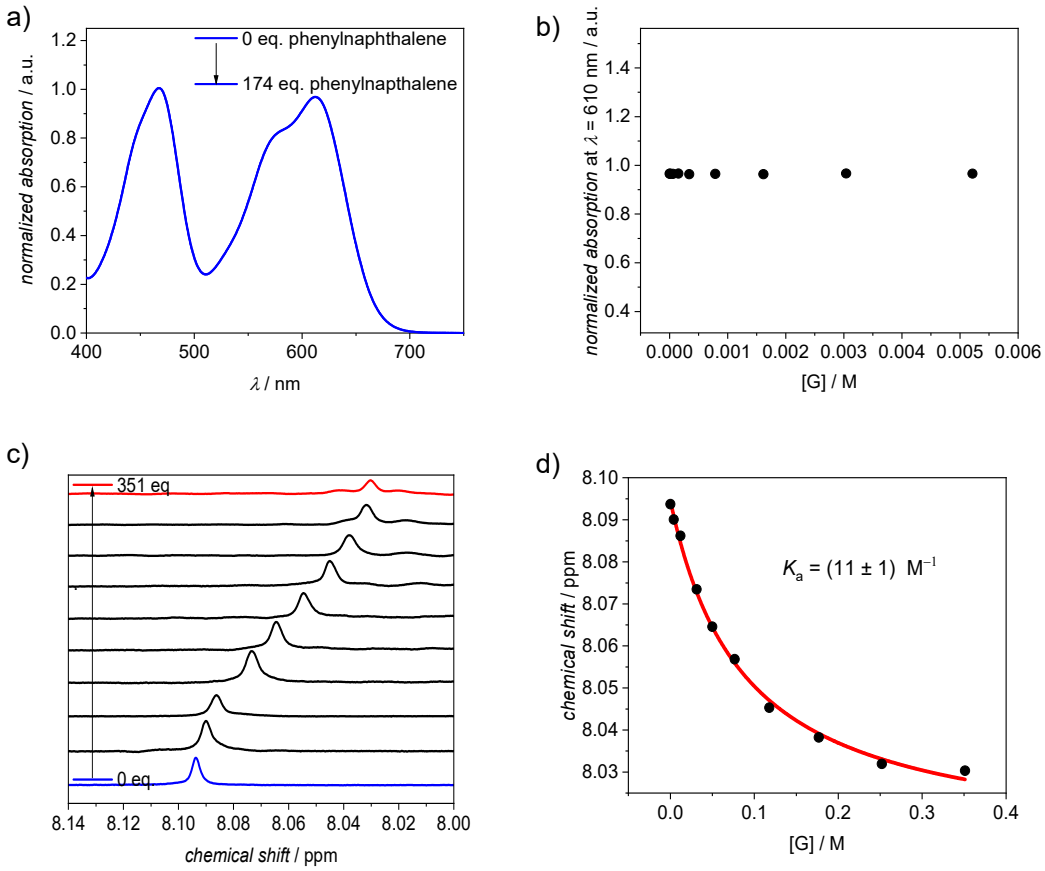

Figure A134. a) UV/vis spectra of cyclophane *rac*-**2** in CCl_4 at 22 °C ($c = 30 \times 10^{-6}$ M) upon the addition of phenylnaphthalene as a guest and b) the resulting plot of the absorption at $\lambda = 566$ nm. c) Excerpt of ^{1}H NMR (CCl_4/MCH-d_{14} 3:1 (v:v), c (*rac*-**2**) = 1.0×10^{-3} M, 295 K) titration experiment of host *rac*-**2** with phenylnapthalene and d) the nonlinear curve fit of the obtained chemical shift versus guest concentration according to the 1:1 binding model.

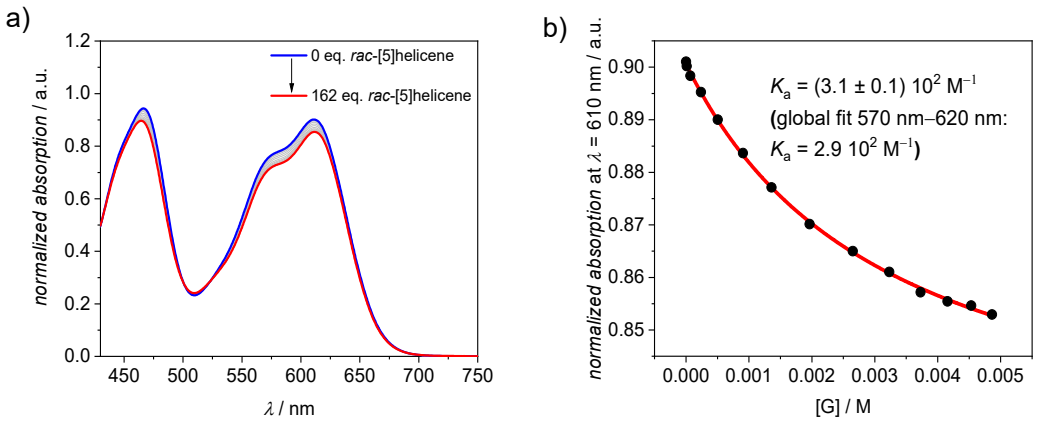

Figure A135. a) UV/vis spectra of cyclophane *rac*-**2** in CCl_4/MCH 3:1 (v:v) at 22 °C (c = 30 × 10^{-6} M) upon the addition of *rac*-[5]helicene as a guest and b) the resulting plot of the absorption at λ = 610 nm with nonlinear curve fit (1:1 binding model, red curve) and binding constants obtained from this curve fit as well as a global fit for the whole $S_0 \rightarrow S_1$ absorption band of the PBI.

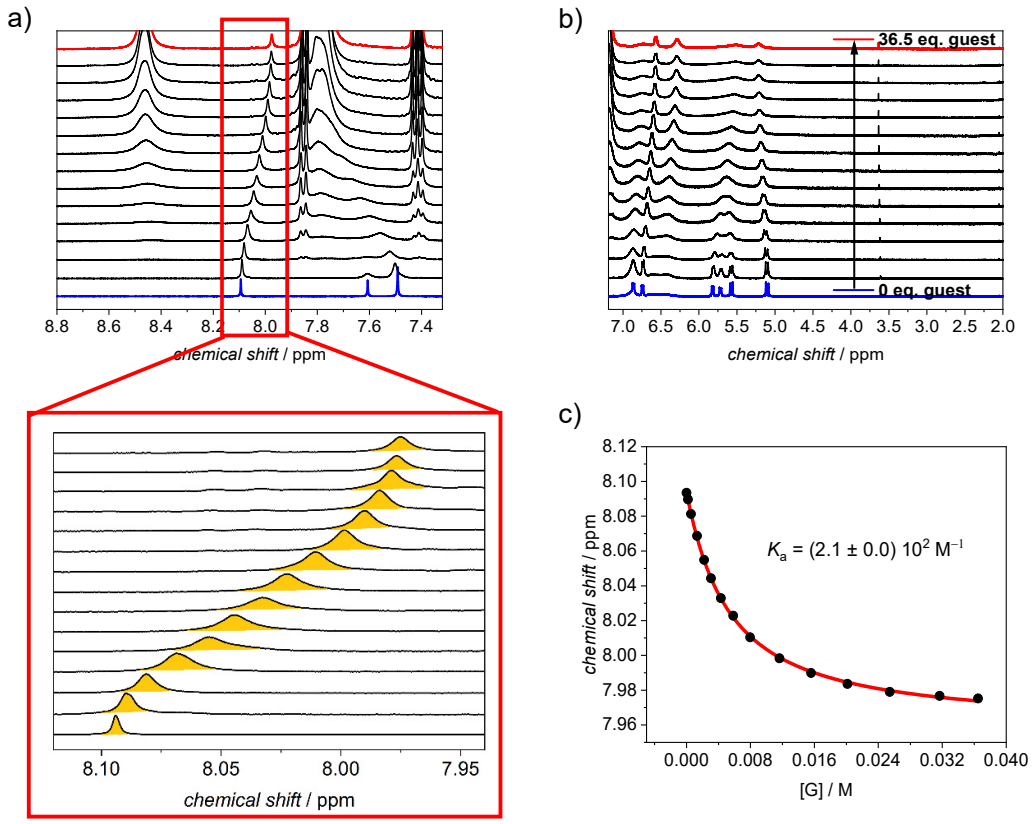

Figure A136. a)-b) Excerpts of ^{1}H NMR (CCl_4/MCH-d_{14} 3:1 (v:v), c (*rac*-**2**) = 1.0 × 10^{-3} M, 295 K) titration experiment of host *rac*-**2** with *rac*-[5]helicene. A zoom-in is shown in order to visualize the upfield shift of the perylene proton upon guest addition, which was used for c) the nonlinear curve fit of the obtained chemical shift versus guest concentration according to the 1:1 binding model.

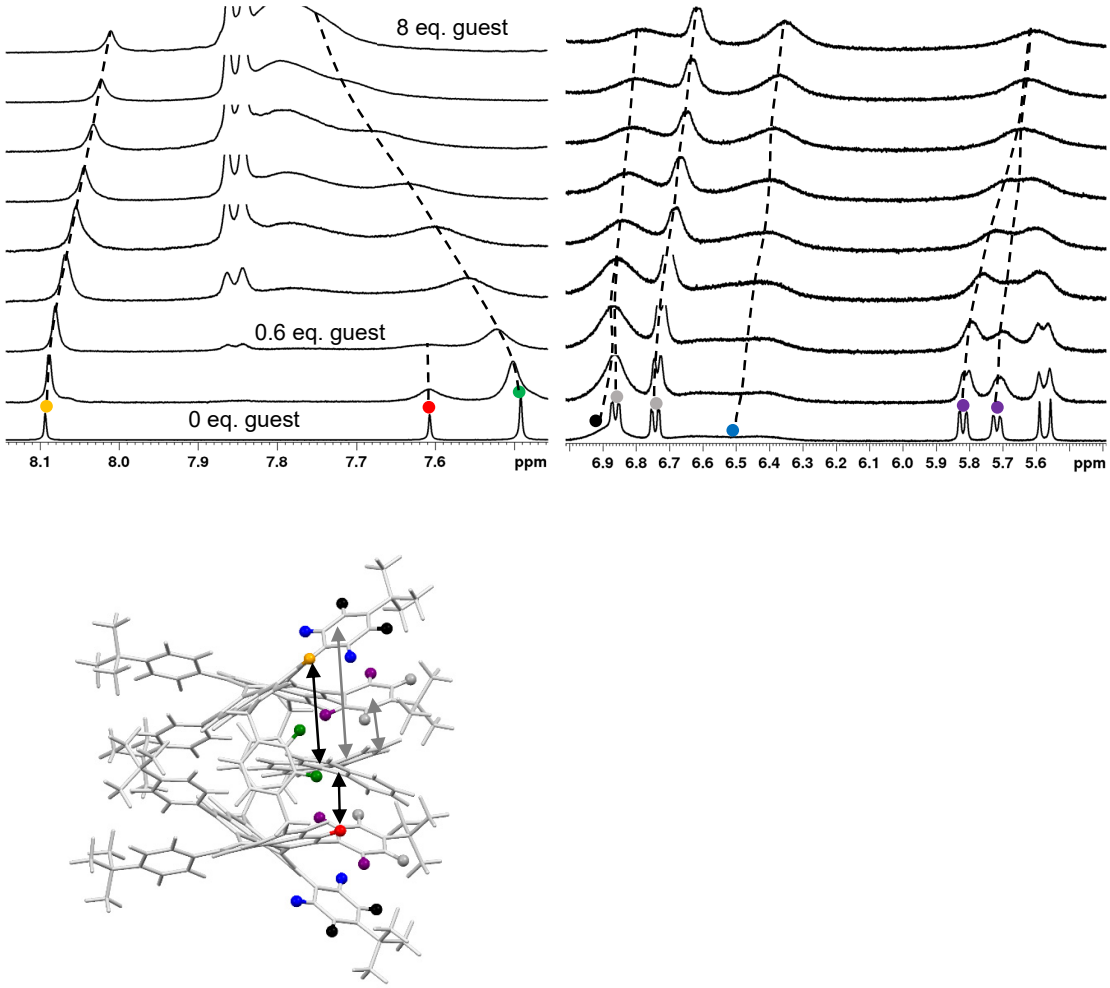

Figure A137. Excerpts of ^{1}H NMR (CCl_4/MCH-d_{14} 3:1 (v:v), *c* (*rac*-**2**) = 1.0 × 10^{-3} M, 295 K) titration experiment from Figure A136 of host *rac*-**2** with *rac*-[5]helicene and DFT optimized structure of *M*-[5]helicene⊂**2**-***PP***. The black and grey double arrows indicate the different distance between the guest and the aromatic protons of the phenyl substituents and the perylene *ortho* protons.

Appendix Note

First, we see a continuous downfield shift of the aromatic xylylene bridge protons upon addition of [5]helicene as these are oriented perpendicular to the aromatic surface of the guest and hence shifted to higher chemical shifts as a result of the guest's ring current. Second, the two non-equivalent perylene *ortho* protons are at very different distances to the guest molecule. As a result, the more distant proton (orange) is only weakly upfield-shifted due to the shielding of the guest's ring current, while the closer proton (red) is extremely broadened already after the addition of 0.6 eq. of guest. Similar, but less pronounced observations, can be made for the bay substituents where the outer phenyl units experience almost no shielding or deshielding upon

guest complexation (protons marked in blue and black). In contrast, we see more distinct shifts and signal broadening of the substituents which are closer to the cavity (protons marked in purple and grey).

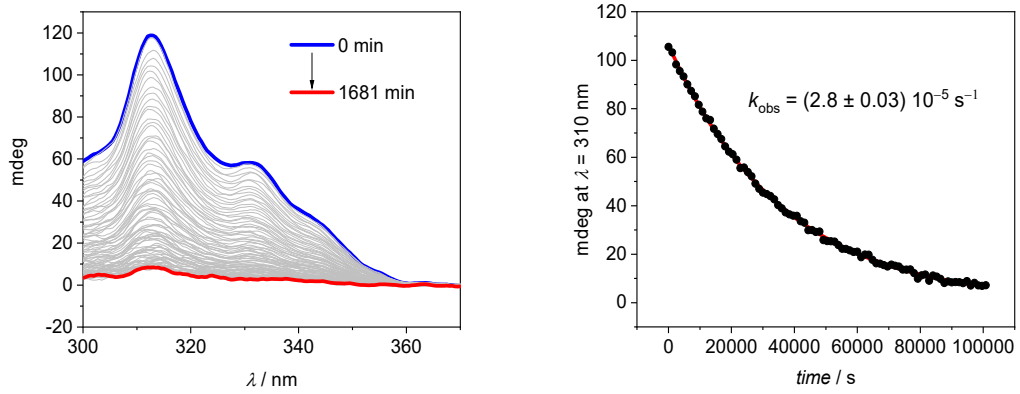

Figure A138. Time-dependent CD spectrum of *P*-[5]helicene (c = 300 µM) in CCl_4/MCH-d_{14} 3:1 at 295 K.

$$S_t = \Delta S e^{-k_{obs}t} + S_\infty \tag{A11}$$

(S: chemical shift or CD signal)[116, 313]

$$\Delta G^{\ddagger} = -RT\ln\left(\frac{k_e h}{k_b T}\right) \tag{A12}$$

(with $k_{obs} = k_{rac} = 2k_e$ (enantiomerization rate constant), R: ideal gas constant, h: Planck constant, k_b: Boltzmann constant, T = 295 K)[239]

Accordingly, we obtain for $\Delta G^{\ddagger}$= 99.6 kJ/mol with $k_e = 1.4 \times 10^{-5}$ s^{-1} (in the absence of the host) and $\Delta G^{\ddagger}$= 99.0 kJ/mol with $k_e = 1.8 \times 10^{-5}$ s^{-1} (in the presence of the host).

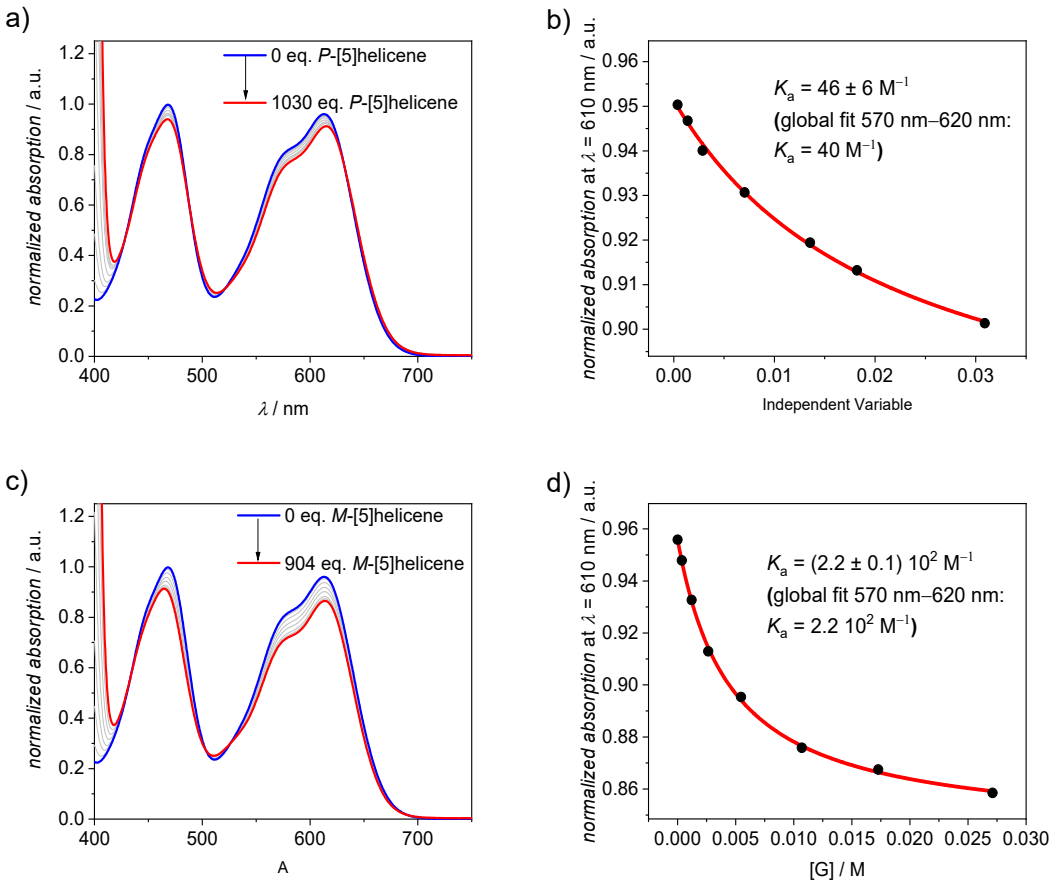

Figure A139. a) UV/vis spectra of cyclophane **2-*PP*** in CCl_4 at 22 °C ($c = 30 \times 10^{-6}$ M) upon the addition of *P*-[5]helicene as a guest and b) the resulting plot of the absorption at $\lambda = 610$ nm with nonlinear curve fit (1:1 binding model, red curve) and binding constants obtained from this curve fit as well as a global fit for the whole $S_0 \rightarrow S_1$ absorption band of the PBI. c) UV/vis spectra of cyclophane **2-*PP*** in CCl_4 at 22 °C ($c = 30 \times 10^{-6}$ M) upon the addition of *M*-[5]helicene as a guest and d) the resulting plot of the absorption at $\lambda = 610$ nm with nonlinear curve fit (1:1 binding model, red curve) and binding constants obtained from this curve fit as well as a global fit for the whole $S_0 \rightarrow S_1$ absorption band of the PBI.

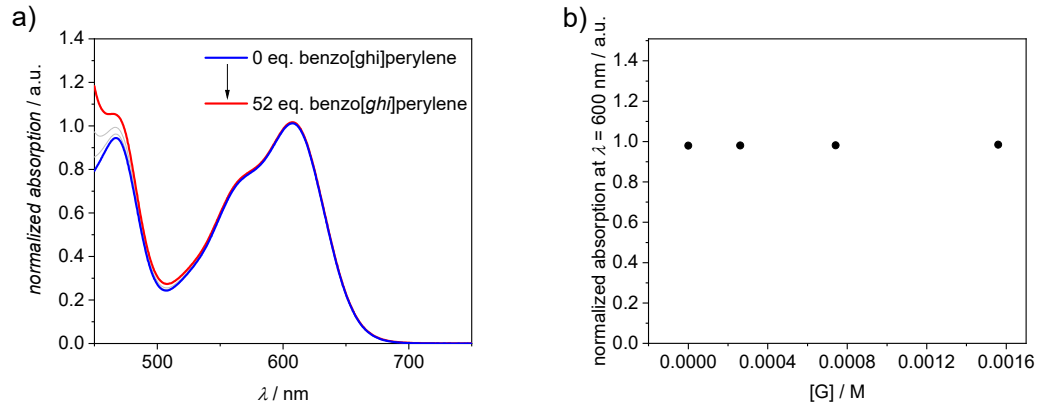

Figure A140. a) UV/vis spectra of cyclophane *rac*-**41a** in CCl_4 at 22 °C ($c = 30 \times 10^{-6}$ M) upon the addition of benzo[*ghi*]perylene and b) the resulting plot of the absorption at $\lambda = 600$ nm.

References

[1] W. Liu, J. F. Stoddart, *Chem* **2021**, *7*, 919–947.

[2] C. J. Pedersen, *J. Am. Chem. Soc.* **1967**, *89*, 7017–7036.

[3] C. J. Pedersen, H. K. Frensdorff, *Angew. Chem. Int. Ed. Engl.* **1972**, *11*, 16–25.

[4] B. Dietrich, J. M. Lehn, J. P. Sauvage, *Tetrahedron Lett.* **1969**, *10*, 2889–2892.

[5] W. D. Curtis, D. A. Laidler, J. F. Stoddart, G. H. Jones, *J. Chem. Soc., Chem. Commun.* **1975**, 833–835.

[6] D. J. Cram, T. Kaneda, R. C. Helgeson, G. M. Lein, *J. Am. Chem. Soc.* **1979**, *101*, 6752–6754.

[7] D. J. Cram, *Angew. Chem. Int. Ed. Engl.* **1986**, *25*, 1039–1057.

[8] D. J. Cram, S. Karbach, Y. H. Kim, L. Baczynskyj, G. W. Kallemeyn, *J. Am. Chem. Soc.* **1985**, *107*, 2575–2576.

[9] D. J. Cram, S. Karbach, Y. H. Kim, L. Baczynskyj, K. Marti, R. M. Sampson, G. W. Kalleymeyn, *J. Am. Chem. Soc.* **1988**, *110*, 2554–2560.

[10] D. J. Cram, *Angew. Chem. Int. Ed. Engl.* **1988**, *27*, 1009–1020.

[11] J.-M. Lehn, *Angew. Chem. Int. Ed. Engl.* **1988**, *27*, 89–112.

[12] C. J. Pedersen, *Angew. Chem. Int. Ed. Engl.* **1988**, *27*, 1021–1027.

[13] D. J. Cram, J. M. Cram, *Science* **1974**, *183*, 803–809.

[14] Z. Liu, S. K. M. Nalluri, J. F. Stoddart, *Chem. Soc. Rev.* **2017**, *46*, 2459–2478.

[15] T. Ogoshi, S. Kanai, S. Fujinami, T.-a. Yamagishi, Y. Nakamoto, *J. Am. Chem. Soc.* **2008**, *130*, 5022–5023.

[16] P. J. Cragg, K. Sharma, *Chem. Soc. Rev.* **2012**, *41*, 597–607.

[17] M. Xue, Y. Yang, X. Chi, Z. Zhang, F. Huang, *Acc. Chem. Res.* **2012**, *45*, 1294–1308.

[18] H. Zhang, Y. Zhao, *Chem. Eur. J.* **2013**, *19*, 16862–16879.

[19] T. Ogoshi, T.-a. Yamagishi, Y. Nakamoto, *Chem. Rev.* **2016**, *116*, 7937–8002.

[20] S. Shinkai, *J. Incl. Phen. and Mol. Recogn. in Chem.* **1989**, *7*, 193–201.

[21] V. Böhmer, *Angew. Chem. Int. Ed. Engl.* **1995**, *34*, 713–745.

[22] J. J. Rebek, *Chem. Commun.* **2000**, 637–643.

[23] W. A. Freeman, W. L. Mock, N. Y. Shih, *J. Am. Chem. Soc.* **1981**, *103*, 7367–7368.

[24] K. Kim, N. Selvapalam, Y. H. Ko, K. M. Park, D. Kim, J. Kim, *Chem. Soc. Rev.* **2007**, *36*, 267–279.

[25] S. J. Barrow, S. Kasera, M. J. Rowland, J. del Barrio, O. A. Scherman, *Chem. Rev.* **2015**, *115*, 12320–12406.

[26] K. I. Assaf, W. M. Nau, *Chem. Soc. Rev.* **2015**, *44*, 394–418.

[27] J. Szejtli, *Chem. Rev.* **1998**, *98*, 1743–1754.

[28] J. F. Stoddart, *Carbohydr. Res.* **1989**, *192*, xii–xv.

[29] M. J. Langton, P. D. Beer, *Acc. Chem. Res.* **2014**, *47*, 1935–1949.

[30] J. Chen, B. L. Hickey, L. Wang, J. Lee, A. D. Gill, A. Favero, R. Pinalli, E. Dalcanale, R. J. Hooley, W. Zhong, *Nat. Chem.* **2021**, *13*, 488–495.

[31] I. Roy, A. H. G. David, P. J. Das, D. J. Pe, J. F. Stoddart, *Chem. Soc. Rev.* **2022**, *51*, 5557–5605.

[32] J. Wankar, N. G. Kotla, S. Gera, S. Rasala, A. Pandit, Y. A. Rochev, *Adv. Funct. Mater.* **2020**, *30*, 1909049.

[33] X. Ma, Y. Zhao, *Chem. Rev.* **2015**, *115*, 7794–7839.

[34] G. Yu, K. Jie, F. Huang, *Chem. Rev.* **2015**, *115*, 7240–7303.

[35] M. Raynal, P. Ballester, A. Vidal-Ferran, P. W. N. M. van Leeuwen, *Chem. Soc. Rev.* **2014**, *43*, 1734–1787.

[36] C. J. Brown, F. D. Toste, R. G. Bergman, K. N. Raymond, *Chem. Rev.* **2015**, *115*, 3012–3035.

[37] Y. Wang, H. Gao, J. Yang, M. Fang, D. Ding, B. Z. Tang, Z. Li, *Adv. Mater.* **2021**, *33*, 2007811.

[38] A. Galan, P. Ballester, *Chem. Soc. Rev.* **2016**, *45*, 1720–1737.

[39] T. Jiao, K. Cai, J. N. Nelson, Y. Jiao, Y. Qiu, G. Wu, J. Zhou, C. Cheng, D. Shen, Y. Feng, Z. Liu, M. R. Wasielewski, J. F. Stoddart, H. Li, *J. Am. Chem. Soc.* **2019**, *141*, 16915–16922.

[40] F. Diederich, K. Dick, *Angew. Chem. Int. Ed. Engl.* **1983**, *22*, 715–716.

[41] F. Diederich, *Angew. Chem. Int. Ed. Engl.* **1988**, *27*, 362–386.

[42] B. Odell, M. V. Reddington, A. M. Z. Slawin, N. Spencer, J. F. Stoddart, D. J. Williams, *Angew. Chem. Int. Ed. Engl.* **1988**, *27*, 1547–1550.

[43] X.-Y. Chen, H. Chen, F. Stoddart, *Angew. Chem. Int. Ed.* **2022**, e202211387.

[44] J. F. Stoddart, *Angew. Chem. Int. Ed.* **2017**, *56*, 11094–11125.

[45] B. L. Feringa, *Angew. Chem. Int. Ed.* **2017**, *56*, 11060–11078.

[46] J.-P. Sauvage, *Angew. Chem. Int. Ed.* **2017**, *56*, 11080–11093.

[47] E. J. Dale, N. A. Vermeulen, M. Juríček, J. C. Barnes, R. M. Young, M. R. Wasielewski, J. F. Stoddart, *Acc. Chem. Res.* **2016**, *49*, 262–273.

[48] T. Jiao, K. Cai, Z. Liu, G. Wu, L. Shen, C. Cheng, Y. Feng, C. L. Stern, J. F. Stoddart, H. Li, *Chem. Sci.* **2019**, *10*, 5114–5123.

[49] X.-Y. Chen, H. Mao, Y. Feng, K. Cai, D. Shen, H. Wu, L. Zhang, X. Zhao, H. Chen, B. Song, Y. Jiao, Y. Wu, C. L. Stern, M. R. Wasielewski, J. F. Stoddart, *Angew. Chem. Int. Ed.* **2021**, *60*, 25454–25462.

[50] M. Juríček, N. L. Strutt, J. C. Barnes, A. M. Butterfield, E. J. Dale, K. K. Baldridge, J. F. Stoddart, J. S. Siegel, *Nat. Chem.* **2014**, *6*, 222–228.

[51] L. Pauling, *Nature* **1948**, *161*, 707–709.

[52] F. M. Menger, *Biochemistry* **1992**, *31*, 5368–5373.

[53] D. E. Koshland, *Proc. Acad. Natl. Sci. USA* **1958**, *44*, 98–104.

[54] D. E. Koshland Jr, *Angew. Chem. Int. Ed. Engl.* **1995**, *33*, 2375–2378.

[55] F. Würthner, C. R. Saha-Möller, B. Fimmel, S. Ogi, P. Leowanawat, D. Schmidt, *Chem. Rev.* **2016**, *116*, 962–1052.

[56] P. Spenst, F. Würthner, *Angew. Chem. Int. Ed.* **2015**, *54*, 10165–10168.

[57] M. Sapotta, P. Spenst, C. R. Saha-Möller, F. Würthner, *Org. Chem. Front.* **2019**, *6*, 892–899.

[58] A. A. Kroeger, A. Karton, *J. Org. Chem.* **2022**, *87*, 5485–5496.

[59] L. Pasteur, *Ann. Chim. Phys.* **1848**, *24*, 442–459.

[60] J. Gal, *Chirality* **2008**, *20*, 5–19.

[61] K. Mori, *Chem. Commun.* **1997**, 1153–1158.

[62] V. Sundaresan, R. Abrol, *Chirality* **2005**, *17*, S30–S39.

[63] K. Mori, *Bioorg. Med. Chem.* **2007**, *15*, 7505–7523.

[64] T. A. Müller, H. P. E. Kohler, *Appl. Microbiol. Biotechnol.* **2004**, *64*, 300–316.

[65] B. S. Sekhon, *J. Pestic. Sci.* **2009**, *34*, 1–12.

[66] M. O'Neill, S. M. Kelly, *Adv. Mater.* **2011**, *23*, 566–584.

[67] Y. Yang, R. C. da Costa, M. J. Fuchter, A. J. Campbell, *Nat. Photon.* **2013**, *7*, 634–638.

[68] Y. Yang, Y. Zhang, Z. Wei, *Adv. Mater.* **2013**, *25*, 6039–6049.

[69] P. Josse, L. Favereau, C. Shen, S. Dabos-Seignon, P. Blanchard, C. Cabanetos, J. Crassous, *Chem. Eur. J.* **2017**, *23*, 6277–6281.

[70] K. Faber, *Chem. Eur. J.* **2001**, *7*, 5004–5010.

[71] C. C. Gruber, I. Lavandera, K. Faber, W. Kroutil, *Adv. Synth. Catal.* **2006**, *348*, 1789–1805.

[72] R. Maeda, T. Wada, T. Mori, S. Kono, N. Kanomata, Y. Inoue, *J. Am. Chem. Soc.* **2011**, *133*, 10379–10381.

[73] A. Hölzl-Hobmeier, A. Bauer, A. V. Silva, S. M. Huber, C. Bannwarth, T. Bach, *Nature* **2018**, *564*, 240–243.

[74] Q. Shi, J. Ye, *Angew. Chem. Int. Ed.* **2020**, *59*, 4998–5001.

[75] M. Rachwalski, N. Vermue, F. P. J. T. Rutjes, *Chem. Soc. Rev.* **2013**, *42*, 9268–9282.

[76] M. Liu, L. Zhang, T. Wang, *Chem. Rev.* **2015**, *115*, 7304–7397.

[77] J. M. Rivera, T. Martín, J. Rebek, *Science* **1998**, *279*, 1021–1023.

[78] J. M. Rivera, S. L. Craig, T. Martín, J. J. Rebek, *Angew. Chem. Int. Ed.* **2000**, *39*, 2130–2132.

[79] R.-J. Li, J. J. Holstein, W. G. Hiller, J. Andréasson, G. H. Clever, *J. Am. Chem. Soc.* **2019**, *141*, 2097–2103.

[80] N. Ousaka, S. Yamamoto, H. Iida, T. Iwata, S. Ito, Y. Hijikata, S. Irle, E. Yashima, *Nat. Commun.* **2019**, *10*, 1457.

[81] P. Pfeiffer, K. Quehl, *Ber. Dtsch. Chem. Ges. (A and B Series)* **1931**, *64*, 2667–2671.

[82] M. Quan, X.-Y. Pang, W. Jiang, *Angew. Chem. Int. Ed.* **2022**, *61*, e202201258.

[83] J. Labuta, J. P. Hill, S. Ishihara, L. Hanyková, K. Ariga, *Acc. Chem. Res.* **2015**, *48*, 521–529.

[84] L. Martínez-Rodríguez, N. A. G. Bandeira, C. Bo, A. W. Kleij, *Chem. Eur. J.* **2015**, *21*, 7144–7150.

[85] S. Allenmark, *Chirality* **2003**, *15*, 409–422.

[86] S. J. Wezenberg, G. Salassa, E. C. Escudero-Adán, J. Benet-Buchholz, A. W. Kleij, *Angew. Chem. Int. Ed.* **2011**, *50*, 713–716.

[87] V. V. Borovkov, J. M. Lintuluoto, Y. Inoue, *Org. Lett.* **2000**, *2*, 1565–1568.

[88] V. V. Borovkov, G. A. Hembury, Y. Inoue, *Acc. Chem. Res.* **2004**, *37*, 449–459.

[89] N. Berova, G. Pescitelli, A. G. Petrovic, G. Proni, *Chem. Commun.* **2009**, 5958–5980.

[90] M. Anyika, H. Gholami, K. D. Ashtekar, R. Acho, B. Borhan, *J. Am. Chem. Soc.* **2014**, *136*, 550–553.

[91] H. Zhu, Q. Li, Z. Gao, H. Wang, B. Shi, Y. Wu, L. Shangguan, X. Hong, F. Wang, F. Huang, *Angew. Chem. Int. Ed.* **2020**, *59*, 10868–10872.

[92] L. Cheng, K. Liu, Y. Duan, H. Duan, Y. Li, M. Gao, L. Cao, *CCS Chem.* **2020**, *3*, 2749–2763.

[93] I. Wong, S. S. Patel, K. A. Johnson, *Biochemistry* **1991**, *30*, 526–537.

[94] A. J. Berdis, *Chem. Rev.* **2009**, *109*, 2862–2879.

[95] L. Lancaster, W. Abdallah, S. Banta, I. Wheeldon, *Chem. Soc. Rev.* **2018**, *47*, 5177–5186.

[96] F. W. Lichtenthaler, *Angew. Chem. Int. Ed. Engl.* **1995**, *33*, 2364–2374.

[97] E. Fischer, *Ber. Dtsch. Chem. Ges* **1894**, *27*, 2985–2993.

[98] A. D. Vogt, E. Di Cera, *Biochemistry* **2012**, *51*, 5894–5902.

[99] L. Kovbasyuk, R. Krämer, *Chem. Rev.* **2004**, *104*, 3161–3188.

[100] N. C. Gianneschi, S. T. Nguyen, C. A. Mirkin, *J. Am. Chem. Soc.* **2005**, *127*, 1644–1645.

[101] M. J. Wiester, P. A. Ulmann, C. A. Mirkin, *Angew. Chem. Int. Ed.* **2011**, *50*, 114–137.

[102] J. Guo, H.-X. Zhou, *Chem. Rev.* **2016**, *116*, 6503–6515.

[103] A. Faulkner, T. van Leeuwen, B. L. Feringa, S. J. Wezenberg, *J. Am. Chem. Soc.* **2016**, *138*, 13597–13603.

[104] Y. Suzuki, T. Nakamura, H. Iida, N. Ousaka, E. Yashima, *J. Am. Chem. Soc.* **2016**, *138*, 4852–4859.

[105] M. Brunori, *FEBS J.* **2014**, *281*, 633–643.

[106] Y. Yuan, M. F. Tam, V. Simplaceanu, C. Ho, *Chem. Rev.* **2015**, *115*, 1702–1724.

[107] D. E. Koshland Jr, *J. Cell. Physiol.* **1959**, *54*, 245–258.

[108] J. Monod, J. Wyman, J.-P. Changeux, *J. Mol. Biol.* **1965**, *12*, 88–118.

[109] A. D. Vogt, E. Di Cera, *Biochemistry* **2013**, *52*, 5723–5729.

[110] Y. Yuan, J. Deng, Q. Cui, *J. Am. Chem. Soc.* **2022**, *144*, 10870–10887.

[111] F. Paul, T. R. Weikl, in *PLoS Comput. Biol., Vol. 12*, **2016**, p. e1005067.

[112] S. Gianni, J. Dogan, P. Jemth, *Biophys. Chem.* **2014**, *189*, 33–39.

[113] P. Chakraborty, E. Di Cera, *Biochemistry* **2017**, *56*, 2853–2859.

[114] A. D. Vogt, N. Pozzi, Z. Chen, E. Di Cera, *Biophys. Chem.* **2014**, *186*, 13–21.

[115] C. M. Hong, D. M. Kaphan, R. G. Bergman, K. N. Raymond, F. D. Toste, *J. Am. Chem. Soc.* **2017**, *139*, 8013–8021.

[116] L.-P. Yang, L. Zhang, M. Quan, J. S. Ward, Y.-L. Ma, H. Zhou, K. Rissanen, W. Jiang, *Nat. Commun.* **2020**, *11*, 2740.

[117] R. Z. Pavlović, R. F. Lalisse, A. L. Hansen, C. A. Waudby, Z. Lei, M. Güney, X. Wang, C. M. Hadad, J. D. Badjić, *Angew. Chem. Int. Ed.* **2021**, *60*, 19942–19948.

[118] G. Hammes Gordon, Y.-C. Chang, G. Oas Terrence, *Proc. Acad. Natl. Sci. USA* **2009**, *106*, 13737–13741.

[119] A. Blanco-Gómez, Á. Fernández-Blanco, V. Blanco, J. Rodríguez, C. Peinador, M. D. García, *J. Am. Chem. Soc.* **2019**, *141*, 3959–3964.

[120] H. L. Anderson, C. A. Hunter, M. N. Meah, J. K. M. Sanders, *J. Am. Chem. Soc.* **1990**, *112*, 5780–5789.

[121] K. Fujita, W.-H. Chen, D.-Q. Yuan, Y. Nogami, T. Koga, T. Fujioka, K. Mihashi, S. Immel, F. W. Lichtenthaler, *Tetrahedron: Asymmetry* **1999**, *10*, 1689–1696.

[122] T. Haino, D. M. Rudkevich, A. Shivanyuk, K. Rissanen, J. J. Rebek, *Chem. Eur. J.* **2000**, *6*, 3797–3805.

[123] S. Le Gac, J. Marrot, O. Reinaud, I. Jabin, *Angew. Chem. Int. Ed.* **2006**, *45*, 3123–3126.

[124] S. Hiraoka, K. Harano, T. Nakamura, M. Shiro, M. Shionoya, *Angew. Chem. Int. Ed.* **2009**, *48*, 7006–7009.

[125] A. N. Swinburne, M. J. Paterson, A. Beeby, J. W. Steed, *Chem. Eur. J.* **2010**, *16*, 2714–2718.

[126] R. P. Sijbesma, S. S. Wijmenga, R. J. M. Nolte, *J. Am. Chem. Soc.* **1992**, *114*, 9807–9813.

[127] S. Wang, T. Sawada, K. Ohara, K. Yamaguchi, M. Fujita, *Angew. Chem. Int. Ed.* **2016**, *55*, 2063–2066.

[128] Y.-Y. Zhan, T. Kojima, T. Nakamura, T. Takahashi, S. Takahashi, Y. Haketa, Y. Shoji, H. Maeda, T. Fukushima, S. Hiraoka, *Nat. Commun.* **2018**, *9*, 4530.

[129] H. Wu, Y. Wang, B. Song, H.-J. Wang, J. Zhou, Y. Sun, L. O. Jones, W. Liu, L. Zhang, X. Zhang, K. Cai, X.-Y. Chen, C. L. Stern, J. Wei, O. K. Farha, J. M. Anna, G. C. Schatz, Y. Liu, J. Fraser Stoddart, *Nat. Commun.* **2021**, *12*, 5191.

[130] D.-N. Yan, L.-X. Cai, P.-M. Cheng, S.-J. Hu, L.-P. Zhou, Q.-F. Sun, *J. Am. Chem. Soc.* **2021**, *143*, 16087–16094.

[131] S. Ibáñez, E. Peris, *Angew. Chem. Int. Ed.* **2020**, *59*, 6860–6865.

[132] J. F. Stoddart, *Chem. Soc. Rev.* **2009**, *38*, 1802–1820.

[133] W. R. Dichtel, O. Š. Miljanić, J. M. Spruell, J. R. Heath, J. F. Stoddart, *J. Am. Chem. Soc.* **2006**, *128*, 10388–10390.

[134] T. Sawada, H. Hisada, M. Fujita, *J. Am. Chem. Soc.* **2014**, *136*, 4449–4451.

[135] W. P. Jencks, *Annu. Rev. Biochem.* **1997**, *66*, 1–18.

[136] E. A. Ruben, J. P. Schwans, M. Sonnett, A. Natarajan, A. Gonzalez, Y. Tsai, D. Herschlag, *Biochemistry* **2013**, *52*, 1074–1081.

[137] Y. Wang, M. Rickhaus, O. Blacque, K. K. Baldridge, M. Juríček, J. S. Siegel, *J. Am. Chem. Soc.* **2022**, *144*, 2679–2684.

[138] S. Yamada, *Chem. Rev.* **2018**, *118*, 11353–11432.

[139] C. R. Kennedy, S. Lin, E. N. Jacobsen, *Angew. Chem. Int. Ed.* **2016**, *55*, 12596–12624.

[140] Y. Zhao, C. Beuchat, Y. Domoto, J. Gajewy, A. Wilson, J. Mareda, N. Sakai, S. Matile, *J. Am. Chem. Soc.* **2014**, *136*, 2101–2111.

[141] A. A. Kroeger, A. Karton, *Org. Chem. Front.* **2021**, *8*, 4408–4418.

[142] P. Spenst, A. Sieblist, F. Würthner, *Chem. Eur. J.* **2017**, *23*, 1667–1675.

[143] M. Sapotta, A. Hofmann, D. Bialas, F. Würthner, *Angew. Chem. Int. Ed.* **2019**, *58*, 3516–3520.

[144] M. Kardos, **14. Juni 1913**, D. R. P. 276357.

[145] F. Würthner, *Chem. Commun.* **2004**, 1564–1579.

[146] C. A. Hunter, J. K. Sanders, *J. Am. Chem. Soc.* **1990**, *112*, 5525–5534.

[147] C. Kaufmann, D. Bialas, M. Stolte, F. Würthner, *J. Am. Chem. Soc.* **2018**, *140*, 9986–9995.

[148] C. Kaufmann, W. Kim, A. Nowak-Król, Y. Hong, D. Kim, F. Würthner, *J. Am. Chem. Soc.* **2018**, *140*, 4253–4258.

[149] Y. Hong, J. Kim, W. Kim, C. Kaufmann, H. Kim, F. Würthner, D. Kim, *J. Am. Chem. Soc.* **2020**, *142*, 7845–7857.

[150] S. Ogi, V. Stepanenko, K. Sugiyasu, M. Takeuchi, F. Würthner, *J. Am. Chem. Soc.* **2015**, *137*, 3300–3307.

[151] W. Wagner, M. Wehner, V. Stepanenko, F. Würthner, *J. Am. Chem. Soc.* **2019**, *141*, 12044–12054.

[152] P. Spenst, R. M. Young, M. R. Wasielewski, F. Würthner, *Chem. Sci.* **2016**, *7*, 5428–5434.

[153] Y. Hong, M. Rudolf, M. Kim, J. Kim, T. Schembri, A.-M. Krause, K. Shoyama, D. Bialas, M. I. S. Röhr, T. Joo, H. Kim, D. Kim, F. Würthner, *Nat. Commun.* **2022**, *13*, 4488.

[154] N. Zink-Lorre, E. Font-Sanchis, Á. Sastre-Santos, F. Fernández-Lázaro, *Chem. Commun.* **2020**, *56*, 3824–3838.

[155] S. Chen, D. Meng, J. Huang, N. Liang, Y. Li, F. Liu, H. Yan, Z. Wang, *CCS Chem.* **2021**, *3*, 78–84.

[156] B. Mahlmeister, R. Renner, O. Anhalt, M. Stolte, F. Würthner, *J. Mater. Chem. C* **2022**, *10*, 2581–2591.

[157] G. Li, Y. Zhao, J. Li, J. Cao, J. Zhu, X. W. Sun, Q. Zhang, *J. Org. Chem.* **2015**, *80*, 196–203.

[158] E. Kozma, W. Mróz, F. Villafiorita-Monteleone, F. Galeotti, A. Andicsová-Eckstein, M. Catellani, C. Botta, *RSC Adv.* **2016**, *6*, 61175–61179.

[159] S. V. Dayneko, E. Cieplechowicz, S. S. Bhojgude, J. F. Van Humbeck, M. Pahlevani, G. C. Welch, *Mater. Adv.* **2021**, *2*, 933–936.

[160] R. Schmidt, M. M. Ling, J. H. Oh, M. Winkler, M. Könemann, Z. Bao, F. Würthner, *Adv. Mater.* **2007**, *19*, 3692–3695.

[161] A. Ringk, W. S. Christian Roelofs, E. C. P. Smits, C. van der Marel, I. Salzmann, A. Neuhold, G. H. Gelinck, R. Resel, D. M. de Leeuw, P. Strohriegl, *Org. Electron.* **2013**, *14*, 1297–1304.

[162] X. Zhan, J. Zhang, S. Tang, Y. Lin, M. Zhao, J. Yang, H.-L. Zhang, Q. Peng, G. Yu, Z. Li, *Chem. Commun.* **2015**, *51*, 7156–7159.

[163] A. Nowak-Król, F. Würthner, *Org. Chem. Front.* **2019**, *6*, 1272–1318.

[164] F. S. Conrad-Burton, T. Liu, F. Geyer, R. Costantini, A. P. Schlaus, M. S. Spencer, J. Wang, R. H. Sánchez, B. Zhang, Q. Xu, M. L. Steigerwald, S. Xiao, H. Li, C. P. Nuckolls, X. Zhu, *J. Am. Chem. Soc.* **2019**, *141*, 13143–13147.

[165] T. Liu, J. Yang, F. Geyer, F. S. Conrad-Burton, R. Hernández Sánchez, H. Li, X. Zhu, C. P. Nuckolls, M. L. Steigerwald, S. Xiao, *Angew. Chem. Int. Ed.* **2020**, *59*, 14303–14307.

[166] C. Schaack, A. M. Evans, F. Ng, M. L. Steigerwald, C. Nuckolls, *J. Am. Chem. Soc.* **2022**, *144*, 42–51.

[167] J. Li, P. Li, M. Fan, X. Zheng, J. Guan, M. Yin, *Angew. Chem. Int. Ed.* **2022**, *61*, e2022025.

[168] Á. J. Jiménez, M.-J. Lin, C. Burschka, J. Becker, V. Settels, B. Engels, F. Würthner, *Chem. Sci.* **2014**, *5*, 608–619.

[169] R. Schmidt, J. H. Oh, Y.-S. Sun, M. Deppisch, A.-M. Krause, K. Radacki, H. Braunschweig, M. Könemann, P. Erk, Z. Bao, F. Würthner, *J. Am. Chem. Soc.* **2009**, *131*, 6215–6228.

[170] P. Osswald, F. Würthner, *J. Am. Chem. Soc.* **2007**, *129*, 14319–14326.

[171] W. Qiu, S. Chen, X. Sun, Y. Liu, D. Zhu, *Org. Lett.* **2006**, *8*, 867–870.

[172] B. Pagoaga, L. Giraudet, N. Hoffmann, *Eur. J. Org. Chem.* **2014**, *2014*, 5178–5195.

[173] R. Renner, B. Mahlmeister, O. Anhalt, M. Stolte, F. Würthner, *Chem. Eur. J.* **2021**, *27*, 11997–12006.

[174] L. Zhang, I. Song, J. Ahn, M. Han, M. Linares, M. Surin, H.-J. Zhang, J. H. Oh, J. Lin, *Nat. Commun.* **2021**, *12*, 142.

[175] W. Yue, W. Jiang, M. Böckmann, N. L. Doltsinis, Z. Wang, *Chem. Eur. J.* **2014**, *20*, 5209–5213.

[176] Z. Xie, F. Würthner, *Org. Lett.* **2010**, *12*, 3204–3207.

[177] Z. Xie, V. Stepanenko, K. Radacki, F. Würthner, *Chem. Eur. J.* **2012**, *18*, 7060–7070.

[178] B. Teichmann, A.-M. Krause, M.-J. Lin, F. Würthner, *Angew. Chem. Int. Ed.* **2022**, *61*, e202117625.

[179] M. M. Safont-Sempere, P. Osswald, K. Radacki, F. Würthner, *Chem. Eur. J.* **2010**, *16*, 7380–7384.

[180] M. M. Safont-Sempere, P. Osswald, M. Stolte, M. Grüne, M. Renz, M. Kaupp, K. Radacki, H. Braunschweig, F. Würthner, *J. Am. Chem. Soc.* **2011**, *133*, 9580–9591.

[181] P. Osswald, M. Reichert, G. Bringmann, F. Würthner, *J. Org. Chem.* **2007**, *72*, 3403–3411.

[182] Y. Nagata, T. Mori, *Front. Chem.* **2020**, *8*, 448.

[183] D. J. Cram, H. Steinberg, *J. Am. Chem. Soc.* **1951**, *73*, 5691–5704.

[184] D. J. Wilson, V. Boekelheide, R. W. Griffin, *J. Am. Chem. Soc.* **1960**, *82*, 6302–6304.

[185] G. P. Moss, P. A. S. Smith, D. Tavernier, *Pure Appl. Chem.* **1995**, *67*, 1307–1375.

[186] W. Geuder, S. Hünig, A. Suchy, *Angew. Chem. Int. Ed. Engl.* **1983**, *22*, 489–490.

[187] M. Bühner, W. Geuder, W.-K. Gries, S. Hünig, M. Koch, T. Poll, *Angew. Chem. Int. Ed. Engl.* **1988**, *27*, 1553–1556.

[188] H. Langhals, R. Ismael, *Eur. J. Org. Chem.* **1998**, *1998*, 1915–1917.

[189] T. A. Barendt, W. K. Myers, S. P. Cornes, M. A. Lebedeva, K. Porfyrakis, I. Marques, V. Félix, P. D. Beer, *J. Am. Chem. Soc.* **2020**, *142*, 349–364.

[190] S. E. Penty, M. A. Zwijnenburg, G. R. F. Orton, P. Stachelek, R. Pal, Y. Xie, S. L. Griffin, T. A. Barendt, *J. Am. Chem. Soc.* **2022**, *144*, 12290–12298.

[191] I. Solymosi, S. Krishna, E. Nuin, H. Maid, B. Scholz, D. M. Guldi, M. E. Pérez-Ojeda, A. Hirsch, *Chem. Sci.* **2021**, *12*, 15491–15502.

[192] G. Ouyang, J. Rühe, Y. Zhang, M.-J. Lin, M. Liu, F. Würthner, *Angew. Chem. Int. Ed.* **2022**, *61*, e2022067.

[193] M. Weh, J. Rühe, B. Herbert, A.-M. Krause, F. Würthner, *Angew. Chem. Int. Ed.* **2021**, *60*, 15323–15327.

[194] J.-M. Lehn, *Supramolecular Chemistry, Concepts and Perspectives*, Wiley-VCH, Weinheim, **1995**.

[195] *Supramolecular Catalysts: Design, Fabrication, and Applications*, World Scientific, Singapore, **2020**.

[196] X. Wang, F. Jia, L.-P. Yang, H. Zhou, W. Jiang, *Chem. Soc. Rev.* **2020**, *49*, 4176–4188.

[197] A. R. A. Palmans, *Mol. Syst. Des. Eng.* **2017**, *2*, 34–46.

[198] F. Toda, K. Tanaka, *Chem. Lett.* **1983**, *12*, 661–664.

[199] W. H. R. Pirkle, S. R., *J. Am. Chem. Soc.* **1987**, *109*, 7190–7191.

[200] F. C. Spano, *Acc. Chem. Res.* **2010**, *43*, 429–439.

[201] J. Rühe, D. Bialas, P. Spenst, A.-M. Krause, F. Würthner, *Org. Mater.* **2020**, *02*, 149–158.

[202] Y. Shen, C.-F. Chen, *Chem. Rev.* **2012**, *112*, 1463–1535.

[203] M. Gingras, *Chem. Soc. Rev.* **2013**, *42*, 1051–1095.

[204] P. Ravat, *Chem. Eur. J.* **2021**, *27*, 3957–3967.

[205] T. Hartung, R. Machleid, M. Simon, C. Golz, M. Alcarazo, *Angew. Chem. Int. Ed.* **2020**, *59*, 5660–5664.

[206] H. Yoo, J. Yang, A. Yousef, M. R. Wasielewski, D. Kim, *J. Am. Chem. Soc.* **2010**, *132*, 3939–3944.

[207] P. Thordarson, *Chem. Soc. Rev.* **2011**, *40*, 1305–1323.

[208] A. E. Hargrove, Z. Zhong, J. L. Sessler, E. V. Anslyn, *New. J. Chem.* **2010**, *34*, 348–354.

[209] G. Wulff, *Chem. Rev.* **2002**, *102*, 1–27.

[210] M. Nishio, Y. Umezawa, K. Honda, S. Tsuboyama, H. Suezawa, *CrystEngComm* **2009**, *11*, 1757–1788.

[211] C. Goedicke, H. Stegemeyer, *Tetrahedron Lett.* **1970**, *11*, 937–940.

[212] A. Brown, C. M. Kemp, S. F. Mason, *J. Chem Soc. A* **1971**, 751–755.

[213] M. Weh, A. A. Kroeger, K. Shoyama, M. Grüne, A. Karton, F. Würthner, *Angew. Chem. Int. Ed.* **2023**, *62*, e202301301.

[214] W. P. Jencks, *Catalysis in chemistry and enzymology*, Courier Corporation, **1987**.

[215] H.-D. Lutter, F. Diederich, *Angew. Chem. Int. Ed. Engl.* **1986**, *25*, 1125–1127.

[216] J. Kang, J. Rebek, *Nature* **1997**, *385*, 50–52.

[217] A. J. Kirby, *Angew. Chem. Int. Ed. Engl.* **1996**, *35*, 706–724.

[218] T. Habicher, F. Diederich, V. Gramlich, *Helv. Chim. Acta* **1999**, *82*, 1066–1095.

[219] M. Yoshizawa, M. Tamura, M. Fujita, *Science* **2006**, *312*, 251–254.

[220] C. Kremer, A. Lützen, *Chem. Eur. J.* **2013**, *19*, 6162–6196.

[221] M. Morimoto, S. M. Bierschenk, K. T. Xia, R. G. Bergman, K. N. Raymond, F. D. Toste, *Nat. Catal.* **2020**, *3*, 969–984.

[222] H. Zhou, X.-Y. Pang, X. Wang, H. Yao, L.-P. Yang, W. Jiang, *Angew. Chem. Int. Ed.* **2021**, *60*, 25981–25987.

[223] X. Huang, X. Wang, M. Quan, H. Yao, H. Ke, W. Jiang, *Angew. Chem. Int. Ed.* **2021**, *60*, 1929–1935.

[224] Y. Lyu, P. Scrimin, *ACS Catal.* **2021**, *11*, 11501–11509.

[225] F. Diederich, H. D. Lutter, *J. Am. Chem. Soc.* **1989**, *111*, 8438–8446.

[226] D. A. Stauffer, R. E. Barrans Jr, D. A. Dougherty, *Angew. Chem. Int. Ed. Engl.* **1990**, *29*, 915–918.

[227] A. McCurdy, L. Jimenez, D. A. Stauffer, D. A. Dougherty, *J. Am. Chem. Soc.* **1992**, *114*, 10314–10321.

[228] A. J. Kennan, H. W. Whitlock, *J. Am. Chem. Soc.* **1996**, *118*, 3027–3028.

[229] K. Wang, J. H. Jordan, X.-Y. Hu, L. Wang, *Angew. Chem. Int. Ed.* **2020**, *59*, 13712–13721.

[230] Y. Murakami, J.-i. Kikuchi, Y. Hisaeda, O. Hayashida, *Chem. Rev.* **1996**, *96*, 721–758.

[231] Y. Zhao, Y. Cotelle, L. Liu, J. López-Andarias, A.-B. Bornhof, M. Akamatsu, N. Sakai, S. Matile, *Acc. Chem. Res.* **2018**, *51*, 2255–2263.

[232] A. A. Kroeger, A. Karton, *Chem. Eur. J.* **2021**, *27*, 3420–3426.

[233] C. García-Simón, R. Gramage-Doria, S. Raoufmoghaddam, T. Parella, M. Costas, X. Ribas, J. N. H. Reek, *J. Am. Chem. Soc.* **2015**, *137*, 2680–2687.

[234] C. Zhao, Q.-F. Sun, W. M. Hart-Cooper, A. G. DiPasquale, F. D. Toste, R. G. Bergman, K. N. Raymond, *J. Am. Chem. Soc.* **2013**, *135*, 18802–18805.

[235] C. Tan, D. Chu, X. Tang, Y. Liu, W. Xuan, Y. Cui, *Chem. Eur. J.* **2019**, *25*, 662–672.

[236] *Comprehensive Supramolecular Chemistry, Vol. 4*, Elsevier Science Ltd, Oxford, **1996**.

[237] A. Spek, *Acta Crystallogr. A* **1990**, *46*, C34.

[238] T. Kaehler, A. John, T. Jin, M. Bolte, H.-W. Lerner, M. Wagner, *Eur. J. Org. Chem.* **2020**, *2020*, 5847–5851.

[239] M. Rickhaus, L. Jundt, M. Mayor, *CHIMIA* **2016**, *70*, 192–202.

[240] S. H. Vosko, L. Wilk, M. Nusair, *Can. J. Phys.* **1980**, *58*, 1200–1211.

[241] C. Lee, W. Yang, R. G. Parr, *Phys. Rev. B* **1988**, *37*, 785–789.

[242] A. D. Becke, *J. Chem. Phys.* **1993**, *98*, 5648–5652.

[243] P. J. Stephens, F. J. Devlin, C. F. Chabalowski, M. J. Frisch, *J. Phys. Chem.* **1994**, *98*, 11623–11627.

[244] F. Weigend, R. Ahlrichs, *Phys. Chem. Chem. Phys.* **2005**, *7*, 3297–3305.

[245] S. Grimme, J. Antony, S. Ehrlich, H. Krieg, *J. Chem. Phys.* **2010**, *132*, 154104.

[246] S. Grimme, S. Ehrlich, L. Goerigk, *J. Comput. Chem.* **2011**, *32*, 1456–1465.

[247] Y. Zhao, D. G. Truhlar, *J. Phys. Chem. A* **2005**, *109*, 5656–5667.

[248] A. V. Marenich, C. J. Cramer, D. G. Truhlar, *J. Phys. Chem. B* **2009**, *113*, 6378–6396.

[249] L. Goerigk, R. Sharma, *Can. J. Chem.* **2016**, *94*, 1133–1143.

[250] P. R. Horn, Y. Mao, M. Head-Gordon, *Phys. Chem. Chem. Phys.* **2016**, *18*, 23067–23079.

[251] N. Mardirossian, M. Head-Gordon, *J. Chem. Phys.* **2016**, *144*, 214110.

[252] S. Grimme, C. Mück-Lichtenfeld, J. Antony, *J. Phys. Chem. C* **2007**, *111*, 11199–11207.

[253] S. Grimme, *Angew. Chem. Int. Ed.* **2008**, *47*, 3430–3434.

[254] A. Nowak-Król, M. I. S. Röhr, D. Schmidt, F. Würthner, *Angew. Chem. Int. Ed.* **2017**, *56*, 11774–11778.

[255] R. G. Lawton, W. E. Barth, *J. Am. Chem. Soc.* **1971**, *93*, 1730–1745.

[256] W. E. Barth, R. G. Lawton, *J. Am. Chem. Soc.* **1966**, *88*, 380–381.

[257] Y.-T. Wu, J. S. Siegel, *Chem. Rev.* **2006**, *106*, 4843–4867.

[258] M. Rickhaus, M. Mayor, M. Juríček, *Chem. Soc. Rev.* **2017**, *46*, 1643–1660.

[259] M. A. Majewski, M. Stępień, *Angew. Chem. Int. Ed.* **2019**, *58*, 86–116.

[260] L. T. Scott, M. M. Hashemi, M. S. Bratcher, *J. Am. Chem. Soc.* **1992**, *114*, 1920–1921.

[261] R. L. Disch, J. M. Schulman, *J. Am. Chem. Soc.* **1994**, *116*, 1533–1536.

[262] P. W. Rabideau, A. Sygula, *Acc. Chem. Res.* **1996**, *29*, 235–242.

[263] T. J. Seiders, K. K. Baldridge, G. H. Grube, J. S. Siegel, *J. Am. Chem. Soc.* **2001**, *123*, 517–525.

[264] Z. Marcinow, A. Sygula, A. Ellern, P. W. Rabideau, *Org. Lett.* **2001**, *3*, 3527–3529.

[265] P. A. Vecchi, C. M. Alvarez, A. Ellern, R. J. Angelici, A. Sygula, R. Sygula, P. W. Rabideau, *Organometallics* **2005**, *24*, 4543–4552.

[266] E. Solel, D. Pappo, O. Reany, T. Mejuch, R. Gershoni-Poranne, M. Botoshansky, A. Stanger, E. Keinan, *Chem. Sci.* **2020**, *11*, 13015–13025.

[267] Y. Yang, T. K. Ronson, Z. Lu, J. Zheng, N. Vanthuyne, A. Martinez, J. R. Nitschke, *Nat. Commun.* **2021**, *12*, 4079.

[268] M. Weh, A. A. Kroeger, K. Shoyama, M. Grüne, A. Karton, F. Würthner, *submitted*.

[269] Y. Tanaka, K. M.-C. Wong, V. W.-W. Yam, *Chem. Eur. J.* **2013**, *19*, 390–399.

[270] E. J. Dale, N. A. Vermeulen, A. A. Thomas, J. C. Barnes, M. Juríček, A. K. Blackburn, N. L. Strutt, A. A. Sarjeant, C. L. Stern, S. E. Denmark, J. F. Stoddart, *J. Am. Chem. Soc.* **2014**, *136*, 10669-10682.

[271] S. Ibáñez, E. Peris, *Angew. Chem. Int. Ed.* **2020**, *59*, 6860-6865.

[272] M. Mahl, M. A. Niyas, K. Shoyama, F. Würthner, *Nat. Chem.* **2022**, *14*, 457-462.

[273] R. A. Boto, F. Peccati, R. Laplaza, C. Quan, A. Carbone, J.-P. Piquemal, Y. Maday, J. Contreras-García, *J. Chem. Theory Comput.* **2020**, *16*, 4150–4158.

[274] K. G. Kennedy, D. T. Miles, *J. Undergrad. Chem. Res.* **2004**, *4*, 145-150.

[275] M. Weh, K. Shoyama, F. Würthner, *Nat. Commun.* **2023**, *14*, 243.

[276] M. M. Safont-Sempere, G. Fernández, F. Würthner, *Chem. Rev.* **2011**, *111*, 5784–5814.

[277] H. Jędrzejewska, A. Szumna, *Chem. Rev.* **2017**, *117*, 4863–4899.

[278] J.-M. Vincent, C. Philouze, I. Pianet, J.-B. Verlhac, *Chem. Eur. J.* **2000**, *6*, 3595–3599.

[279] N. Saito, R. Terakawa, M. Yamaguchi, *Chem. Eur. J.* **2014**, *20*, 5601–5607.

[280] F. Zhang, K. Radacki, H. Braunschweig, C. Lambert, P. Ravat, *Angew. Chem. Int. Ed.* **2021**, *60*, 23656–23660.

[281] X. Liu, Z. Shi, M. Xie, J. Xu, Z. Zhou, S. Jung, G. Cui, Y. Zuo, T. Li, C. Yu, Z. Liu, S. Zhang, *Angew. Chem. Int. Ed.* **2021**, *60*, 15080–15086.

[282] E. Murguly, R. McDonald, N. R. Branda, *Org. Lett.* **2000**, *2*, 3169–3172.

[283] A. M. Costero, M. Colera, P. Gaviña, S. Gil, L. E. Ochando, *New. J. Chem.* **2006**, *30*, 1263–1266.

[284] D. E. Fagnani, M. J. Meese Jr, K. A. Abboud, R. K. Castellano, *Angew. Chem. Int. Ed.* **2016**, *55*, 10726–10731.

[285] C. G. Claessens, T. Torres, *J. Am. Chem. Soc.* **2002**, *124*, 14522–14523.

[286] M. Mizumura, H. Shinokubo, A. Osuka, *Angew. Chem. Int. Ed.* **2008**, *47*, 5378–5381.

[287] M. Gsänger, J. H. Oh, M. Könemann, H. W. Höffken, A.-M. Krause, Z. Bao, F. Würthner, *Angew. Chem. Int. Ed.* **2010**, *49*, 740–743.

[288] T. R. Schulte, J. J. Holstein, G. H. Clever, *Angew. Chem. Int. Ed.* **2019**, *58*, 5562–5566.

[289] M. Ueda, T. Aoki, T. Akiyama, T. Nakamuro, K. Yamashita, H. Yanagisawa, O. Nureki, M. Kikkawa, E. Nakamura, T. Aida, Y. Itoh, *J. Am. Chem. Soc.* **2021**, *143*, 5121–5126.

[290] C. Liu, Y. Jin, D. Qi, X. Ding, H. Ren, H. Wang, J. Jiang, *Chem. Sci.* **2022**, *13*, 7014–7020.

[291] R. Amemiya, M. Yamaguchi, *Org. Biomol. Chem.* **2008**, *6*, 26–35.

[292] D. D. Boehr, R. Nussinov, P. E. Wright, *Nat. Chem. Biol.* **2009**, *5*, 789–796.

[293] H. N. Motlagh, J. O. Wrabl, J. Li, V. J. Hilser, *Nature* **2014**, *508*, 331–339.

[294] C. A. Hunter, *Chem. Soc. Rev.* **1994**, *23*, 101–109.

[295] J. C. Barnes, M. Juríček, N. L. Strutt, M. Frasconi, S. Sampath, M. A. Giesener, P. L. McGrier, C. J. Bruns, C. L. Stern, A. A. Sarjeant, J. F. Stoddart, *J. Am. Chem. Soc.* **2013**, *135*, 183–192.

[296] E. J. Dale, N. A. Vermeulen, A. A. Thomas, J. C. Barnes, M. Juríček, A. K. Blackburn, N. L. Strutt, A. A. Sarjeant, C. L. Stern, S. E. Denmark, J. F. Stoddart, *J. Am. Chem. Soc.* **2014**, *136*, 10669–10682.

[297] M. Mahl, M. A. Niyas, K. Shoyama, F. Würthner, *Nat. Chem.* **2022**, *14*, 457–462.

[298] W. Yang, G. Longhi, S. Abbate, A. Lucotti, M. Tommasini, C. Villani, V. J. Catalano, A. O. Lykhin, S. A. Varganov, W. A. Chalifoux, *J. Am. Chem. Soc.* **2017**, *139*, 13102–13109.

[299] W. Yang, R. R. Kazemi, N. Karunathilake, V. J. Catalano, M. A. Alpuche-Aviles, W. A. Chalifoux, *Org. Chem. Front.* **2018**, *5*, 2288–2295.

[300] B. Mahlmeister, M. Mahl, H. Reichelt, K. Shoyama, M. Stolte, F. Würthner, *J. Am. Chem. Soc.* **2022**, *144*, 10507–10514.

[301] N. Berova, K. Nakanishi, *Exciton Chirality Method: Principles and Applications, Chapter 12 in Circular Dichroism: Principles and Applications*, 2 ed., Wiley, **2000**.

[302] A. C. Hernandez-Perez, A. Vlassova, S. K. Collins, *Org. Lett.* **2012**, *14*, 2988-2991.

[303] S. Sengupta, R. K. Dubey, R. W. M. Hoek, S. P. P. van Eeden, D. D. Gunbaş, F. C. Grozema, E. J. R. Sudhölter, W. F. Jager, *J. Org. Chem.* **2014**, *79*, 6655–6662.

[304] D. J. Miller, M. Bashir-Uddin Surfraz, M. Akhtar, D. Gani, R. K. Allemann, *Org. Biomol. Chem.* **2004**, *2*, 671–688.

[305] N. Hoffmann, J.-P. Pete, *J. Org. Chem.* **1997**, *62*, 6952–6960.

[306] Seybold G., W. G., *Dyes Pigm.* **1989**, *11*, 303.

[307] Origin(Pro), Version 2020, OriginLab Corporation, Northampton, MA, USA.

[308] T. Naranjo, K. M. Lemishko, S. de Lorenzo, Á. Somoza, F. Ritort, E. M. Pérez, B. Ibarra, *Nat. Commun.* **2018**, *9*, 4512.

[309] W. Kabsch, *Acta Crystallogr. D* **2010**, *66*, 125–132.

[310] Bruker, XPREP Version 2014/2, Bruker AXS Inc., Madison.

[311] G. M. Sheldrick, *Acta Crystallogr. A* **2015**, *71*, 3–8.

[312] G. M. Sheldrick, *Acta Crystallogr. C* **2015**, *71*, 3–8.

[313] M. A. Khan, D. J. Goss, *Biochemistry* **2012**, *51*, 1388−1395.

[314] M. Hesse, H. Meier, B. Zeeh, *Spectroscopic Methods in Organic Chemistry*, Thieme, Stuttgart, **1997**.

[315] G. Bodenhausen, R. R. Ernst, *J. Am. Chem. Soc.* **1982**, *104*, 1304−1309.

[316] P. J. Stephens, F. J. Devlin, C. F. Chabalowski, M. J. Frisch, *J. Phys. Chem.* **1994**, *98*, 11623−11627.

[317] C. Gonzalez, H. B. Schlegel, *J. Chem. Phys.* **1989**, *90*, 2154−2161.

[318] C. Gonzalez, H. B. Schlegel, *J. Phys. Chem.* **1990**, *94*, 5523−5527.

[319] M. J. Frisch, **2016**, et al. Wallingford, CT.

[320] Y. Shao, e. al., *Mol Phys.* **2015**, *113*, 184–215.

[321] C. F. Macrae, I. Sovago, S. J. Cottrell, P. T. A. Galek, P. McCabe, E. Pidcock, M. Platings, G. P. Shields, J. S. Stevens, M. Towler, P. A. Wood, *J. Appl. Crystallogr.* **2020**, *53*, 226–235.

[322] C. S. Jones, E. Elliott, J. S. Siegel, *Synlett* **2004**, *2004*, 187−191.

[323] available free of charge via http://supramolecular.org (10.08.2022).

[324] R. Sens, K. H. Drexhage, *J. Lumin.* **1981**, *24*, 709–712.

[325] M. J. Frisch, e. al. , Gaussian 16, Revision A.03, Gaussian Inc. Wallingford CT, 2016.

[326] M. A. Spackman, D. Jayatilaka, *CrystEngComm* **2009**, *11*, 19–32.

Individual Contribution

The coauthors of the manuscripts included in this partially cumulative thesis are informed and agree with the reprint and the respective individual contributions as stated below.

Deracemization of Carbohelicenes by a Chiral Perylene Bisimide Cyclophane Template Catalyst

M. Weh, J. Rühe, B. Herbert, A.-M. Krause, F. Würthner, *Angew. Chem. Int. Ed.* **2021**, *60*, 15323−15327.

Autor	**M.W.**	**J.R.**	**B.H.**	**A.-M.K.**	**F.W.**	**∑ in Prozent**
Forschungsdesign	2%	1%			3%	6%
Synthese/Charakterisierung	38%		12%			50%
Optische Untersuchungen	3%					3%
Kristallstrukturanalyse				5%		5%
Titrationsstudien	9%	5%				14%
NMR Studien	5%					5%
(TD)-DFT Rechnungen	1%					1%
Verfassen d. Publikation	6%				3%	9%
Korrektur d. Publikation		1%			3%	4%
Koordination d. Publikation	1%				2%	3%
Summe	**65%**	**7%**	**12%**	**5%**	**11%**	**100%**

π–π Catalysis Made Asymmetric - Enantiomerization Catalysis Mediated by the Chiral π-System of a Perylene Bisimide Cyclophane

M. Weh, A. A. Kroeger, K. Shoyama, M. Grüne, A. Karton, F. Würthner, *Angew. Chem. Int. Ed.* **2023**, *62*, e202301301.

Autor	**M.W.**	**A.A.K.**	**K.S.**	**M.G.**	**A.K.**	**F.W.**	**∑ in Prozent**
Forschungsdesign	4%	4%			1%	1%	10%
Synthese/Charakterisierung	18%						18%
Zeitabhängige CD Studien	5%						5%
Kristallstrukturanalyse			1%				1%
Titrationsstudien	2%						2%
NMR Studien	8%			1%			9%
(TD)-DFT Rechnungen		33%					33%
Verfassen d. Publikation	6%	6%			1%	1%	14%
Korrektur d. Publikation					1%	2%	3%
Koordination d. Publikation	1%	1%			1%	2%	5%
Summe	**44%**	**44%**	**1%**	**1%**	**4%**	**6%**	**100%**

Preferential Molecular Recognition of Heterochiral Guests within a Cyclophane Receptor

M. Weh, K. Shoyama, F. Würthner, *Nat. Commun.* **2023**, *14*, 243.

Autor	**M.W.**	**K.S.**	**F.W.**	**∑ in Prozent**
Forschungsdesign	3%		4%	7%
Synthese/Charakterisierung	37%			37%
Optische Untersuchungen	5%			5%
Kristallstrukturanalyse		8%		8%
Titrationsstudien	18%			18%
NMR Studien	3%			3%
(TD)-DFT Rechnungen	5%			5%
Verfassen d. Publikation	6%		3%	9%
Korrektur d. Publikation			4%	4%
Koordination d. Publikation	1%		3%	4%
Summe	**78%**	**8%**	**14%**	**100%**

Acknowledgement/Danksagung

Zunächst möchte ich mich herzlich bei **Prof. Dr. Frank Würthner** für die Möglichkeit zur Anfertigung dieser Arbeit auf einem spannenden Thema und in einer exzellenten Gruppe unter hervorragenden Bedingungen bedanken. Ich danke ihm für die vielen wissenschaftlichen Diskussionen, die kritischen und konstruktiven Ratschläge und Anregungen, sowie für die Hilfe beim gemeinsamen Verfassen und Überarbeiten von Manuskripten und nicht zuletzt auch für das mir entgegengebrachte Vertrauen, die persönliche Wertschätzung und die damit verbundenen Freiheiten. Außerdem möchte ich mich für die Unterstützung bei der Bewerbung für ein Kekulé Stipendium bedanken und die vielleicht einmalige Möglichkeit für mich in San Diego an einer internationalen Konferenz teilzunehmen. Lieber Frank, vielen Dank für alles!

Weiterhin bedanke ich mich bei **Dr. David Bialas** und **Dr. Matthias Stolte** für die wissenschaftlichen Diskussionen und für die Unterstützung in ihrer Rolle als Subgroupleiter. Herrn Dr. Matthias Stolte bin ich nicht nur für seine Expertise in allen Bereichen der optischen Spektroskopie dankbar, sondern auch insbesondere für die vielen motivierenden Worte, die er stets für mich übrig hatte, wenn es einmal nicht optimal lief.

Mein besonderer Dank geht außerdam an **Dr. Asja Kroeger**, die durch theoretische Betrachtungen tiefere Einblicke in die Ergebnisse dieser Thesis ermöglichte und diese damit noch zusätzlich aufzuwerten vermochte. Ich bedanke mich für die sehr gute Zusammenarbeit, die insbesondere Kapitel 4, jedoch auch Kapitel 5 dieser Arbeit betrifft. In diesem Zusammenhang danke ich auch **Prof. Dr. Amir Karton**, der zusammen mit **Prof. Dr. Frank Würthner** diese Kollaboration erst möglich gemacht hat. Für die Hilfe bei allen anderen Rechnungen möchte ich insbesondere **Niyas Mundakkamattathil Abdul Salam** aber auch **Dr. Menyhárt Botond Sárosi** meinen Dank aussprechen.

Für die finanzielle Unterstützung in Form eines Chemiefonds-Stipendiums bin ich dem **Verband der Chemischen Industrie e.V.** zu großem Dank verpflichtet.

Einen wichtigen Beitrag zu dieser Arbeit haben außerdem **Dr. Kazutaka Shoyama**, **Ana-Maria Krause** und **Olga Anhalt** geleistet, indem sie teils komplizierte Einkristall-strukturanalysen erfolgreich durchführten und mir die Ergebnisse zur Verfügung stellten. Ich bedanke mich vielmals bei allen dreien.

Bei **Dr. Matthias Grüne**, **Patricia Altenberger** und **Stefanie Schmitt** bedanke ich mich für die Aufnahme von NMR-Spektren am 600 MHz Spektrometer und die hilfsbereite, freundliche

Atmosphäre in der NMR Abteilung. Ähnliches möchte ich an **Dr. Juliane Adelmann** richten, die für die massenspektrometrischen Messungen Sorge getragen hat.

Ich danke dem gesamten technischen Personal des AK Würthner für die Hilfen im Laboralltag und die großen Bemühungen ein Umfeld zu schaffen, das es erlaubt der Forschung ohne Störungen nachzugehen, sowie den Sekretärinnen für die Hilfe bei administrativen und organisatorischen Aufgaben. Genannt seien hier insbesondere **Petra Seufert-Baumbach**, **Anja Rausch**, **Julius Albert**, **Maximilian Roth**, **Eleonore Klaus** und **Sarah Bullnheimer**.

Mein Dank gilt weiter meinen Praktikanten **Christopher Fischer** und **Jonas Hartmann**, meinen Auszubildenden **Lukas Schmidt** und **Maximilian Nowack** und meinen Bachelorstudenten **Benedikt Herbert** und **Alexander Gerstner** für die synthetische Unterstützung

Tim Schlossarek, **Lara Kleine-Kleffmann**, **Jessica Rühe** und meiner alten Freundin aus der Zeit des Bachelor- und Masterstudiums **Sophie Ricker** danke ich für das Korrekturlesen (von Teilen) dieser Arbeit recht herzlich.

Dem gesamten **AK Würthner** und dem **AK Beuerle** danke ich für die schöne gemeinsame Zeit, die vielen lustigen Stammtische, die unterhaltsamen Kaffeepausen und das wirklich tolle Miteinander im täglichen Laboralltag. Ich würde gerne noch einige Leute hervorheben, aber das würde nun wirklich den Rahmen dieser Danksagung sprengen.

Zu guter Letzt bedanke ich mich bei allen Menschen, die mir außerdhalb des Labors beigestanden haben und möchte hier insbesondere **Saskia Mengeler** für die außerordentlich hingebungsvolle Unterstützung danken.

List of Publications

Deracemization of Carbohelicenes by a Chiral Perylene Bisimide Cyclophane Template Catalyst

M. Weh, J. Rühe, B. Herbert, A.-M. Krause, F. Würthner, *Angew. Chem. Int. Ed.* **2021**, *60*, 15323–15327.

Preferential Molecular Recognition of Heterochiral Guests within a Cyclophane Receptor

M. Weh, K. Shoyama, F. Würthner, *Nat. Commun.* **2023**, *14*, 243.

π–π Catalysis Made Asymmetric - Enantiomerization Catalysis Mediated by the Chiral π-System of a Perylene Bisimide Cyclophane

M. Weh, A. A. Kroeger, K. Shoyama, M. Grüne, A. Karton, F. Würthner, *Angew. Chem. Int. Ed.* **2023**, *62*, e202301301.